

# SiNW-based Biosensors for Profiling Biomarkers in Breast Tumor Tissues

THÈSE N° 7013 (2016)

PRÉSENTÉE LE 18 MAI 2016

À LA FACULTÉ INFORMATIQUE ET COMMUNICATIONS

LABORATOIRE DES SYSTÈMES INTÉGRÉS (IC/STI)

PROGRAMME DOCTORAL EN MICROSYSTÈMES ET MICROÉLECTRONIQUE

ÉCOLE POLYTECHNIQUE FÉDÉRALE DE LAUSANNE

POUR L'OBTENTION DU GRADE DE DOCTEUR ÈS SCIENCES

PAR

Francesca PUPPO

acceptée sur proposition du jury:

Prof. Y. Leblebici, président du jury  
Prof. G. De Micheli, Dr S. Carrara, directeurs de thèse  
Prof. M. Di Ventra, rapporteur  
Prof. P. M. Sarro, rapporteuse  
Prof. A. Radenovic, rapporteuse



ÉCOLE POLYTECHNIQUE  
FÉDÉRALE DE LAUSANNE

Suisse  
2016



Life is what happens to you  
while you're busy making other plans.  
— John Lennon

To my beloved parents. Without their love, wisdom, and guidance,  
I would have not the courage to strive to achieve my dreams.



# Acknowledgements

This work is the result of a long journey that started four years ago in LSI, EPFL. I am now ready to move on to the next phase of my life but not without expressing all my appreciation and gratitude to all the people who made all this possible by helping me and by sharing part of my life with in Switzerland.

I would first like to express my sincere and warmest thank you to both my supervisors, Prof. Giovanni De Micheli (in art *nanni*) and Dr. Sandro Carrara, for offering me the opportunity to work on such an advanced field of technology, with limitless resources, freedom to explore and patience. Thank you for the trust you put in me from the beginning, including my pre-doctoral internship. I am deeply grateful to nanni for his countless support, precious advices, understanding, and insightful comments throughout the development of this research. Thank you for the huge support he demonstrated in this last year of Ph.D. and his continuous supervision and motivational support in the very last period of “stressful” thesis and proposal writing. He demonstrated to understand and support my ambitions for the future, he taught me and guided me by providing a number of precious comments and suggestions. I want to express my deepest gratitude also to Sandro for the constant exchange, precious advices, and continuous help in the application related experiments, from the subject formulation to the analysis of the results. I am also very grateful to him for always being able to counteract my pessimism, by patiently supporting me with constant encouragements throughout my research. I feel I have learned so much from the comments and corrections of both my supervisors; I hope I will have the opportunity to demonstrate how much their help has been relevant to my personal growing. Thank you to them also for the perfect friendly atmosphere they have been able to create in LSI.

I want to thank the members of my thesis jury: the president Prof. Yusuf Leblebici, Prof. Massimiliano Di Ventra, Prof. Pasqualina M. Sarro, and Prof. Aleksandra Radenovic, for accepting to read my thesis, and the time and effort they have put in evaluating it and providing useful feedbacks.

Thank you to Prof. Yusuf Leblebici for the interesting discussions we had during the research. Thank you to Prof. Pasqualina Sarro for the useful exchanges. My sincere gratitude to Dr. Marie-Agnès Doucey for giving me the opportunity to collaborate on this project. Thank you for teaching and supervising me on the biological/chemical side of my research. Thank you for the support, the innovative ideas, and the interesting exchanges. My sincere thank you to Prof. Massimiliano Di Ventra (in art *Max*) for offering me the opportunity to perform an exchange project in his lab at UC, San Diego. Thank you for the fruitful exchanges and

## Acknowledgements

---

the constant support. My deepest gratitude is directed also to Dr. Fabio Traversa, for his supervision throughout the entire exchange research. A theoretical work is not easy stuff for an experimentalist like I am, but it can become so if you have somebody like Fabio around. Thank you to his continuous input, his valuable comments, his patience and technical support, and finally, his extreme optimism. Thank you to both Max and Fabio for the kind “hospitality” in their lab, the happy and constructive lunch and coffee breaks, and their motivational support. I want to express my warmest gratitude to Michele. He helped me so much in this research that I have been always thinking about him as my third supervisor/mentor. Thank you for the technical support, the endless constructive discussions (about scientific topics and not only!), the constant advices and corrections and, finally, his friendship. Thank you also to Pierre-Emmanuel for the fruitful inputs in this research, the interesting discussions and the extreme kindness he always demonstrated.

Thank you to all the CMi staff. In particular, I want to thank Zdenek, Cyrille, Joffrey, Didier and Anthony for their constant availability and support.

Thank you to my Master's students Ardalan Lotfi and Alessandro Vallero for the help and collaborative spirit. Thanks to Dr. Ali Zaher, from the University of Oslo, for the great collaboration on the design of the CMOS readout circuit. I want to thank the technical support entourage at LSI: Christina, Anil and Rodolphe. A special thank to Christina: thank you for the prompt answers to all questions, solutions to all problems, and constant support. LSI would not be such a nice and organized lab without her presence and without her smile!

I also would like to thank present and past members of the LSI. Thank you to Camilla, Irene, Andrea, Federico, Vasilis, Sara, Cristina, Shashi, Srini, Wenqui, Jaume. A special thank you goes to Jacopo, for his ability of making me smile, no matter what, and my office mates Michele and Julien. Thank you also to Francesca for the coffee and lunch breaks we spent together. A special thank to the “Self-Assembly Beer Group” (Oliver and Andrea) for all the beers we drunk together, our parties, for all the support and friendship they showed to me. Thank you to my amazing volley-ball team “The Dream Team”, without which my life in Switzerland would have not been the same. My special thank you to Saska and Ombri for offering me the real, precious friendship I have always desired. Thank you to my best friend Veronica who, even is far away, I always feel at my side.

I have a very special and warm thought for my partner, Fabio. Thank you for your motivational support, your valuable advices, your patience, your smile, your enthusiasm..well, thank you for being all you are..thank you for showing me the love I have always dreamed about.

And last but not least, the warmest thank you is directed to my family. Thank you to my grandmother Olga who has always followed and supported me in each phase of my life. Thank you to my beloved brother Riccardo and his wonderful wife Arianna. Ricky, even if far, you are present in each step I do in my life and, like when we were kids, to me, you will always be a model to follow (although I have always tried not to show it :) ). Finally, my parents are the persons who really made all this possible. Thank you for their uninterrupted love, unconditional support, and presence in the best and worst periods of this long journey, as well as for all the precious teachings that made me the person who I am now and that will drive me throughout my entire life.

# Abstract

Breast cancer is the most common life-threatening malignancy in women of most developed countries today, with approximately 200,000 new cases diagnosed every year. About 30% of these cases progress to metastatic disease and death. Considering that one-third of these cancer deaths could be decreased if detected and treated early, new strategies for early breast cancer detection are needed to improve the efficacy of current diagnostics. The sensitive analysis of proteins such as breast cancer biomarkers has become the focus of intensive research due to its relevance to tumor diagnosis and therapy decision-making. However, the state-of-the-art diagnostic tools still lack the level of resolution needed for the detection of biomarkers at the very early stage of the disease, when treatments have more probability of success, and when protein concentration in tumor tissue is still very low.

Nanotechnologies have shown great potential for the development of high-sensitive, portable devices for clinical applications. In particular, *Silicon NanoWires* (SiNWs), with their unique properties such as the high surface-to-volume ratio and the size comparable to biomolecules, and combined with the specificity of immune-sensing techniques, are natural candidates for the fabrication of nanosensors. Thanks to their compatibility with conventional *Complementary Metal Oxide Semiconductor* (CMOS) technology, SiNWs have been incorporated in standard *Field Effect Transistors* (FETs). In biosensing, *Silicon NanoWire Field Effect Transistors* (SiNW-FETs) have been shown a promising method for the label-free detection of trace amounts of biomolecules. However, detection of Antigen (Ag) using Antibody (Ab)-immobilized SiNW-FETs is limited by ionic screening effects that reduce the sensor responsiveness and limit their applicability in tumor tissue.

Here, we propose novel SiNW-based biosensing strategies with the aim of overcoming current sensitivity limitations of conventional SiNW-FET biosensors for the detection of breast cancer biomarkers in real human samples. Specifically, we address this goal by investigating two different approaches of biosensing. In the first method, we push the sensitivity and specificity of SiNW-FETs to their limits by proposing an alternative way of doing sensing in dry conditions. We show that in-air electrical measurements of Ab-Ag binding have the big advantage of increased Debye screening length in non-bulk solutions, and enable highly sensitive (femtomolar) and specific measurements in breast tumor extract.

Then, we present a completely novel biosensing paradigm that shows, for the first time, the use of memristive effects in fabricated SiNWs for biodetection purposes. This novel detection method has been named *Voltage Gap* (VoG)-biosensing as it is based on the changes of the VoG parameter, observed in the hysteretic characteristic of memristive devices, as a function

## Abstract

---

of biomolecules. In this research, we demonstrate the use of the memristive-based VoG effect in *Schottky Barrier* (SB) SiNWs for the high-resolution sensing of ionic and biological species both in ideal buffer solutions and in real tumor tissue extracts. Moreover, we propose an original theory enabling the physical interpretation and prediction of the mechanisms underlying the VoG-biosensing method in memristive devices. Finally, we demonstrate the potential of our system for future integration in a multi-panel VoG-biosensing platform. We fabricated a PDMS microfluidics enabling selective and high-quality functionalization of the nanowires. We also realized a CMOS readout circuit for multiplexed VoG acquisition. The simulations demonstrate the feasibility of the approach and the potential for the integration of the reader with a portable and automated biosensing platform. Microfluidics and VoG reader will enable fast, concurrent detection of multiple angiogenic and inflammatory ligands in tumor tissue. This will highly improve the level of knowledge of the cancer disease by capturing the heterogeneity and the complexity of the tumor microenvironment, thus leading to novel opportunities in breast cancer diagnosis.

Key words: nanotechnology, device fabrication, silicon nanowires, SiNW-FETs, Schottky barrier, voltage gap, biosensors, breast tumor biomarkers, tumor extract, sensitivity, detection in air.



## Sommario

Oggi, il cancro al seno è il tumore maligno più comune nelle donne dei paesi più sviluppati, con circa 200.000 nuovi casi diagnosticati ogni anno. In circa il 30% di questi casi la malattia progredisce verso metastasi e morte. Considerando che un terzo dei decessi per questo tumore potrebbe essere diminuito se individuato e trattato anticipatamente, è necessario trovare nuove strategie per la diagnosi precoce del cancro al seno con l'obiettivo di migliorare l'efficacia della diagnostica attuale. L'analisi di proteine quali biomarcatori del cancro al seno è diventata il fulcro dell'attuale ricerca grazie alla sua rilevanza per il processo decisionale di diagnosi e terapia del tumore. Tuttavia, lo stato dell'arte degli attuali strumenti di diagnostica non ha ancora raggiunto il livello di risoluzione necessario per l'individuazione di biomarcatori nella prima fase della malattia, quando i trattamenti hanno più probabilità di successo, e quando la concentrazione di proteine nel tessuto tumorale è ancora molto bassa.

Le nanotecnologie hanno dimostrato un grande potenziale per lo sviluppo di dispositivi portatili, ad alta sensibilità, per applicazioni cliniche. In particolare, i *nanofili di silicio (SiNW)*, con le loro proprietà uniche come l'elevato rapporto superficie-volume e la dimensione paragonabile alle biomolecole, combinate con la specificità delle tecniche immunologiche, sono candidati naturali per la realizzazione di nanosensori. Grazie alla loro compatibilità con la tecnologia convenzionale CMOS, sono stati integrati negli standard *transistor ad effetto di campo (FET)*. I biosensori basati sul *SiNW-FET* hanno dimostrato di essere un metodo *label-free* promettente per il rilevamento di tracce di biomolecole. Tuttavia, il rilevamento dell'antigene (Ag) usando il *SiNW-FET* modificato con anticorpi è limitato dagli effetti di *screening* ionico che riducono la capacità di risposta del sensore e la sua applicabilità in tessuto tumorale.

Qui, vi proponiamo nuove strategie di *detection* basate su biosensori a *SiNW* con l'obiettivo di superare i limiti di sensibilità della tecnologia convenzionale basata sul *SiNW-FET* per l'individuazione di biomarcatori del tumore al seno in campioni umani. In particolare, affrontiamo questo obiettivo studiando due diversi approcci di *biosensing*. Nel primo metodo, portiamo agli estremi la sensibilità e la specificità dei biosensori *SiNW-FET* proponendo un modo alternativo di fare *detection* in asciutto. Dimostriamo che la misura elettrica, in aria, dell'associazione *Ab-Ag* ha il grande vantaggio di determinare una maggiore *Debye screening length* rispetto al caso in soluzione; questo rende possibile la *detection* altamente sensibile (femtomolare) e specifica nel tessuto tumorale del seno.

Inoltre, vi presentiamo un paradigma di *detection* completamente nuovo basato su un biosensore che, per la prima volta, si basa sugli effetti memristivi dei *SiNWs*. Questo metodo è stato nominato *Voltage-Gap (VoG)-biosensing* in quanto si basa sulla variazione del parame-

## Sommario

---

tro VoG, osservata nella caratteristica isteretica dei dispositivi memristivi, in funzione delle biomolecole. In questa ricerca, dimostriamo l'uso dell'effetto VoG in nanofili memristivi con barriera *Schottky* per la detection ad alta risoluzione di specie ioniche e biologiche, sia in soluzioni tampone che in estratti di tessuto tumorale vero e proprio. Inoltre, vi proponiamo una teoria originale che ci permette l'interpretazione fisica e la previsione dei meccanismi che regolano i biosensori-VoG in dispositivi memristivi. Infine, dimostriamo il potenziale del nostro sistema per la sua futura integrazione in una piattaforma *multi-panel* di biosensoristica basata sul Voltage-Gap. Abbiamo fabbricato una microfluidica in PDMS che ci permette di fare funzionalizzazione selettiva e di alta qualità sui nanofili. Abbiamo anche realizzato un circuito di lettura CMOS per l'acquisizione multiplexata di VoG. Le simulazioni dimostrano la fattibilità di questo approccio e il potenziale per l'integrazione del lettore in una piattaforma portatile e automatizzata. La microfluidica e il circuito consentiranno la rilevazione veloce e simultanea di multipli fattori angiogenici e infiammatori nel tessuto tumorale. Questo migliorerà il livello di conoscenza del tumore catturando l'eterogeneità e la complessità del microambiente tumorale, portando così a nuove opportunità nella diagnosi del cancro al seno.

Key words: nanotecnologie, fabbricazione di dispositivi, nanofili di silicio, SiNW, SiNW-FET, barriera Schottky, voltage gap, biosensori, biomarcatori del tumore al seno, estratto tumorale, sensibilità, rilevamento in asciutto

# Indice

<b>Acknowledgements</b>	<b>i</b>
<b>Abstract (English/Italiano)</b>	<b>iii</b>
<b>List of figures</b>	<b>xi</b>
<b>List of tables</b>	<b>xxi</b>
<b>List of acronyms</b>	<b>xxiii</b>
<b>1 Introduction</b>	<b>1</b>
<b>Introduction: Silicon Nanowires, from electronics to medicine</b>	<b>1</b>
1.1 Silicon Nanowires . . . . .	2
1.2 Field Effect Transistors (FETs) for Bio/Chemical sensing . . . . .	3
1.2.1 Ion Sensitive Field Effect Transistors . . . . .	4
1.2.2 Bio-Field Effect Transistors . . . . .	4
1.2.3 Immuno-FET . . . . .	5
1.3 The importance of nano-scale devices . . . . .	6
1.4 SiNW-FET based sensor . . . . .	7
1.5 Applications of SiNW-FET to medicine . . . . .	9
1.5.1 Biomarker detection . . . . .	9
1.5.2 Other applications . . . . .	11
1.6 The Debye screening effect: limitations in biosensing . . . . .	11
1.7 Memristive systems . . . . .	13
1.7.1 The pure memristor . . . . .	13
1.7.2 Memristive devices: state-of-the-art of the technology . . . . .	16
1.7.3 Memristive SiNW . . . . .	16
1.8 Thesis scope and objectives . . . . .	18
1.8.1 The biomedical impact . . . . .	18
1.8.2 The challenge of sensing in breast tumor extract . . . . .	18
1.8.3 Objectives of the thesis . . . . .	18
1.9 Thesis outline . . . . .	20
	vii

<b>2 Silicon Nanowire fabrication</b>	<b>21</b>
2.1 Overview on nanowire fabrication . . . . .	21
2.1.1 Bottom-up approach . . . . .	22
2.1.2 Top-down approach . . . . .	24
2.1.3 Advantages and disadvantages of the top-down approach . . . . .	27
2.2 SiNW-FET fabrication . . . . .	28
2.2.1 Process flow . . . . .	29
2.2.2 Fabrication results: device inspection . . . . .	31
2.3 Memristive NWs: the full process flow . . . . .	31
2.3.1 Choice of the substrate . . . . .	32
2.3.2 Phase 1 - EBL alignment markers definition . . . . .	32
2.3.3 Phase 2 - Nickel Silicide contacts formation . . . . .	33
2.3.4 Phase 3 - Nanowire formation . . . . .	35
2.4 Chapter summary and contributions . . . . .	38
<b>3 Silicon nanowire biofunctionalization</b>	<b>45</b>
3.1 Label-free detection . . . . .	45
3.2 Choosing the receptors: the antibody-antigen system . . . . .	46
3.3 Silicon nanowire modification for sensing: state-of-the-art . . . . .	48
3.3.1 Surface functionalization: principles . . . . .	48
3.3.2 Silanization for antibody immobilization . . . . .	48
3.3.3 The importance of surface blockers . . . . .	50
3.4 SiNW bio-functionalization: experimental procedure . . . . .	51
3.5 Results . . . . .	53
3.6 Chapter summary and contributions . . . . .	55
<b>4 In-air high sensitive detection of biomarkers with SiNW-FETs</b>	<b>57</b>
4.1 Electrical characterization of SiNW-FETs . . . . .	57
4.2 In-air sensing: experimental design . . . . .	58
4.2.1 Sensing in dry conditions: experimental set-up . . . . .	58
4.3 VEGF detection in PBS with SiNW-FET: results . . . . .	60
4.3.1 Sensing . . . . .	61
4.4 Detection of anti-rabbit in breast tumor extract . . . . .	62
4.4.1 Experimental procedure . . . . .	63
4.4.2 Tumor extract preparation . . . . .	63
4.4.3 Experimental requirements in tumor extract . . . . .	64
4.4.4 Antigen detection in tumor extract with SiNW-FET: results . . . . .	66
4.5 Chapter summary and contributions . . . . .	69
<b>5 A novel approach for high-sensitive biodetection: the VoG-biosensing</b>	<b>71</b>
5.1 The VoG approach: background . . . . .	72
5.2 Electrical characterization of memristive SiNWs . . . . .	73
5.2.1 A memristive system? . . . . .	73

5.2.2	The voltage gap in functionalized wires . . . . .	74
5.2.3	The repeatability of the voltage gap . . . . .	74
5.3	The VoG-based sensing . . . . .	76
5.3.1	Humidity measurement . . . . .	78
5.3.2	In-air measurement of ions in liquid-like thin films . . . . .	80
5.3.3	VEGF detection in PBS . . . . .	84
5.3.4	Detection of anti-rabbit in breast tumor extract . . . . .	86
5.4	Chapter summary and contributions . . . . .	88
<b>6</b>	<b>Modeling the VoG-biosensing</b>	<b>91</b>
6.1	Introduction . . . . .	91
6.2	Model . . . . .	92
6.2.1	Equivalent circuit . . . . .	92
6.2.2	Inter- and intra-band hopping through surface states . . . . .	93
6.2.3	Diffusion on surface states: traps energy level population . . . . .	95
6.2.4	Electronic transport in the bulk of a SiNW . . . . .	98
6.2.5	Electrical phenomena at the junctions . . . . .	99
6.3	Model implementation . . . . .	101
6.4	Steady state conditions . . . . .	101
6.5	Results and discussion . . . . .	102
6.6	Physical interpretation of experimental data . . . . .	107
6.6.1	The effect of ions . . . . .	107
6.6.2	Antibody VS Antigen: charging/decharging surface phenomena . . . . .	109
6.7	Chapter summary and contributions . . . . .	110
<b>7</b>	<b>Biosensors integration</b>	<b>113</b>
7.0.1	Introduction . . . . .	113
7.1	The biosensing platform design . . . . .	115
7.1.1	Microfluidics: mask design . . . . .	116
7.1.2	Masks fabrication . . . . .	117
7.1.3	Process flow for metal lines integration with the sensor chip . . . . .	118
7.1.4	Process flow for microfluidic fabrication . . . . .	120
7.1.5	Biosensors-microfluidics integration: preliminary results . . . . .	126
7.2	CMOS circuit design for fast and parallel VoG acquisition . . . . .	127
7.2.1	Circuit description . . . . .	128
7.2.2	Circuit simulations and results . . . . .	131
7.2.3	Results . . . . .	132
7.3	Redundancy in the voltage gap based biosensing platform . . . . .	133
7.3.1	Chapter summary and contributions . . . . .	135

## Indice

---

<b>8 Conclusions and outlook</b>	<b>137</b>
8.1 Main achieved results . . . . .	137
8.1.1 Achievements with SiNW-FET biosensors . . . . .	138
8.1.2 Achievements with VoG-biosensors . . . . .	139
8.2 Prospects on future applications . . . . .	141
<b>Bibliography</b>	<b>159</b>
<b>Curriculum Vitae</b>	<b>161</b>

# Elenco delle figure

1.1	a) Structure of an ISFET. RE, reference electrode; VG, gate voltage; $V_{DS}$ , drain-source voltage; $I_D$ , drain current. b) Definition of threshold voltage variation, $V_{th}$ , and readout sensitivity, $S_{out}$ . . . . .	3
1.2	a) Schematic set-up and functional principle of a (bio-)chemical sensor that is based on an ISFET, consisting of receptor, transducer and signal processing. Reprinted from [25]. b) Schematic structure of an ImmunoFET with immobilised antibody (Ab) molecules. Ag, antigen molecules. . . . .	5
1.3	Scale bar comparing the size of nanodevices to the size of biological entities. Reprinted from [12]. . . . .	7
1.4	A schematic overview of sensing principles. A p-type NW-FET device biased to operate at the optimum sensitivity regime: (a) A positively charged ligand will deplete the NW (p-type) resulting in a decrease of the conductance; (b) on the contrary, a negatively charged ligand will accumulate the NW and an increase of conductance is expected. Adapted from [44]. . . . .	8
1.5	a) Schematic representation of the Debye screening length $\lambda_D$ from the FET surface. The electrostatic potential arising from charges on the protein or DNA decays exponentially toward zero with distance. b) Structure and size of an IgG2 antibody molecule (Protein Data Bank). . . . .	13
1.6	Symmetry diagram showing the six distinct possible realizations based on the four circuit variables. Adapted from [79]. . . . .	14
1.7	Symbol representing a memristor in an electric circuit. . . . .	15
1.8	a) An idealized I-V curve of a memristive system subjected to a periodic voltage. The result is a Lissajous figure, i.e. a pinched hysteresis curve. b) demonstrates the hysteresis collapse observed with a tenfold increase in sweep frequency. The insets in the I-V plots in b and c show that for these examples the charge is a single-valued function of the flux, as it must be in a memristor. Reprinted from [82]. . . . .	16

## Elenco delle figure

---

2.1	(I) VLS growth mechanism: a) Deposition of metal catalyst and formation of nanodroplets. b) Continuous alloying and nucleation resulting in NW growth at the pre-defined sites of the previously formed nanodroplets. c) Growing heterostructure NWs by alternating the gas precursors. d) Coaxially grown NW by using lattice matching and two or more growing steps. Reprinted from [108]. (II) Schematics of experimental setups for SiNW growth. a) CVD, b) annealing in reactive atmosphere, c) evaporation of SiO, d) MBE, e) laser ablation, and f) solution-based growth. Image adapted from [106]. (III) Examples of NWs grown via VLS with various techniques of forming catalysts nanodroplets: (a) laser ablation (b) LPCVD (c) MBE. Reprinted from [108–110]. . . . .	23
2.2	(a) Interaction of electrons with a typical semiconducting substrate coated with a thin PR layer. Image adapted from [118]. On the right, the effect of a beam of electrons on a positive (dissolution) and a negative resist (cross linking). . . . .	24
2.3	Top-down SiNW fabrication procedure based on Bosch etching: (a) a PR mask is patterned on crystalline silicon; (b) physical/chemical SF <sub>6</sub> etching is applied, creating an undercut below the mask pattern; (c) the patterned Si layer is then masked by a thin conformal layer resulting from the C <sub>4</sub> F <sub>8</sub> gas; (d) anisotropic SF <sub>6</sub> plasma removes the vertically accessible surface passivation, and (e) etches the unprotected region creating a new undercut, that leads to (f) a new nanowire. Reprinted from [121]. . . . .	25
2.4	SEM micrograph of a structure etched using DRIE on a silicon bulk wafer. Scallop-ing due to the cycling nature of the etching is visible on the sidewalls. The number of scallops typically indicates the number of etching cycles, although the first isotropic etching step may not result in a visible groove, due to the surface imperfections, including native oxide, require a breakthrough time. Reprinted from [121]. . . . .	26
2.5	Top-down SiNW microfabrication procedure based on anisotropic wet etch: (a) lithography and etch steps for SiN layer patterning (BOX: buried oxide layer and Si DL: silicon device layer of the SOI substrate); (b) silicon device layer PDE and local oxidation; (c) second PDE and size reduction; (d) gate oxidation and contact metalization. Reprinted from [124]. . . . .	27
2.6	(Left) Schematic top view of the chip layout with enlarged view of one device cross section. (Right) Fabrication process flow of SiNWs: (a) oxide deposition and patterning by dry etching; (b) 45° rotation of the mask to expose only <100> planes; (c) silicon etching in AZ400K developer: (d) SiNW after oxide mask removal.	29
2.7	SEM images of the fabricated SiNW-FETs. . . . .	30
2.8	AFM image of the channel area of a fabricated SiNW-FET. . . . .	31
2.9	Process flow related to the fabrication of SB memristive SiNWs. . . . .	32



2.10 EBL alingment markers. (a) Conceptual view of a wafer after the formation of $20 \times 20 \mu\text{m}^2$ alignment markers by etching. (b) Schematic representation of the cross section of the marker after dry etching of the device layer, BHF wet etching of the BOX and further dry etching of the Si substrate. (c) Tilted SEM view of an etched marker in an SOI substrate. . . . .	34
2.11 NiSi S/D contacts. (a) Mask layout, designed in Cadence Virtuoso, for the EBL patterning of S/D regions. (b) SEM top view of the obtained NiSi contacts after EBL, Ni deposition, lift-off and annealing. (c) Zoomed view of the mask layout in (a) showing the disposition of the wire within the nano-gap between the NiSi pillars. (c) SEM view of the corresponding area of the device where a 420 nm long nanowire will be subsequently formed. . . . .	36
2.12 Imaging of fabricated vertically-stacked DRIE-etched nanowires with length of $1 \mu\text{m}$ and width of $\approx 80 \text{ nm}$ . (a) SEM top view of the device. (b) SEM tilted view of the vertical stack between NiSi pillars. (c) FIB/SEM imaging reporting the a tilted view of the stack. Contact between the parts is resulting from the DRIE process optimized for smaller nanowires. (d) AFM view of a fabricated device. .	37
2.13 SEM imaging of fabricated vertically-stacked DRIE-etched nanowires with length of 420 nm and width of $\approx 35 \text{ nm}$ . (a) SEM tilted view of one device featuring free-standing, vertically-stacked, round-shaped SiNWs bridging the NiSi contacts. (b) SEM top view of the device. (c) A zoomed. view of another NW stack . . . . .	39
3.1 (a) Schematic representation of the “lock-and-key” interaction between the Ab paratope and the Ag epitope. (b) Working principle of a SiNW-FET based immunosensor. The antibody molecule is immobilized on the SiNW surface and can specifically capture the target antigen molecule. When a negatively charged antigen molecule binds on an n-type SiNW-FET, a depletion of charge carriers inside the SiNW leads to a decrease in the electrical conductance. . . . .	47
3.2 (a) Chemical reactions for covalent silane binding to hydroxylated silicon oxide surface. The process consists of: 1) hydrolysis; 2) condensation of silanol and covalent binding; 3) thermal curing. B) In reality, silanes form irregular layers due to electrostatic interaction, polymerization in solution and molecular inversion. Irregular layers result from a 3-steps process: 1) condensation; 2) physisorption; 3) molecular inversion. Adapted from [139]. . . . .	49
3.3 Conceptual description of the functionalization of SiNW devices with Ab (Phase 1 to Phase 5) for the specific binding of target Ag (Phase 6). . . . .	51
3.4 Schematic explanation of the surface blocking principle, after Ab coupling, to prevent nonspecific binding. . . . .	51

3.5	Fluorescence detection of negative (1) and positive (2) antigen (anti-rabbit-Cy5) binding in device modified with their specific antibodies (anti-CD28 rabbit). (a) Fluorescence test after different surface treatments on Si wafer. (b) Summary of the performed surface modification and test results. Best result of dense Ab layer formation occurred when using GPTS linker molecules and Ab concentration of 5mg/ml in PBS. . . . .	53
3.6	Fluorescence imaging of a functionalized (a) SiNW-FET and (b) memristive SiNW.	54
3.7	Fluorescence characterization of a fabricated SiNW functionalized with Ab by using a nano-spotting system from NanoInk (Skokie, IL, USA). (a) Device before the surface modification, and (b) after, with a zoomed view on the channel with deposited biomaterial. . . . .	54
3.8	SEM characterization of the functionalization process performed on NWs. (a) Nanowire before the surface treatments, and (b) after the Ab-modification. . .	55
4.1	(a) Schematic drawing of SiNW-FETs on a 10 mm × 15 mm die, with zoomed view on a device cross-section with back-gate configuration for sensing purpose. (b) $I_{ds} - V_{bg}$ characteristics of a fabricated SiNW-FET. Figures adapted from [100, 101].	58
4.2	(Left) Conceptual schema summarizing the main phases of the in-air sensing approach. Ab-Ag interaction happens in liquid during the incubation (b); detection is done by electrical measurement in dry conditions (c). (Right) Increased Debye length as result of counterions depletions after removal of the the liquid bulk. . . . .	59
4.3	(a) Calibration curve for a fabricated SiNW-FET. Error bars stand for the standard deviation calculated on repeated estimates of the current slope. (b) Threshold voltage shift in the $I_{ds} - V_{bg}$ characteristic showing the effect of the increased amount of Ag on the majority carrier enhancement in the nanowire. Adapted from [100, 101] . . . . .	61
4.4	The crystallographic structure of an antibody showed with all the residues (A) or with only the positively (B) or negatively (C) charged ones. Reprinted from [95].	62
4.5	Conceptual schema of the SiNW-FET based biosensing method in tumor extract: (1) Breast tissue biopsy; (2) tumor extract (TE) preparation; (3) rabbit antigen dilution in TE; (4) sensor incubation in TE for Ab-Ag interaction. Adapted from [101]. . . . .	63
4.6	Statistics on washing steps for non-specific tumor protein removal from the surface of SiNW-FETs (a) and arrays of SiNW-FETs (b). The column height represents the conductance variation $\Delta g$ measured after incubation and washing of the sensors with respect to the baseline acquired before any exposition. The error bars stand for the standard deviations of repeated measurements after multiple washing steps on the sensors. Reprinted from [101]. . . . .	65

4.7	Sensing of rabbit antigen after sensor exposure to Ag breast tumor extract solution. (a) Response of an individual SiNW-FET sensor to the antigen concentration [AG] (0fM, 5fM, 65fM, 165fM). (b) Array of SiNW-FETs. Response to [AG] 5fM, 15fM, 65fM, 165fM. The error bars stand for the intra-device error calculated as standard deviations of repeated measurements after multiple washing steps on the sensor. Reprinted from [101]. . . . .	66
4.8	(a) $I_{ds} - V_{ds}$ characteristics for nanowires exposed to increasing femtomolar concentrations of rabbit antigen diluted in tumor extract. (b) Calibration for the sensor shown in (a). The error bars correspond to the standard deviation for 3 different measurements (confidence interval of 68.2%). Adapted from [101]. . .	68
4.9	A non-specific antigen (Ag), diluted in tumor extract at same concentration as the specific one (70 fM), determines a smaller conductance signal. In the considered device, the signal is also very closed to the curve acquired on the same wire in the absence of specific Ag (Ab). This result demonstrates the specificity of the sensor. Image adapted from [101]. . . . .	69
5.1	$I_{ds} - V_{ds}$ curves taken (1) before and (2) after wire functionalization with an all around AB layer demonstrating the origin of a current minima gap with the presence of a biomolecular layer. (b) Current minima gaps for $-1V \leq V_{ds} \leq +1V$ clearly showing the decreasing trend of the voltage gap with increasing antigen concentration: (1) 0 fM, (2) 5 fM, (3) 10 fM antigen solution. Arrows indicate sweep directions. Images adapted from [95]. . . . .	72
5.2	(a) Hysteretic $I_{ds} - V_{ds}$ characteristic of a bare silicon nanowire device. (b) The dependence of the hysteresis on the frequency ( $f$ ) of the measurement observed on some of the fabricated devices. $f$ was determined by changing the scan rate at 10 mV/sec, 40 mV/sec, and 100 mV/sec, respectively. . . . .	73
5.3	Pinched hysteresis loop in bare nano-fabricated nanowire devices (magenta dashed line), and voltage gap appearance in memristive-biosensors after the biomodification (blue solid line). . . . .	75
5.4	Reproducibility of the VoG parameter. (a,b) $I_{ds} - V_{ds}$ characteristics acquired on 4 of the tested devices to show the appearance of the voltage gap after antibody modification. (c) Statistics on the complete set of VoG-biosensors. Reprinted from [150]. . . . .	76
5.5	Superimposed semi-logarithmic $I_{ds} - V_{ds}$ characteristics acquired on memristive SiNWs after anti-VEGF Ab-functionalization. It shows scarce reproducibility of the current, and very high repeatability of the voltage gap parameter. . . . .	77
5.6	(a) Effect of the humidity on the VoG parameter. Calculated average voltage gap as function of the humidity in bare biosensors (black dashed line) and biomodified ones (red solid line). (b) Reproducibility of the VoG measurement at fixed humidity of $59.5 \pm 0.2$ %rH. 20 memristive-biosensors have been tested. Images adapted from [102]. . . . .	79

## Elenco delle figure

---

5.7	Effects of pH on the voltage gap parameter. (a) Average VoG behavior of 5 devices as a function of increasing pH. (b) Semi-logarithmic $I_{ds} - V_{ds}$ curves of one of the tested devices showing the increased VoG at high pH (red line) with respect to the bare case. The variations of the voltage gap is dependent also on the balance of $Na^+$ and $Cl^-$ ions in the prepared NaCl solution as discussed in the text and further explained in Chapter 6. Images adapted from [103] . . . . .	82
5.8	Effects of ammonium ions ( $NH_4^+$ ) on the voltage gap (VoG). Positive ions in the formed liquid-like thin film determine a voltage memory in the device as effect of surface states charging phenomena. . . . .	83
5.9	Calibration curves for VEGF sensing with VoG-biosensors. (a,b) Biosensors with 420 nm long and $35 \pm 10$ nm wide SiNWs; (c,d) biosensors with 1 $\mu m$ long and $90 \pm 9$ nm wide wire channel. All the graphs confirm proper biomodification with anti-VEGF (blue point in (a,b) and blue line in (c,d)) with reduced value with respect to the bare case (red line), and detection of occurring Ab-Ag binding (decreasing VoG). The sensing is demonstrated by the quasi-linear behavior of the voltage gap as effects of increasing concentrations of Ag. . . . .	85
5.10	$I_{ds} - V_{ds}$ characteristic, in the semi-logarithmic scale for a VoG-biosensor incubated in different solutions of rabbit antigen in tumor extract, with concentration 25 fM (green line), 50fM (blue line) and 75fM (red line). Shrinking of the voltage gap as effect of charge compensation from antigen uptake. . . . .	86
5.11	Calibration curve for sensing of rabbit antigen. Average behavior of multiple VoG-biosensors. The target molecules were specifically uptaken on the antibody sites from the starting tumor extract solution, then measured in-air. Error bars stand for the standard deviation of the measurement on different devices. . . .	88
6.1	At the silicon surface silicon atoms are missing and unpaired valence electrons exist forming electrically active interface traps. . . . .	92
6.2	Equivalent circuit representing the multiple transport mechanisms in SiNW. Reprinted from [104]. . . . .	93
6.3	Sketch of the formation/recombination of energetic surface levels. Neutral (black spheres), acceptor-like (blues spheres) and donor-like (red spheres) states are from surface defects. Charging phenomena at the surface take place via binding of charged species such as antibodies. Reprinted from [104]. . . . .	94
6.4	Energy band diagram showing acceptor and donor type surface states and their distribution in the band gap at the surface of the semiconductor. a) The situation when the doping concentration is such that the Fermi level $W_F$ coincides with the neutral level $W_0$ . b) The situation where the semiconductor is p-type and a positive net surface charge is created because of unoccupied donor surface states. c) The situation where the semiconductor is n-type and a negative net surface charge is created because of occupied acceptor surface states. Reprinted from [167]. . . . .	95

6.5 The approximated energy band diagram of silicon surface states. a) Surface state energy levels as continuum in the silicon band gap. b) Approximated view of surface trap energies as discrete energy levels. . . . . 98

6.6 Experimental (a) and simulated (b)  $I_{ds} - V_{ds}$  characteristics of a SiNW before any surface bio-modification. Both curves have pinched hysteresis loop, similar to the hysteresis of memristive-like behavior, and same current peak. Blue and red lines stand for the forward and backward current branches. [The parameters chosen for this simulation are:  $k_{a0}^a = 3.5 \cdot 10^{-4}$  Hz,  $k_{n0}^a = k_{a0}^a / [8.4 \cdot (N_0 - n_{d,0}) / n_{d,0}]$ ,  $k_{n0}^d = 2 \cdot 10^{-4}$  Hz,  $k_{d0}^d = (N_0 - n_{d,0}) / n_{d,0} \cdot k_{n0}^d$ ,  $\tilde{C}_a \sim \tilde{C}_d = 10^{-12}$  F,  $R_a = 10^3$  M $\Omega$ ,  $R_d = 10^6$  M $\Omega$ ,  $\sigma = 6.5$ ,  $\beta_a = \beta_d = 1/2$ ,  $f_a = 2.8 \cdot 10^{14}$ ,  $f_d = 3 \cdot 10^{10}$ ,  $f_s = 2 \cdot 10^{16}$ ,  $\Delta E = 253$  eV,  $n_d / N_0 = 0.01$ ,  $N_0 = 8.5$ ]. Reprinted from [104]. . . . . 103

6.7 Modeling the voltage-gap. a) Semi-logarithmic  $I_{ds} - V_{ds}$  characteristic from experimental measurements acquired from a fabricated SiNW functionalized with antibodies. The voltage-gap appears as a result of the adsorption of positively charged species onto the nanowire and the interaction with the oxide surface states. b) Simulated total  $I_{ds} - V_{ds}$  curve. c) Components of the characteristic reported in panel b): diffusion current due to the surface states in the oxide (solid line); drift current in the oxide (dashed line); diffusion current in the SiNW (dotted line). d) Individual contributions of acceptor (solid line), and donor (dashed line) states to the diffusive current at the NW surface. [The parameters chosen for this simulation are:  $k_{a0}^a = 3.5 \cdot 10^{-5}$  Hz,  $k_{n0}^a = k_{a0}^a / [14 \cdot (N_0 - n_{d,0}) / n_{d,0}]$ ,  $k_{n0}^d = k_{n0}^{d,BARE} \cdot 10^4$ ,  $k_{d0}^d = (N_0 - n_{d,0}) / n_{d,0} \cdot k_{n0}^d$ ,  $\tilde{C}_a \sim \tilde{C}_d = 10^{-12}$  F,  $\sigma = 6.5$ ,  $\beta_a = \beta_d = 1/2$ ,  $f_a = 2.8 \cdot 10^{14}$ ,  $f_d = 3 \cdot 10^{14}$ ,  $f_s = 2 \cdot 10^{16}$ ,  $\Delta E = 253$  eV,  $n_{d,0} = 0.69$ ,  $N_0 \approx 40$ .] Reprinted from [104]. . . . . 105

6.8 a) Simulated  $I_{ds} - V_{ds}$  characteristics modeling the increasing uptake of antigen molecules onto a bio-modified nanowire. The parameters chosen in these simulations are:  $\sigma = 6.5$ ,  $\beta_a = \beta_d = 1/2$ ,  $\tilde{C}_a \sim \tilde{C}_d = 10^{-12}$  F,  $\Delta E = 253$  eV,  $f_a = 2.8 \cdot 10^{14}$ ,  $f_d = 3 \cdot 10^{10}$ ,  $f_s = 2.5 \cdot 10^{15}$ . Only some of the parameters in the model vary affecting the hysteresis and the voltage-gap, demonstrating the importance of the charge imbalance induced by the dynamic modification of the surface states. Moving from plot (i) to plot (vi),  $n_{d,0}$  decreases from 0.5 to 0.07,  $N_0$  decreases from 47 to 8.4, and the donor rate constant  $k_{n0}^d$  decreases exponentially from  $k_{n0}^d = 3.5 \cdot 10^4 k_{n0}^{d,BARE}$  (i) to four orders of magnitude smaller in case (vi). b) Reports the variation of VoG as a function of  $n_{d,0}$  (blue axes) and compares it to the calibration data from experiments (Section 5) in breast tumor extract (TE) (red axes). As the antigen concentration increases the positively charged surface states decrease due to charge compensation, thus determining a reduction of the voltage-gap. Reprinted from [104]. . . . . 106

6.9 (a) Effects of pH on the voltage gap in NaCl saline solution. (b) Effect of ammonium ions. . . . . 108

6.10 Antibody and antigen effect on the voltage gap. . . . . 110

6.11 Residues charge at physiological pH. . . . . 110

## Elenco delle figure

---

7.1	Design of a biosensor chip that integrates the VoG-biosensors array and the microfluidic platform. External electrodes enable the connection to an external CMOS readout circuit for parallel measurements. . . . .	116
7.2	Schematic description of the designed microfluidic device. (a) Cross-sectional view of the channel for delivering the fluid from the inlet reservoir towards the outlet reservoir, flowing through the sensor area. (b) Top view of the system illustrating the disposition of the array of 9 sensors, arranged perpendicular to the fluid flow. . . . .	117
7.3	Mask design prepared in Cadence Virtuoso for the lithographic patterning of (a) an array of memristive SiNWs (with zoomed view in (b)), integrated with a microfluidic platform thanks to Al metal lines and external Al electrodes (c). . .	118
7.4	Process flow for the fabrication of a photolithography mask. . . . .	119
7.5	Fabricated masks for Al lines (a) and SU-8 microfluidic mold. . . . .	119
7.6	Process flow for the fabrication of Aluminum lines. . . . .	120
7.7	(a) Wafer after photolithography and Al lift-off. (b) Final sensing chips. . . . .	120
7.8	SEM images of metal lines for contacting the NiSi pads of memristive SiNWs. (a) and (b) differ in terms of length and width of the Al lines. . . . .	121
7.9	Conceptual representation of the main steps of the process flow for microfluidics fabrication. . . . .	122
7.10	SU-8 mold fabricated on a silicon substrate. . . . .	124
7.11	Fabricated PDMS microfluidic devices. . . . .	124
7.12	Set-up for experiments with microfluidics. (a) A peristaltic pump is used to pump the liquid inside the microchannel, to the biosensors. (b) One microtube is connected to the outlet and deliver the fluid to a beaker for solution waste. (c) The other microtube is connected to the the inlet and sucks the solution from fresh sample. (d) Zoomed view of the connections to the microfluidic device. .	125
7.13	a. Microfluidics. . . . .	126
7.14	b. Drop-casting. . . . .	126
7.15	Fluorescence detection of Ab-Cy5 attached on the fabricated chips. . . . .	126
7.16	Schematic representation of the circuit solution for voltage gap acquisition on one single biosensor. . . . .	128
7.17	Configurable voltage ramp circuit shared by all sensors. (a) The voltage ramp circuit. (b) Control signals for the voltage ramp circuit. . . . .	129
7.18	Fault detector circuit. . . . .	129
7.19	Layout of the analog part. . . . .	129
7.20	Basic signals arriving from the analog domain to the digital one. . . . .	131
7.21	Real measurements from a memristive device after biofunctionalization and antigen uptake are used as input signal of the simulation. The cross signal (green line) demonstrates the proper detection of the current crossings and thus the voltage gap. . . . .	132
7.22	Applied method for statistical analysis. The study consists of three major steps that have to be repeated $T$ times for any subset containing $N$ nanowires. . . . .	133

7.23 Percentage of sets containing $N$ bare sensors satisfying condition 1 on their voltage gap mean. . . . .	134
7.24 Percentage of sets containing $N$ Ab-sensors satisfying condition 1 on their voltage gap mean. . . . .	134
7.25 Percentage of sets containing $N$ Ab-Ag-sensors satisfying condition 1 on their voltage gap mean. . . . .	134
8.1 Prototype of a portable biosensing platform based on high-sensitive VoG devices functionalized with different antibodies (Ab1, Ab2, Ab3). The platform will be used for in-lab, fast, automated, and multiplexed detection of biomarkers in tumor extract (TE). . . . .	142





## Elenco delle tabelle

1.1	BioFET classification . . . . .	6
1.2	SiNW-FET applications in biosensing . . . . .	10
2.1	DRIE parameters employed for the nanowire etching on bulk and SOI substrates. The parameters are adapted for the Alcatel AMS200 SE dry etcher of EPFL CMI [129]. Note that the parameters refer to a single etching cycle. Multiple cycles are used to fabricate nanowire stacks with a different number of nanowires. . .	37
2.2	Process runcard for the fabrication of the DG-SiNWFET devices on an SOI substrate. Typical substrate parameters are: 340 nm-thick boron-doped device layer with $\approx 10\Omega\cdot\text{cm}$ resistivity and $2\mu\text{m}$ BOX thickness. <i>Zn</i> in the Equipment column refers to the location of the equipment in the CMI cleanroom. . . . .	41
2.2	Table continued from previous page. . . . .	42
2.2	Table continued from previous page. . . . .	43
7.1	SU-8 spin-coating parameters . . . . .	123
7.2	Hotplate parameters for soft bake of SU-8 before UV exposure (a) and post-exposure bake of the resist (b). . . . .	123



# List of acronyms

<b>Acronym</b>	<b>Definition</b>
SiNW	Silicon NanoWire
NW	NanoWire
CMOS	Complementary Metal Oxide Semiconductor
FET	Field Effect Transistor
SiNW-FET	Silicon NanoWire FET
VoG	Voltage Gap
ISFET	Ion Sensitive FET
CNT	Carbon NanoTube
ChemFET	Chemically Sensitive FET
BioFET	Biologically modified FET
Ab	Antibody
Ag	Antigen
ImmunoFET	Immuno Sensitive FET
NW-FET	Nanowire FET
PBS	Phosphate Buffered Saline
GAA	Gate All-Around
ALD	Atomic Layer Deposition
SB FET	Schottky Barrier FET
SOI	Silicon On Insulator
SB	Schottky Barrier
DRIE	Deep Reactive Ion Etching
VLS	Vapor Liquid Solid
VSS	Vapor Solid Solid
CVD	Chemical Vapor Deposition
MBE	Molecular Beam Epitaxy
LPCVD	Low Pressure Chemical Vapor Deposition
VLSI	Very Large Scale Integration
EBL	Electron-Beam Lithography
FIB	Focused Ion Beam
NIL	Nano Imprint Lithography
PR	PhotoResist

## List of acronyms

---

<b>Acronym</b>	<b>Definition</b>
SEM	Scanning Electron Microscope
PDE	Plane-Dependent Etching
TMAH	tetramethylammonium hydroxide
KOH	Potassium Hydroxide
PECVD	Plasma Enhanced Chemical Vapor Deposition
BHF	Buffered HF
AFM	Atomic Force Microscopy
S/D	Source and Drain
BOX	Buried OXide
PMMA	Poly(Methyl MethAcrylate)
LER	Line Edge Roughness
QCM	Quartz Crystal Microbalance
SPR	Surface Plasmon Resonance
DNA	Deoxyribonucleic Acid
APTES	3-AminoPropylTriethoxySilane
PNA	Peptide Nucleic Acid
APTMS	3-(Trimethoxysilyl)Propyl Aldehyde
BSA	Bovine Serum Albumin
NFDM	Non-Fat Dry Milk
PEG	PolyEthylene Glycol
PVA	PolyVinyl Alcohol
PVP	PolyVinylPyrrolidone
GPTS	GlycidoxyPropylTrimethoxySilane
VEGF	Vascular Endothelial Growth Factor
anti-VEGF	VEGF Antibody
TE	Tumor Extract
TEM	Tie-2 Associated Monocytes

# 1 Introduction

To date, a variety of sensing techniques have been used for biological research and medicine applications. However, the growing number of cancer cases being diagnosed worldwide and the increased number of fatalities due to late disease detection demonstrate the crucial need for more powerful diagnosis tools. Several essential factors, such as ultra-sensitivity, specificity, high-speed data delivery, and low-cost diagnostics must be considered when designing new biosensors for real-time detection.

Thanks to their unique properties, nanomaterials and nanostructures have demonstrated new opportunities in the development of high-sensitive biosensors. Nanostructures are very small structures with at least one of their dimensions in the nanoscale ( $10^{-9}$  m range). *Silicon NanoWires* (SiNWs), in particular, are extremely small wires with cross-section in the nanoscale size. Because of typical aspect ratios of length to width in the order of 1000 or more, they are often referred to as one-dimensional (1D) systems. Thanks to their size, *NanoWires* (NWs) have distinct and diverse electrical, physical, and mechanical properties that are not shared by the corresponding bulk material. These properties can be translated into specific functionalities and used for the fabrication of integrated circuits, electronic components, or sensing devices for medical applications. Providing a quick response, durability, and allowing standard Silicon chemical modification techniques, SiNWs have become promising candidates for sensing, competing with their mechanical and optical counterparts. Moreover, thanks to their fabrication compatibility with well known *Complementary Metal Oxide Semiconductor* (CMOS) processing, they have shown easy integration with standard *Field Effect Transistor* (FET) technology, currently being the basic structural element in micro biosensors. In particular, *Silicon NanoWire FETs* (SiNW-FETs) are emerging as ultrasensitive sensors for direct and label-free detection of chemical and biological species. Their potential has been widely demonstrated, but their application for high-sensitive detection in real patient samples, as well as their large-scale production and circuit integration, are yet beyond to be fully exploited. The aim of this thesis is to improve the state-of-the-art nanoelectronics by proposing both improvement and novelty in the field of detection of cancer markers in breast tumor tissues. First, we will present a novel approach of detection based on the electrical measurement of biological species in dry conditions that pushes the sensitivity capabilities of SiNW-FET

technologies to their limits by taking advantage of the increased Debye screening length in non-bulk solutions. Then, we will show, for the first time, that nanowires featuring characteristics reminiscent of memristive (resistive with memory) systems, currently extensively studied mainly for memory and logic circuits applications, can be also employed for sensing. In particular, we will propose a novel electronic-based biosensing paradigm, the so called *Voltage Gap* (VoG)-biosensing method, which combines the molecular selectivity of immuno-assays to the sensitivity power of memristive SiNW. The detailed investigation of this new approach will demonstrate promising capabilities and potential for becoming a valid alternative to the traditional *Ion Sensitive FET* (ISFET) technology.

In this chapter we will give an introduction to the thesis work. In particular, we will first describe the state-of-the-art of standard SiNW-FET sensing technology, pointing out their main limitations for sensing in liquid. Then, we will introduce the topic of memristive devices, showing their main applications and discussing the new opportunities of using memristive SiNW for sensing purposes. We will then report the scope and objective of the thesis, describing the final goal of the performed work together with the main challenges and issues to address. Finally, we will present an outline of the thesis.

### 1.1 Silicon Nanowires

Over the past 20 years, nanomaterials, such as quantum dots [1], nanoparticles [2, 3], nanowires [4–6], nanotubes [7], nanogaps [8], and nanoscale films [9] have received enormous attention due to their suitable properties for designing novel nanoscale biosensors. Their growing exploitation in sensing is due to the excellent advantages they offer via miniaturization of the devices which increases sensitivity and also allow the fabrication of multiplex systems such as high density protein arrays [10, 11].

The dimension of these nanostructures are comparable to the sizes of biological and chemical species, and thus provide a perfect feature to study most biological entities, such as nucleic acids, proteins, viruses, and cells [12]. In addition, the high surface-to-volume ratio for nanomaterials allows a huge proportion of the constituent atoms in the material to be located at, or close to, the surface. As a consequence, surface atoms play an extremely important role in determining the physical, chemical, and electrical properties of nanomaterials, making them very sensitive devices capable of low concentration and even single molecule detection.

Among nanomaterials, NWs have become significant candidates for nanoscale sensing applications. In particular, the reproducible and tunable conducting properties of semiconducting nanowires combined with surface binding provide a very different and powerful approach to nanomedicine. NWs can be made from metallic, dielectric, composite and semiconductor materials. Metallic NWs are conducting at all times and are mainly tapped for the applications in fuel cell, gas sensing and as electrodes due to the large surface area-to-volume ratio [13–15]. Composite NWs are compatible for photonics and gas sensing due to the material sensitivity to specific gas [16, 17]. For the purpose of bio- or chemical sensing applications, semiconductor materials, mainly silicon, are used. This is due to the electronic property of semiconductor

## 1.2. Field Effect Transistors (FETs) for Bio/Chemical sensing

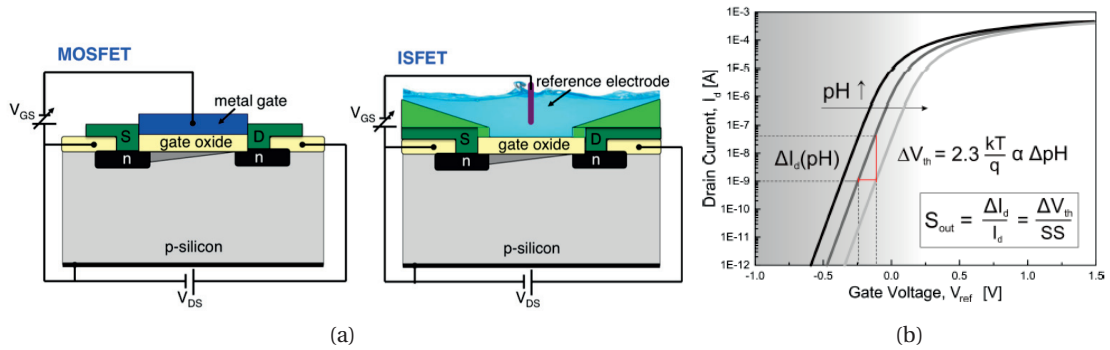


Figure 1.1 – a) Structure of an ISFET. RE, reference electrode; VG, gate voltage;  $V_{DS}$ , drain-source voltage;  $I_D$ , drain current. b) Definition of threshold voltage variation,  $V_{th}$ , and readout sensitivity,  $S_{out}$ .

materials that can be easily tuned via doping and applied gate voltages. This electrical tuning has also been demonstrated to affect the sensitivity capabilities [18, 19]. NWs can also benefit from existing and mature silicon industry processing and be easily integrated with the well-developed FET technology. Moreover, SiNW surfaces can be readily modified thanks to well established silicon and silicon oxide functionalization techniques, thus making SiNW-FETs particularly attractive for the label-free detection of biological species.

## 1.2 Field Effect Transistors (FETs) for Bio/Chemical sensing

FETs can be suitable candidates for sensors, owing to their ability to directly translate the interaction of the target molecule with the detector element on the FET surface into a readable electrical signal [5].

A FET is built from three-terminals (Figure 1.1a): the source and drain electrodes that are connected through the semiconducting channel and a gate that regulates the channel width. An additional fourth terminal, the back gate, is shown in Figure 1.1a, and it is, sometimes, used to ensure reference ground-potential to the device. The gate electrode either enhance or depletes the carriers of the channel depending on the voltage applied between the gate and source. Depending on the potential the FET response will be in an inversion, linear or depletion mode which will have an impact on signal transduction and the directionality of the channel current. The signal readout is the current passing from source to drain, where the charge carriers may be holes or electrons depending on the doping conditions of the silicon nanowire. Boron is a common dopand for p-type sensors while phosphorous and arsenic are used for n-type sensors.

The dependence of conductance on gate voltage makes FET natural candidates for electrically-based sensing since the electric field resulting from binding of charged species to the gate dielectric is virtually equivalent to applying a voltage using a gate electrode.

### 1.2.1 Ion Sensitive Field Effect Transistors

The ISFET was first invented by Bergveld [20] in 1970 and has been introduced as the first miniaturised silicon-based chemical sensor for pH and ion measurements. At present, there exist numerous different ISFET structures and processes for their fabrication, but the principle of using an electric field to create regions of excess charge in a semiconductor substrate in order to enhance or diminish the local conductivity is common to all of them.

The functionality of an ISFET can be explained by comparing the sensor with a conventional MOSFET. The ISFET is then a MOSFET in which the metal gate is replaced by an ion-sensitive membrane, an electrolyte solution in contact with the gate oxide and a reference electrode immersed in the solution, as illustrated in Figure 1.1a [20, 21]. ISFETs that are selective towards other ions, so-called *Chemically Sensitive FET* (ChemFET) can be obtained by means of an additional surface modification of the gate insulator or by deposition of subsequent specific membranes on top of the gate insulator [22–24].

For operating an ISFET, the gate voltage,  $V_{GS}$ , is applied by a reference electrode (e.g., Ag/AgCl electrode), which is also responsible for fixing the potential of the test solution (analyte). The potential at the silicon surface is then function of the reference electrode and the amount of charges present in the solution as long as their contribution is not negligible at the ISFET surface. In the case of a pH-sensitive ISFET, the gate insulator (typically  $Si_3N_4$ ,  $Al_2O_3$  or  $Ta_2O_5$ ) senses the  $H^+$ -ion concentration, generating an interface potential on the gate insulator. The pH response can be explained by the so-called site-binding theory. According to this model, in contact with an aqueous solution, the surface of the gate insulator hydrolyses into ionisable sites (e.g., OH groups). These active groups are either able to bind or release hydrogen ions in a dynamic exchange process. Thus, their protonation state changes with the pH of the surrounding analyte.

The resulting pH-dependent electrical surface charge of the gate insulator leads to a modulation of the channel conductance and, consequently, of the drain current  $I_d$  of the ISFET. Thus, by measuring changes in the drain current, the pH value of the test solution can be determined quantitatively. In particular, as illustrated in Figure 1.1b, a change of the surface potential will result in a change of the ISFET threshold voltage  $V_{th}$ , which can be measured by sweeping the reference electrode or by monitoring the  $I_d$  value at fixed  $V_{ref}$  value.

### 1.2.2 Bio-Field Effect Transistors

*Biologically modified FETs* (BioFETs) can be simply constructed from an ISFET by modifying the gate oxide by coupling it with different biological recognition elements, the bio-receptor, as schematically shown in Figure 1.2(a) [25]. In these devices, the charge (or potential) effect is used to transduce the recognising phenomena. The most critical point in information transfer from the biological recognition to the transducer is the interface between these two domains [26]. BioFETs can be classified according to the biorecognition element that is used for detection. They can be subdivided as reported in Table 1.1: enzyme-modified FET (EnFET); *Immuno Sensitive FET* (ImmunoFET); DNA-modified FET (DNA-FET); cell-based FET.



## 1.2. Field Effect Transistors (FETs) for Bio/Chemical sensing

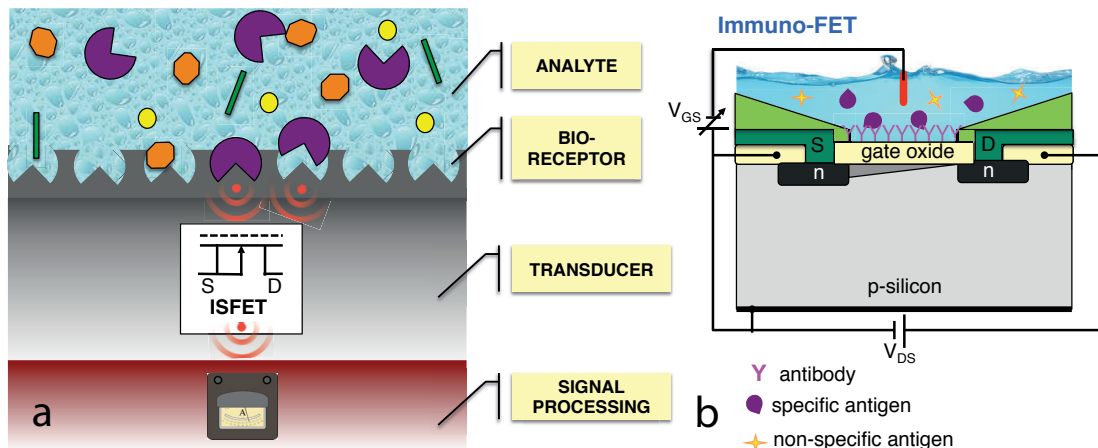


Figure 1.2 – a) Schematic set-up and functional principle of a (bio-)chemical sensor that is based on an ISFET, consisting of receptor, transducer and signal processing. Reprinted from [25]. b) Schematic structure of an ImmunoFET with immobilised antibody (Ab) molecules. Ag, antigen molecules.

The biosensors proposed in this thesis are based on immunologically modified electronic devices for high specific detection of antigens in tumor environments. For a better understanding of their functionalities, the basic operating principle of the standard ImmunoFET is described in the following section.

### 1.2.3 Immuno-FET

The high recognition ability of biological molecules is well represented by an antibody–antigen interaction. An antibody is a complex biomolecule consisting of hundreds of individual amino acids arranged in a highly ordered sequence; the antigen can be any macromolecule against which the antibody has been generated as a result of the defensive mechanism of the organism known as the immune response. Proteins with molecular weights greater than 5000 Daltons are generally immunogenic [27], i.e. susceptible to being recognized and bound by antibody with extremely high specificity. A minor chemical modification of the molecular structure of the antigen can dramatically lower its affinity towards the original antibody. Thus, immunosensors may be useful for mimicking the human immune system functioning, and consequently they can serve as excellent clinical diagnostic tools.

The possibility to directly monitor antibody–antigen interactions, has attracted many attempts to develop biosensors in which the actual recognition takes place in a layer of antibodies at the surface of the sensor. In an Immuno-FET, which is shown schematically in Figure 1.2(b), the gate oxide is modified by immobilising antibodies or antigens. Since a FET basically represents a surface-charge measuring device, and since antibodies and antigens (or more generally, proteins) are mostly electrically-charged molecules, the formation of an antibody–antigen complex on the surface of an ISFET leads to a detectable change in the charge distribution and

<b>BioFETs</b>	<b>Basic mechanisms of potential generation</b>
EnFET	Catalytic reaction product ( <i>e.g.</i> , between enzyme and its substrate)
Immuno-FET	Surface polarization effects due to antigen-antibody affinity reactions
DNA-FET	Surface charge redistribution caused by DNA (deoxyribonucleic acid) hybridization
Cell-based FET	Potential changes that are coming from living biological systems as a result of more sophisticated (bio-)chemical processes ( <i>e.g.</i> , action potential of nerve cells)

Tabella 1.1 – BioFET classification

thus, directly modulate the drain current of the ISFET. Under ideal conditions, the ImmunoFET is theoretically capable of measuring the concentration of immunomolecules with a very low detection limit and a wide concentration range [28]. Ideal conditions are: a truly capacitive interface at which the immunological binding sites can be immobilized; a nearly complete antibody coverage; highly charged antigens and a very low ionic strength.

Many research efforts have been expended to realize this idea; however, the results obtained were unsatisfactory due to a fundamental limitation: the effect of the Debye screening in solution (Section 1.6). Moreover, the limited sensitivity in solution of FET-based devices is also correlated to their planar structure [29], which led to a growing interest for improving the sensitivity capabilities of FET-based sensors by integrating nanoscale materials as channel.

### 1.3 The importance of nano-scale devices

The downsizing of silicon electronic components from the micro- to the nano-scale has steadily progressed in the past decades in several different research field, such as nanoelectronics, bionanosensors and nanophotonics [17, 30, 31]. The dimension-related phenomena, driving the sensitivity of the sensor [32], combined with the range of methods for surface functionalizations (especially for silicon-based devices), offer an ideal platform for highly sensitive yet selective biosensors. A NW- based device with at least one of its dimensions in the 1-100nm range has a high-surface-to-volume ratio. This provides a large interaction area for a small footprint and confines charge carriers in a very thin (almost one-dimensional) structure. Therefore, changes generated by the interaction of the bio-species at the NW surface are more significant, and can thus be detected with higher sensitivity for small concentration and higher output resolution or signals. This offers ultra-high sensitivity detection possibilities for very low concentrations of a sample, which is not available in corresponding micro-scale sensing devices. Besides possessing a high-surface-to-volume ratio, NWs are also relatively comparable in size to the species of interest such as proteins, cells, viruses and other biological entities (Figure 1.3), making NWs an ideal candidate for interfacing at best to biological molecules [12].

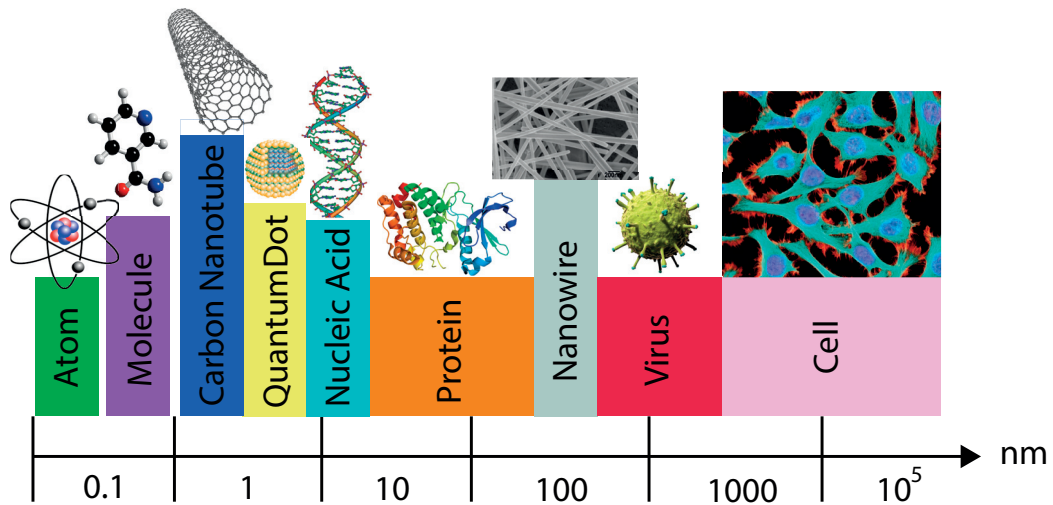


Figure 1.3 – Scale bar comparing the size of nanodevices to the size of biological entities. Reprinted from [12].

#### 1.4 SiNW-FET based sensor

The physical properties limiting sensor devices fabricated in planar semiconductors can be readily overcome by exploiting nanoscale FETs. There are several technical improvements which illustrate the importance of size effects and justify the development of nanoscale FET biosensors [33]. First, biological recognition at the sensor surface is reflective of the entirety of the physical signal across the whole sensor device. Thus, the sensitivity of the device, relating to its signal-to-noise ratio, is improved by increasing the surface-to-volume ratio. Whereas attachment of a biomolecule to a macroscale planar device affects the surface characteristics, attachment to a nanoscale wire affects the bulk characteristics. Second, many of the biological molecules of interest in biomedical applications are known to have sizes on the micro- or nanoscale. Thus, a device with submicron or nanoscale dimensions will have the best efficiency as a biological sensor. Third, as the device size is reduced to the nanoscale, properties such as the mobility of the charge carrier change [34] finite size effects dominate the device character, and nanodevice performance is enhanced.

In recent years, one-dimensional semiconducting nanomaterials, such as SiNWs and *Carbon NanoTubes* (CNTs) configured with FETs have attracted great attention as ideal biosensors [35, 36]. NWs and CNTs can be used for label-free, direct real-time electrical detection of biomolecule binding [37]. In particular semiconducting NWs are ideal candidates for biosensing applications. They have electrical properties and sensitivity that can be tuned reproducibly by controlling dopant type and concentration, and NW diameter [37–39]. Moreover, they can benefit of the existing massive knowledge on chemical modification of silicon oxide surfaces [40, 41] for tailoring SiNW surfaces with biological or chemical receptors. Finally, being made of the same material of the substrate, they are well adapted to the well-established CMOS technology. SiNW-FETs are FETs with a channel being the SiNW itself. The SiNW channel is isolated from the substrate by a layer of oxide, which is also known as *Buried OXide* (BOX).

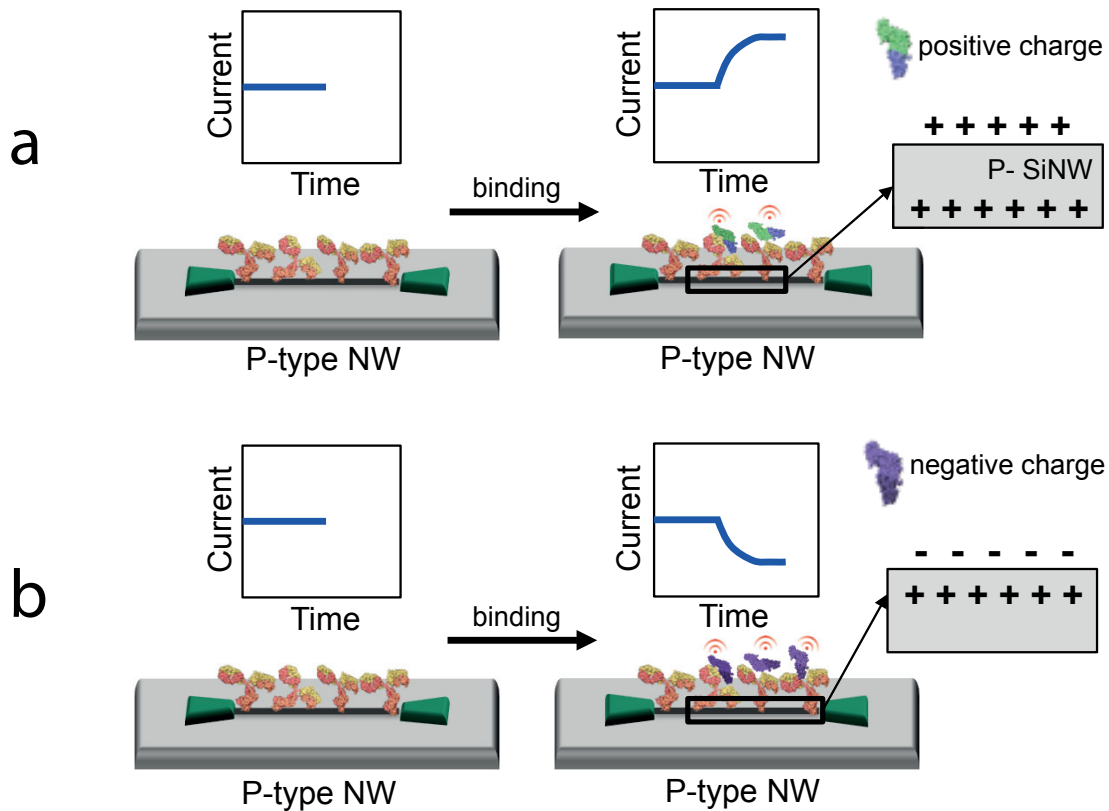


Figura 1.4 – A schematic overview of sensing principles. A p-type NW-FET device biased to operate at the optimum sensitivity regime: (a) A positively charged ligand will deplete the NW (p-type) resulting in a decrease of the conductance; (b) on the contrary, a negatively charged ligand will accumulate the NW and an increase of conductance is expected. Adapted from [44].

A typical configuration of a SiNW-FET sensor is indicated in Figure 1.4, together with a typical biasing configuration. The device consists of either boron (p-type) or phosphorous (n-type) doped NWs (single or array) between two metallic contacts or highly doped silicon regions (the source, S and the drain, D). SiNW-FET devices show substantial advantages compared to state-of-the-art [?] First, the carrier mobility is order of magnitudes larger than that in planar Si devices with comparable dopant concentrations. In addition, the on-state current ( $I_{on}$ ) for the SiNW-FET is larger than state-of-the-art Si-FETs; the average subthreshold slope approaches the theoretical limit [42] and the average transconductance is about 10 times larger. These improvements lead to substantial benefits for high-speed and high-gain devices, but also enhance the response in SiNW-FET based sensing.

SiNW-FETs become biosensors by integrating biological recognition groups to the surface of the nanowire [37, 43]. When the functionalized sensor device is exposed to a solution containing biological species, such as a protein, which has a negative (positive) charge in aqueous solution, specific binding leads to an increase (decrease) in the surface negative charge and an increase (decrease) in conductance for a p-type nanowire device (Figure 1.4). This detection method runs in real-time and the binding process can literally be viewed as it occurs.

### 1.5 Applications of SiNW-FET to medicine

Over the past years, the invention of biosensors has become increasingly important for many biological purposes. This section briefly reviews the main applications of SiNW-FETs in biosensing. Some of the most important works have been listed in Table 1.2.

From the very beginning, the most frequent applications of SiNW-FET sensors were focused on monitoring protein—protein interactions, such as the binding between an antibody and antigen. Protein to protein binding also identifies the major mechanism for biomarker detection in disease diagnosis, one of the main applications of SiNW-FETs in medicine. Due to its relevance within the scope of this thesis, the following section will give a more detailed overview on biomarker detection with SiNW-FETs.

#### 1.5.1 Biomarker detection

In the field of medicine, a biomarker is an indicator of normal, pathological processes or pharmacological response in the human body. It can be any detectable and measurable parameter such as physical, chemical or biological in the body, most commonly associated with specific biological elements, such as cells, proteins, nucleic acids and small molecules. A biomarker is often present under normal conditions, but is elevated or diminished in case of disease. In clinical diagnostics, biomarker detection can be applied to disease screening which indicates a presence or absence of a particular disease in a particular specimen.

Tumor markers are substances that are produced by the human body in response to cancer or other kinds of disease. Tumor markers can be detected in higher than normal levels in blood, urine or body tissues of patients with certain types of cancer. These include isoenzymes, hormones, oncofetal antigens, differentiation antigens, oncogenes and their products, tissue specific proteins, mucin and other glycolipids and glycoproteins. Tumor markers can be used to predict the response to certain types of therapy such as surgery and chemotherapy or estimate the risk of future relapse. Biomarkers are present in human samples typically in very low concentrations, and their detection and measurement in a biological environment is extremely challenging and requires novel and accurate biosensing techniques.

During the last decade, research in the SiNW-FET biosensor field has rapidly expanded with the fundamental aim to improve the sensitivity and specificity of the biomarker-based quantification methods. Label-free and real-time biomarker detection using SiNW-FETs has been demonstrated by various groups. Zheng *et al.* utilized SiNW-FETs arrays for  $10^3$  fg/mL concentration detection of multiple biomarkers involving prostate specific antigen (PSA), carcinoembryonic antigen (CEA) and mucin-1 (tumor) detection [46] using clusters of SiNW arrays. Chua *et al.* reported on the successful detection of fg/mL concentration of human cardiac troponin-T (cTnT) markers, while cardiac troponin (cTnI) in the order of  $10^6$  fg/mL concentration was reported by Kong *et al.* [49]. Within the framework of lab-on-a-chip, microfluidic chips offer the possibility of prepurifying and changing the buffer salt concentration before flowing to SiNW-FETs as demonstrated by Stern *et al.* [52], providing a detection limit in the concentration range of  $10^6$  fg/mL. Although SiNW-FETs provide a remarkably ultra-low

## Capitolo 1. Introduction

REFERENCE	APPLICATION
<b>Protein-protein interaction</b>	
Cui <i>et al.</i> [45]	Streptavidin-Biotin binding
Zheng <i>et al.</i> [46] Kim <i>et al.</i> [47] Li <i>et al.</i> [48]	Prostate Specific Antigen (PSA) detection
Kong <i>et al.</i> [49]	Cardiac Troponin I (acute myocardial infarction)
Chua <i>et al.</i> [50]	Cardiac biomarker detection
Wang <i>et al.</i> [51]	Small molecules detection for drug screening purpose
Zheng <i>et al.</i> [46]	Cancer markers detection: PSA, Carcinoembryonic antigen, Mucin-1
Stern <i>et al.</i> [52]	IgG, IgA detection
<b>DNA detection</b>	
Gao <i>et al.</i> [53] Hahm <i>et al.</i> [54]	DNA, RNA detection with PNA (Peptide Nucleic Acid)-modified SiNWs
Gao <i>et al.</i> [55] Li <i>et al.</i> [56] Stern <i>et al.</i> [57] Bunimovich <i>et al.</i> [58]	ssDNA detection via DNA hybridization
<b>Virus detection</b>	
Patolsky <i>et al.</i> [44]	Detection of Influenza Virus A
Chiang <i>et al.</i> [59]	Detection of H <sub>5</sub> N <sub>2</sub> Avian Influenza Virus (HIV) via reversible surface functionalization
Zhang <i>et al.</i> [60]	Dengue virus detection via integration of SiNW sensor with reverse transcription-polymerase chain reaction (RT-PCR)
<b>Bioelectricity recording</b>	
Patolsky <i>et al.</i> [61]	Study of neuron electrical activity
Qing <i>et al.</i> [62]	Neuron mapping study
Cohen-Karni <i>et al.</i> [63] Eschermann <i>et al.</i> [64] Pui <i>et al.</i> [65]	Bioelectricity recordings of cardiac cells
Poghossian <i>et al.</i> [66]	Cellular signals detection
Tian <i>et al.</i> [67]	Intracellular recording with 3D nano-FET

Tabella 1.2 – SiNW-FET applications in biosensing

concentration detection limit, challenges remain in detecting directly from the patient's blood sample or tumor tissue extracts without any further pretreatment on a chip level where various problems such as non-specific binding, high salt concentration and low/short ionic strength in the blood sample could decrease the performance of SiNW-FETs sensor [68, 69]. Most of the very successful sensing of biomarkers performed so far were indeed performed in ideal conditions, i.e. in *Phosphate Buffered Saline* (PBS) solutions, recreating pH conditions most

---

## 1.6. The Debye screening effect: limitations in biosensing

similar to the biological environment, yet much less challenging than the protein content in a real tumor human specimen (see Section 1.8.2).

### 1.5.2 Other applications

Most tumor markers are proteins. However, patterns of gene expression and changes to DNA have also been used as tumor markers. Capacitance-based measurements of DNA have been used, for example, as label-free cancer marker detection approach [70]. In particular, also SiNW-FET biosensors can be employed for DNA and RNA sensing. Due to the large amount of negative charges in the phosphate backbones of DNA or RNA, SiNW-FETs offer a good candidate for monitoring DNA or RNA hybridizations, because the hybridizations cause the accumulation or depletion of charge carriers in the SiNW-FET, leading to a conductance change. Peptide nucleic acid (PNA), an artificially synthesized polymer similar to DNA, is commonly used in biological research, especially in DNA or RNA hybridizations. Specific PNA-modified SiNW-FET sensors have recently been established to diagnose Dengue virus infection, too [60]. This strategy provides a platform not only to diagnose virus infection, but also to monitor early cancer symptoms [71]. Patolsky *et al.* reported on using SiNW-FETs for single virus particle detection of Influenza A with real time real-time electrical detection [44]. In addition to these applications, using nano- and neuro-technologies to couple electrical interfacing with neural systems has shown great potential to unveil many details of neuron studies [72]. In the past few years, SiNW-FETs have been applied for electro-physiological measurements by recording signals from neuron cells and tissues, e.g., recording the electrical signal from a single neuron [61] and cardiomyocyte cells [63]. Finally, the successful construction of 3D nano-FET probes for recording electrical signals from single cells [67] makes SiNW-FET sensors achieve a high goal in the design of nanobiosensors.

## 1.6 The Debye screening effect: limitations in biosensing

One of the most critical considerations for designing optimal protocols for label-free sensing using NW-FETs is the so-called Debye screening length between the sensor surface and the analyte.

Typically, the analyte consists of dilutions of biomarkers in physiological solutions that create a surrounding similar to the normal physiological environment. In such ionic landscape, it happens that the electric field affected by the surface charge density of biomolecules near the sensor surface vanishes beyond the Debye screening length, which is the distance over which the electric field is screened out by mobile charge carriers such as electrons or ions in the solution.

Specifically, the surface charges of biomolecules in a buffer solution are shielded by oppositely charged buffer ions, namely the counterions. On a certain length scale, the number of net negative (positive) charges approaches the number of positive (negative) charges on the

molecules. The electrostatic potential that results from the variation in the surface charge density of the analyte molecules exponentially declines towards zero due to the screening effect (Figure 1.5(b)). This critical length scale is called the Debye-Hückel length ( $\lambda_D$ ) [68, 73]. For an electrolyte buffer solution, the Debye-Hückel length is expressed by the following equation:

$$\lambda_D = \frac{1}{\sqrt{4\pi l_B \sum_i \rho_i z_i}} \quad (1.1)$$

where  $l_B$  is the Bjerrum length = 0.7 nm,  $\sum_i$  is the sum over all ion species, and  $\rho_i$  and  $z_i$  are the density and valence, respectively, of ion species  $i$  [74]. The screening directly depends on the Debye-Hückel length  $\lambda_D$ . Stern *et al.* demonstrated the effect of molecular charge shielding with a dissolved solution with oppositely charged ions on the p-type nanowire FET sensor response using a biotin-streptavidin system [68]. In this example, negatively charged streptavidin, whose pI value (isoelectric point, *i.e.*, the pH at which a molecule carries no net electric charge) is approximately 5.6, and the biotinylated FET surface are conjugated through the affinity between streptavidin and biotin. Upon streptavidin-biotin binding, a significant up-shift in the drain current of the p-type FET was observed. In the buffer solution with ionic strength of a  $0.01 \times$  PBS, where the value of  $\lambda_D$  is nearly 7.3 nm, most of the charge of streptavidin was unshielded to a large extent near the FET surface, thereby influencing the carrier density. On the other hand, the use of the ionic strength of a  $0.1 \times$  PBS buffer, with a  $\lambda_D$  value of approximately 2.3 nm, showed a partial screening effect of the charge of streptavidin. Finally, using the ionic strength of a  $1 \times$  PBS buffer ( $\lambda_D$  = around 0.7 nm), the majority of the charge of the protein was properly screened. These results strongly indicate that ionic concentrations play a major role in the detection sensitivity of devices.

For optimal sensing, the Debye length must be carefully selected for NW-FET measurements of specific target species. Its effect on the sensitivity of the biosensor is also related to the size of the biomolecules we want to detect. Indeed, as schematically illustrated in Figure 1.5(a), molecules binding to the devices are removed from the sensor surface by a length scale that depends on the size of the receptor proteins or DNA linkers integrated with the sensor surface. For example, considering that an antibody is typically 10-15 nm long (Figure 1.5(b)), the binding of antigen molecule will occur at a distance that falls outside, or at the limit, of the Debye screening length of the sensor, thus resulting in a lowered sensitivity of the measurement. Whereas, DNA oligos and small molecules are shorter and the corresponding detection of complementary DNA strands or interaction of small molecule determine an increased biosensor response because falling inside the Debye length (Figure 1.5(a)). This is also the reason why most of recent results of biosensing with SiNW-FETs have been achieved with DNA-based detection [46, 75].

Gao *et al.* have recently reported that the optimal sensitivity of SiNW-FET in biosensing can be achieved by judiciously selecting the subthreshold: in this regime, carriers in the wire have long screening length and the field effect of surface charges can gate the whole SiNW [19]. Schönenberger *et al.* have proposed instead the alternative solution of creating a conformal



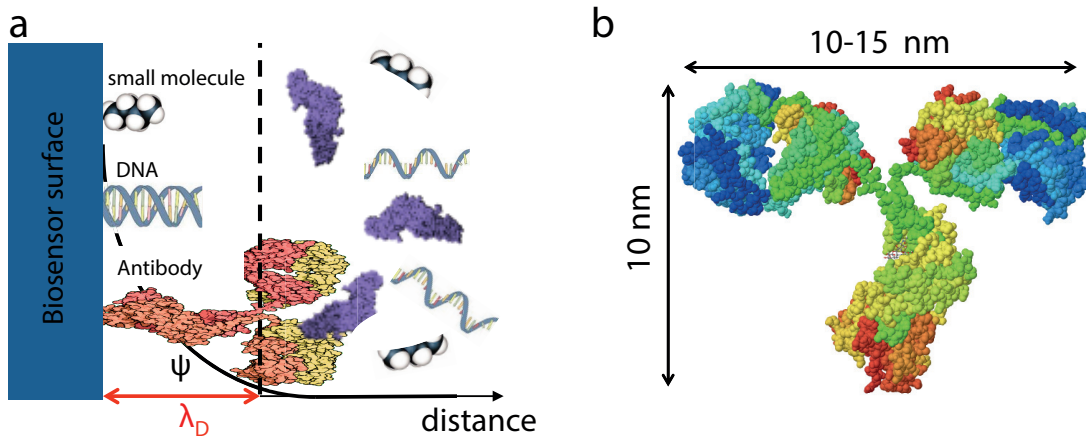


Figure 1.5 – a) Schematic representation of the Debye screening length  $\lambda_D$  from the FET surface. The electrostatic potential arising from charges on the protein or DNA decays exponentially toward zero with distance. b) Structure and size of an IgG2 antibody molecule (Protein Data Bank).

thin coating of high quality and dense oxide *Atomic Layer Deposition* (ALD) layer all over the device to remove the leakage current [76].

In this thesis, we will demonstrate that we managed to overcome the Debye screening limitation by proposing a novel paradigm of detection in dry condition. In this approach, we ensure antibody-antigen interaction and binding by incubation of the biosensor in the analyte solution; then, after washing procedures and drying of the surface, detection of occurred Ab-Ag binding is performed through electrical acquisition in air. This method prevents the charged antigen molecule to be screened because of the increased  $\lambda_D$  resulting from the bulk solution that has been now removed.

## 1.7 Memristive systems

The interest for memristive devices has been rapidly increasing in recent years, thanks to the very different applications they can be used for. The majority of current research on memristive systems is dedicated to the study and implementation of memories and logic circuits [77, 78]. In this thesis we will report the first molecular sensing based on nanofabricated sensors showing memristive-like behavior.

The following section reports the state-of-the-art of memristive systems and serves as theoretical background to the most original and important work performed within this thesis.

### 1.7.1 The pure memristor

The term memristor was first introduced by Leon Chua in 1971 [80]. While studying the mathematical fundamentals of circuit theory, he postulated the existence of a fourth base

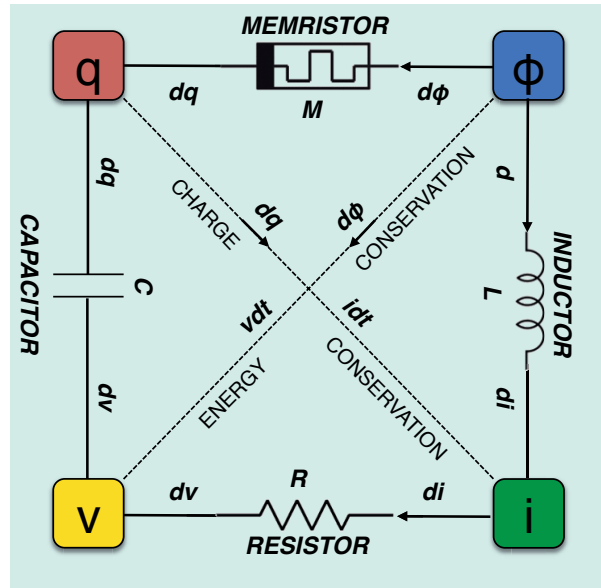


Figura 1.6 – Symmetry diagram showing the six distinct possible realizations based on the four circuit variables. Adapted from [79].

electronic element in addition to resistor, inductor and capacitor. He named this element “memristor”, due to its behavior, comparable to a resistor with memory. The three basic circuit elements resistor, capacitor, and inductor are defined by a relationship between two of the four axiomatic circuit variables: the voltage ( $v$ ), the current ( $i$ ), the charge ( $q$ ), and the flux ( $\varphi$ ). The total number of their possible combinations is six, as schematically shown in the symmetry diagram of Figure 1.6 [80], but Chua noted that only five of these combinations had led to established relationships. Two of them are the definition of current  $i = dq/dt$  and Faraday’s law of induction  $\varphi = \int_{-\infty}^t v(\tau) dt$ . The other three are the definitions of the well-known basic circuit elements, the capacitor, the resistor, and the inductor:

$$C = \frac{dq}{dv} \tag{1.2}$$

$$R = \frac{dv}{di} \tag{1.3}$$

$$L = \frac{d\varphi}{di} \tag{1.4}$$

The last relationship between electric charge,  $q$ , and magnetic flux,  $\varphi$  remained undefined. The fourth circuit element was postulated by Chua who named it memristor (resistor with memory) based on the property of changing its resistance depending on how much charge flowed through it [80]. The relationship between flux and charge is defined as the memristance:

$$M = \frac{d\varphi}{dq} \tag{1.5}$$

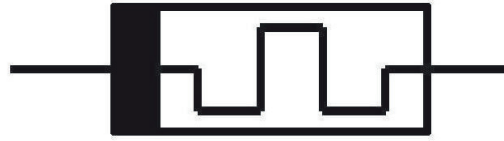


Figura 1.7 – Symbol representing a memristor in an electric circuit.

Figure 1.7 shows the electronic symbol of a memristor element. From the symmetry diagram in Figure 1.6, we see how the memristor finds its natural place in the circuit theory along with the five other combinations of pairs of circuit variables. A broad generalization of memristors to an interesting class of nonlinear dynamical systems called memristive systems was introduced by Chua in 1976 [81]:

$$v = R(x, t)i \quad (1.6)$$

$$\frac{dx}{dt} = f(x, t) \quad (1.7)$$

which looks like a nonlinear time-varying version of Ohm's law. As defined by Eq. 1.6, the memristor depends on the state variable  $x$  that describes the state of the system and  $x$  is time dependent. This time dependence of the state variable provides the memory of the system. Thus the resistance will vary with the amount of charge passed through the element and in general not be a constant.

The most salient feature of memristive systems is its zero-crossing property. In spite of the memory effect which normally introduces phase shifts in conventional systems, memristors are incapable of energy discharge and they introduce no phase shift between the input and output waveforms, i.e. the output of a memristive system is zero whenever the input is zero. This zero-crossing property manifests itself in the form of a Lissajous figure which always passes through the origin (Figure 1.8a). Among the various properties of memristive systems, the frequency response of the Lissajous figure is especially interesting. As the excitation frequency increases toward infinity, the Lissajous figure shrinks and tends to a straight line passing through the origin (Figure 1.8b), except for some cases where the stability property is not satisfied. The physical interpretation of this phenomenon is that the system possesses certain inertia and cannot respond as rapidly as the fast variation in the excitation waveform and therefore must settle to some equilibrium state. This implies that the hysteretic effect of the memristive system decreases as the frequency increases and hence it eventually degenerates into a purely resistive system.

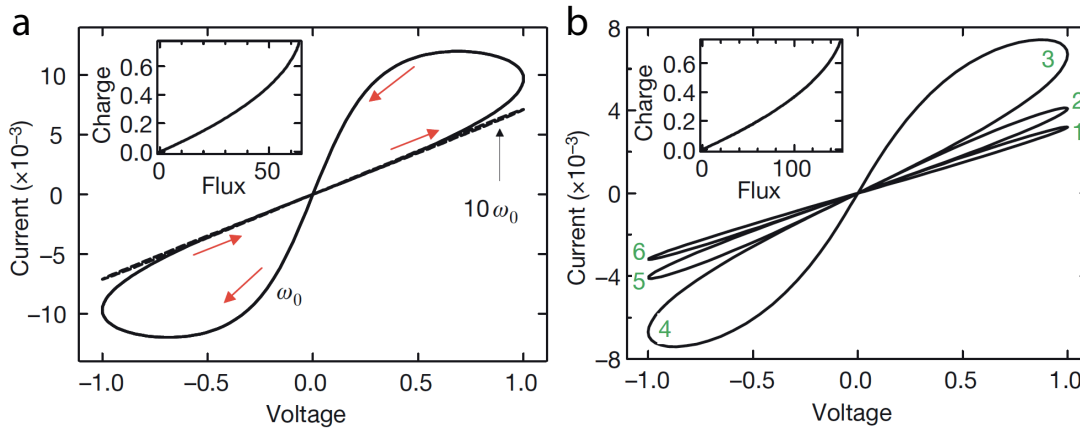


Figure 1.8 – a) An idealized I-V curve of a memristive system subjected to a periodic voltage. The result is a Lissajous figure, i.e. a pinched hysteresis curve. b) demonstrates the hysteresis collapse observed with a tenfold increase in sweep frequency. The insets in the I-V plots in b and c show that for these examples the charge is a single-valued function of the flux, as it must be in a memristor. Reprinted from [82].

### 1.7.2 Memristive devices: state-of-the-art of the technology

Memristive devices have been already used for different applications. A number of applications have been suggested especially in the fields of logic design and memory [78]. In particular, memristors-based digital circuits have been introduced in dense programmable logic circuits [83], Resistive RAM memories [84, 85], 3-D Field Programmable Gate Arrays (FPGA) [86, 87], as well as design of Cellular Neural Networks for the emulation of the biophysics and temporal dynamics of real synapsis [81, 88].

Among all possible memristor-based technologies and their applications, the introduction of memristive nanowires is of particular relevance to the scope of our thesis. For this reason, in this section we mainly focus on memristive device based on nanowires by briefly reviewing their most recent applications.

### 1.7.3 Memristive SiNW

Starting from the first realization of a memristive device by Strukov *et al.* [82], solid state research has focused towards the implementation of novel technologies for memristor-based applications. A first example of nanowire-based memristive technology is the one proposed in [89]. In this work, the functionalization of nanowires with redox active molecules was shown to give rise to the typical memristive pinched hysteresis loop.

Recently, multiterminal memristive devices based on CMOS nanowire technology have been realized, and used mostly for logic and memory applications [90].

The fabrication of the first three-terminal memristive device based on poly-crystalline Si nanowires (poly-SiNWs) was proposed by Ben Jamaa *et al.* [91]. The device, made of undoped

poly-Si, Cr/nichrome source and drain contacts and the substrate used as long back gate, showed ambipolar behavior, *i.e.*, a current conductance under either high positive or negative gate voltage. More importantly it was characterized by a memristive hysteresis in the  $I_{ds} - V_{ds}$  characteristics that was associated with charge trapping mechanisms at the interface states between the channel and the gate oxide. These devices were proposed for logic/memory applications, such as the definition of new logic families and hybrid logic/memory gates, and for the design of a circuit cell reproducing a hysteretic negative differential resistance [90]. Sacchetto *et al.* have then proposed memristive devices based on the *Gate All-Around (GAA) Schottky Barrier FET* (SB FET) concept with SiNW channels on bulk-Si or *Silicon On Insulator* (SOI) wafers [92]. The nano-structures showed hysteretic behavior reminiscent of a two-terminal monolithic memristive device, as reflected by the  $I_{ds} - V_{ds}$  curve, for forward  $V_{ds}$  sweep, not identical to the same curve for backwards  $V_{ds}$  sweep. Also in this case the memristive hysteretic behavior was attributed to the presence of interface states at the metal/-semiconductor junctions as reported in literature for Schottky diodes [42].

The memristive behavior reported for the *Schottky Barrier* (SB) SiNW-FETs was tuned by operating on the polarity of the gate voltage. This type of behavior is linked with the double conductance, for holes and electrons. The ambipolarity was controlled by using an additional control gate, such that it blocked one type of carrier conductance. Following this principle, four-terminal memristive SB SiNW-FETs were built [90]. Four-terminal GAA SB Si nanowire FETs were used for the first time with sensing purposes and were demonstrated to enable low current and temperature sensing [93].

Only few years ago, Sacchetto *et al.* [94] and Carrara *et al.* [95], showed the first evidence of the potential use of memristive effects in nano-structured devices for biosensing applications. In particular, they first suggested Schottky-barrier silicon nanowire devices functionalized with antibody films and exhibiting electrical behaviors reminiscent of memristive devices as biosensors. This research opened the way to the development of a completely new bio-detection mechanism based on memristive SiNWs. However, despite the presented results, a deep understanding of the mechanisms underlying the dependence on biomolecules of the memristive effect in silicon nanowires was still lacking.

In this thesis we propose important advancements in this new field of research for biosensing applications. In particular we will demonstrate, that fabricated memristive nanowires can be used for high-sensitive measurements of biological species. By investigation of the memristive properties in the devices through a number of accurately designed experiments, we will confirm the evidence of the peculiar dependence of the hysteretic behavior on biomolecules, and, more relevantly, we will show the achieved detection of ultra-low concentration of biomarkers in tumor extract. Furthermore, we will present theoretical studies providing the description and prediction of the memristive effect variations as result of biomolecules. Our work will pave the way to a revolution in the SiNW-based technology for biosensing.

### 1.8 Thesis scope and objectives

#### 1.8.1 The biomedical impact

The objective of this thesis is the realization of a biosensor based on SiNWs overcoming the main limitations of the traditional ISFET technology. The final aim is the detection and profiling of biomarkers, such as angiogenic and inflammatory ligands, in the very hostile environment of patient breast tumor specimens, and at the very early stage of the tumor disease. The final goal is very challenging, mainly because the concentration of biomarkers in the human organism at the early stage of the disease is very low and still below the detection limit of the state-of-the-art diagnostic tools.

The developments we propose in this thesis will open the way to the realization of novel biosensors with ultra-highly sensitive and specific capabilities. The femtomolar detection of biomarkers directly from tumor tissue will provide new opportunities both in terms of more powerful tools for cancer diagnosis, and of novel therapeutic strategies.

The application to biological and medical sciences is innovative and required strong multidisciplinary efforts in the fields of experimental oncology and electronics.

#### 1.8.2 The challenge of sensing in breast tumor extract

To date, the major limitation to the characterization of the tumor microenvironment is the inability of the current technologies to reach the sensitivity required for the analysis of very limited amounts of patient specimens. Human tumor specimens are indeed often of small size, unique, and thus precious biological samples. Moreover, they are sites of uncontrolled deregulated cellular proliferation that induces very fast changes in the protein landscape under investigation. Thus, to date, the tumor microenvironment remains ill-defined due to its complexity and its instability.

One major concern of sensing with high-sensitive SiNWs in a real tumor extract solution is the background noise determined by the non-specific molecules characterizing the human tissue. The screening of the biosensor with respect to the target biomarkers is determined not only by ions from the dissolved salts of the physiological solution, but also by bigger charged species, such as proteins, growth factors, adipocytes, fibroblast enzymes, and more.

A further issue related to the sensing in a highly active environment such as a tumor specimen, is the presence of enzymes characterized by a very pronounced digesting activity. These factors not only digest the proteins and thus the target molecules that are diluted in the tumor extract but can also attack the antibodies immobilized onto the NW surface thus deteriorating the sensor capabilities.

#### 1.8.3 Objectives of the thesis

To date, the approaches to profile inflammatory and angiogenic ligands in specific tumor zones are extremely limited. We decided to approach this challenging project by proposing improved

SiNW based devices for ultra high-sensitive measurements in the very critical landscape of the tumor tissue.

So far, nanowires have been proposed several times as ISFET for pH [96, 97], cancer markers [46] or DNA [98, 99] detection in fluids (Section 1.5). The successful detection of antigens with antibody-functionalized NW-FETs has been recently achieved with femto-molar sensitivity in an assay buffer solution by several groups. Moreover, protein analysis using nanowires has been rarely adopted for detection in real human samples, and when proposed, results have shown increased detection limit due to the low signal-to-background. The reduced sensitivity and reproducibility in real sample is mainly due to Debye screening effects and lack of specificity (Section 1.6). To the best of our knowledge, only few works have been published on SiNWs-based sensing in extracts from tumor cells. They all demonstrate DNA detection [46, 75], and not the more challenging antibody/antigen based detection in real human samples.

The main aim of this thesis is to go beyond the sensitivity and reproducibility properties of standard nanowire based biosensing techniques with the main goal of detecting biomarkers in the very hostile breast tumor environment, with high specificity. We decided to address this challenge by investigating two different approaches of biosensing with the two main objectives of:

- pushing to their limits sensitivity and specificity of current SiNW-FET technologies for biosensing;
- proposing an alternative approach based on memristive SiNWs for improved sensing resolution.

Specifically, we discuss how we achieved these aims by proposing the innovative in-air biodetection strategies reported as follows:

1. **Biodetection with SiNW-FET in-air biosensors** We show how we managed to enhance the state-of-the-art of SiNW-FET technologies by proposing an alternative way of doing sensing with very high quality SiNW-FETs based on in-air biosensing measurements. Sensing of biomolecules is performed in dry conditions after exposure of the device to the target solution, followed by washing and drying operations. In-air electrical measurements of interaction phenomena, occurred between the immobilized antibodies and the specific antigens in liquid, showed the advantage of increased Debye screening length in non-bulk solutions, and enable highly specific measurements in real human samples [100, 101].
2. **Biodetection with SiNW-based in-air VoG-biosensors** We present a novel electronic-based biosensing paradigm which combines the molecular selectivity of immuno-assays to the sensitivity power of memristive SiNWs and the in-air detection paradigm. This novel method of biodetection has been named VoG-biosensing in memristive devices, as it is based on the changes in the VoG parameter, observed in memristive devices, as

a function of biomolecules. Memristive effects in nano-devices have been proposed mostly for applications in memory and logic circuits (Section 1.7.2), but never exploited as sensors of biological molecules. This thesis first proposed the VoG approach that is related to the use of the peculiar hysteretic behavior in Schottky Barrier SiNW devices as alternative paradigm for biodetection [102–104]. In this research, we deeply investigate the use of SiNWs with characteristics reminiscent of memristive systems for more reproducible and high-resolution sensing of ionic and biological species both in ideal buffer solutions and in real tumor tissue extracts.

### 1.9 Thesis outline

The thesis chapters are organized as follow. In Chapter 2, an introduction to the most common NW fabrication methods used in literature is proposed, followed by (i) the description of the process flow developed at TUDelft for the fabrication of *SiNW-FET*, and (ii) the detailed presentation of the process flow developed and implemented at EPFL for the physical implementation of memristive SiNWs. In Chapter 3, the technique used for the chemical modification of the SiNW surface with antibodies is presented and discussed in terms of specificity of the biofunctionalized area. In Chapter 4, the experimental set-up used for sensing with the fabricated devices, both in buffer solution and in tumor extract, is firstly introduced; the in-air electrical characterization of SiNW-FETs before and after exposure to antigen is then presented for demonstrating the high-sensitivity and specificity reached thanks to the measurement in dry conditions. In Chapter 5, the innovative topic of sensing with the VoG approach in memristive SiNW technology is firstly introduced; the in-air electrical characterization of the biosensor is then presented and discussed for varying humidity conditions, and pH variation; the successful detection of biomarkers after exposure both in buffer and tumor extract is then presented. In this thesis, we will refer to voltage-gap based biosensors as VoG-biosensors, and to the voltage-gap parameter of detection as VoG. In Chapter 6, a detailed presentation of the developed and implemented physics-based compact model that describes the occurrence of the voltage-gap in bio-modified Shottky barrier SiNWs, and links this effect to the interaction of charged species with the surface of the wires is proposed. In Chapter 7, the possibility of improving the performances of the VoG-biosensor by integrating the device with a microfluidic system, as well as with a CMOS circuit appositely designed for parallel voltage-gap measurements is also discussed. Finally, the conclusions are drawn in Chapter 8 together with prospects for future applications in multi-panel platform for breast cancer diagnosis.



## 2 Silicon Nanowire fabrication

This chapter provides the technological details relative to the fabrication of the sensor devices used in this work. Two classes of devices have been fabricated and then characterized. The first class is about high-quality CMOS-compatible SiNW-FETs fabricated at the Delft University of Technology, Netherlands, and then biomodified and used at EPFL for sensing purposes (Chapter 4). The second class deals with SiNWs featuring memristive characteristics fabricated at EPFL and then characterized in detail for detecting biomarkers with the novel VoG approach (Chapter 5). We refer to this second group of devices as memristive NWs. Upon biofunctionalization with antibody, they will be referred to as VoG-biosensors. For both kinds of biosensors, a top-down silicon nanowire-based device fabrication approach is chosen: the SiNW-FETs are manufactured by a *Plane-Dependent Etching* (PDE) process; the memristive NWs fabricated at EPFL are obtained by a single *Deep Reactive Ion Etching* (DRIE) etching step leading to vertically-stacked nanowires. In the following, we describe more in detail the geometry and dimension of the presented devices. First, we introduce the most common SiNW fabrication techniques used in literature and their advantages and disadvantages. Then, we present the fabrication process flow of the studied devices. As the detailed fabrication process of the SiNW-FETs was developed at TUDelft by another Ph.D. student, only a brief presentation of the main fabrication steps is introduced. This is then followed by a detailed description of the complete process flow implemented at EPFL, together with a discussion on the challenges and the methods employed to obtain the final measured memristive NWs.

### 2.1 Overview on nanowire fabrication

A number of techniques have been proposed in literature to fabricate semiconducting nanowires to be used as electrical channel in sensing devices. There are two major fabrication techniques in preparing silicon nanowires: *top-down* and *bottom-up* approaches. In the top-down methodology, the structures are etched out of a whole (e.g., a crystalline substrate), whereas in the bottom-up, the structures are grown from precursor gases and particles, and subsequently assembled and positioned to create the device channels. In this section, we summarize the main techniques proposed in literature, and present pros and cons of each

category. Even though, both for SiNW-FETs and memristive NW, we chose a top-down approach, bottom-up methods are also included in this overview, because of the numerous works published on biosensing with SiNWs obtained with this fabrication methodology.

### 2.1.1 Bottom-up approach

#### Nanowire grow methods

Bottom-up methods include a large variety of techniques allowing the growth of nanowires of different lengths, cross-sectional profiles, materials and properties. Typically, growth of nanowires is initiated using catalyst nanoparticles which are put in a reactive atmosphere containing a silicon (or other elements) precursor species. The precursor reacts with the surface of the nanoparticle depositing the silicon, and a wire grows in a certain direction from the particle.

Numerous ways exist to the bottom-up fabrication of semiconductor nanowires. The *Vapor Liquid Solid* (VLS) is the key mechanism for silicon nanowire growth, and the most commonly used technique to semiconductor nanowire production, more in general. The VLS mechanism relies on a vapor phase precursor of the nanowire material, which impinges on a liquid phase seed particle (Figure 2.1I(a), from which unidirectional nanowire growth proceeds (Figure 2.1(b)). Simply turning off the source can adjust the final length of the nanowire. The diameter of the grown NWs corresponds directly to the diameter or the size of the melted catalyst nanodroplets on the substrate surface. Heterostructures of NWs can be grown by the same mechanism (Figure 2.1I(c)) but with one or more layers of different materials being added horizontally or radially to the existing layer. This is done by alternating the precursors used and taking into account the difference between the lattice constant of different materials [31, 105]. In addition to VLS-type nanowire growth mechanisms, there exists a range of other routes to produce bottom-up grown nanowires. Most important in the context of wire growth is the so called *Vapor Solid Solid* (VSS) mechanism, which comes into play when wire growth is catalyzed by a solid catalyst particle instead of a liquid catalyst droplet. Other approaches [106, 107], differing for the technique employed to provide the precursor to the catalyst nanoparticle surface, include the *Chemical Vapor Deposition* (CVD), annealing in a reactive precursor-rich atmosphere, evaporation and reaction of SiO as a precursor, *Molecular Beam Epitaxy* (MBE), laser ablation of a precursor target, solution-based techniques allowing the use of different, non-gaseous precursor molecules. Figure 2.1II(a-f), shows a schematic view of the experimental setups of different techniques employed to provide the precursor Si to the catalyst nanoparticle surface and grow the wires. Figure 2.1III shows *Scanning Electron Microscope* (SEM) images of nanowires grown on a substrate via VLS and different techniques of forming catalysts: (a) laser ablation (b) *Low Pressure Chemical Vapor Deposition* (LPCVD) (c) MBE.

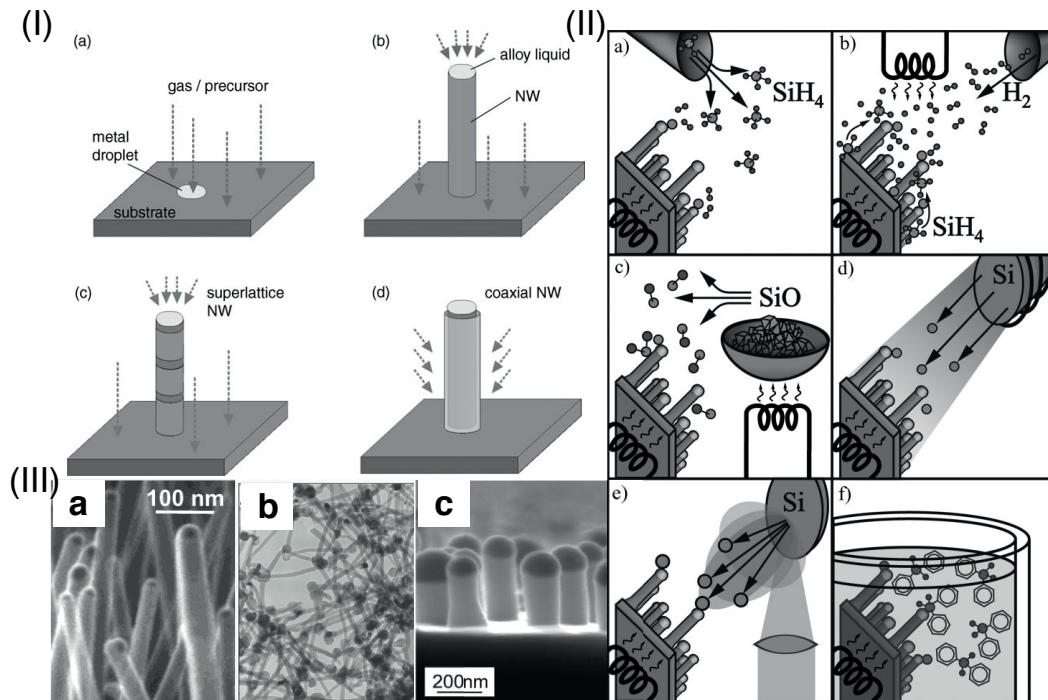


Figure 2.1 – (I) VLS growth mechanism: a) Deposition of metal catalyst and formation of nanodroplets. b) Continuous alloying and nucleation resulting in NW growth at the pre-defined sites of the previously formed nanodroplets. c) Growing heterostructure NWs by alternating the gas precursors. d) Coaxially grown NW by using lattice matching and two or more growing steps. Reprinted from [108]. (II) Schematics of experimental setups for SiNW growth. a) CVD, b) annealing in reactive atmosphere, c) evaporation of SiO, d) MBE, e) laser ablation, and f) solution-based growth. Image adapted from [106]. (III) Examples of NWs grown via VLS with various techniques of forming catalysts nanodroplets: (a) laser ablation (b) LPCVD (c) MBE. Reprinted from [108–110].

### Nanowire transfer and alignment techniques

Bottom-up grown semiconductor nanowires are typically produced as entangled meshes of nanowires and, as a result, lack the periodic ordering and placement required for large-scale semiconductor device. There have been a number of techniques developed to transfer and align semiconductors to be used as transistors channel. Electric field-based alignment techniques [107, 111], including dielectrophoresis [112, 113], have been shown to allow precise control over nanowire position with respect to metallic contact pads; however, these techniques have not yet demonstrated the high density of aligned nanowires required for high volume manufacturing. Microfluidic alignment [114], contact printing [115] and evaporation induced alignment [116] techniques have all demonstrated the capability to create parallel nanowire arrays, in some cases with high areal density. However, these techniques lack the prerequisite precision of control over nanowire placement, required for individual nanowire

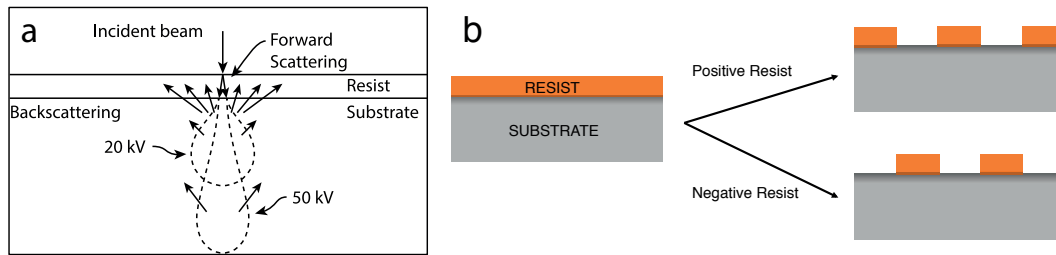


Figure 2.2 – (a) Interaction of electrons with a typical semiconducting substrate coated with a thin PR layer. Image adapted from [118]. On the right, the effect of a beam of electrons on a positive (dissolution) and a negative resist (cross linking).

addressability within very *Very Large Scale Integration* (VLSI) technology. Directed growth approaches, like epitaxial nanowire growth, and hard-templated nanowire growth allow to produce regular and uniform nanowire arrays.

In general, fine control of the final NW density and position on a final substrate is a strong limiting factor to CMOS integration. Nevertheless, numerous groups have demonstrated very high performance electronic and sensing devices using bottom-up NW [?, 46, 54, 117].

### 2.1.2 Top-down approach

The top-down method is typically carried out through lithographic processes combined with an electron beam technique that defines NWs by physically etching a single-crystalline silicon wafer. Many different approaches, including *Electron-Beam Lithography* (EBL), *Focused Ion Beam* (FIB) lithography, *Nano Imprint Lithography* (NIL), etching techniques, have been developed for the definition of nanowires, mostly derived from integrated circuit processing. In this section, only the methods relevant to the scope of this thesis will be introduced.

#### Electron beam lithography

E-beam lithography is generally used in nano-technology to define small structures with very high resolution. By manipulating a beam of electrons, an object of dimensions as small as a few nanometers can be patterned on a layer of *PhotoResist* (PR). Similar to optical lithography, EBL is based on the principle that some polymers are sensitive to electrons. More precisely, by absorbing the energy of secondary electrons activated by inelastic scattering of the primary electrons with the macromolecules of the polymer (Figure 2.2(a)), either chain secession (positive resist) or cross linking (negative resist) can occur (Figure 2.2(b)). Thus the desired pattern can be directly written into the resist and later be transferred to the substrate by etching techniques.

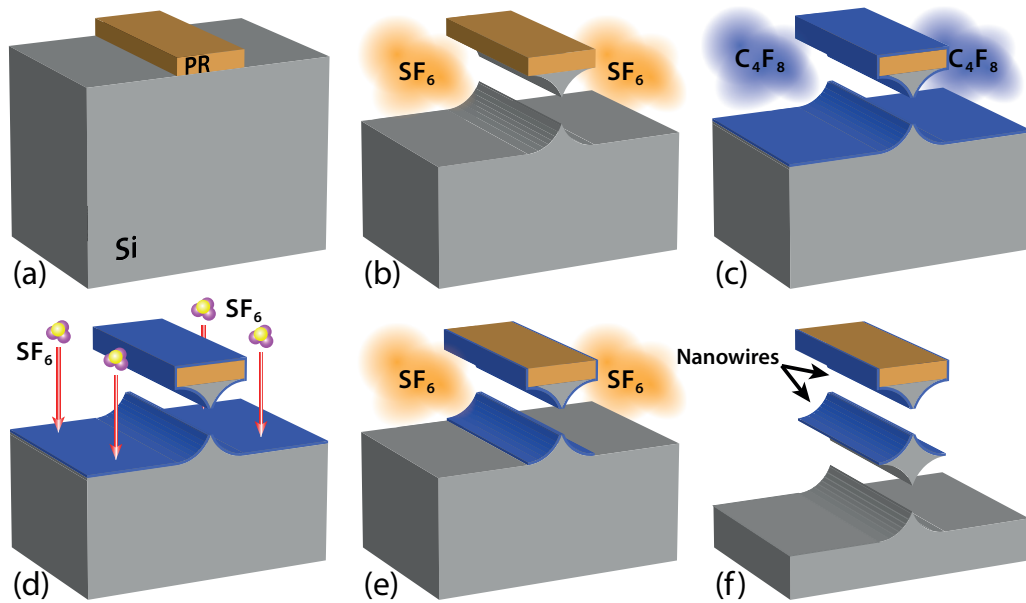


Figure 2.3 – Top-down SiNW fabrication procedure based on Bosch etching: (a) a PR mask is patterned on crystalline silicon; (b) physical/chemical  $\text{SF}_6$  etching is applied, creating an undercut below the mask pattern; (c) the patterned Si layer is then masked by a thin conformal layer resulting from the  $\text{C}_4\text{F}_8$  gas; (d) anisotropic  $\text{SF}_6$  plasma removes the vertically accessible surface passivation, and (e) etches the unprotected region creating a new undercut, that leads to (f) a new nanowire. Reprinted from [121].

### Deep reactive ion etching

The method we used in the memristive NWs process flow is based on dry DRIE (or Bosch) process, from the original patent developed in 1996 [119]. This technique consists of alternating a quasi-isotropic etching step, based on  $\text{SF}_6$ , for silicon, with an organic passivation step based on Octafluorocyclobutane ( $\text{C}_4\text{F}_8$ ).

This method was proposed for the fabrication of nanowires in 2007 by Ng *et al.* [120] and further developed by Sacchetto *et al.* [90] for the fabrication of nanowire-based active devices. A simplified version of the process of fabrication of SiNWs by DRIE is schematically explained in Figure 2.3. After creating a thin PR line on a substrate (Figure 2.3(a)), the first step consists of an isotropic Si etching with  $\text{SF}_6$ , lasting one to a few seconds, creating a groove with a small undercut at the edges of the PR pattern (Figure 2.3(b)). Then, a thin passivation layer is deposited by polymerization of the second precursor  $\text{C}_4\text{F}_8$  (Figure 2.3(c)), which inhibits further Si etching on the surfaces shadowed vertically by the photoresist mask (Figure 2.3(d)). Only the horizontal exposed PR surfaces are cleaned from the organic layer by the  $\text{SF}_6$  etching (Figure 2.3(e)). Finally, a new undercut is produced by chemical etching with  $\text{SF}_6$  leading to a new nanowire (Figure 2.3(f)).

Figure 2.4 shows a *Scanning Electron Microscope* (SEM) image of pillar and nanowire structures patterned and etched in bulk silicon. Scalping due to the cycling nature of the etching is visible on the sidewalls. Where the pattern width becomes thin enough, the scallops at the

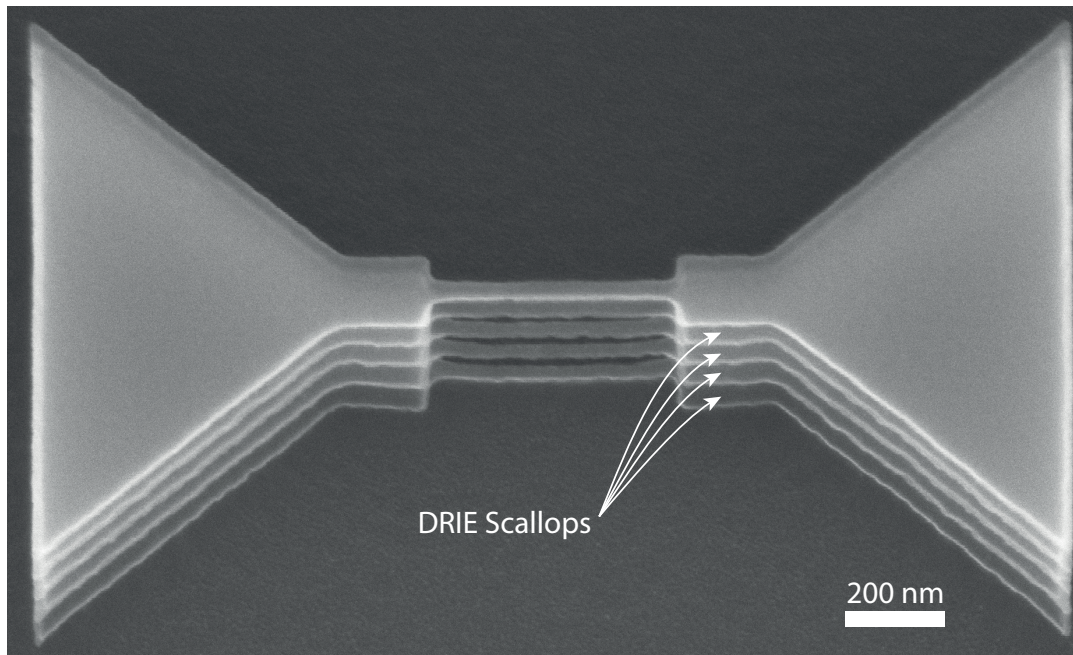


Figura 2.4 – SEM micrograph of a structure etched using DRIE on a silicon bulk wafer. Scalloping due to the cycling nature of the etching is visible on the sidewalls. The number of scallops typically indicates the number of etching cycles, although the first isotropic etching step may not result in a visible groove, due to the surface imperfections, including native oxide, require a breakthrough time. Reprinted from [121].

two sides of the pattern touch, releasing discrete nanowires. The number of scallops typically indicates the number of etching cycles.

### Crystalline Plane-Dependent Etching

In silicon micromachining, wet anisotropic etching is preferred compared to dry etching when large 3D structures with low roughness side walls and tilted surfaces are required. Moreover, thanks to the orientation-dependency and controllable etching rate, nano-scale devices can be fabricated without the need of expensive and time-consuming nanolithography such as E-beam. Typically, wet etching is an isotropic event, i.e., a non-directional etching with constant and uniform etching rate in all directions. In a crystalline material such as single crystalline Si, the etch rate is typically lower in the densely packed lattice compared to loosely packed lattices. Si has a diamond-like lattice structure as described by the Miller indices [122]. The density of atoms on a Si wafer differs according to the planes, with the  $\langle 111 \rangle$  plane being the densest, followed by  $\langle 100 \rangle$  plane. Meanwhile, the  $\langle 110 \rangle$  planes are the loosely packed planes. Thus, the etching rate in a wet etcher differs depending on crystalline orientation with  $\langle 110 \rangle$  as a faster etching plane followed by  $\langle 100 \rangle$ , while  $\langle 111 \rangle$  is the slowest etching plane. Because of this dependence of the etch rate on the plane orientation, this approach has been named PDE [123].

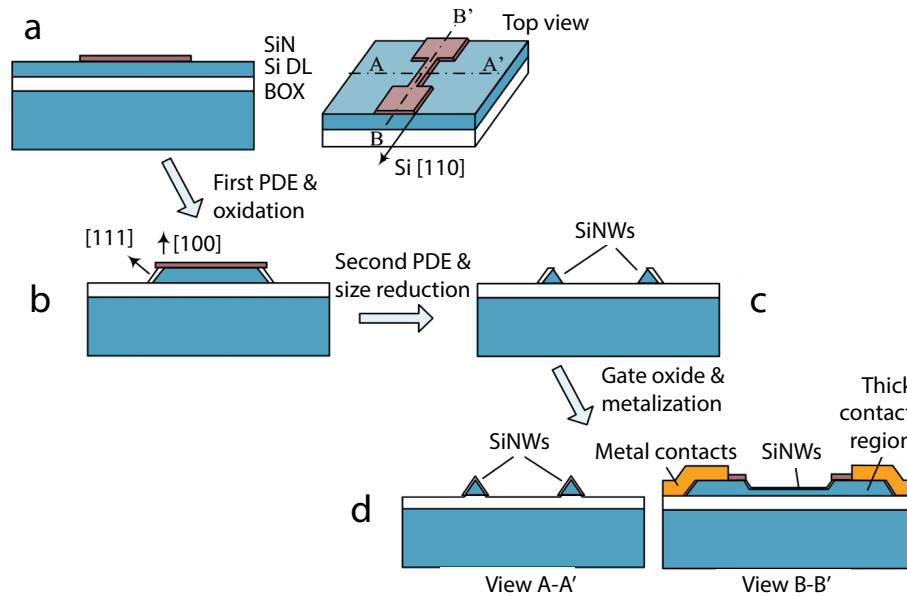


Figura 2.5 – Top-down SiNW microfabrication procedure based on anisotropic wet etch: (a) lithography and etch steps for SiN layer patterning (BOX: buried oxide layer and Si DL: silicon device layer of the SOI substrate); (b) silicon device layer PDE and local oxidation; (c) second PDE and size reduction; (d) gate oxidation and contact metalization. Reprinted from [124].

Up to date, most of the silicon nanowires fabricated via top-down microfabrication techniques offer one or two crystalline surfaces/planes, and many groups [52, 124, 125] have opted for this methodology.

In Figure 2.5, we report an example of wet anisotropic etching developed by Chen *et al.* [124] for the fabrication of sub-30nm single crystalline  $\langle 111 \rangle$  planes SiNWs. Briefly, a thin silicon nitride (SiN) layer, deposited by LPCVD on top of a Silicon-On-Insulator (SOI) layer, is patterned by a first lithography step performed by aligning the mask along the [110] direction of the silicon device layer crystalline plane (Figure 2.5(a)). The wafer is then etched using aqueous *tetramethylammonium hydroxide* (TMAH), an alkaline solution whose etching rate of the  $\langle 111 \rangle$  plane is significantly slower compared to the  $\langle 100 \rangle$  plane. This results in a trapezoidal silicon region with precisely defined sidewall angles defined by the intersection between the planes. The exposed  $\langle 111 \rangle$  facets are then thermally oxidized (Figure 2.5(b)). Subsequently, a second lithography step is performed to pattern the SiN mask, and a second PDE step, stopping on the  $\langle 111 \rangle$  plane, is carried out until definition of triangular SiNWs (Figure 2.5(c)). After removal of the nitride and oxide layer, two triangular shape SiNWs with two  $\langle 111 \rangle$  planes side by side existing in parallel are clearly visible as shown in Figure 2.5(d-e).

### 2.1.3 Advantages and disadvantages of the top-down approach

Top-down methods are currently employed in all CMOS industrial processes, thanks to numerous advantages they revealed compared to the bottom-up techniques. The pros and cons of

## Capitolo 2. Silicon Nanowire fabrication

---

using top-down methodologies are listed here below:

### Pros:

- Standard semiconductor techniques are used to precisely design and fabricate the desired device or device-array pattern on the final substrate. This means that there is no need to add separate processing steps to produce some device parts (e.g., the nanowire) which would then have to be transferred to the final substrate and aligned, with the risk of increased variability and contamination.
- Top-down processes allow the complete control over physical and electronic degrees of freedom. The geometry and alignment of the nanowire can be fully controlled because channel structure and properties are all equal by construction with e-beam lithography and standard semiconductor processing techniques. On the contrary, bottom-up fabricated structures normally rely on precursor particles that can vary in size and shape leading to fabrication of wires that are always different, in term of cross-section and length.
- Since the device shapes are drawn once on a lithographic mask and then transferred by lithography to a substrate, top-down approaches can be used for large scale integration.

### Cons:

- Very expensive instruments, such as e-beam or FIB, are typically needed to achieve high resolution.
- While the bottom-up method permits the synthesis of SiNWs of high crystallinity, designated dopant density, easily controlled diameters, and core-shell radial layers of different materials, directly in growth chamber and in a cost-effective preparation, top-down methods do not allow flexibility in the design of the actual channel structures.
- Top-down methods consist of lithographic patterning and etching processes. Therefore, any irregularity in the lithographic mask and photoresist will translate into a source of variation at device level. High surface roughness and defects can arise from aggressive etching steps, contamination or mask irregularities. Grown structures can instead be fabricated with atomically smooth surfaces.

## 2.2 SiNW-FET fabrication

In this section, we will describe the process flow for the fabrication of the SiNW-FET arrays used in the following for biological experiments. Because these devices have been designed and fabricated by Moh *et al.* [126], in the clean room of the Microelectronics Department (DIMES) of TUDelft, Netherlands, the whole process will be presented without going too much



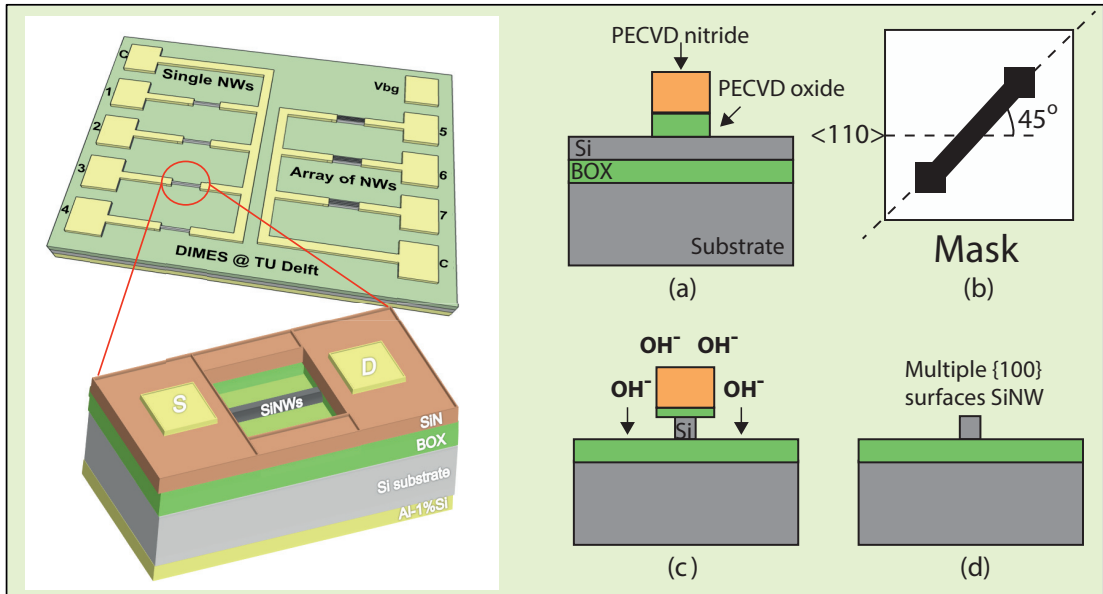


Figura 2.6 – (Left) Schematic top view of the chip layout with enlarged view of one device cross section. (Right) Fabrication process flow of SiNWs: (a) oxide deposition and patterning by dry etching; (b)  $45^\circ$  rotation of the mask to expose only  $\langle 110 \rangle$  planes; (c) silicon etching in AZ400K developer; (d) SiNW after oxide mask removal.

into the details.

### 2.2.1 Process flow

Figure 2.6 reports, on the left side, the schematic layout of the fabricated SiNW-FET arrays, and on the right side, the simplified process flow diagram for the NW formation. Conventional 4-inch SOI wafers from SOITEC France, with 340 nm thick top silicon layer with a crystalline lattice of (100) and 400 nm thick buried oxide were used. In order to optimize the device sensitivity for biosensing purposes, p-type FET devices were created by Boron implantation with doping concentration in the range of  $10^{16}$ - $10^{17}$   $\text{cm}^{-3}$  and of  $10^{19}$   $\text{cm}^{-3}$ , in the body and in the contact regions, respectively. Boron activation inside Si was carried out directly after the implantations step through an annealing process. SiNWs were then defined by PDE (Section 2.1.2). The most important steps for PDE definition of SiNWs are depicted in the right side of Figure 2.6. *Plasma Enhanced Chemical Vapor Deposition* (PECVD) oxide and nitride were patterned into micron size slabs by standard photolithography and used as masking materials for this process (a). The mask was rotated with an angle of  $45^\circ$  to align the pattern to the  $\langle 110 \rangle$  direction (b). The NWs are formed by gradually reducing the slab width with AZ400K developer (solution of 15%  $\text{K}_2\text{BO}_3$  in water) (c) with total etching time of 100 mins. The AZ400K developer is used preferred over TMAH or *Potassium Hydroxide* (KOH) solutions

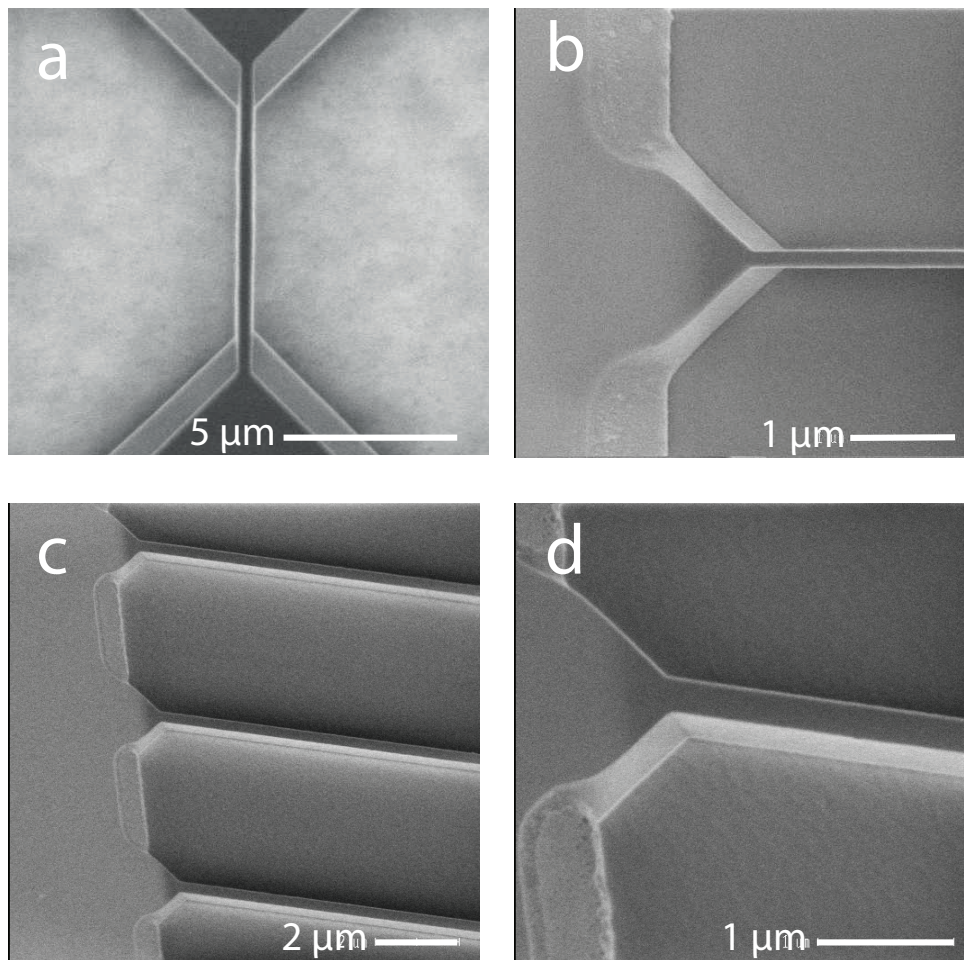


Figura 2.7 – SEM images of the fabricated SiNW-FETs.

due to its slower, but constant etching rate. The developer etches silicon both vertically down into the wafer and also laterally underneath the oxide and nitride mask. The vertical etch stops at the buried oxide layer, while the lateral under-etching continues inwards, further decreasing the dimension of the wires. Phosphoric acid (85%) at 157 °C is used to remove the PECVD nitride layer followed by *Buffered HF* (BHF) (1:7) etching to remove the PECVD oxide layer (d). Then, contact pads are formed by depositing aluminum and 1% of Si on the drain and source region as well as on the backside of the wafer to form the back gate. The gate terminal was formed at the backside of the device to have the surface available for functionalization and interaction with the mesurands. For the purpose of sensing in liquid environment, drain-source and part of the defined SiNW-FETs are electrically isolated with Low-stress oxide and nitride PECVD and opened using 0.55% HF. The last step is the alloying process at 400 °C in mixture of nitrogen/hydrogen gas mixture (3:0.5) for 20 minutes for a better contact to the highly doped Si layers. Both individual SiNW-FETs and arrays of SiNW-FETs were fabricated and then used for biosensing.

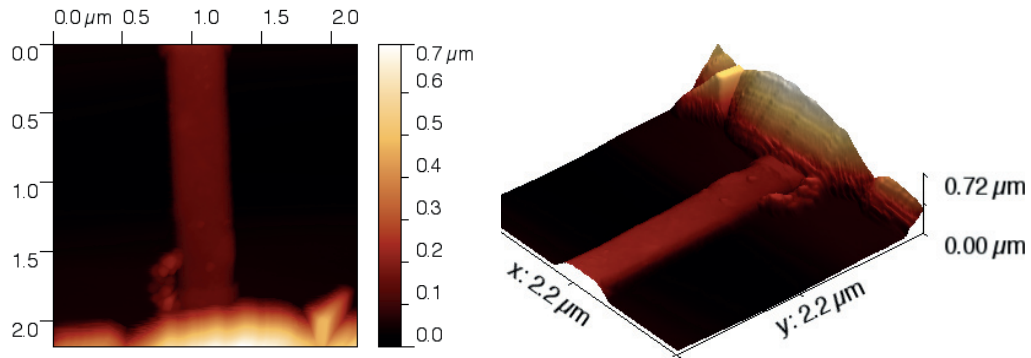


Figura 2.8 – AFM image of the channel area of a fabricated SiNW-FET.

#### 2.2.2 Fabrication results: device inspection

In Figure 2.7 we show the SEM images of the fabricated devices reporting: a 100nm wide SiNW-FET (a), a zoomed view on the NW straight sidewalls (b), a tilted view of a SiNW-FET array (c) and of the straight sidewall nanowire (d).

With this process, the width of the wires can be easily controlled by controlling the etching time. An other important parameter is the surface quality. Top-down processing of nanoscale structures often leads to high surface roughness. The performed fabrication, instead, defined high quality structures and surfaces. Indeed, the plane-dependent etching enabled the formation of well shaped nanostructures, with smooth and straight sidewalls. As demonstrated by the images, the silicon surface of the nanowire is flat, thus favoring the achievement of good and homogeneous functionalization with bio-receptors.

*Atomic Force Microscopy* (AFM) imaging was also performed on the fabricated samples in order to have a higher resolution characterization of the nanowire surface morphology. In Figure 2.8 the channel area of the sensor, corresponding to the passivation opening onto the central part of the nanowire, is shown.

### 2.3 Memristive NWs: the full process flow

In this section we report the detailed description of the full process flow for the fabrication of Schottky Barrier (SB) SiNW devices with memristive properties. This process has been developed at EPFL and implemented by me in the clean room of our university, the Center of Micronanotechnology (CMi) [127], EPFL.

Figure 2.9 shows an overview of the fabrication process, providing a schematic description with cross-section views of the device at various processing steps. The process consists of three main phases, each of which is composed of different steps that will be explained in details, including some information about the fabrication equipment employed in our university cleanroom. A detailed runcard of the full fabrication process is also provided at the end of the chapter (Table 2.2).

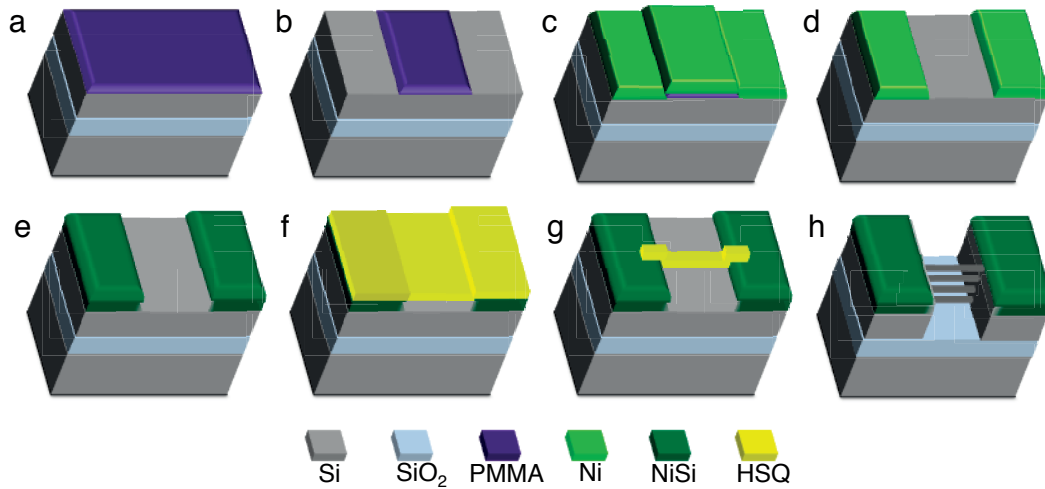


Figura 2.9 – Process flow related to the fabrication of SB memristive SiNWs.

### 2.3.1 Choice of the substrate

In our fabrication process, SOI wafers are chosen as substrate. SOI substrates are used in semiconductor manufacturing, especially microelectronics, to provide straightforward isolation of the active devices. Device isolation is, indeed, a critical feature required for the proper functioning of the fabricated devices and for improved performances.

On bulk Si substrate, in the case of nanowire channels supported by small pillars, the parasitic conductive path between the two pillars through the underlying bulk may increase the  $I_{off}$  current leakage.

In our case, despite the higher unit cost compared to plain bulk silicon substrates, SOI substrates guarantee good  $I - V$  device characterization by forcing all the current injected at the *Source and Drain* (S/D) electrode through the device channel. Nevertheless, the processing of SOI wafers has been revealed extremely delicate mainly due to the presence of the BOX layer. Specifically the BOX interferes with any process involving charged particles, typically plasma (dry etching) and device imaging through SEM and FIB analysis. This is due to charging effects, which often reduce or enhance the effect of ions/electrons interacting with the substrate surfaces and structures.

### 2.3.2 Phase 1 - EBL alignment markers definition

The developed process flow exploits multiple subsequent EBL steps to define the various structure composing the device. Alignment patterns are thus required on the substrate in order to achieve the alignment between subsequent lithographic patterns. Typically, in optical lithography, the alignment markers can be defined at the time of the first mask of the fabrication process. However, the markers have to be reliably detectable by our EBL system (Vistec EBPG5000+ [128], running at 100keV), in subsequent patterning steps. Because of that, the first phase of our device fabrication process is specific for the definition of alignment patterns

on the substrate (Step 1-2 in Table 2.2). Moreover, the markers themselves have to be defined by EBL, due to the fine mask-to-mask alignment necessary for the proper implementation of our process. Specifically, the markers definition consists of the two following steps:

### Step 1.1:

A thick, 550nm ZEP520 100% photoresist is spin coated at 2000 rpm and exposed by electron beam with a dose of  $220 \mu C/cm^2$ .

### Step 2.1:

The markers, consisting of squared cavities in the wafer, are created by a deep etching of the substrate. For bulk silicon substrate, this step is straightforward and consists of a single anisotropic Si etch (2 min 30 sec Si\_Opto recipe on the CMi Alcatel AMS 200 SE dry etching tool [129]) of  $\approx 2.5\mu m$  deep.

In the case of a SOI substrate, however, this step is more critical because the electron beam cannot detect these shallow (340 nm) markers if only the device layer is etched. Moreover, during the entire fabrication process, the markers are covered by thin films multiple times, and their edge positions become less reliable. For this reasons, SOI marker definition includes a first anisotropic etch of the device layer, followed by wet etching in BHF bath of the BOX and finally a further anisotropic dry etching of the Si bulk down to about  $2 \mu m$ . BHF is preferred to plasma etching because of the low selectivity of plasma-based oxide etching to the PR mask, which would result in damaging the PR layer and compromising the deep etching of the substrate below the BOX.

Figure 2.10(a) represents in a simplified way a view (not in scale) of a silicon wafer with the electron beam alignment markers on it. The markers are  $20 \mu m^2$  patterns etched inside the substrate as schematically described in Figure 2.10(b), where a cross section of the marker after dry and wet etching is reported. Figure 2.10(c) reports a tilted SEM view of an etched marker square corner in a SOI substrate.

### 2.3.3 Phase 2 - Nickel Silicide contacts formation

A critical step in the SiNW fabrication process is the formation of silicided S/D contacts (Step 3-6 in Table 2.2). The contact pads were designed large enough to allow subsequent electrical characterization with the probe station. A mid gap metal, stoichiometric nickel silicide (NiSi), was chosen to produce S/D regions.

The main reason for substituting doped S/D of conventional MOSFETs is their high contact access resistance. As device channel lengths are scaled down to nanometer dimensions, the on-resistance of the intrinsic device is improved (reduced). However, the parasitic S/D resistances are becoming more and more dominant with respect to the reduced channel resistances. The elimination of highly doped S/D regions and the introduction of metal S/D contacts

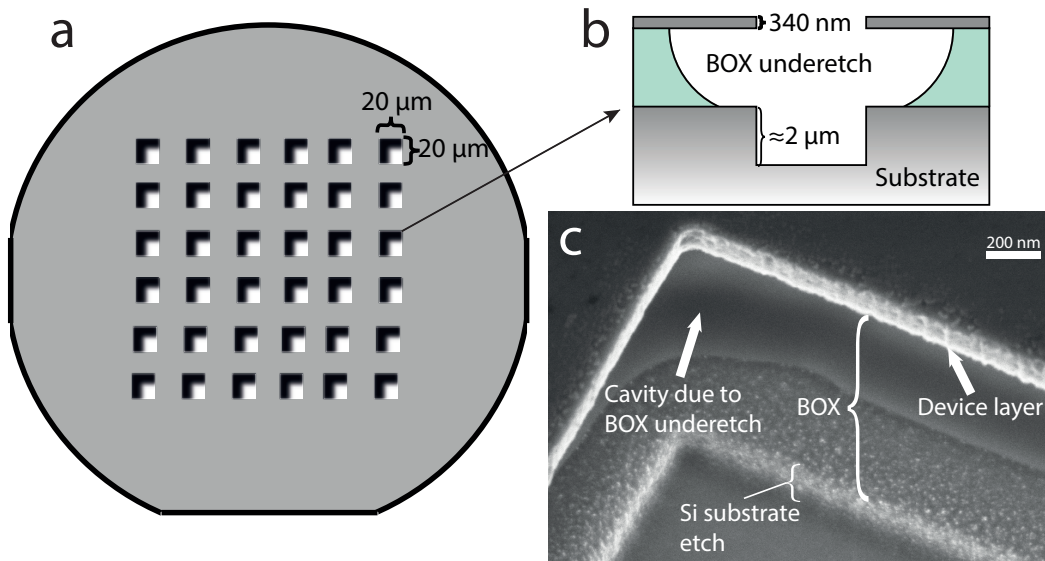


Figura 2.10 – EBL alignment markers. (a) Conceptual view of a wafer after the formation of  $20 \times 20 \mu\text{m}^2$  alignment markers by etching. (b) Schematic representation of the cross section of the marker after dry etching of the device layer, BHF wet etching of the BOX and further dry etching of the Si substrate. (c) Tilted SEM view of an etched marker in an SOI substrate.

allow to address this issue by lowering the access resistance to the device channel through rectifying SB contacts. Moreover, the employment of NiSi contacts permits a simplification of the fabrication process, since no dopant implantation and activation annealing steps are necessary in silicided SB S/D process.

The process for the formation of NiSi S/D contacts is composed of four main steps.

### Step 2.1: S/D contacts EBL patterning

The first step consists of the patterning of S/D regions by EBL on a positive photoresist for subsequent metal deposition and lift-off. After 5 min of dehydration on the hotplate ( $180^\circ$ ), the wafer is spin coated with 120 nm thick polymeric PR, the *Poly(Methyl MethAcrylate)* (PMMA). First, low molecular weight PMMA495K is spin coated (4000 rpm) on the wafer; then, after 10 min of PR baking on the hotplate, the substrate is spin coated (4000 rpm) with a second layer of high molecular weight PMMA950K, and subsequently baked at  $180^\circ$  for 10 min for resist polymerization. The PR is then exposed on the electron beam (dose of around  $220 \mu\text{C}/\text{cm}^2$ ), developed in MiBK(Methyl isobutyl ketone):IPA(isopropanol) 1:3, and used for Ni deposition.

### Step 2.2: Nickel deposition

Before Ni deposition, the coated wafer is processed in an Oxford PRS900 oxygen plasma tool for PMMA descum ( $\approx 15$  sec). This step is typically used for removing final portions of exposed

resist, and minimizing surface roughness features for metalization. In addition, in order to guarantee a good adhesion of the deposited metal to the substrate, the exposed Si surfaces are thoroughly cleaned from native oxide in BHF bath for 15 sec, and immediately transferred to an Alliance-Concept DP650 sputtering tool. The cleanness of the surface is of paramount importance for the proper reaction of Ni with the underlying Si structures. With this respect, the employed sputtering tool provides the possibility to perform short non-aggressive Ar ion plasma cleaning steps to the substrate to remove any native oxide before the actual metal sputtering without breaking the chamber vacuum. Then, a 45 nm Ni blanket deposition step is performed by sputtering.

### Step 2.3: Nickel lift-off

Lift-off consists of the dissolution of the sacrificial layer (PR) together with the parts on the substrate that are covering it; i.e., after this process, only the Ni parts deposited in the exposed surfaces of the wafer, where the resist has been removed by EBL, will remain. Lift-off is performed by leaving the coated wafer immersed in acetone overnight for dissolution of the sacrificial layer.

### Step 2.4: Nickel Silicide formation

Finally, the substrate is processed with a three-step annealing procedure in forming gas ( $H_2-N_2$ ) atmosphere, with a  $25^\circ C/min$  ramp-up from room temperature. In the three steps, the temperature is maintained at  $200^\circ C$  for 20 min,  $300^\circ C$  for 20 min, and at  $400^\circ C$  for 20 min, respectively. In this process, the Ni is allowed to fully consume while diffusing in the Si, and the final NiSi layer thickness is determined via the initial metallic Ni layer thickness.

In Figure 2.11(a-b) we show the mask layout, designed in Cadence Virtuoso, for the NiSi contacts lithography, attached to the SEM images of corresponding fabricated structures. Figure 2.11(c-d) reports a zoomed view of the active area of the device: the mask layout in (c) shows the disposition of the wire in the nano-gap between the NiSi pillars, (d) a SEM view of the corresponding area of the device where a 420 nm long nanowire will be subsequently formed.

### 2.3.4 Phase 3 - Nanowire formation

Phase 3 is the most critical, and it is the actual step required to fabricate the silicon nanowire devices (Step 7-8 in Table 2.2). This phase consists of an EBL step which defines the nanowire thickness and length of the NW bridging the NiSi pillars. In our process, this patterning step has the smallest critical dimension of the three main process layers, i.e., the nanowire pattern width of 40–60 nm. In this mask, we want to etch away most of the wafer surface, maintaining only the nanowires, and the formed NiSi S/D contacts, also used for electrical characterization.

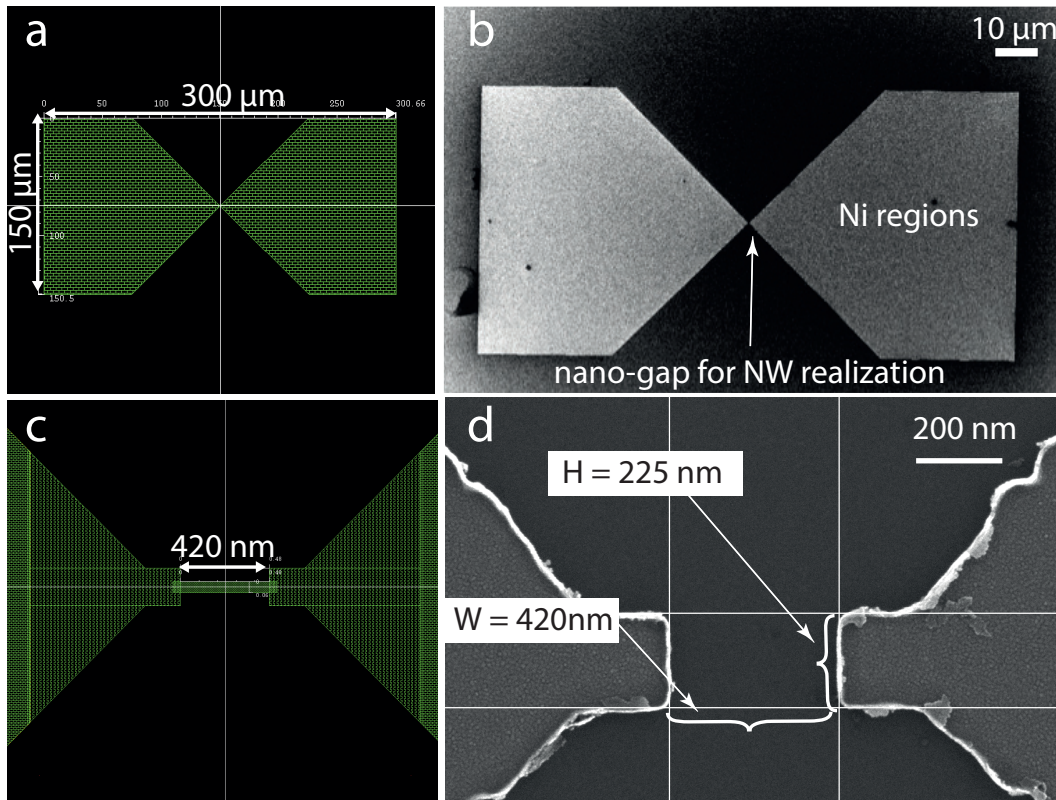


Figura 2.11 – NiSi S/D contacts. (a) Mask layout, designed in Cadence Virtuoso, for the EBL patterning of S/D regions. (b) SEM top view of the obtained NiSi contacts after EBL, Ni deposition, lift-off and annealing. (c) Zoomed view of the mask layout in (a) showing the disposition of the wire within the nano-gap between the NiSi pillars. (d) SEM view of the corresponding area of the device where a 420 nm long nanowire will be subsequently formed.

### Step 3.1: Nanowire mask

EBL is used to pattern the nanowire mask on a high performance resist. For the high resolution and pattern requirements, we chose a negative tone photoresist, namely *Hydrogen SilsesQuioxane* (HSQ) at 2% concentration. This PR has good dry etching selectivity to Si and allows to obtain a thin,  $\approx 50\text{nm}$  layer by spin-coating. Moreover, HSQ allows for a fast exposure (negative tone) and high resolution, which translates into low *Line Edge Roughness* (LER) and smoother NW profiles [130]. After spin-coating, the photoresist is exposed with electron beam (dose of  $\approx 1800 \mu\text{C}/\text{cm}^2$ ), and subsequently developed for 30 sec in MF-CD26.

### Step 3.2: Nanowire DRIE etching

After the patterning of the HSQ mask, the nanowires are defined through a single etching step comprising multiple DRIE cycles. DRIE is performed in the Alcatel AMS 200 SE plasma Si etcher, with a 22 sec long etching. Table 2.1 summarizes the main process parameters defined for the etching. Due to the requirements of the Alcatel AMS 200 etcher, a critical step has to



### 2.3. Memristive NWs: the full process flow

Gas	Inactive state [sccm]	Active state [sccm]	Priority	Duration [s]		Power [W]	Duration [ms]
C <sub>4</sub> F <sub>8</sub>	0	75	1	1.5	High	40	10
SF <sub>6</sub>	0	100	2	2.8	Low	0	90

(a) Gas flow settings.

(b) Chuck generator pulse settings.

Tabella 2.1 – DRIE parameters employed for the nanowire etching on bulk and SOI substrates. The parameters are adapted for the Alcatel AMS200 SE dry etcher of EPFL CMi [129]. Note that the parameters refer to a single etching cycle. Multiple cycles are used to fabricate nanowire stacks with a different number of nanowires.

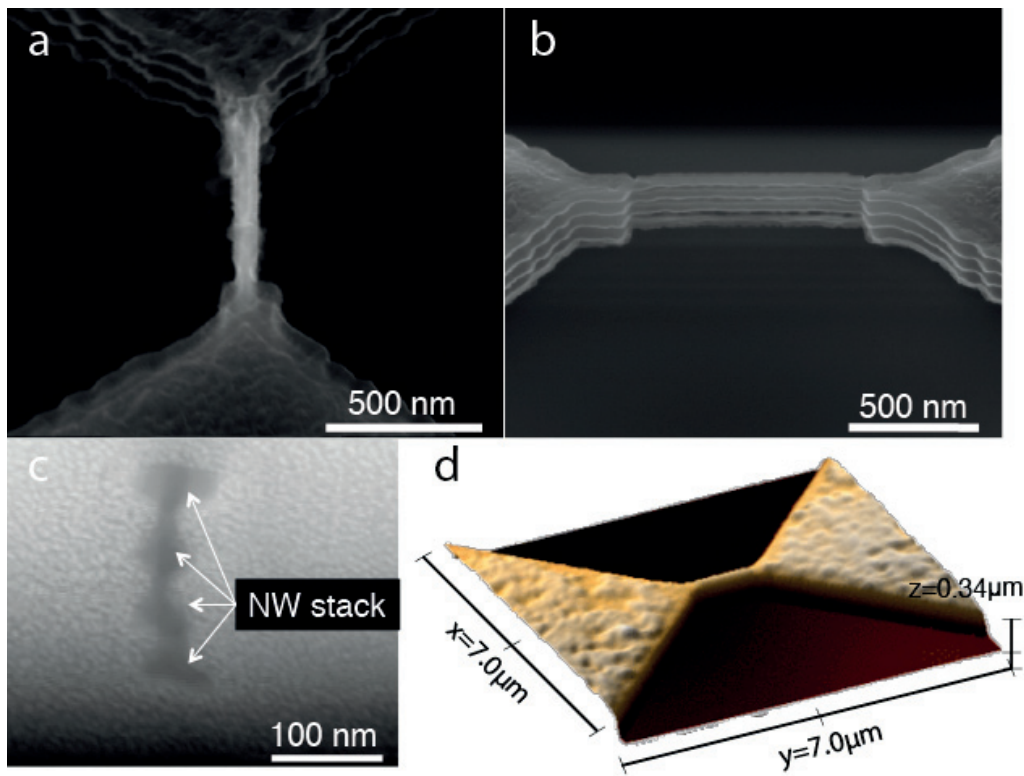


Figura 2.12 – Imaging of fabricated vertically-stacked DRIE-etched nanowires with length of 1  $\mu\text{m}$  and width of  $\approx 80\text{ nm}$ . (a) SEM top view of the device. (b) SEM tilted view of the vertical stack between NiSi pillars. (c) FIB/SEM imaging reporting a tilted view of the stack. Contact between the parts is resulting from the DRIE process optimized for smaller nanowires. (d) AFM view of a fabricated device.

be performed before loading the wafer in the etching tool: the unreacted Ni parts from the annealing are finally removed by dissolution in hot 3:1 piranha solution (H<sub>2</sub>SO<sub>4</sub>:H<sub>2</sub>O<sub>2</sub>). This phase can be very risky and lead to the complete removal of the previously patterned NiSi structures whenever the diffusion of Ni to the Si device layer did not happen properly during

the annealing step.

Figure 2.12 reports SEM and AFM images of fabricated vertically-stacked DRIE-etched nanowires. We fabricated SiNWs with different geometry. The ones subsequently used for biosensing have (i) length of 1  $\mu\text{m}$  and width of  $\approx 80$  nm, (ii) length of 420 nm and width of 30-60 nm. In Figure 2.12 we show nanowires 1  $\mu\text{m}$  long and  $\approx 80$  nm wide. Figures 2.12(a) and (b) report, respectively, the SEM top and tilted view of the vertically stacked structures bridging NiSi S/D contacts. The scalloped trench resulting from the Bosch process is clearly visible. The nanowires, whose shape is not round but more rectangular, are vertically stacked, but there is still some contact between the parts, as demonstrated by the FIB/SEM image in Figure 2.12(c). This is the result of the DRIE process that was optimized for smaller structures with higher length to width aspect ratio (Figure 2.13). AFM was also performed (Figure 2.12(d)) to check the surface rugosity of the obtained structures, non negligible after the full fabrication process. In Figure 2.13(a-c), we present the results of the fabrication process for devices designed with a smaller geometry, i.e. length of 420 nm and width of 35 nm. Figure 2.13(a) reports a SEM tilted view of one of the obtained structures. As demonstrated by the low definition of S/D contact pads, the NiSi lithography for the formation of large contact areas was not very good in this case, most probably due to too aggressive piranha etching after Ni annealing. Despite this irregularities, the lithographic mask for the formation of nanowires worked well as demonstrated by the SEM image view on the vertically-stacked, free-standing SiNWs bridging the large pillars (Figure 2.13(a)). Compared to the bigger structures shown in Figure 2.12, here the wires have a more defined round shape and do not touch in the stack, demonstrating the better matching of the Bosch process parameters (Table 2.1)(a) with this design. Figure 2.13(b) shows a SEM top view of the fabricated nano device, and Figure 2.13(c) a zoomed view of another NW stack.

Optimization of the nanowire lithography and etching process can lead to thinner, more defined and more round nanowires. Specifically, lower  $\text{C}_4\text{F}_8$  gas flow rate will produce more round wires [131], while the nanowire thickness can also be controlled by tuning the original PR pattern.

## 2.4 Chapter summary and contributions

In this chapter, we introduced the key technologies required to produce top-down and bottom-up semiconducting nanowires, with a focus on the PDE technique [126] for SiNW-FET fabrication, and our top-down DRIE-based approach for vertically-stacked SB SiNW manufacturing. We reported the fabrication process of SiNW-FETs designed by Moh *et al.* [126] and performed in the clean room of DIMES, TUDelft. Because our goal was to use these devices for biosensing applications, the most important feature to highlight is that the developed PDE process, based on plane-dependent etching, demonstrated to have the advantage of creating smooth and straight sidewalls SiNWs. Indeed, smoothness and high quality of device surface is of paramount importance for achieving homogeneous and reliable bio-functionalization of the nanowire.

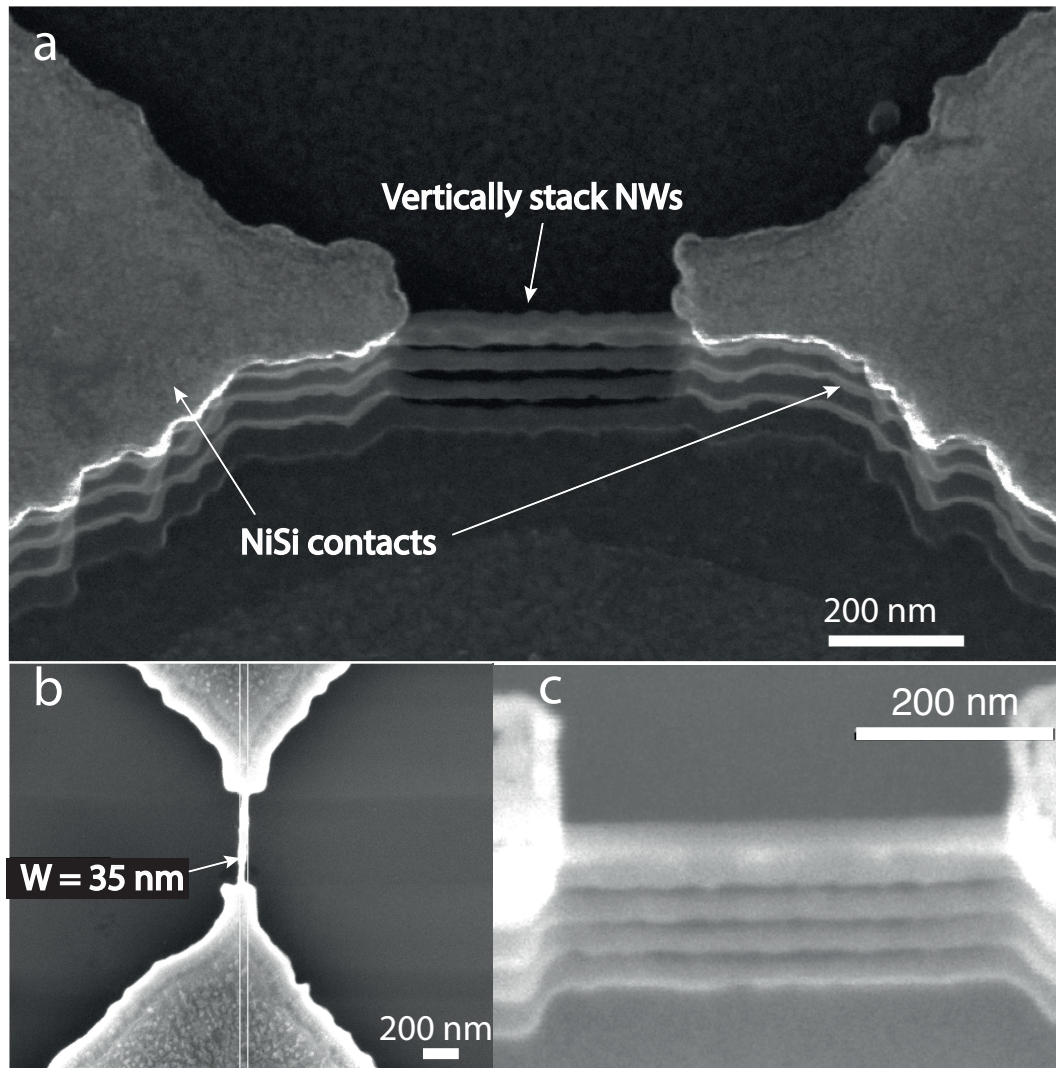


Figura 2.13 – SEM imaging of fabricated vertically-stacked DRIE-etched nanowires with length of 420 nm and width of  $\approx 35$  nm. (a) SEM tilted view of one device featuring free-standing, vertically-stacked, round-shaped SiNWs bridging the NiSi contacts. (b) SEM top view of the device. (c) A zoomed. view of another NW stack

After presenting the main structure of SiNW-FETs, we moved to present and discuss the full process flow designed and implemented by me at EPFL for the fabrication of SB SiNW devices. These devices will demonstrate, in the following chapters, to have memristive footprints usable for biosensing. We described the employed two-mask process based on e-beam lithography to implement contact pad SiNW devices. In general, we can summarize as follows the main points of strength of our process:

- Simple, symmetric device design: in this fabrication, we chose simple materials (low doping Si, NiSi) and non-aggressive processes.

## Capitolo 2. Silicon Nanowire fabrication

---

- Device isolation: the use of SOI substrates guarantees proper device isolation in the case of large contact pads.
- CMOS compatibility: the proposed device fabrication relies on a fully top-down, CMOS-compatible process flow, thus allowing straightforward integration in more complex CMOS circuits.
- Si chemical compatibility: the fabricated Si nanowires are fully compatible with well developed silicon functionalization techniques available in the state-of-the-art of silicon-based devices. In our device, due to the idea of performing sensing measurements in air, no further step of passivation was added, thus simplifying the process flow. The native oxide will be used as interfacial layer for antibody linking.

Tabella 2.2 – Process runcard for the fabrication of the DG-SiNWFET devices on an SOI substrate. Typical substrate parameters are: 340 nm-thick boron-doped device layer with  $\approx 10\Omega\cdot\text{cm}$  resistivity and  $2\mu\text{m}$  BOX thickness. Zn in the Equipment column refers to the location of the equipment in the CMI cleanroom.

<b>Step</b>	<b>Process</b>	<b>Equipment</b>	<b>Recipe</b>
<b>Step 1 EBL Mask 1 Lithography – EBL Alignment Markers</b>			
1.1	Wafer dehydration	Z7/Hot plate	200 °C (180 °C at surface) for 5 min
1.2	ZEP 100% PR spin coating	Z7/ATMse OPTIspin SB20 manual coater	2000 rpm program (1 min spin time), 600 nm target thickness
1.3	PR pre-bake	Z7/Hot plate	200 °C (180 °C at surface) for 5 min
1.4	e-beam exposure	Z7/Vistec EBPG5000+ EBL tool	Exposure dose: 220 $\mu\text{C}/\text{cm}^2$
1.5	PR development	Z7/Solvent wet bench	n-Amyl Acetate bath for 1 min 45 s
1.6	Substrate rinsing and drying	Z7/Solvent wet bench	9:1 MiBK:IPA bath for 40 s
<b>Step 2 Alignment Marker Etching</b>			
2.1	SOI device layer etching	Z2/AMS200 Si etcher	Si_OPTO for 1 min
2.2	BOX wet etching	Z2/Plade Ox wet bench	Clean BHF bath for 30 min
2.3	Substrate rinsing and drying	Z2/Plade Ox wet bench	FFR + Trickle tank DI water baths, standard recipe
2.4	Bulk etching	Z2/AMS200 Si etcher	Si_OPTO for 1 min
2.5	ZEP removal	Z2/Oxford PRS900	Oxygen plasma, 20 min recipe
<b>Step 3 EBL Mask 2 Lithography – EBL S/D Contacts Patterning</b>			
1.1	Wafer dehydration	Z7/Hot plate	200 °C (180 °C at surface) for 5 min

*Continued on the next page...*

Tabella 2.2 – Table continued from previous page.

Step	Process	Equipment	Recipe
1.2	ZEP 100% PR spin coating	Z7/ATMsse OPTispin SB20 manual coater	2000 rpm program (1 min spin time), 600 nm target thickness
1.3	PR pre-bake	Z7/Hot plate	200 °C (180 °C at surface) for 5 min
1.4	e-beam exposure	Z7/Vistec EBPG5000+ EBL tool	Exposure dose: 220 $\mu\text{C}/\text{cm}^2$
1.5	PR development	Z7/Solvent wet bench	n-Amyl Acetate bath for 1 min 45 s
1.6	Substrate rinsing and drying	Z7/Solvent wet bench	9:1 MiBK:IPA bath for 40 s
<b>Step 4-6 Nickel Silicide Contact Creation</b>			
12.1	Native oxide removal	Z2/Plade Ox wet bench	Clean BHF for 15 s
12.2	Substrate rinsing and drying	Z2/Plade Ox wet bench	FFR + Trickle tank DI water baths, standard recipe
12.3	Surface plasma cleaning	Z11/DP650 sputtering tool	Standard 1 min RF Ar plasma etching recipe RT_E
12.4	Nickel deposition	Z11/DP650 sputtering tool	25 nm target Ni thickness, recipe RT__Ni_unif for 132 s @ 3.8Å/s
12.5	Annealing	Z3/Centrotherm furnace	20 min @ 200 °C + 20 min @ 300 °C + 20 min @ 400 °C, 25 °C/min ramp-up
12.6	Piranha excess metallic nickel removal	Z2/Piranha wet bench	2 baths, 5 min per bath
12.7	Rinsing/drying	Z2/Piranha wet bench	Quick dump rinsing + fine rinsing baths, standard recipe
<b>Phase 7 EBL Mask 3 Lithography – Nanowire Pattern Definition</b>			
3.1	Wafer priming	Z7/Bases wet bench	CD-26 developer bath for 1 min
3.2	Rinsing	Z7/Bases wet bench	Water tank until 15 M $\Omega$ /cm resistivity is reached
3.3	Wafer dehydration	Z7/Hot plate	200 °C (180 °C at surface) for 5 min

*Continued on the next page...*

Tabella 2.2 – Table continued from previous page.

<b>Step</b>	<b>Process</b>	<b>Equipment</b>	<b>Recipe</b>
3.4	HSQ 2% PR spin coating	Z7/ATMsse OPTIspin SB20 manual coater	3000 rpm program (1 min spin time), 50 nm target thickness
3.5	E-beam exposure	Z7/Vistec EBPG5000+EBL tool	Dose: 1500 – 1800 $\mu\text{C}/\text{cm}^2$ . PEC $\eta = 0.6$ for large pads devices, $\eta = 1.2$ for small pillar devices
3.6	PR development	Z7/Bases wet bench	CD-26 developer bath for 2 min
3.7	PR post-bake	Z7/Hot plate	200 °C (180 °C at surface) for 10 min
3.8	PR hardening	Z2/Oxford PRS900	Oxygen plasma 10 min recipe
<b>Step 8</b>	<b>Nanowire DRIE Process</b>		
4.1	SOI layer etching	Z2/AMS200 Si etcher	MM_SOI_ACCU DRIE recipe for 22 s on 340 nm device layer
4.2	HSQ removal	Z2/Plade Ox wet bench	Clean BHF bath for 15 s
4.3	Substrate rinsing and drying	Z2/Plade Ox wet bench	FFR + Trickle tank DI water baths, standard recipe
4.4	Inspection	Z15/SEM Zeiss MERLIN	





## 3 Silicon nanowire biofunctionalization

The main objective of this thesis is the sensing of angiogenic and inflammatory ligands in breast tumor extracts. In order to achieve this goal, the fabricated nanowire devices have to be converted to biosensors by modifying the nanowire channel surface with probe molecules that are specific to target biomarkers in the tumor environment. As introduced in Chapter 1, we chose an immunoassay-based technique appositely optimized for detecting biomarkers both in buffer solutions and real biological samples. The *Antibody-Antigen* (Ab-Ag) reaction is, indeed, widely known to be selective and sensitive due to its high affinity binding capability and unique structure that allows only compatible structures of antibody (“lock”) and antigen (“key”) to bind together (uptake). In this chapter, we describe the details of the functionalization process for modifying the nanowire surface with antibodies. Specifically, we first introduce the importance of label-free detection in biosensors and the chosen immunoassay approach; we then give an overview of the state-of-the-art silicon chemistry techniques developed for immuno-sensing applications; next, we present the experimental procedure employed for the biomodification of both the SiNW-FET and the memristive-NW devices. Finally, we show some results of the performed functionalization, and we conclude with some remarks on the main contributions and requirements of the proposed approach.

### 3.1 Label-free detection

Specific molecular detection is enabled by recognition events between molecules that have specific affinities, examples of which are antigen-antibody binding, nucleic acid hybridization, and receptor-ligand binding. In a typical assay, a probe molecule with specific affinity to the target molecule of interest is immobilized on a surface. The test analyte is washed over the surface and, if the target is present, it will bind specifically to the probe. These binding events are most routinely transduced by reporter molecules such as fluorescent, chemiluminescent, redox, or radioactive labels. The high concentration sensitivity achievable by label-dependent methods, as well as their applicability to a wide range of molecules have ensured their widespread use. However, there are a number of advantages which label-independent methods can offer, which explains why recent research in this field is strongly focused on the develo-

### Capitolo 3. Silicon nanowire biofunctionalization

---

ment of label-free biosensors. Here below, we highlight the major advantages of label-free techniques compared to the labeled-based approach:

- Labeling steps are not necessary, thus minimizing costs in time and resources.
- Labeling yield can be difficult to control, introducing variability among measurements. Label-free methods do not suffer from these limitations, thus providing better control on the detection.
- Label-free methods eliminate the time constraints of fluorescence-based assays, which are susceptible to bleaching or quenching.
- Some biomolecular systems are difficult or impossible to tag, or reporter molecules interfere with biological function.
- Label-free methods can provide direct, continuous, real-time measurements of biological events.
- Label-free methodologies are inexpensive because they use low-cost chemicals.

Currently, a few label-free detection systems are commercially available. Most notable among these are *Quartz Crystal Microbalance* (QCM) systems [132, 133] and *Surface Plasmon Resonance* (SPR) systems [134, 135]. These techniques, mostly applied to DNA detection, still lack the ultra-high sensitivity needed for sensing ultra-low concentrations of biomarkers in tumor landscape (order of fM, aM). Moreover, these sensors have not yet been fully integrated into micro-analytical system. Using capacitance and impedance based systems is another option in developing label-free immuno-sensors for cancer markers detection. These methodologies have demonstrated high sensitivity and low limit of detection (femtomolar) for DNA hybridization and cancer biomarker detection [70, 136]. However, they all showed biosensing in ideal conditions, and not in real tumor samples.

The understanding of biology at a systems level requires quantitative, dynamic measurement of biological processes, beyond the capability of current technologies. This thesis is concerned specifically with the development of two techniques of SiNW-based immuno-sensing (Chapter 1), with detection methods directly measuring, with ultra-high resolution and specificity, intrinsic electrical charge associated with biomolecules, without the need for intermediary reporter molecules.

## 3.2 Choosing the receptors: the antibody-antigen system

The biosensors we developed belong to the class of immunosensors. Immunosensors are well known among analytical methods for their extremely low detection limits. Immunoassays and immunosensors have been developed for both quantitative and qualitative applications. They can be used to detect trace levels of bacteria, viruses, drugs, hormones, pesticides,

### 3.2. Choosing the receptors: the antibody-antigen system

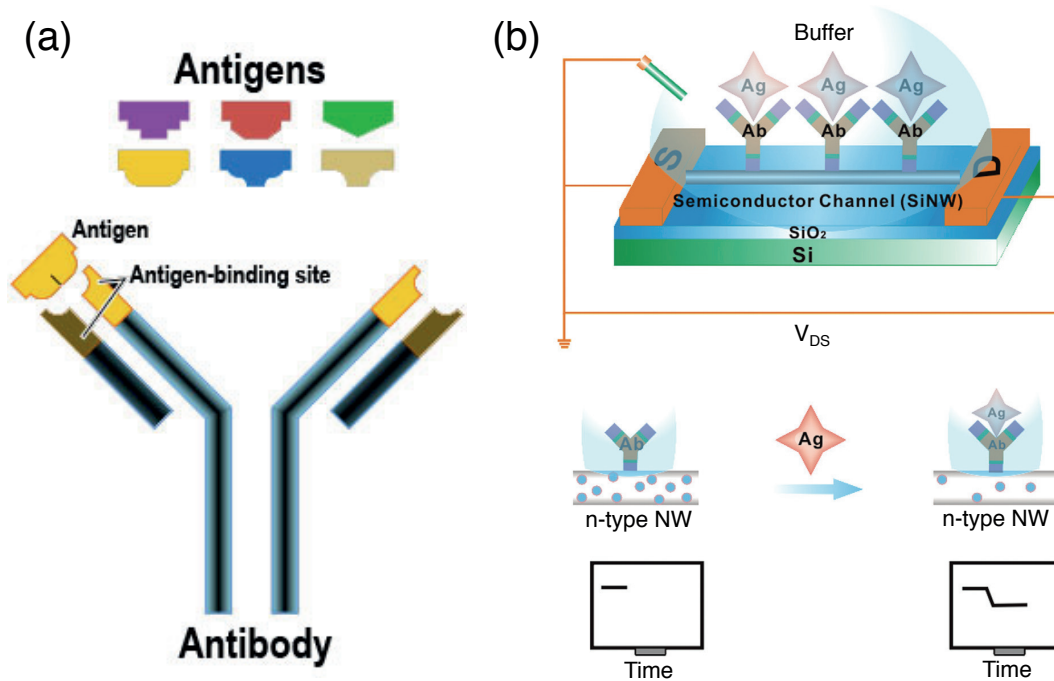


Figure 3.1 – (a) Schematic representation of the “lock-and-key” interaction between the Ab paratope and the Ag epitope. (b) Working principle of a SiNW-FET based immunosensor. The antibody molecule is immobilized on the SiNW surface and can specifically capture the target antigen molecule. When a negatively charged antigen molecule binds on an n-type SiNW-FET, a depletion of charge carriers inside the SiNW leads to a decrease in the electrical conductance.

and numerous other chemicals [137]. The immunoaffinity reaction in immunosensors often involves an irreversible binding of the antigen (Ag) to the antibody (Ab) binding site(s). The binding is strongly specific; this specificity is given by the high degree of complementarity necessary between the Ab binding site (a paratope) and the compatible binding region of the Ag (the epitope) in order for the noncovalent interactions to result in the formation of a stable Ab-Ag complex. This highly specific immunoaffinity reaction is an interaction between the Ab molecule (a large Y-shaped glycoprotein), and the Ag (the biomarker of interest) which is often a protein. Typically, in immunoassays, the Ab bind to an Ag that was used to produce the antibodies in a host organism such as a rabbit or a mouse with high specificity and affinity. In Figure 3.1(a) we sketch the structure of an antibody, indicating the affinity binding site (paratope) where antigen molecules bind with their epitope segment. The specificity is given by the “lock-and-key” interaction: only the complementary Ag (“key”) have access to the antibody binding site (“lock”). Figure 3.1(b) schematically introduces the potential of a sensor built by combining the specificity properties of the Ab-Ag reaction system with high sensitivity of SiNW technologies.

### 3.3 Silicon nanowire modification for sensing: state-of-the-art

#### 3.3.1 Surface functionalization: principles

In order to build a SiNW-based immunosensor similar to the one schematically reported in Figure 3.1(b), the surface of the device has to be modified with the antibody species. Main goal of the surface functionalization, or modification, is to reliably attach the receptors (antibodies) to achieve a sensor with a stable capture layer while preserving the function of receptors towards the target (antigen). This function will depend on the binding mechanism and the steric hindrance that the antibody protein will build once immobilized onto the device surface, at high receptor densities. The overall biochemical surface treatment has to be accurately designed as it also hinders unspecific adsorption which reduces the background noise.

Receptors can be attached to surfaces using a variety of mechanisms. Typically, in order to provide chemical compatibility with the present surface end groups, and sometime to improve the sensor performance by bringing the receptor at a certain distance from the surface [138], the receptors are bound to the inorganic transducer via linker molecules.

Among the possible mechanisms to attach any molecular layer or chemical linkers to the substrate is physisorption. Physisorption summarizes interactions based on relatively weak mechanisms due to van der Waals forces, electrostatic or the much stronger hydrophobic interactions. These processes are however reversible. Another option is to make use of the high affinity of streptavidin and biotin for surface functionalization. Receptors like DNA, peptides or molecules like lipids are commercially available with attached biotin [139]. Stronger binding occurs when linkers are chemisorbed, non-oriented or via oriented covalent binding. Two approaches, electrostatic adsorption and covalent binding, have been mainly adopted for use in SiNW biosensors [140]. Electrostatic adsorption uses the attractive force responsible for adsorbing ionic solute on an oppositely charged adsorbent [58]. Chemisorption by covalent binding via linker molecule is the method we employed for the functionalization of our SiNW-based devices, and is based on the binding of probe molecules on the SiNW surface by covalent bonds.

Since oxide can grow on the SiNW surface naturally, a number of methods rely on the functionalization of the oxide layer using silane chemistry. In this section we will mainly focus on its description, since this is also the approach we adopted for our sensors.

#### 3.3.2 Silanization for antibody immobilization

In general, the most applied method to functionalize  $\text{SiO}_x$  surfaces is silanization, i.e. the self-assembly of organofunctional alkoxy silane and chlorosilane molecules on surface [141]. Organosilanes are organic molecules whose central Si atom offers four binding sites. The principal structure is summarized in the formula  $\text{X}_3\text{Si}(\text{CH}_2)_n\text{R}$ . X represents a hydroxyl group consisting in most applications of alkoxy groups (methanol or ethanol) for attachment to the inorganic surface. The central Si atom and R are linked by a short carbon chain  $(\text{CH}_2)_n$  and R is

### 3.3. Silicon nanowire modification for sensing: state-of-the-art

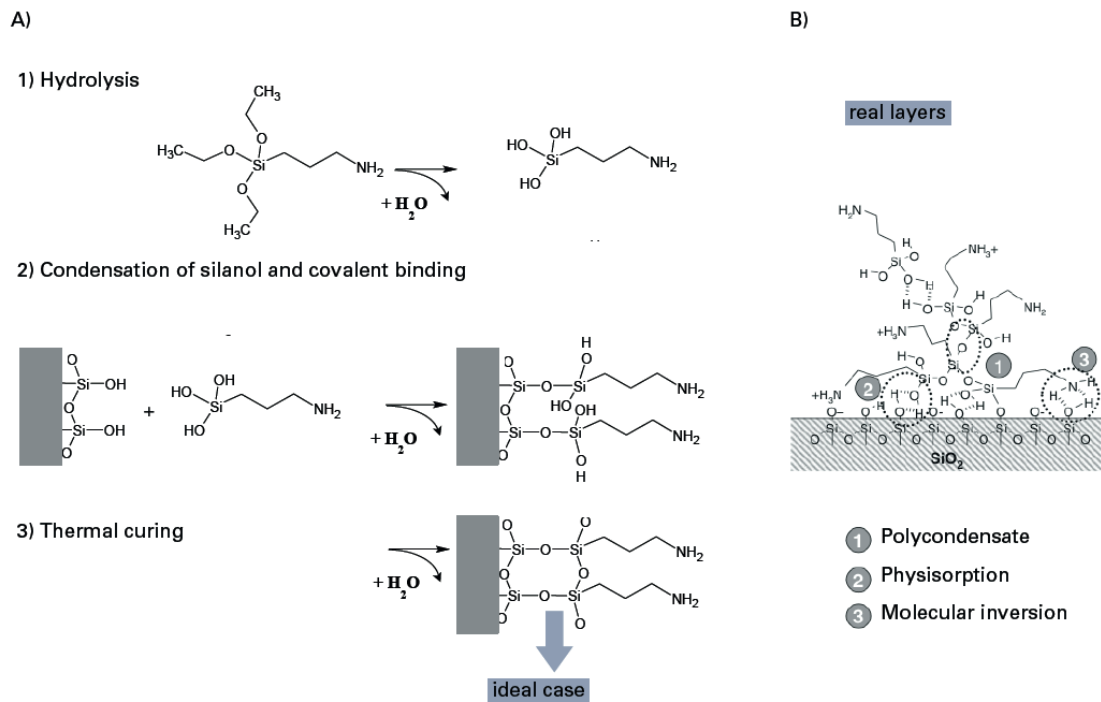


Figure 3.2 – (a) Chemical reactions for covalent silane binding to hydroxylated silicon oxide surface. The process consists of: 1) hydrolysis; 2) condensation of silanol and covalent binding; 3) thermal curing. B) In reality, silanes form irregular layers due to electrostatic interaction, polymerization in solution and molecular inversion. Irregular layers result from a 3-steps process: 1) condensation; 2) physisorption; 3) molecular inversion. Adapted from [139].

the terminal functional group for direct receptor or cross-linker attachment. Typical terminal groups for further cross-linker or receptor binding are aldehyde, primary amine, mercapto or epoxy groups. In the presence of water, hydrolysis occurs leading to reactive OH groups attached to the central Si atom (silanols) that can interact with surfaces equally exposing OH groups via hydrogen bonding. Organosilanes are thus well suited to covalently link to OH-terminated surfaces, that can easily be created on  $\text{SiO}_x$  surfaces by cleaning in piranha solution, or with oxygen/air plasma treatment [142]. In theory, the resulting monolayers are well ordered; in reality, effects like polymerization in solution, physisorption due to e.g. electrostatic interactions and molecular inversion which reduces the number of desired functional groups, occur [142]. In Figure 3.2 we propose a schematic representation of the formation of a silane monolayer onto  $\text{SiO}_x$  surfaces.

The most popular linker molecule is *3-AminoPropylTriethoxySilane* (APTES). This reagent yields amino groups ( $-\text{NH}_2$ ) on the surface that is reactive toward amino groups present in the chemical structure of proteins, and can thus be used to covalently immobilize antibodies [47]. APTES was also used to attach *Peptide Nucleic Acid* (PNA) [60] and DNA [52] onto silicon surfaces [69, 141]. Since APTES is amine-terminated, a bifunctional linker is required to bind the amine-terminated PNA (or DNA) probe onto the surface. The bifunctional linker

### Capitolo 3. Silicon nanowire biofunctionalization

---

most typically employed is glutaraldehyde, which constitutes of two aldehyde terminals. One end would bind to the amine-terminated APTES and the other end free to immobilize the amine-terminated PNA (or DNA) [60]. A very common linker for Si/SiO<sub>2</sub> NW functionalization is also *3-(Trimethoxysilyl)Propyl Aldehyde* (APTMS). This linker produces an aldehyde-rich surface that can be directly used to covalently immobilize monoclonal antibodies [44, 46, 51], amino-terminated PNA [53], and DNA oligonucleotides [46].

In addition to using the oxide layer on the SiNW surface, this can be etched away by submerging the NWs into dilute hydrofluoric acid (HF). In this way, stable Si-C bonds can subsequently be formed on the generated hydrogen-terminated SiNWs via photochemical hydrosilylation, resulting in SiNWs coated with amino groups, which were used to immobilize probe molecules to detect proteins and DNA [52, 73].

#### 3.3.3 The importance of surface blockers

Antibodies immobilized onto the biosensors surface through silane linkers specifically bind their target antigen. However, the surface modification layer is never perfect and compact and often features inhomogeneity and unoccupied sites. Non-specific binding of other proteins or biomolecules to unoccupied spaces on the surface can be detrimental to the specificity and sensitivity of the assay results. Non-specific binding to the surface can be minimized by saturating these unoccupied binding sites with a blocking molecules. Surface blockers are substances used to reduce nonspecific binding without taking an active part in specific assay reactions. In particular, an ideal surface blocker should:

- inhibit nonspecific binding (passive and covalent) of assay components (i.e., antibodies, proteins) to the surface;
- inhibit nonspecific protein-protein interactions;
- exhibit no cross-reactivity with subsequent assay components;
- act as a stabilizer for biomolecules;
- exhibit low enzyme activity (or other activity that may interfere with the detection method);
- not disrupt the bonds that immobilize the specific protein or biomolecule to the surface;
- exhibit consistent, reproducible performance with every lot.

Blocking methods and reagents are typically chosen in an empirical manner, depending on the applications they are used for. The best method is usually determined on the basis of different factors: the type of surface; the type of biomolecule immobilized to the surface; the type of detection probe/system employed. The two major classes of reagents are proteins and detergents. Among detergents, the most commonly used are Tween 20 and Triton X-100. Protein blockers are typically used in immuno-sensing applications, as they provide a permanent and stable passivation of the surface by blocking non-occupied sites and spacing out and stabilizing biomolecules bound to the surface to reduce steric hindrance and denaturation problem associated with solid phase assay [143]. Among protein blockers the most used are:

### 3.4. SiNW bio-functionalization: experimental procedure

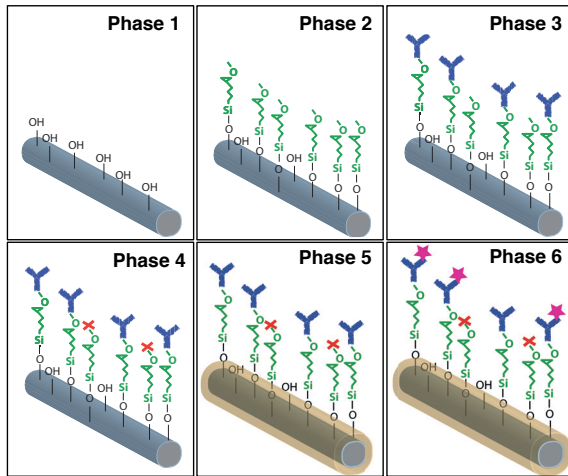


Figure 3.3 – Conceptual description of the functionalization of SiNW devices with Ab (Phase 1 to Phase 5) for the specific binding of target Ag (Phase 6).

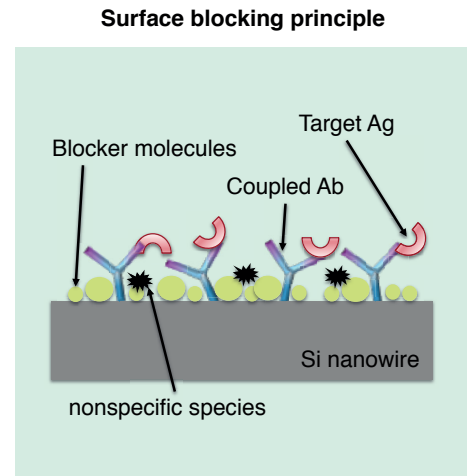


Figure 3.4 – Schematic explanation of the surface blocking principle, after Ab coupling, to prevent nonspecific binding.

*Bovine Serum Albumin (BSA), Non-Fat Dry Milk (NFDM), fish gelatin, whole sera.* Alternative blockers include also polymers such as *PolyEthylene Glycol (PEG), PolyVinyl Alcohol (PVA), and PolyVinylPyrrolidone (PVP)*. These blocking reagents are known for their ability to coat hydrophobic surfaces and render them both non-binding as well as hydrophilic.

### 3.4 SiNW bio-functionalization: experimental procedure

Figure 3.3 graphically depicts the different phases of surface treatment involved in the chemical protocol of SiNW biomodification.

Both SiNW-FET and memristive SiNW devices were functionalized using a modification of the procedure described by Kim *et al.* [47]. Antibody was coupled to the nanowire surface by covalent attachment and silane chemistry techniques. The process can be summarized in different phases that are listed here below.

#### Phase 1 - Surface hydroxylation

The surface is first cleaned with piranha solution (1:1,  $H_2SO_4:H_2O_2$ ) to make it highly hydrophilic and sets OH groups into the surface for interaction with the silanol terminations of the organosilane linker molecules.

### Capitolo 3. Silicon nanowire biofunctionalization

---

#### Phase 2 - Silane chemistry

A silane was chosen as linker molecule for the coupling of antibodies to the Si surface of the wire. *GlycidoxyPropylTrimethoxySilane* (GPTS), and not the conventionally used APTES linker, is chosen because observed to enable better Ab-Ag interaction and reduced background noise. A solution 1% of GPTS in ethanol containing 10mM acetic acid is prepared and used to expose the device surface to the silane species. The exposure to the solution is performed for 60 min at room temperature. In order to wash away the unreacted GPTS molecules, the surface is then washed by dipping the NW device in a solution of ethanol/acetic acid three times, 5 min each. A self-assembled monolayer with terminal amino groups is then obtained by heating the sample in a dry oven at 110 °C for 15 min.

#### Phase 3 - Antibody coupling

Antibody covalent coupling to the nanowire surface is carried out by exposing the surface to a 0.01 × PBS (Phosphate Buffered Saline) solution containing 0.5 mg/ml antibody via overnight incubation at room temperature. After the incubation, the sample surface is thoroughly washed with three subsequent bath of the same buffer, 5 min each. The anchoring of antibodies onto GPTS is provided by SH, NH<sub>2</sub>, and COOH groups on the proteins. The anchoring with the NH<sub>2</sub> groups is the most efficient binding. NH<sub>2</sub> groups are contained in Lysine and Arginines residues, which are widely spread over the entire antibody surface [70]. This determined a randomly oriented antibody layer.

#### Phase 4 - Ethanolamine blocking layer

In order to prevent nonspecific binding of proteins during the detection measurement, the remaining active GPTS-derived groups that did not react with the silanol terminations are passivated by applying 10 mM ethanolamine in PBS solution at room temperature. Washing process is further performed to remove unreacted molecules.

#### Phase 5 - Gelatin blocker for specificity control

An additional blocking step is carried out with PBS containing 3% gelatin from cold water fish skin [144, 145]. This further blocking phase is of paramount importance to the formation of a stable and specific receptor layer, due to the passivation property of neutrally-charged gelatin molecules that aims to prevent the empty sites of the device active area from interacting with charged non-specific species from the analyte solution. Figure 3.4 proposes a conceptual description of the surface blocking principle with blocker molecules. The passivation coating of unreacted sites of the device surface with a neutral-charge polymer enables measurements with increased signal-to-background.





(a) Fluorescence detection.

	1	2
Linker	GPTS	GPTS
Ab	No	Yes
Ag-Cy5	No	Yes

(b) Surface treatments.

Figura 3.5 – Fluorescence detection of negative (1) and positive (2) antigen (anti-rabbit-Cy5) binding in device modified with their specific antibodies (anti-CD28 rabbit). (a) Fluorescence test after different surface treatments on Si wafer. (b) Summary of the performed surface modification and test results. Best result of dense Ab layer formation occurred when using GPTS linker molecules and Ab concentration of 5mg/ml in PBS.

### Phase 6 - Antigen binding

Once functionalized, the modified surface is stored in PBS at 4 °C until use. When employed for sensing experiments, the biomodified device is removed from the fridge, cleaned in fresh PBS solution and gently dried with N<sub>2</sub> flow. For antibody-antigen reaction, the biosensor is incubated for 1 hour, at room temperature, in a prepared solution of either PBS or tumor extract (see Chapter 4) with desired concentration of specific Ag. This phases will be explained in detail in the following chapter.

## 3.5 Results

In Figure 3.5 we shows the results of fluorescence detection after the modification of the surface of a Si wafer sample. In this experiment, we verified the proper use of GPTS as linker molecule, and the quality of the formed antibody layer at chosen Ab concentration. Figure 3.5(a) reports the fluorescence microscopy of a wafer die modified with (1) only GPTS, and (2) GPTS with subsequent incubation in anti-CD28 rabbit antibody solution (5 mg/ml in PBS) (Table in 3.5(b)). Both sides of the wafer were then incubated in a PBS solution of labeled antigen (anti-rabbit-Cy5). As predicted, only treatments in (2) led to coupling of antibody as demonstrated by the positive fluorescence signal (black) indicating successful binding of specific antigen. Moreover, among several surface treatment tests, data in (2) confirmed the best quality formation of antibody layer, as we can observe from the high fluorescence signal. This test guided us towards the choice of the best concentration for Ab to be used in the functionalization process (Phase 3).

Fluorescence imaging was also carried out both on SiNW-FETs and the fabricated memristive-NWs; the results are reported in Figure3.6. Although the use of a low resolution optical microscope, we observed fluorescence after functionalization: we captured a black back-

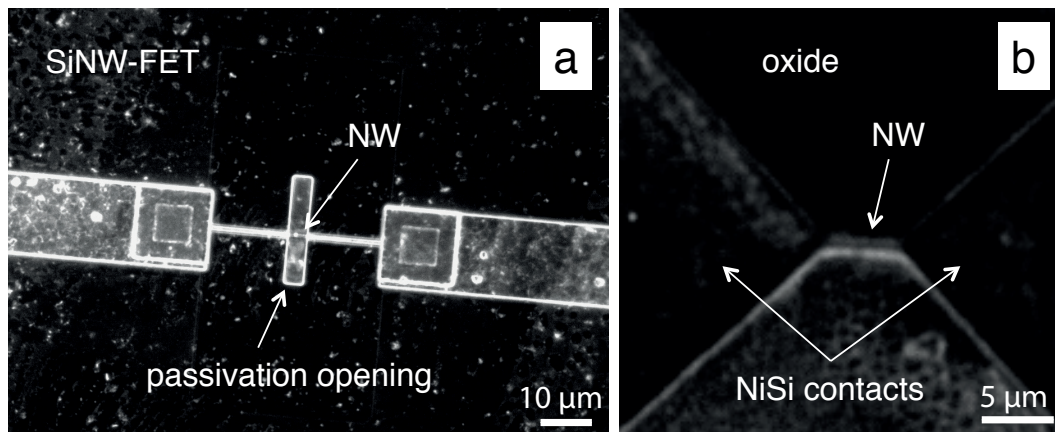


Figura 3.6 – Fluorescence imaging of a functionalized (a) SiNW-FET and (b) memristive SiNW.

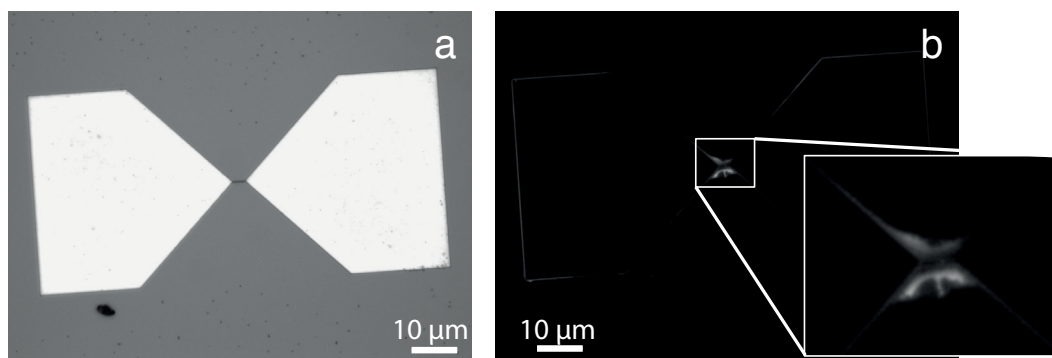


Figura 3.7 – Fluorescence characterization of a fabricated SiNW functionalized with Ab by using a nano-spotting system from NanoInk (Skokie, IL, USA). (a) Device before the surface modification, and (b) after, with a zoomed view on the channel with deposited biomaterial.

ground signal prior to the surface modification; then, after the biolayer formation, we detected the fluorescence signal (white) produced by the Ab-Ag-Cy5 complex (Figure 3.6). The imaging shows that the most important signal comes from the NWs demonstrating their functionalization; fluorescence also results from some non active parts around the channel, because of the presence of dangling bonds.

We also experimented the use of the nano-spotter NanoInk's NLP 2000 System (Skokie, IL, USA) for high-resolution modification of our samples. The nano-spotter was used to deposit antibody solution with sub-micron accuracy and precision. Figure 3.7 shows the results of the subsequent fluorescence characterization. We report the bright field image in (a) to show the complete nanowire device comprising of two large NiSi contact regions and a 5 μm long SiNW in between. The fluorescence signal (Figure 3.7(b)) is mainly determined by the NW region, demonstrating that Ab-Cy5 is immobilized on the channel. However, similar fluorescence is observed also along the border of the NiSi pads, thus showing a little spreading of the solution and not complete localization of the Ab film on the active area. Despite the promising results, the nano-spotting system was not used for the rest of the work, due to the low performance

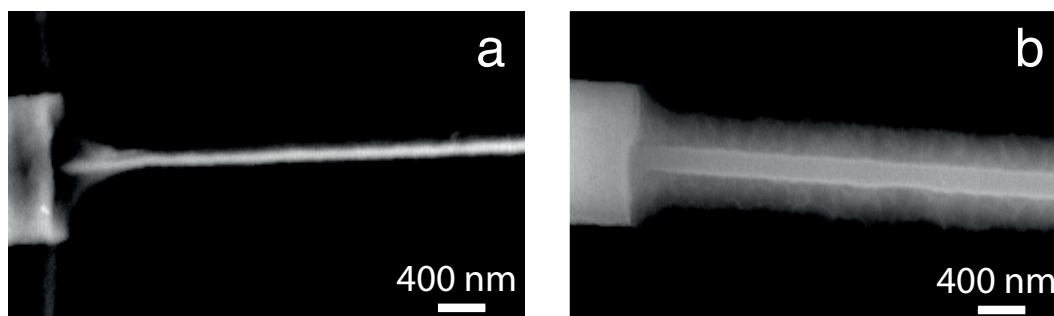


Figure 3.8 – SEM characterization of the functionalization process performed on NWs. (a) Nanowire before the surface treatments, and (b) after the Ab-modification.

of the system in depositing material on the smaller fabricated wires. Because of the spotter working principle based on the release of solution droplets after the contact between a cantilever and the target material, nanowire with diameter of 60 nm and length of 420 nm did not support the mechanical stress and got broken.

Furthermore, Figure 3.8 shows the SEM images taken before (a) and after functionalization of SiNWs (b). The comparison of the two images demonstrates that there is the formation of a compact biolayer all around the nanowire, thus showing that the adopted chemical protocol described in Section 3.4 is very successful for the fabrication of a high quality Ab film.

### 3.6 Chapter summary and contributions

In this chapter we described the details relative to the functionalization process of SiNWs. The successful formation of a high quality biolayer of receptors on the device surface, is a key ingredient in the development of label-free, high sensitive and specific biosensors.

The developed chemical protocol is based on silane chemistry to provide the linker molecules for antibody coupling to the surface, and blocking steps for passivating the unreacted sites and surface of the device and avoid nonspecific binding. This technique was used to modify both FET-based SiNWs and memristive SiNWs. The results demonstrated that the biomodification strategy was successful in the formation of a compact antibody film, the specificity of which will be discussed later in Chapter 4 and Chapter 5.

We also showed successful functionalization of bigger wires with a nano-spotting system, though without succeeding the very fine modification of our memristive devices. Spotting systems with very high resolution and little mechanical stress on target materials could enhance the sensing properties of our devices by enabling selective functionalization in the active area and not on the oxide all around. This would also reduce the loss of biological material, so precious when working with human samples. Microfluidic can also strongly improve the device performances for the same reasons. It would increase the interaction rate between reagents and reduce the time necessary both for the functionalization and the antigen binding. The design and fabrication of a first prototype for integration of the fabricated SiNW sensors with a microfluidic system will be discussed in Chapter 7.



## 4 In-air high sensitive detection of biomarkers with SiNW-FETs

This chapter collects all the measurements carried out with the SiNW-FETs fabricated as described in Chapter 2 (Section 2.2), and subsequently biofunctionalized as presented in Chapter 3. In the first section, we provide the electrical characterization of bare devices before any surface modification. Then, we introduce the experimental set-up for the novel sensing in dry conditions and discuss relative advantages compared to the traditional ISFET-based sensing in liquid. We show its application to the sensing of cancer biomarkers. The results demonstrate that this novel sensing approach enables the detection of femtomolar concentrations of biomolecules thanks to the in-air measurements of specific Antibody-Antigen (Ab-Ag) binding, both in ideal Phosphate Buffered Saline (PBS) solution and in the more challenging breast tumor extract.

### 4.1 Electrical characterization of SiNW-FETs

Electrical characterization of SiNW-FETs after fabrication was carried out at DIMES, TUDelft, using a probe station and a parameter analyzer (Agilent 4156C or Hewlett-Packard 4145B). All SiNW-FET devices addressed in this chapter are based on the configuration reported in Figure 4.1(a) where the nanowires are formed on a p-type Si substrate, thus leading to p-type depletion-mode characteristics. Figure 4.1(b) shows  $I_{ds} - V_{bg}$  curves of a SiNW-FET defined through the PDE-based fabrication process already described in Chapter 2 (Section 2.2). Accumulation of holes (majority charge carriers) happens when the applied negative back-gate voltage is higher than the threshold voltage thus forming a complete channel for the current to pass through; depletion will occur when a positive back-gate voltage is applied, and no current flows in the device. For positive and increasing  $V_{ds}$ , higher current values are observed as visualized in Figure 4.1(b). Linear  $I_{ds} - V_{bg}$  curves when back-gate voltage,  $V_{bg}$ , is zero demonstrate the good electrical contact between drain-source and metal layers.

After checking the proper functioning of the SiNW-FET devices, their surface was functionalized according to the chemical procedure presented in Chapter 3 and used for sensing.

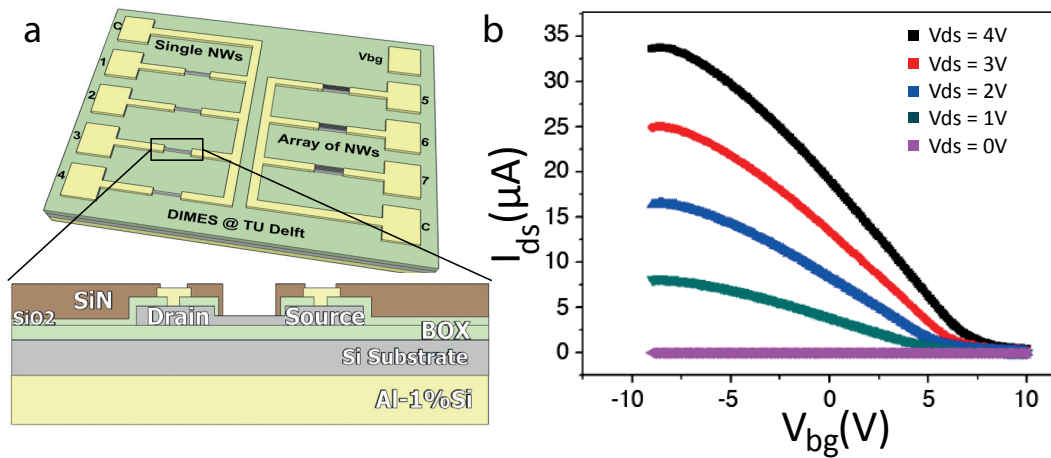


Figura 4.1 – (a) Schematic drawing of SiNW-FETs on a 10 mm×15 mm die, with zoomed view on a device cross-section with back-gate configuration for sensing purpose. (b)  $I_{ds} - V_{bg}$  characteristics of a fabricated SiNW-FET. Figures adapted from [100, 101].

## 4.2 In-air sensing: experimental design

The successful detection of antigens with NW-FETs functionalized with antibody has been recently achieved with femto-molar sensitivity in an assay buffer solution by several groups [140, 146]. On the contrary, protein analysis using nanowires has not been yet adopted to detect tumor in real human tumor samples due to the low signal-to-noise ratio in the measures. To the best of our knowledge, only few works have been published on SiNW-based sensing in extracts from tumor cells. They all demonstrate DNA detection [46, 75], and not the more challenging antibody/antigen based detection. The reason of achieved detection only with DNA is due to the fact that, typically, short DNA oligos are used in such kind of sensing, while the Ab/Ag detection involves much larger biomolecules that usually fall outside, or at the limit, of the Debye length (see Chapter 1). In this thesis, we present instead the successful, ultra-highly sensitive detection of antigen not only in ideal PBS, but, more important, in the complex breast tumor environment, thanks to the novel approach of measuring in dry conditions, under high relative humidity. In-air measurement of the Ab-Ag binding phenomena enables higher sensitivity thanks to the increased Debye screening length (Section 1.6 in Chapter 1). In the following section we describe the experimental set-up for detection in air and the related advantages in sensing.

### 4.2.1 Sensing in dry conditions: experimental set-up

Electrical characterization of the SiNW-FET biosensors was carried out in the LSI wet laboratory, EPFL, using a Signatone H-100 Probe Station and a Keithley 6430 Sub-Femtoamp SourceMeter. All the measurements were performed in air with the sample in dry conditions. In order to ensure a proper control over the experimental conditions, humidity and temperature were continuously monitored. We performed all the measurements at relative humidity

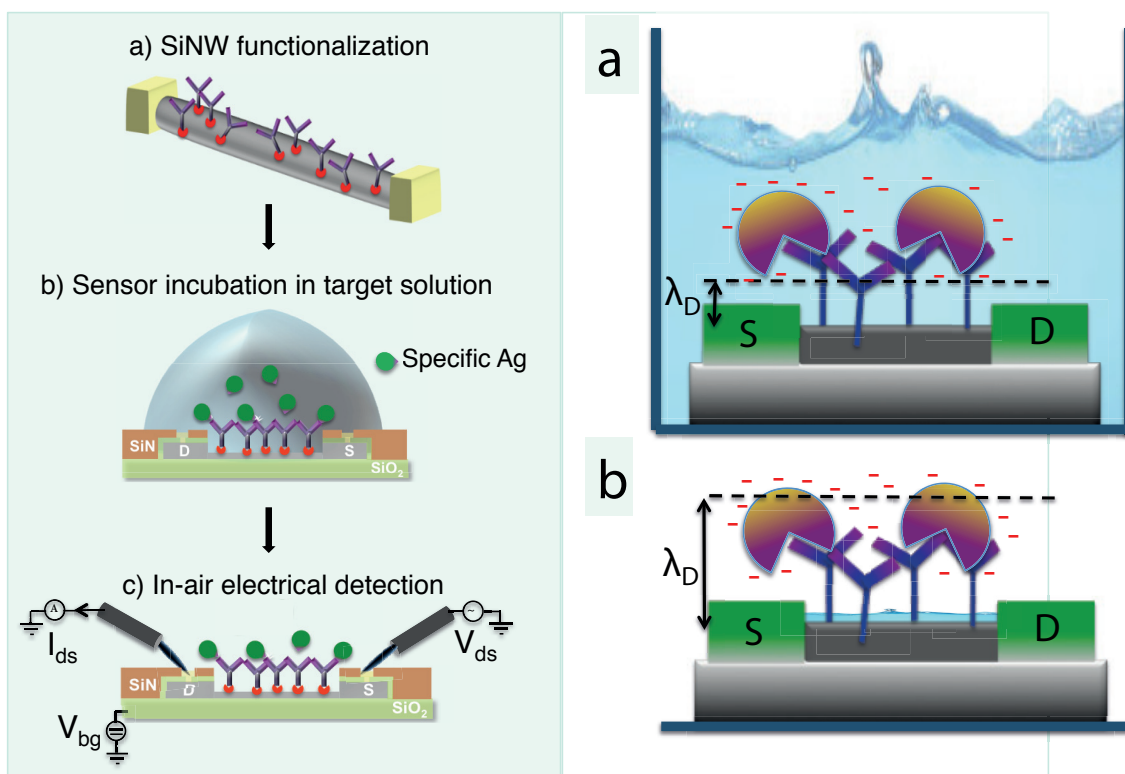


Figure 4.2 – (Left) Conceptual schema summarizing the main phases of the in-air sensing approach. Ab-Ag interaction happens in liquid during the incubation (b); detection is done by electrical measurement in dry conditions (c). (Right) Increased Debye length as result of counterions depletions after removal of the the liquid bulk.

(rH) of 50% and temperature 21°C.

After the functionalization, the device, stored in PBS solution and at 4°C until use, is taken from the fridge, and after some time for temperature stabilization, its surface is washed in fresh PBS solution and gently dried with N<sub>2</sub> flow. The device is then loaded in the probe station and source-to-drain current versus source-to-drain voltage ( $I_{ds} - V_{ds}$ ) characteristics are acquired in order to obtain the baseline signal after biofunctionalization, and before exposure to target molecules.

For antigen sensing, the experimental protocol is schematically sketched in Figure 4.2(left). The device is incubated for 1 hour, at room temperature, in a solution of Ag diluted with known concentration. Experiments have been made either in PBS or in tumor extract (see tumor extract preparation in Section 4.4.1). The incubation of 1 hour was found to be a good compromise for allowing the target molecules to diffuse to the immobilized antibody for binding, and, meanwhile optimising the sample-preparation time. Specifically, for the case of detection in tumor extract, avoiding long incubation time is of paramount importance to the proper evolution of the experiment, too (Section 4.4.1). A critical phase in the sample preparation before electrical measurement, is the accurate cleaning of the device surface for proper removal of non-specific and unreacted species. Repeated washing steps were found

to be necessary for increasing signal-to-noise and enhancing both sensitivity and specificity of the detection. In order to determine the selectivity of the method, the response of a set of SiNW-FET sensors was tested under specific conditions before the real detection experiment. The sensors were subjected to repeated incubations in either PBS or tumor extract, depending on the sensing target, and subsequent washing and drying cycles. The statistical analysis of the conductance variation as a function of the different washing procedure is reported in Section 4.4.1, in the most critical case of detection in highly noisy tumor landscape.

When the most of the nonspecific material is removed from the sensor surface through washing, the device are loaded in the probe station and electrically tested for conductance acquisition. The conductance is calculated as slope of the  $I_{ds} - V_{ds}$  characteristic ( $\frac{\delta I_{ds}}{\delta V_{ds}}$ ). A number of devices is electrically tested for statistical analysis. After the acquisition, the sensor chip is incubated a second time in a solution of antigen at known concentration, and the full experimental procedure is repeated several times until completed calculation of the sensor calibration.

As introduced in Chapter 1 (Section 1.6), the most critical feature of label-free sensing using SiNW-FETs in liquid is the Debye screening. Counterions from the bulk solution screen with their charge the electrical signal of target species, reducing the sensing capabilities of the sensors. The more ions (also from charged biomolecules) are in the electrolyte, the bigger is the screening and the smaller the so-called Debye-Hückel length ( $\lambda_D$ ) when screened (Figure 4.2(right, a)). By washing multiple times the sensor after incubation, we get rid of the most of the nonspecific material avoiding both salts deposition and nonspecific binding. By measuring the sample after drying, the sensitivity is also improved because of the increased Debye length resulting from the removed bulk solution and the relative reduced counterions screening (Figure 4.2(right, b)). Worth to note that, although the sensor chip is dried after cleaning steps, its surface is never completely dry, but a thin film of liquid is formed at the air-nanowire interface [103]; this is due to the surrounding humid environment, and is presumably to be considered an important factor for the stable and proper activity of the Ab-Ag system.

### 4.3 VEGF detection in PBS with SiNW-FET: results

This section collects successful results of biomarker sensing with SiNW-FET biosensors in the ideal environment of PBS solution. We detected very low concentrations (order of fM) of *Vascular Endothelial Growth Factor* (VEGF) by biofunctionalizing the device surface with specific monoclonal *VEGF Antibody* (anti-VEGF).

VEGF is a promoter for the formation of blood vessels in embryogenesis and wound healing, and it is also a major regulator of pathological angiogenesis. Angiogenesis is highly active in various ischemic and inflammatory diseases, and is also one of the major mechanisms governing the tumor growth. These biological properties make VEGF an important therapeutic target and diagnostic biomarker [147, 148]. Its detection and profiling in specific regions of the tumor tissue can be very challenging.



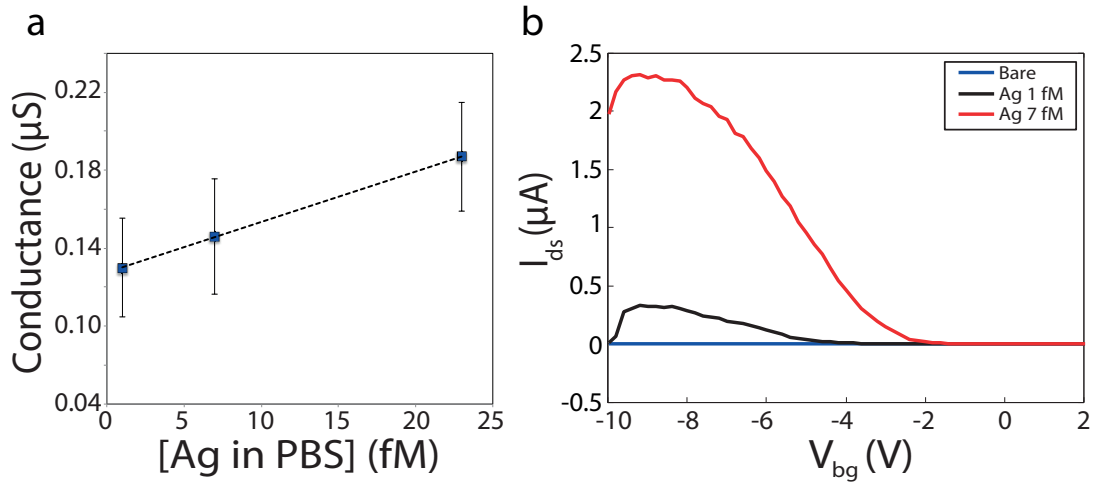


Figure 4.3 – (a) Calibration curve for a fabricated SiNW-FET. Error bars stand for the standard deviation calculated on repeated estimates of the current slope. (b) Threshold voltage shift in the  $I_{ds} - V_{bg}$  characteristic showing the effect of the increased amount of Ag on the majority carrier enhancement in the nanowire. Adapted from [100, 101]

#### 4.3.1 Sensing

Electrical characteristics were acquired from single wires at different antigen concentrations according to the experimental procedure presented in Section 4.2.1. In Figure 4.3(a) we plot data related to an anti-VEGF-functionalized SiNW-FET device after subsequent cycles of incubation, cleaning, and measurement of differently concentrated VEGF solution. Each point in the diagram refers to the conductance value averaged between subsequent acquisitions, at different concentrations of VEGF in PBS. The conductance was evaluated as slope of the  $I_{ds} - V_{ds}$  characteristic at low  $V_{ds}$  voltage, that was observed to be the most sensitive range. The error bars stand for the inter-device error calculated as standard deviation of three different measurements of the same sensor. The analysis of conductance showed the increase of conductivity as function of VEGF concentration, thus confirming the detection of occurring immuno-recognition events between antibody and antigen molecules. An according shift of the threshold voltage ( $V_{th}$ ) was also observed in the corresponding  $I_{ds} - V_{bg}$  curves (Figure 4.3(b)).

These data well confirm the literature and the theoretical considerations on the working principle of SiNW-FET based biosensors. According to what introduced in Section 1.4 of Chapter 1, we expected to observe an increased current flowing through the functionalized transistor channel when negative antigen molecules bind to their specific antibody. Considering their structural composition, we observe that antibody and antigen species are proteins, thus consisting of long amino acid chains. Each amino acid is characterized by a specific side chain composed of residues. Under correct physiological conditions (pH 7.4), that match with

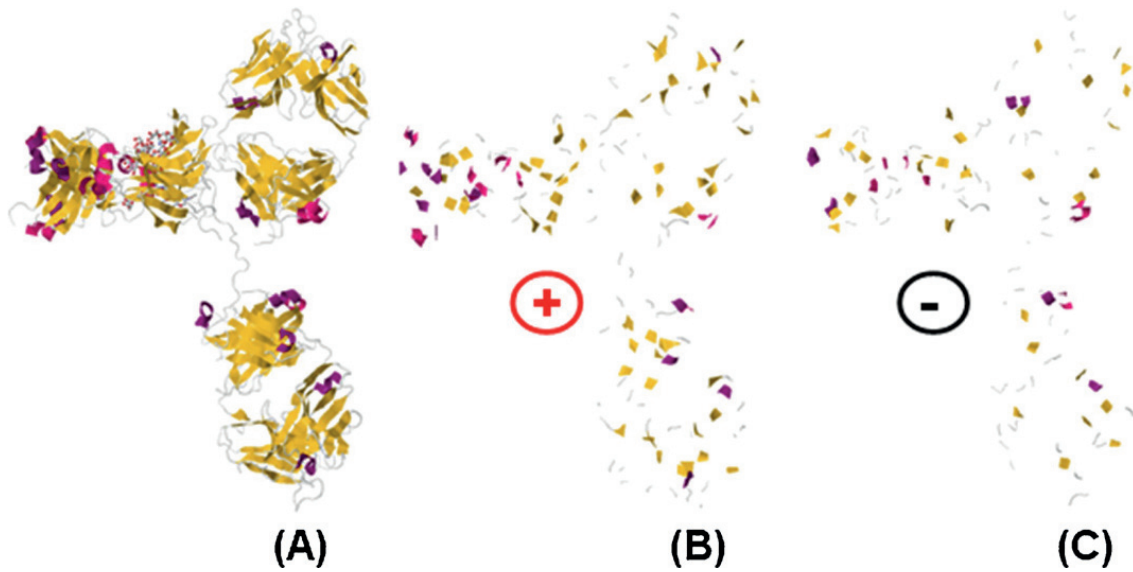


Figura 4.4 – The crystallographic structure of an antibody showed with all the residues (A) or with only the positively (B) or negatively (C) charged ones. Reprinted from [95].

the standard laboratory experimental conditions, arginine and lysine residues are positively charged while aspartic and glutamic acids are negatively charged. For example, in an antibody (Figure 4.4A), positively charged residues (Figure 4.4B) are in excess with respect to negatively charged ones (Figure 4.4C), even if the charge distribution is quite similar [95]. VEGF antigen molecules have a complementary structure and charge configuration in its epitope (the molecule part that interacts with the antibody), in order to interact with the binding sites of their specific antibodies through weak and noncovalent bonds such as electrostatic interactions, hydrogen bonds, Van der Waals forces, and hydrophobic interactions [149]. When Ab-Ag binding occurs, an excess of negative charge accumulates at the nanowire surface. This extra charge acts by enhancing the majority carriers in the p-type wire (see Figure 1.4 in Section 1.4), and increases the channel conductivity. The calibration curve presented in Figure 4.3(b) confirms that our sensor is detecting negatively charged VEGF antigen as demonstrated by the increasing channel conductance as a function of increasing concentration of VEGF in PBS solutions. In addition to confirm data in literature, these data show that the developed anti-VEGF-SiNW-FET sensor successfully succeeded in measuring pathogenic factors like VEGF in a very low concentration range (fM) taking advantage of the increased  $\lambda_D$  in dry conditions.

#### 4.4 Detection of anti-rabbit in breast tumor extract

In this section, we present the more interesting results obtained with p-type SiNW-FET biosensors in a much more complex environment, i.e. a human breast tumor extract containing 100.000 fold mass excess of non-specific proteins. Given the complexity of such a noisy envi-

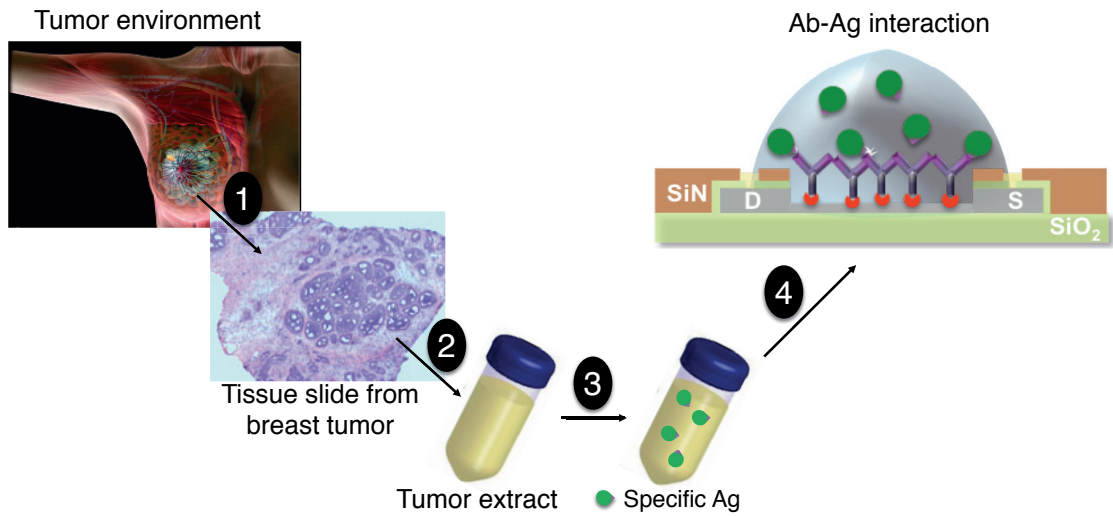


Figure 4.5 – Conceptual schema of the SiNW-FET based biosensing method in tumor extract: (1) Breast tissue biopsy; (2) tumor extract (TE) preparation; (3) rabbit antigen dilution in TE; (4) sensor incubation in TE for Ab-Ag interaction. Adapted from [101].

ronment, we decided to investigate the sensor capabilities by analyzing its performance in sensing exogenously added rabbit antigen, used as a model of any tumor marker, in human tumor extract. In the following, we first describe the experimental procedure discussing the major considerations in the design of the experiment; then, we briefly present the process of preparation of a diluted tumor extract, and how we faced the main issue of sensor instability and nonspecificity. Finally, we show and discuss the most relevant results of sensitivity and specificity of the developed sensor.

#### 4.4.1 Experimental procedure

Figure 4.5 propose a conceptual representation of the experiment designed for sensing in *Tumor Extract* (TE) with SiNW-FETs. First, a tumor extract is prepared (Section 4.4.2) by mechanical disruption of tumor biopsies from patient (1) and diluted in buffer solution (2); then, exogenous rabbit antigen (Section 4.4.3) is diluted at known concentration in the breast tumor extract (2). The solution is then used to incubate the fabricated sensor for 1 hour at room temperature and to enable specific immuno-recognition events between the surface immobilized receptors and the rabbit antigen (4). As for the procedure performed for VEGF sensing in PBS (Section 4.3), the sample is thoroughly rinsed after incubation to eliminate unreacted antigen molecules (Section 4.4.3), gently dried under flow, and measured in air under controlled humidity and temperature conditions.

### 4.4.2 Tumor extract preparation

Tumor biopsies were provided from the CHUV (Centre Hospitalier Universitaire Vaudois in Lausanne), and processed for tumor extract preparation by the staff of the Ludwig Center for Cancer Research of the University of Lausanne (UNIL). To capture the complexity of the tumor microenvironment, a tumor extract is prepared by mechanical disruption of a pool of 10 distinct human breast tumor biopsies. Following breast tumor resection, a fresh tumor tissue is sectioned into small pieces with a scalpel, the fragments were snap frozen in liquid N<sub>2</sub>, and homogenized with a mortar and a pestle. The resulting tissue powder is resuspended in sterile water and further homogenized with a tip sonicator. The mixture is then clarified by centrifugation and the protein concentration of the resulting supernatant adjusted at 1, mg/ml. The specific antigen is spiked in the tumor extract using 100.000 fold molar excess of nonspecific tumor proteins.

### 4.4.3 Experimental requirements in tumor extract

In order to investigate the potential of fabricated SiNW-FET sensor devices for high-sensitive detection of marker proteins in tumor tissue, we first decided to focus on the detection of exogenously added rabbit antigen in a breast tumor extract. This antigen is spiked at a defined concentration in the tumor extract in order to emulate the presence of a cancer biomarker in the tumor environment. In fact, since the behavior of the wires in the presence of tissue extract is unpredictable, due to the high concentration of water and nonspecific proteins, the use of an antigen that is unknown to the tumor landscape can help in ensuring for the specificity of the detection measurement. Moreover, we employed an anti-rabbit antibody/antigen pair that was used for preliminary sensing in PBS with the VoG approach of memristive SiNWs (see Chapter 5), thus enabling us to compare detection sensitivity levels.

A further consideration for developing good devices for detection in tumor specimens is the potential sensor instability as a consequence of the high enzymatic activity of the tumor environment. In fact, despite of repeated dilution steps of tumor samples in PBS, the final tumor extract still presents a relevant amount of enzymes, i.e. proteases, that are species featuring a very pronounced digesting activity. Proteases digest proteins, thus, can be dangerous both for the stability of the tumor environment as well as of the diluted target antigen molecules can lose their functionalities, and the stability of the sensor surface, where the immobilized antibodies can be modified or digested, too. Both phenomena would lead to the deterioration of the sensor capabilities.

Thanks to the collaboration with the Ludwig Center for Cancer Research, UNIL, we had the opportunity to determine the stability of antigens in tumor extract with RPP arrays (Reverse Phase Protein Array). We observed that the antigen maintained its structural conformation for about 2 hours at room temperature. The idea of incubating the sensor for a duration smaller than 2 hours (1 hour) (Section 4.2.1) was found in agreement with these data because in this way we guaranteed the sensor stability thanks to design of the experiment in which after the incubation, all the measurements had to be performed in air, after removal of tumor tissue

#### 4.4. Detection of anti-rabbit in breast tumor extract

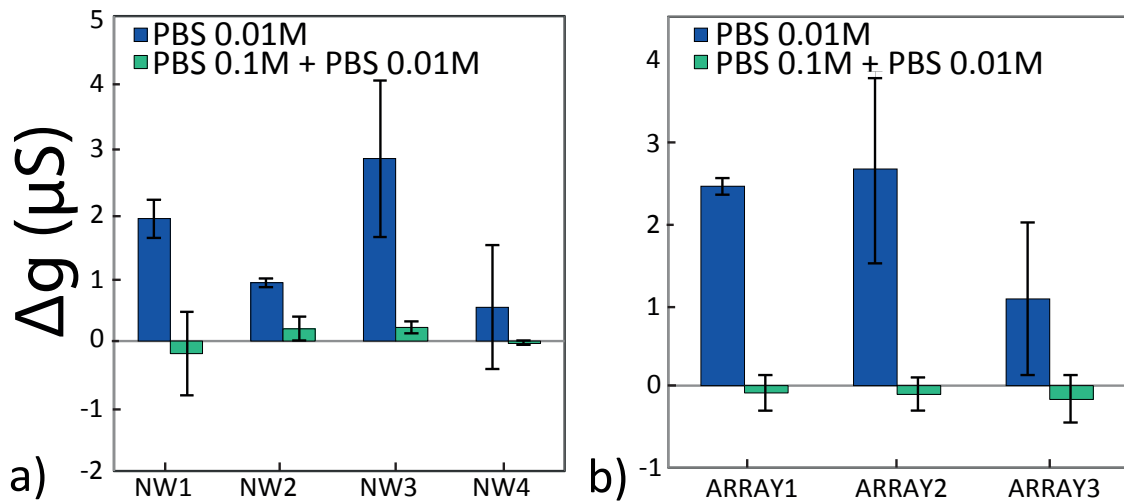


Figure 4.6 – Statistics on washing steps for non-specific tumor protein removal from the surface of SiNW-FETs (a) and arrays of SiNW-FETs (b). The column height represents the conductance variation  $\Delta g$  measured after incubation and washing of the sensors with respect to the baseline acquired before any exposition. The error bars stand for the standard deviations of repeated measurements after multiple washing steps on the sensors. Reprinted from [101].

residues through multiple washing steps (see following section).

#### The importance of nonspecific molecules removal

In order to determine the selectivity of the method, the response of a set of SiNW-FET sensors taken from the same fabrication batch was tested under specific conditions before the real detection experiment. The sensors were subjected to repeated incubations in PBS solutions, and subsequent washing and drying cycles. The corresponding conductance variations  $\Delta g$  were calculated as difference between the nanowire conductance acquired before (baseline) and after the sensor exposition to the solutions. Same control tests were carried out by exposing the nanowires to tumor extract solutions that did not contain target molecules.

In Figure 4.6(a,b), we report the conductance variation data acquired from biofunctionalized individual SiNW-FET and device array, respectively, after incubation in tumor extract and subsequent washing using two different methods. The column height represents the  $\Delta g$  acquired on the device; the error bars correspond to the standard deviation of multiple expositions of the sensor to cleaning solutions of PBS. A very similar behavior was observed both in single devices (a) and in arrays of SiNW-FETs (b). Washing the samples with only low concentrated buffer solution (0.01M PBS) did not show good results in term of nonspecific material removal. This is demonstrated by the high conductance variation  $\Delta g$  introduced by the incubation with tumor extract and the following washing steps (blue columns in both panels of Figure 4.6). Indeed, when compared to the baseline, the conductance resulted increased as effect of the tumor proteins left on the silicon surface as consequence of an

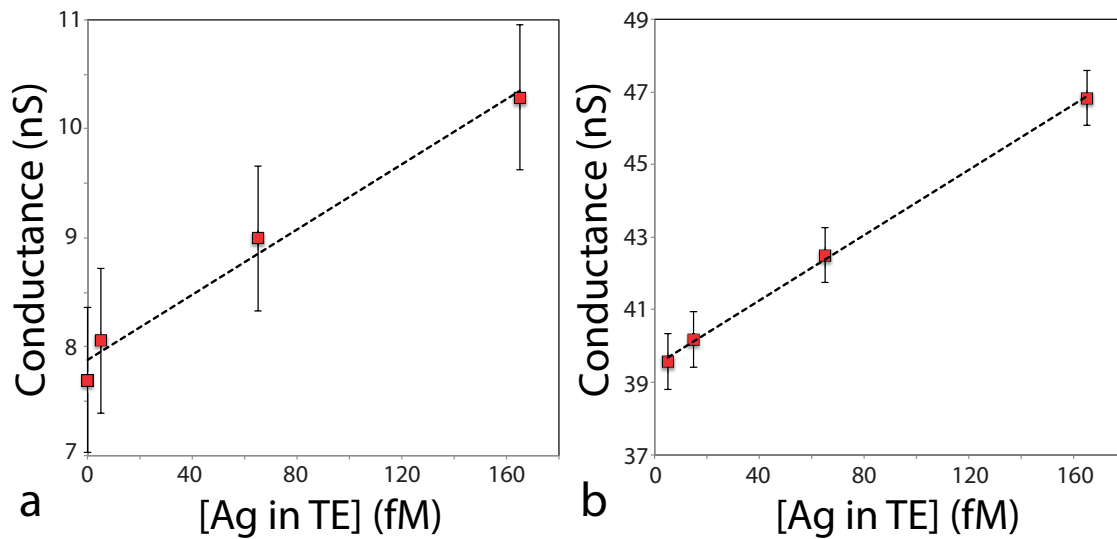


Figure 4.7 – Sensing of rabbit antigen after sensor exposure to Ag breast tumor extract solution. (a) Response of an individual SiNW-FET sensor to the antigen concentration [AG] (0fM, 5fM, 65fM, 165fM). (b) Array of SiNW-FETs. Response to [AG] 5fM, 15fM, 65fM, 165fM. The error bars stand for the intra-device error calculated as standard deviations of repeated measurements after multiple washing steps on the sensor. Reprinted from [101].

unsuccessful cleaning. In order to get rid of the unreacted proteins and tumor components, and to avoid salts deposition onto the modified silicon surface, the best washing protocol was found to be a 3-cycle rinsing step of 5 min per wash, with PBS 0.1M first, and with PBS at lower ionic strength (0.01M PBS ) then. As clearly shown in the figure, this second washing process enabled a good cleaning of the device surface. The  $\Delta g$  calculated in this case is indeed very small if compared to the previous one (green columns in both panels), and the variability of the data (error bars in the graphs) appeared reduced, too.

#### 4.4.4 Antigen detection in tumor extract with SiNW-FET: results

##### Sensing rabbit-Ag with single SiNW-FETs and arrays: pM detection

After determination of the impact of the tumor extract on sensor characteristics and sensitivity, and after the definition of a good method for removal of most of the nonspecific mass of tumor proteins, we employed the anti-rabbit SiNW-FET device for detection of low concentrated (order of  $10^{-15} - 10^{-13}$  M) rabbit antigen in tumor environment.

The data show that the incubation with specific rabbit antigen molecules results in concentration dependent conductance changes in SiNW-FET sensors. In particular, best results were achieved in the concentration range 5 to 200 fM both for individual devices and arrays of nano-sensors, as shown in Figure 5.10(a,b). The nanowire conductance changes as linear function of the target concentrations in the breast tumor extract. Here, the error bars define the reproducibility of the results. The repeatability of the measurement is defined for individual

#### 4.4. Detection of anti-rabbit in breast tumor extract

---

nanowire sensors and not for sets of similar devices averaged together. In fact, the intra-device standard deviation calculated considering different individual devices was calculated to be 4.7 nA; the one related to a set of different arrays of SiNW-FETs (inter-device) resulted 8.5 nA. As expected, this inter-device error was observed to be evidently bigger than the intra-device variation. The measured discrepancy can be associated to variability introduced by the nanotechnology process, noise in the measurement due to bad electrical contact with the probe station, or variability in the bio-modification method. Considering the good quality of the fabricated structures and surfaces (SEM images in Section 2.2.2), we mainly believe that the different behavior of devices belonging to the same chip (Figure 4.1(a)) derives from two most probable causes. First, we observe that the source and drain (S/D) pads for electrical contact of the fabricated devices are made of Aluminum, and that piranha solution, necessary for cleaning the nanowire surface and creating the OH groups for functionalization (Chapter 3), is selective for Al, i.e. can etch Al structures. Because of that, S/D contacts, made of Al material that is not completely annealed, resulted partly damaged in some of the devices due to the pre-cleaning process. This certainly can introduce noise in the electrical measurements and variability. Second, both the bio-functionalization process and the incubation are performed by simple diffusion of the reagents (GPTS, Ab, Ethanolamine, Ag) to the sensor surface, without the use of any microfluidic or high-resolution spotting system that could improve the sensor Ab-coverage and its homogeneity (Section 3.6). Surface treatments on devices of same chip can thus lead to larger intra-device variability, too.

The inter-device variability leads to the necessity of calibrating each single sensors. Because of the difficulties in the normalization of the results, we preferred to consider the reproducibility on individual devices. The error bars, thus, stand for the intra-device error that was estimated by performing statistics on several sensors (single and arrays), for the conductance changes deriving from the exposition to PBS after incubation in tumor extract solutions. As observed in Section 4.4.3, the washing steps cannot fully clean the silicon surface; a small but non-negligible variations (Figure 4.6) in the sensor conductivity is present as due to salts and biological components present in the tumor extract that can agglomerate onto the sensing device. Although non-null, this error does not hide the effect of specific detection events at the nanowire surface and the figure clearly shows an increasing trend of the conductance as function of increasing antigen concentrations.

Moreover, it is worth to note that the sensing measurements with arrays of SiNW-FETs show a reduced variability if compared with the case of individual devices. The current acquired on arrays was found larger than the one measured on single SiNW-FETs. The resulting enhanced signal-to-noise ratio could be a first reason for the diminished intra-device variability. More probably, the improved sensing performance and repeatability of the experiment are associated with an increased probability of Ab-Ag binding, due to the larger accessible sensing area provided by multiple nanowires in the array.

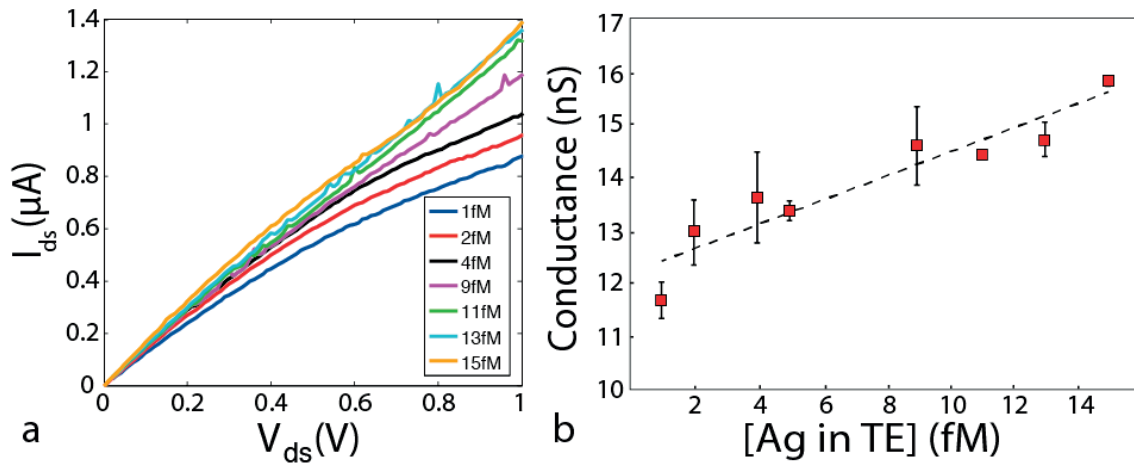


Figure 4.8 – (a)  $I_{ds} - V_{ds}$  characteristics for nanowires exposed to increasing femtomolar concentrations of rabbit antigen diluted in tumor extract. (b) Calibration for the sensor shown in (a). The error bars correspond to the standard deviation for 3 different measurements (confidence interval of 68.2%). Adapted from [101].

### Sensing rabbit-Ag: fM detection

By analyzing the several measurements performed with SiNW-FET sensors, we observed that some devices were able to detect lower concentrations of target species in the tumor landscape. In the experiment whose results are plotted in Figure 4.8(a,b), we applied a larger number of concentration points, in a much lower range (fM), and we demonstrated the occurring detection of rabbit antigen in tumor within the femtomolar range on a single device. Figure 4.8(a) shows the plots of current versus voltage with rabbit antigen at a series of concentrations for an anti-rabbit modified SiNW device. As proved by the increasing slope of the  $I_{ds} - V_{ds}$  characteristic, the channel conductivity clearly increases as function of antigen concentration, confirming the occurring trapping of target molecules. Figure 4.8(b) illustrate the calibration curve for the corresponding biosensor. Each point represents the conductance value, calculated as  $\frac{\delta I_{ds}}{\delta V_{ds}}$ , in correspondence of the chosen Ag concentration. The error bars stand for the standard deviation of 3 repeated measurements for each point. The rising behavior of the nanowire conductance demonstrates the antigen-antibody detection in tumor extract.

### Specificity control

Figure 4.9 shows the outcome of a competitive binding experiment for the investigation of the device specificity in the very hostile tumor environment. An antibody prepared in rabbit was used as nonspecific antigen. It was diluted in an equally concentrated tumor extract, in the same concentration range as the specific anti-rabbit antigen (70 fM). First, one biofunctionalized device was incubated in tumor extract solution with 70 femto moles of nonspecific Ag, it was washed according to the procedure of Section 4.4.3, dried and



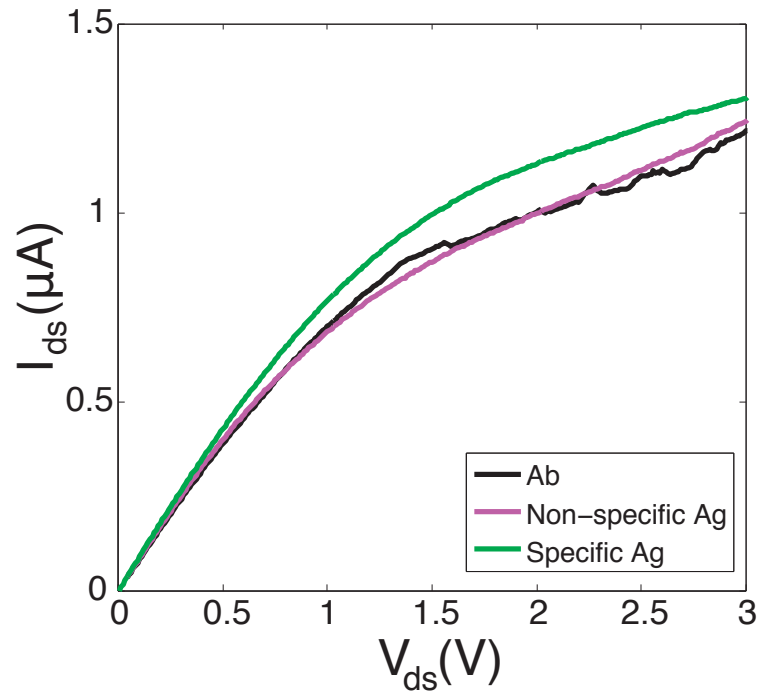


Figure 4.9 – A non-specific antigen (Ag), diluted in tumor extract at same concentration as the specific one (70 fM), determines a smaller conductance signal. In the considered device, the signal is also very closed to the curve acquired on the same wire in the absence of specific Ag (Ab). This result demonstrates the specificity of the sensor. Image adapted from [101].

measured in the probe station in dry conditions. The pink curve in Figure 4.9 was acquired from the prepared devices. Once the electrical test was finished, the same process was carried out with an equally concentrated specific rabbit Ag in tumor extract. The corresponding characteristics is reported in green in Figure 4.9. In black we visualize the baseline signal, i.e. the  $I_{ds} - V_{ds}$  curve acquired before the sensing experiment, prior to exposing the nanowire device to specific and nonspecific proteins, after the biofunctionalization. As clearly shown in Figure 4.9, the electrical signal acquired under exposure of the sensor to 70 fM specific analyte results increased with respect to the conductance measured for a corresponding concentration of nonspecific protein. Moreover, the nonspecific characteristic (pink line) is superimposed to the one acquired on the same wire in the absence of specific Ag (only Ab layer on the wire) (black line), thus demonstrating that during the incubation in solution of nonspecific molecules, no Ab-Ag interact because of the selectivity of the test, and no change in the wire conductance is registered. This result is a very important evidence of the high specificity of our biosensor.

## **4.5 Chapter summary and contributions**

In this chapter we presented our improvements in the state-of-the-art of SiNW-FET in the development of biosensors for specific, label-free and highly sensitive immunodetection.

In particular, we proposed an innovative way of sensing that pushed to the limit the sensing capabilities of the FET-based device by showing that anti-VEGF modified nanowire structures sense very low concentration (fM) of pathogenic factors diluted in controlled PBS solutions and measured in- air.

More importantly, we demonstrated the feasibility of using SiNW-FET biosensors in real applications with tumor extracts for the detection of cancer markers. Tumor extracts were prepared by mechanical disruption of human breast tumor biopsies and exogenous rabbit antigen was diluted in it. Data showed specific and highly sensitive antigen detection in the range 5-200 fM. Comparisons with previous works of VEGF detection in ideal conditions (PBS solution) (Section 4.3) demonstrate that a higher detection limit was calculated for SiNW-FET biosensing in tumor extract. This result is absolutely expected if considering that the wires sense antigen in the presence of a 100.000 mass excess of non-specific protein. Occurring fM-pM sensing events in such a complex environment, as well as data from competitive binding experiments, are instead the proof that our sensors are sensitive and extremely resistant to noise.

The achieved femtomolar sensitivity derives from the high-quality of the fabricated nano devices, and more important, from the novel proposed approach of sensing in dry conditions for reduced Debye length.

The proposed results open the way to future development of SiNW-FET based devices for detection in real patient specimens. The results collected in this chapter represent an important contribution of this work in the more broader objective of sensing and quantifying specific angiogenic and inflammatory ligands present in the tumor tissue. Thanks to the achieved high-sensitivity and the knowledge acquired throughout a careful investigation of the background signal from nonspecific agents in the active tumor tissue, vascular factors and other important proteins regulatory of the tumor environment can be also target. Further suggestions for advancements and possible alternative strategies will be given in Chapter 8.

## 5 A novel approach for high-sensitive biodetection: the VoG-biosensing

In this chapter we propose a detailed investigation of a completely novel sensing approach that we called *Voltage Gap* (VoG)-based biosensing with memristive SiNWs. The devices are crystalline SiNWs with NiSi Schottky-barriers contacts, fabricated through a DRIEs process that has been already described in Section 2.3. Their electrical characterization pointed out a peculiar hysteretic behavior in the  $I_{ds} - V_{ds}$  characteristics that is related in some extent to memristive effects. Because of that, and in order to well distinguish the suggested sensing paradigm from the traditional ISFET-based technique, we sometime refer to the newly developed sensor as *memristive biosensor* too, although the fabricated devices do not always reproduce all the features of the pure memristor. This behavior is modified, in a predictable way, by biomolecules approaching the nanowire surface. In this chapter we show the attempt to explore the potential of this system in the field of nanobiosensing, and we propose the voltage gap paradigm as a valid alternative to the more traditional conductance-based sensing technique in SiNW-FET devices.

First, we introduce the background of this innovation and we give a preliminary definition of the voltage gap parameter. Then, we show the electrical characterization of our devices in bare conditions when they show memristive-like behavior, and its modification after biofunctionalization with antibodies that leads to the appearance of the voltage gap. Next, we begin the exploration of the main features of the novel sensing method such as the VoG variation as a function of the relative humidity or of ions from dissolved salts in solution. More importantly, we present results of biosensing with the goal of detecting femto moles of VEGF in ideal conditions. Then, we show the performance of the method in the more challenging tumor extract for sensor calibration with rabbit antigen, demonstrating the sensitivity and specificity of our approach in real human samples.

To note that, in this chapter, we present only the experimental results obtained with the implemented VoG method in SiNWs, while the physical interpretation of this approach is discussed in detail in Chapter 6 where we will describe the developed model that explains the observed complex phenomena.

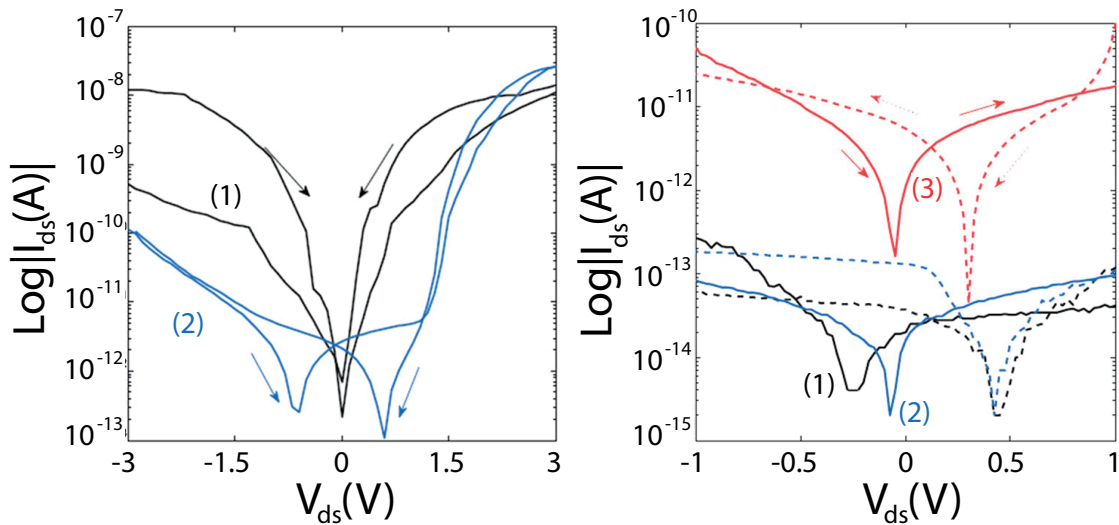


Figure 5.1 –  $I_{ds} - V_{ds}$  curves taken (1) before and (2) after wire functionalization with an all around AB layer demonstrating the origin of a current minima gap with the presence of a biomolecular layer. (b) Current minima gaps for  $-1V \leq V_{ds} \leq +1V$  clearly showing the decreasing trend of the voltage gap with increasing antigen concentration: (1) 0 fM, (2) 5 fM, (3) 10 fM antigen solution. Arrows indicate sweep directions. Images adapted from [95].

## 5.1 The VoG approach: background

Many works have been already published in literature about the possibility to exploit silicon nanowire FETs for molecular detection. Most of these proposed methods are based on direct measurement of the change in DC conductance of the nanowire due to attachment of target molecules to the specifically functionalized surface (Section 1.4). As presented in Chapter 4, we exploited, and further developed one of these approaches, with SiNW-FETs. On the other hand, memristive devices have been studied and used for different applications, but all of them related to electronics for memory and logic [78], none of them for biosensing purposes. It is only recently that the modification of the memristive effect have been related to biological molecules, paving the way to the investigation of a completely novel biodetection paradigm based on memory effects registered on functionalized SiNW devices [94, 95].

Due to the nano-scale of the fabricated geometries, silicon nanowire devices, having NiSi Schottky barriers, were discovered to show hysteretic properties that were imputed to memristive devices [95]. When the channel of the NW device was functionalized with antibody molecules, and the  $I_{ds} - V_{ds}$  curves were acquired under dried conditions in ambient air, a difference in voltage between the current minima reached in the forward and backward branches appeared (Figure 5.1(a)). The data also suggested that this voltage difference registered in nanofabricated memristive silicon nanowires functionalized with biomolecular films is dependent on the concentration of protein solutions, thus revealing the potential for a new biomolecular detection mechanism (Figure 5.1(b)).

Moving from these preliminary investigations, this thesis is aimed at giving a wider presenta-

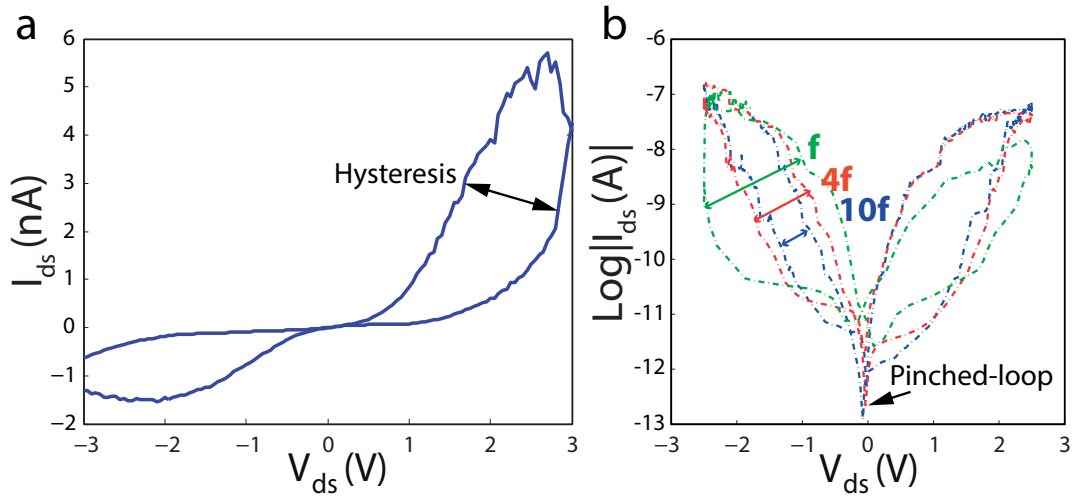


Figure 5.2 – (a) Hysteretic  $I_{ds} - V_{ds}$  characteristic of a bare silicon nanowire device. (b) The dependence of the hysteresis on the frequency ( $f$ ) of the measurement observed on some of the fabricated devices.  $f$  was determined by changing the scan rate at 10 mV/sec, 40 mV/sec, and 100 mV/sec, respectively.

tion of the sensing capabilities of the voltage gap based sensor, and at proposing an accurate investigation of the physical factors contributing to its appearance and modification as a function of biomolecules. In this chapter, we start by the characterization of the sensing potential of the novel paradigm of detection. We refer to Chapter 6 for the physical interpretation and modeling.

## 5.2 Electrical characterization of memristive SiNWs

### 5.2.1 A memristive system?

The memristive devices used in this thesis are NiSi Schottky-barrier SiNWs fabricated with the top-down method described in Chapter 2 (Section 2.3). Electrical measurements were carried out in order to characterize their behavior before the modification with surface receptors. Electrical characterization was performed in the LSI laboratory, EPFL, using a Signatone H-100 Probe Station and a Keithley 6430 Sub-Femtoamp SourceMeter. They consisted of the acquisition of the current flowing through the two terminals of the nanowire channel, as the source-to-drain current versus the potential applied to these terminals ( $I_{ds} - V_{ds}$ ). All the measurements were carried out in dry conditions, under controlled temperature and humidity conditions. In particular, a humidity sensor for a constant monitoring of the relative humidity (rH) conditions was necessary because of the non-negligible impact of the humid surrounding environment on the voltage gap (see Section 5.3.1).

Figure 5.2(a,b) shows the linear and semi-logarithmic scaled  $I_{ds} - V_{ds}$  characteristics acquired on one of the fabricated devices, for external voltages varying as a piecewise linear waveform

with a voltage step of 50 mV/sec, and double sweeping from  $-3$  V to  $+3$  V. In (b) we report characteristics at varying frequency, and in the semi-logarithmic scale for a better definition of the null voltage gap parameter and its comparison with future electrical acquisitions. The conductivity of the wire is very similar to the ones reported in literature in similar structures [95], and reminiscent of a memristive system. This is confirmed by the hysteretic values of the current for same bias voltages (Figure 5.2(a)), by the pinched-loop at zero voltage, and the frequency-dependence Figure 5.2(b). According to the memristor theory (Section 1.7) at increasing frequency of the external voltage signal, indeed, the device responds by shrinking the width of the hysteresis lobes, and keeping a pinched double-loop at 0 V (Figure 5.2(b)). Worth to note is that, in our case, electrical testing of the wires could not be performed at high frequency due to the very low current at which the current minima could be observed (pA-fA). Because of that, the frequency was modified in a low range of values by increasing the speed of the measurements with the reduction of the voltage step (range 10 mV/sec to 100 mV/sec). Despite we observed that the presence of a memristive effect in the nanowires is a necessary condition for having biosensing, the feature of most interest to us is not the memory in term of current, but a memory in voltage that is expressed by variations of the pinched hysteresis loop. The pinched loop was observed in most of the formed nanowire devices, before any modification of the surface, as indicated in Figure 5.2(b) at 0 V. Looking at the bare case (magenta dashed line), we observe that in the forward and backward branches of  $I_{ds} - V_{ds}$  curve, the graph shows a memristive effect, as encoded by different current values for the same bias value (hysteresis), while the curve shows a pinched-loop, that is the major footprint of a memristor [81]. When the surface of the memristive nanowire is modified with a biomolecular layer of antibodies (Chapter 3), the hysteretic pinched-loop is lost (blue solid line), and the current reaches the minimum at  $-0.45$  V during the forward branch and at  $+0.45$  V in the backward one. This voltage difference between the two current minima is the voltage-gap.

### 5.2.2 The voltage gap in functionalized wires

The effect of lost memristive pinched-loop is well represented in Figure 5.3, where the superimposed characteristics indicate the  $I_{ds} - V_{ds}$  curves registered from the same memristive device before the functionalization process (magenta dashed line), and after the surface modification with anti-VEGF antibody (blue solid line), respectively. The memristive footprint of pinched hysteresis is lost upon bio-functionalization of the device. Antibodies show their net positive charge contribution (Section 4.3.1) acting by creating a sort of voltage memory, the voltage gap, appearing as the voltage difference between the current minima for backward and forward regimes.

### 5.2.3 The repeatability of the voltage gap

The voltage gap is also found a repeatable parameter, that is a characteristic very important for a biosensing system when dealing with nano-scale based sensors. A proof of the high reproducibility of the registered VoG in memristive devices after functionalization is proposed

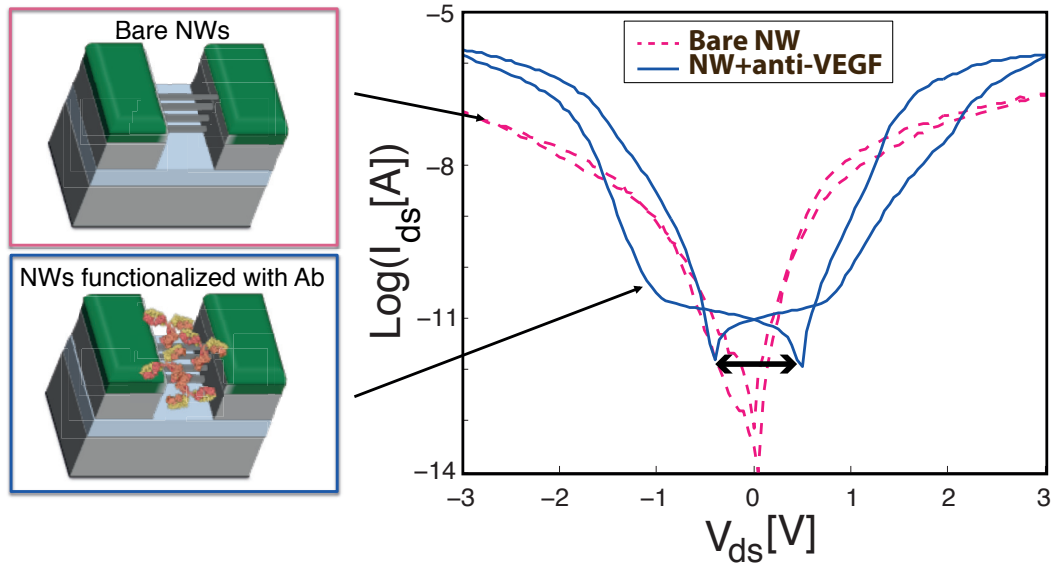


Figure 5.3 – Pinched hysteresis loop in bare nano-fabricated nanowire devices (magenta dashed line), and voltage gap appearance in memristive-biosensors after the biomodification (blue solid line).

in Figure 5.4. The statistics was performed on 18 SiNW devices belonging to the same fabrication batch, and with same geometrical characteristics (length 420 nm and a width of  $35 \pm 10$  nm). For clarity, in Figure 5.4(a) and (b) we report only four of the acquired  $I_{ds} - V_{ds}$  curves. The curves in Figure 5.4(a) were acquired on bare memristive devices, while Figure 5.4(b) on biofunctionalized ones. The electrical characterization was performed under controlled environmental conditions, %60 rH and  $21^\circ\text{C}$ . The comparison clearly shows that the net charge from antibodies induces a change in the memristive hysteresis whose effect is the appearance of the voltage-gap.

Contrarily to the current parameter, that shows high variability, the voltage difference formed between the forward and backward zero crosses was registered and found highly repeatable in all tested devices. This repeatability is demonstrated in Figure 5.4(c) that shows the distribution of the voltage-gap over the complete set of 18 nano-devices. The error bars stand for the standard deviation of the measurement and show that the variability inter-device is not negligible. It is mainly dependent on the variability of the top-down fabrication process which did not result in perfectly equivalent structures. In addition, the measurement set-up, is not trivial. As already discussed for the case of SiNW-FETs (Section 4.4.4), the electrical characterization is done in a probe station where the electrical contact of the probe needles to the source and drain contacts of the device is made manually, and thus can slightly differ from one NW to the other. Finally, also the biofunctionalization process can introduce some degrees of variability when the area of device to modify is not perfectly flat but rough and non-homogeneous as cause of aggressive etching processes.

The environment conditions can affect the acquisition, too [95]. All the characterization is

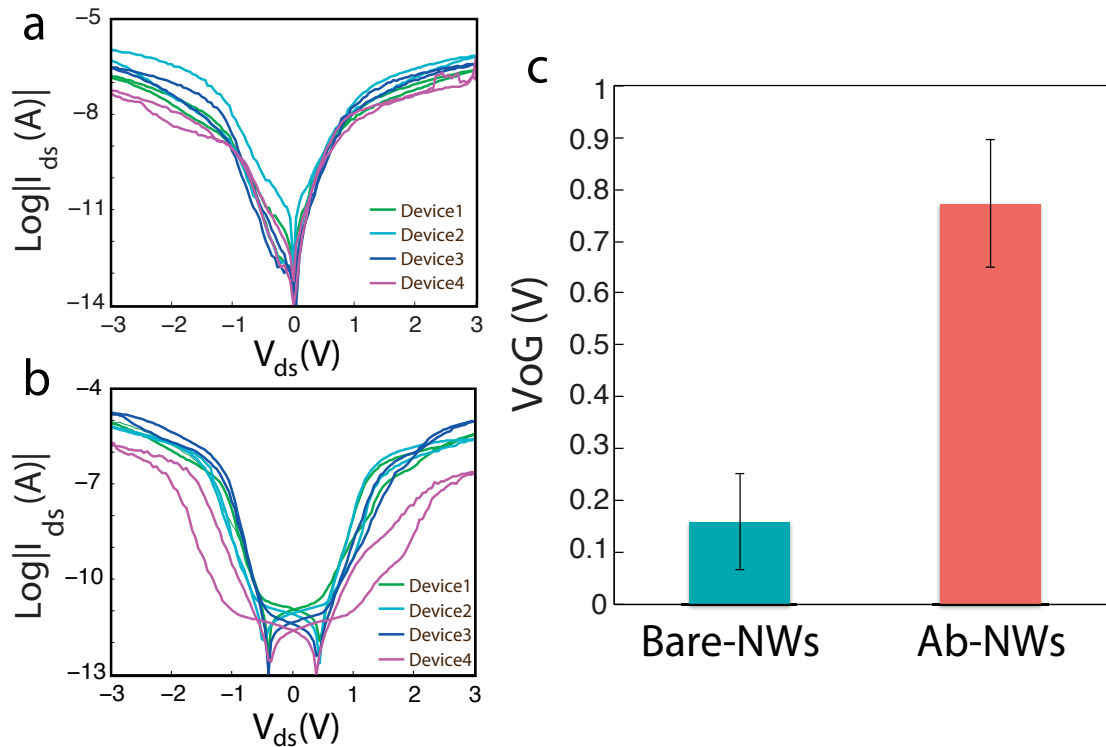


Figure 5.4 – Reproducibility of the VoG parameter. (a,b)  $I_{ds} - V_{ds}$  characteristics acquired on 4 of the tested devices to show the appearance of the voltage gap after antibody modification. (c) Statistics on the complete set of VoG-biosensors. Reprinted from [150].

carried out while monitoring the surrounding rH and temperature conditions, but we observed that the voltage value at which forward and backward curves cross the zero-point current is not null, and defines a non-pinned hysteresis. In our case the memristive effect is mostly due to the nano-scale dimensions of the device and its modification to surface charge trapping processes (see Chapter 6) that are strongly affected by any charged molecules found in proximity of the nanowire surface. Specifically, water molecule adsorption from the humid surrounding environment onto bare SiNWs can also contribute to this effect (see Section 5.3.1), leading to an increased of the VoG in bare NWs.

### 5.3 The VoG-based sensing

The VoG-sensing is based on the modification of the memristive effects in SiNWs. In this thesis, we had the opportunity to use the well developed SiNW-FET biosensing technology as benchmarking for the investigation of memristive-biosensors. With both technologies, we performed similar experiments, in dry conditions, under the same induced varying conditions of the surrounding environment. The effect of voltage memory formation and variation as effect of external charges coming from ions or biomolecules, was never observed in SiNW-FETs that, instead, only revealed variations in terms of wire conductance and current maxima (see



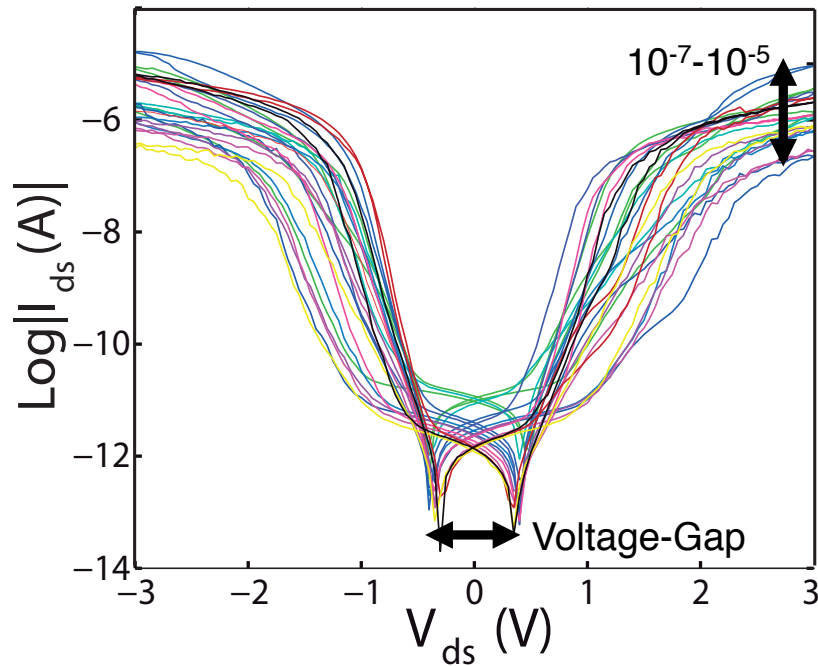


Figura 5.5 – Superimposed semi-logarithmic  $I_{ds} - V_{ds}$  characteristics acquired on memristive SiNWs after anti-VEGF Ab-functionalization. It shows scarce reproducibility of the current, and very high repeatability of the voltage gap parameter.

Chapter 4). On the other hand, memristive nanowires functionalized with a biolayer of antibodies showed not always consistent and non-repeatable variations of the current maxima, but a very high reproducibility in terms of voltage gap. This behavior is well represented in Figure 5.5. Here, the  $I_{ds} - V_{ds}$  curves demonstrate a very high current inter-device variability, as highlighted by the values in the y-coordinate that differ for almost two orders of magnitude. Unlike the current data, the difference in voltage between the current minima is very reproducible. As already shown also in the previous section, the VoG encodes very well the presence of biomolecules all-around the nanowire.

These observations demonstrate that the memristive hysteresis in nanowires is a necessary condition for biosensing, as it has never been observed in the SiNW-FET technology. It is associated with the nano-scale size of the nanowires, much smaller in the case of memristive devices, and surface state trapping deriving from surface roughness and defects in memristive-biosensors (Chapter 6). Moreover, the voltage-gap is a valid parameter for reliable biodetection and provides a valid alternative for the realization of novel biosensors.

In the following sections we show the potentials for high-sensitive biomarker detection based on the VoG by presenting all the results relative to sensing with the novel memristive-biosensors.

### 5.3.1 Humidity measurement

As briefly mentioned above, the current properties of biomodified nanowire samples can be strongly affected by the environment conditions, in particular the humidity [95]. Silicon nanowire shows in itself a relevant dependence on humidity [151, 152]. In fact, due to the large surface-to-volume ratio, nanowires present a large amount of hydroxyl groups (OH) that enable the adsorption of water molecules. This makes the surface highly hydrophilic, determining the high sensitivity to humidity. Although the sensing has been designed to be performed in dry conditions, it has been noted that also dried organic samples are affected by water molecules adsorbed from humid environment [153].

#### Experimental procedure

In order to study the effect of water molecules on the hysteretic current and, more specifically, on the voltage gap, nanowire biosensors were tested under different conditions of ambient relative humidity. Before testing them, the devices were gently dried under a nitrogen flow, and loaded inside a sealed measurement chamber for about 20 minutes in order to get steady equilibrium condition. A sensor recording the chamber humidity was positioned inside the chamber. A wet towel introduced inside the measurement chamber allowed us to raise the humidity; whereas, silica gel or saturated salt solutions were employed to reduce the chamber rH. When the humidity reached a stable value, the  $I_{ds} - V_{ds}$  characteristics were acquired from one device at one time.

In order to investigate the effect of the air relative humidity, repeated acquisitions were performed on same nanowires but at increasing rH. For this aim, memristive SiNWs belonging to the same wafer die were tested just after the fabrication process, and after their modification with anti-VEGF antibody. Due to the large statistical error affecting current measurements, a clear analysis of the modifications in the hysteresis current peaks as function of the humidity could not be achieved. Instead, we observed that the changes in the voltage gap follow a well reproducible behavior in devices characterized by same functionalization and same dimensions.

#### Results

In Figure 5.6 we present the effect of humidity on the voltage gap relative to the two cases of nanowires measured before and after functionalization with anti-VEGF antibodies. The voltage gap was measured on 20 identical wires, before and after the biofunctionalization, in three different humidity conditions. The control of the humidity during the acquisition was not trivial. Because of that, the curve acquisition from same memristive devices, before and after the functionalization, could not be performed exactly at the same rH values, but similar humidity windows were taken into account. Specifically, bare NWs were tested at  $41.1 \pm 0.2$  %rH,  $45.7 \pm 0.3$  %rH and  $57.9 \pm 0.4$  %rH; the same ones but with biomodified surface at  $30.2 \pm 0.1$  %rH,  $45.5 \pm 0.1$  %rH and  $59.5 \pm 0.2$  %rH. The data were acquired at an average temperature

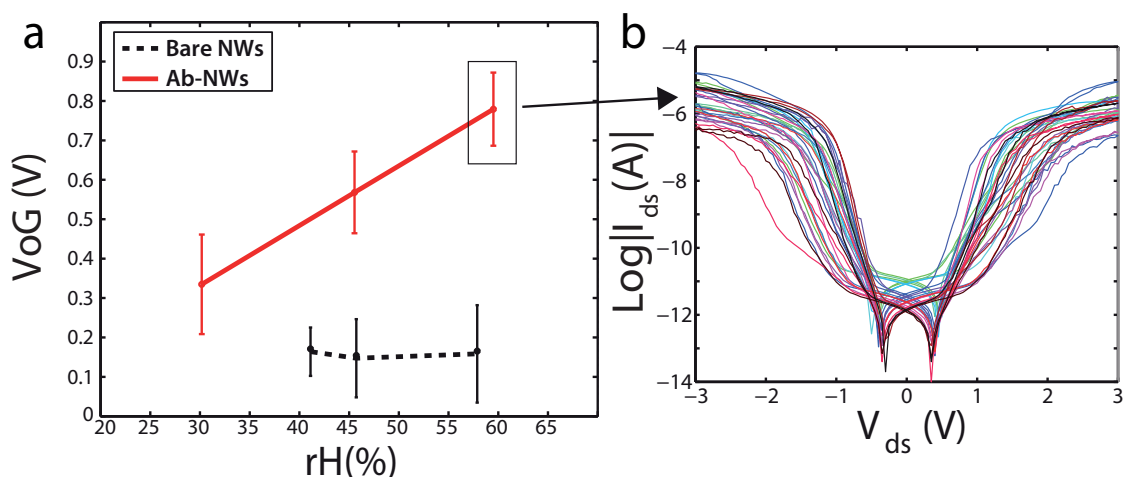


Figure 5.6 – (a) Effect of the humidity on the VoG parameter. Calculated average voltage gap as function of the humidity in bare biosensors (black dashed line) and biomodified ones (red solid line). (b) Reproducibility of the VoG measurement at fixed humidity of  $59.5 \pm 0.2$  %rH. 20 memristive-biosensors have been tested. Images adapted from [102].

of 23 °C. Each voltage gap point in Figure 5.6 was calculated as the mean value obtained from the  $I_{ds} - V_{ds}$  curve registered from the 20 devices under same relative humidity condition.

The first important observation concerns the different behavior expressed by nanowires with and without surface biomodification. If we compare data related to the memristive effect before (black dashed line) and after anti-VEGF functionalization of the same wires (red solid line), we can easily see that the minima voltage gap is roughly constant in the case of bare devices, and very close to zero. The constant, quasi-zero behavior shows the stability of our biosensor prior to any modification in the surrounding humid environment.

We also note that the reported data show a certain degree of inter-device variability. The error bars of Figure 5.6 define the standard deviation calculated on the 20 devices, before and after the surface modification, respectively; each of them was tested under a fixed humidity. The revealed variability can be attributed to defects easily insertable with fabrication processes not fully repeatable, or to non homogeneous distribution of biological species in functionalized nanowires. A slight change induced by humidity variations is also consistent with the well known theory of silicon dangling bonds on raw silicon surfaces [154, 155]. Because these pending Si-OH chemical groups enable weak interactions with molecules present in the surrounding air environment, they can lead to a changing response time and hysteresis curve [152]. Despite the analyzed variability, most of the wires behaved the same way when tested at fixed humidity conditions, as confirmed by the superimposed characteristics reported in Figure 5.6(b). Here, 20 devices were tested under a relative humidity of  $59.5 \pm 0.2$  %. The reported data can be considered as an important evidence of the good reproducibility of our memristive biosensor. Finally, and more importantly, each device of Figure 5.6(b) shows a clear voltage gap between the forward and backward current minima of the hysteresis, demonstrating the presence of a biomolecular layer on the wire surface. As represented by the graph in (a), the voltage

gap fluctuations when varying the humidity conditions clearly appear strongly amplified for antibody-modified nanowires. At a biochemical level, anti-human VEGF antibody is a protein containing -S, O and -N terminal groups that can create bonds with water molecules. N—O and S—H interactions are known to be much stronger than the ones existing between Si and -OH groups, and can be one of the main reasons explaining how the detection parameter, the voltage gap, differs between the two cases. Furthermore, looking at the minima voltage gap acquired from the  $I_{ds} - V_{ds}$  characteristics of functionalized NWs, the changing voltage gap is clearly following a steep increasing behavior. In particular, the red line in Figure 5.6(a) demonstrates that the voltage gap in anti-VEGF modified nanowires linearly increases as function of the humidity within the investigated range. This phenomenon agrees with the finding that organic film can adsorb water molecules from the surrounding humid environment [153], resulting in an increased modification of the charge distribution at the silicon nanowire surface when a potential is applied.

### 5.3.2 In-air measurement of ions in liquid-like thin films

Extensive literature exists so far on the effect of pH (detection of  $H^+$ ) and different ions, on SiNW-FET based biosensors (Section 1.2.1). These data concern the variations of conductivity of the FET wire channel in liquid solutions of different pH, or ionic concentrations. No one has ever investigated what happens when the detection is performed in dry conditions, in surrounding humid air, like in the approach we propose. Moreover, to the best of our knowledge, no data has been published yet on the effect of inorganic ions on the hysteretic characteristic of a memristive device, neither.

In this section we discuss the effect of ionic concentration on the voltage gap, as further proof of ionic interactions occurring at the nanowire surface, thanks to the formation of a liquid-like thin film at the nanowire/air interface that creates the conditions for ions mobility [156].

### Experimental procedure

First, to understand the effect of the ions on memristive sensors in air, electrical measurements were acquired on several devices after subsequent incubations in saline solution with different ionic concentrations. All measurements were performed on dried samples after incubation. The pH of a starting 150 mM NaCl solution was moved towards either bigger or smaller values by adding small volumes of base or acid solutes. NaOH was used as base and HCl as acid. The pH was monitored with a pH-meter (pH-phenomenal pH Lab Set pH1000L by VWR) before use. The memristive NWs were incubated for 1 hour, at room temperature, in the prepared solution, by depositing a drop of NaCl onto the devices. When exposed to room temperature, the device dried and was then loaded inside a measurement chamber where it was left for about 15 min in order to get steady equilibrium condition. Then, electrical characterization was performed to study the hysteresis in function of ion concentration, in terms of voltage gap calculated between the forward and backward current minima of the  $V_{ds}$  curves. For analyzing the trend of variation of the voltage gap parameter, a second experiment was

carried out by exposing the surface of the nanowires to ammonia solution. Ammonia 25% in H<sub>2</sub>O was used for the incubation; as in the case reported above, the measurements were acquired in air when the solution has been dried.

Electrical acquisition was performed with the use of a Karl Suss PM8 Manual Probe Station and an Agilent B1500A Semiconductor Device Analyzer. Source-to-drain characteristics were registered at a fixed back-gate potential  $V_{bg} = 0$  V, while double sweeping  $V_{ds}$  between  $-5$  and  $+5$  V. The voltage gap was calculated as voltage difference between the forward and backward current minima of the  $V_{ds}$  curves. The electrical measures were performed at room temperature, and the humidity of the chamber was controlled and kept constant at 47 %rH during the acquisition.

## Results

Figure 5.7(a) reports the mean behavior of the voltage gap as function of increasing pH. In particular, each point represents the mean of the voltage gaps calculated from the hysteretic curves acquired on five SiNWs 420 nm long and  $35 \pm 10$  nm wide. The error bars in the graph stand for the standard deviation related to the measurements of 5 different devices. The wires behave very similarly when measured singularly, i.e. the voltage gap clearly shows an increase as effect of net charges from ions dissolved in the solution of incubation. Figure 5.7(b) shows an example of hysteresis in the  $I_{ds} - V_{ds}$  characteristic calculated from one memristive NW of the tested set; it was measured just following the fabrication process (dashed blue line) and then after its exposure to NaCl solution at pH 12 and subsequent drying (solid red line). Noticeably, the nanowire is behaving as a quasi pure memristive system before the incubation, with quasi zero voltage gap of  $0.1 \pm 0.08$  V. The voltage memory increases by contacting the sensor with an electrolytic medium (dashed line). Specifically, the voltage gap increases a little compared to the starting condition of bare nanowires, as indicated by the central point of the calibration curve registered at pH 6.2; it then features a larger increase for high pH (pH=12), and a small decrease when reducing the pH to 3. The clear modification of the hysteresis, with forming and varying voltage gaps occurring upon exposure to ionic solutions, demonstrates that this behavior is related to the concentrations of ions “released” from the starting solution and charging the SiNW surface. These charges happen to change the electrical properties of the memristive sensors in a predictable way. This behavior was also confirmed by testing bigger NWs having a length of  $1 \mu\text{m}$  and a diameter of  $90 \pm 9$  nm.

We associate the dependence of the hysteretic voltage gap on pH to the compensation/decompensation of charges at the nanowire surface through surface states recombination/generation processes in the native oxide of the device. The hypothesis of charging phenomena at the nanowire surface was confirmed via physical modeling of our voltage gap based sensor, as will be discussed in detail in Chapter 6. According to this hypothesis, and observing the graph of Figure 5.7(a), some of the ions from the solution charge the surface traps at high pH, and when the pH drops down, the decompensation diminishes as if it was due to disappearance of the excess of this ionic species. In ideal conditions, according to the Gouy–Chapman–Stern model, protons should be the only ionic species that approaches the native oxide at the nanowire

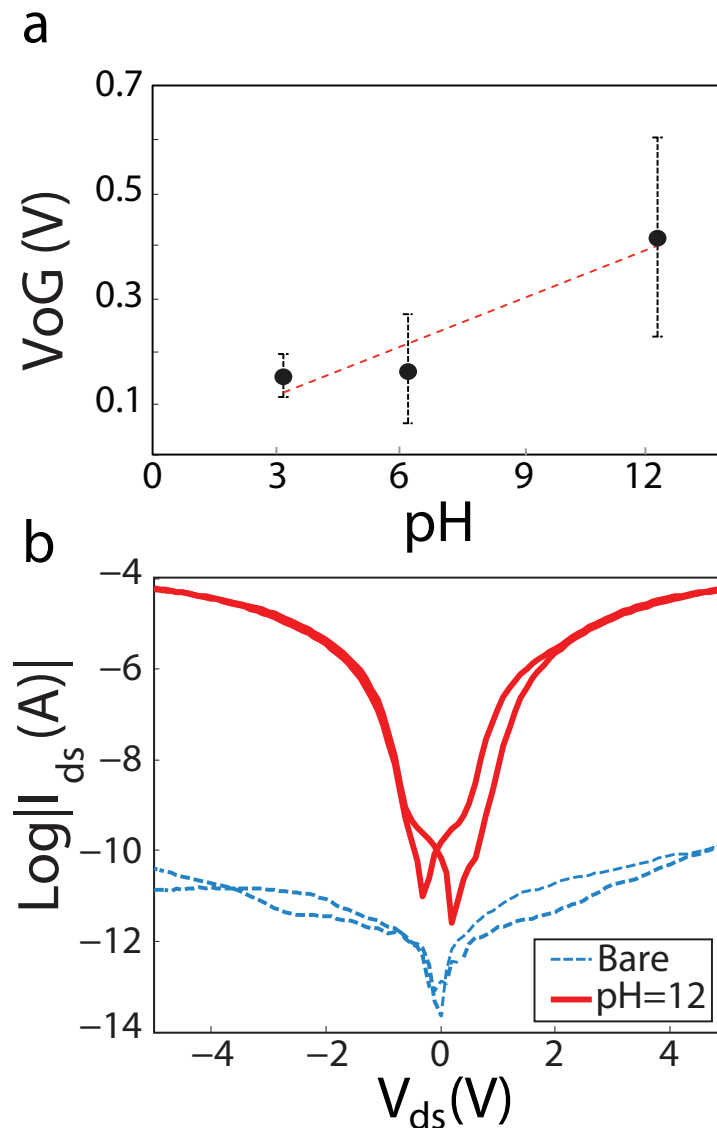


Figure 5.7 – Effects of pH on the voltage gap parameter. (a) Average VoG behavior of 5 devices as a function of increasing pH. (b) Semi-logarithmic  $I_{ds} - V_{ds}$  curves of one of the tested devices showing the increased VoG at high pH (red line) with respect to the bare case. The variations of the voltage gap is dependent also on the balance of  $\text{Na}^+$  and  $\text{Cl}^-$  ions in the prepared NaCl solution as discussed in the text and further explained in Chapter 6. Images adapted from [103]

surface, due to the dimensions that make them small enough and poorly hydrated by water molecules [157], unlike the ions of other dissolved species (NaCl). This means, that the hysteretic behavior should change only according to variations of  $\text{H}^+$  concentration, and not the ones relative to other ions. In our experiment, the high molarity of the NaCl solution, and thus, the concentration of  $\text{Na}^+$  and  $\text{Cl}^-$  ions in solution, could largely contribute to the modification of

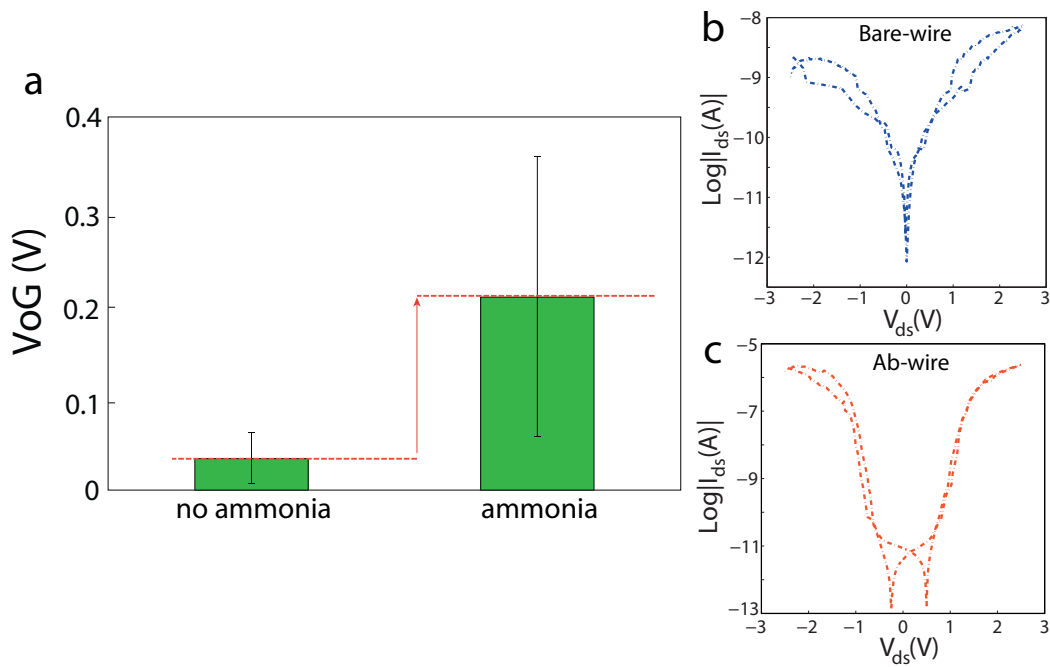


Figure 5.8 – Effects of ammonium ions ( $\text{NH}_4^+$ ) on the voltage gap (VoG). Positive ions in the formed liquid-like thin film determine a voltage memory in the device as effect of surface states charging phenomena.

the voltage gap in memristive sensor, affecting the surface trapping mechanism. In particular, sodium ions, in the different pH conditions, seem to have most of the effect on the voltage gap modification, showing a presumable better affinity of surface states in the native oxide for this ionic species compared to the other ions.

More importantly, we observed variations of the  $I_{ds} - V_{ds}$  as effect of detected changes in ionic concentration with measurements performed in air, after everything was dried; by comparison with traditional sensing in liquid with ISFET based technologies, one would not expect to observe such result. Indeed, a liquid-like thin film is formed at the nanowire surface [156], thus creating the conditions for the interface phenomena to take place. Two main factors confirm this observation. The first one is related to the sensitivity of SiNWs to the environment humidity, as already discussed in Section 5.3.1. Nanowire and nanotube field effect transistors lying on a  $\text{SiO}_2$  surface exposed to the ambient environment show hysteresis due to the charge trapping by water molecules existing all around [102, 158, 159]. Secondly, water adsorption also occurs on dried salt clusters [160] and organic layers [153], as well as on our device, due to the drying of highly concentrated NaCl solution. Thus, a water film is adsorbed on the surface of the nanowire, and the resulting aqueous environment enables the dissolution of the salt, and the movement of the ions towards the hydroxyl groups of the native oxide at the nanowire surface [156].

In Figure 5.8, we report the statistic performed on 11 memristive SiNWs after the fabrication process on bare surfaces (left column), and after their incubation, for 1 hour at room tempe-

perature, in a solution of ammonia 25% (right column). Thermal and plasma annealing with high concentration of ammonia has been demonstrated a good strategy for passivation of oxide surfaces, for example in the annealing of 4H-silicon carbide metal-oxide-semiconductor capacitors [161]. In our case, we demonstrate that the thin-liquid film condition formed at the nanowire surface after drying a solution of ammonia induces an increase of the voltage memory in the memristive characteristic of our device, thus revealing charging effects of some defects at the interface. The excess of charges comes from ammonium ions ( $\text{NH}_4^+$ ) released from the solution, and free to move in the film of water that passively adsorbed on the SiNW surface. This charging effect is demonstrated by the increased voltage gap that was measured on a set of device (Figure 5.8) after incubation in ammonia. The registered mean value of the voltage gap is illustrated in the histogram of Figure 5.8(a); the error bars stand for the standard deviation of the statistic on 11 wires and report a large error due to the geometrical variability of the tested nanowires. Despite the measured variability, it is evident the enhanced memory effect expressed by the increased voltage gap. We report also the  $I_{\text{ds}} - V_{\text{ds}}$  characteristic of one of the analyzed device for better showing the lost pinched hysteresis loop as effect of ammonium ions (a,b). A complete interpretation of this phenomenon will be again discussed in Chapter 6, and compared with the case of Na ions mobility in varying pH environments. The charging effect from biomolecules reported in the following sections will be discussed as well.

### 5.3.3 VEGF detection in PBS

We demonstrate in this section that the fabricated memristive SiNWs enable the detection of cancer markers diluted in buffer solution in the extremely low concentration range 0 to 10 fM. The results point out the potential for the development of ultra-high sensitivity detection system. fM detection in liquid has been already demonstrated by different groups, but never in an ultra-high resolution range as the one possible here thanks to the proposed paradigm based on the voltage gap and the measurement in air. In the following sections we describe, the experimental set-up and the most relevant results we collected.

#### Experimental procedure

Sensing experiments were carried out using a Signatone H-100 Probe Station and a Keithley 6430 Sub-Femtoamp SourceMeter, in direct current (DC) regime with drain-source  $I_{\text{ds}} - V_{\text{ds}}$  being swept in the range  $-3$  V to  $+3$  V, and voltage step of 50 mV. The back-gate was fixed at  $V_{\text{bg}} = 0$  V.  $I_{\text{ds}} - V_{\text{ds}}$  characteristics were acquired while constantly monitoring the environment condition, at room temperature and 55 % of relative humidity in order to maximize the voltage-gap. The fabricated memristive devices were functionalized with anti-VEGF antibodies, according to the procedure used for SiNW-FETs, and described in detail in Chapter 3. The sensing experiments were performed following the same procedure already discussed in Section 4.2.1, exposing the biosensors to different concentration of specific growth factor antigen. The dilutions were performed in ideal condition, i.e. a buffer solution. After incuba-



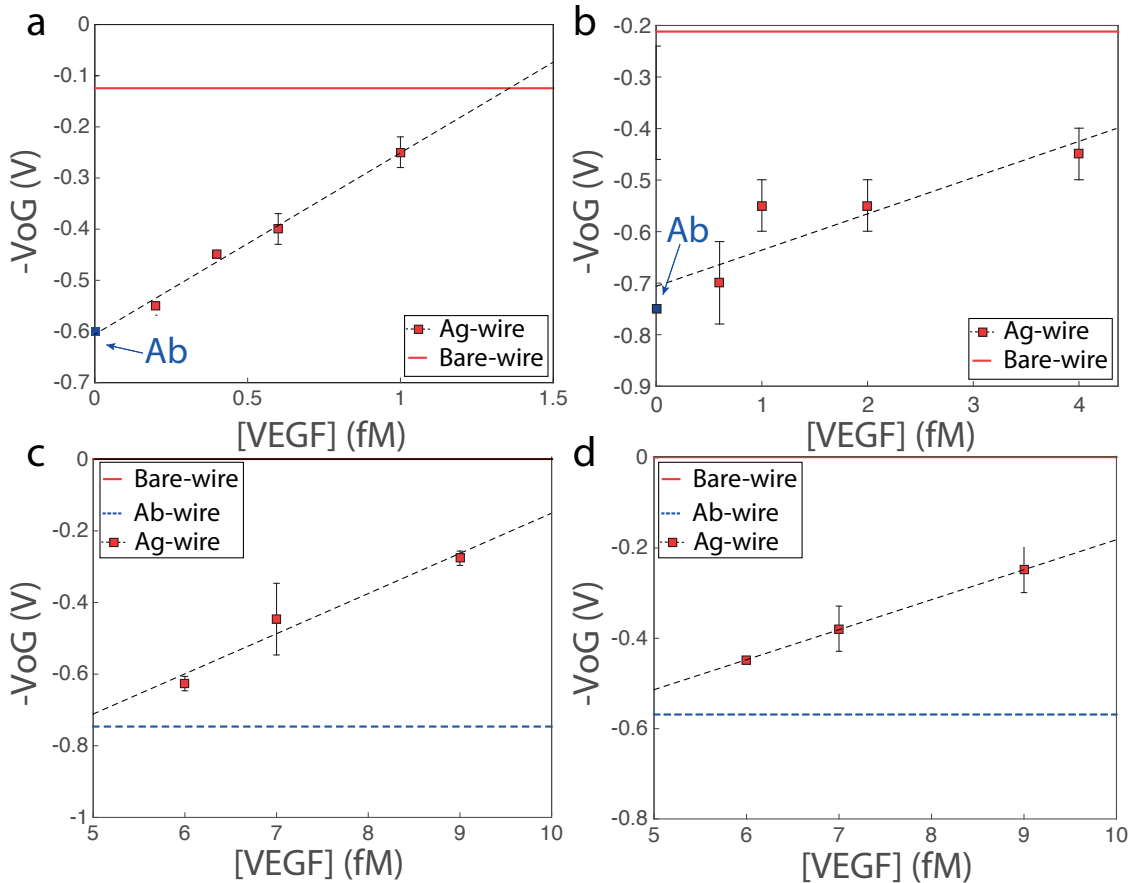


Figure 5.9 – Calibration curves for VEGF sensing with VoG-biosensors. (a,b) Biosensors with 420 nm long and  $35 \pm 10$  nm wide SiNWs; (c,d) biosensors with  $1 \mu\text{m}$  long and  $90 \pm 9$  nm wide wire channel. All the graphs confirm proper biomodification with anti-VEGF (blue point in (a,b) and blue line in (c,d)) with reduced value with respect to the bare case (red line), and detection of occurring Ab-Ag binding (decreasing VoG). The sensing is demonstrated by the quasi-linear behavior of the voltage gap as effects of increasing concentrations of Ag.

tion, the SiNW sensors were removed from solution, gently dried under  $\text{N}_2$  flow, loaded in the characterization tool and measured in dry conditions.

## Results

Figure 5.9(a-d) show examples of acquired calibration curves for the detection of VEGF molecules through implementation of the voltage gap approach. (a) and (b) report the case of two nanowires 420 nm long and  $35 \pm 10$  nm wide; (c) and (d) VoG-based sensing with SiNWs  $1 \mu\text{m}$  long and  $90 \pm 9$  nm wide. The error bars stand for the standard deviation of multiple measures with the same sensor. In all graph, data confirm the successful immobilization of antibody on the nanowire surface, as demonstrated by the lost pinched hysteresis loop, registered in bare devices (red line in the plot), upon bio-functionalization of the device (blue

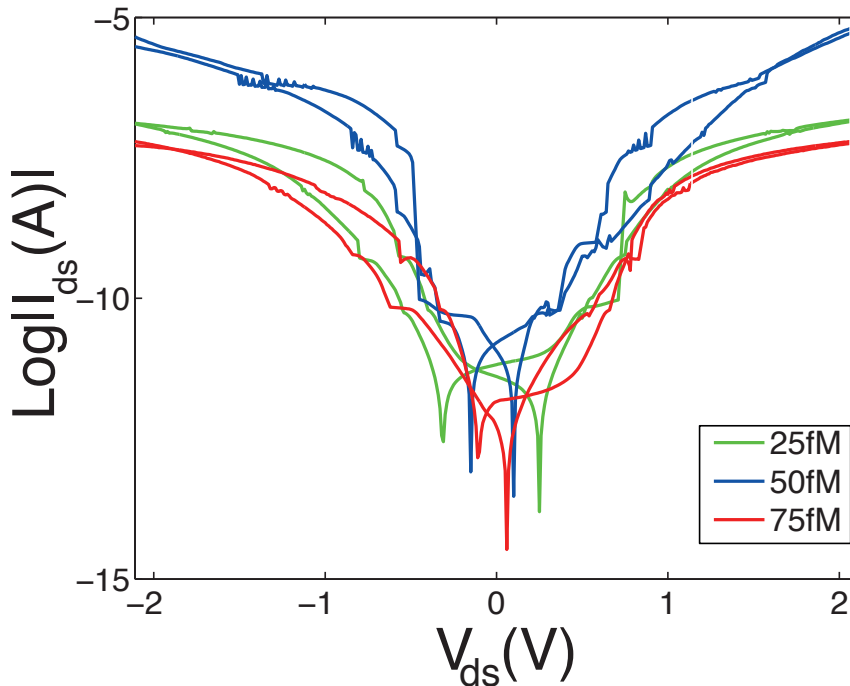


Figure 5.10 –  $I_{ds} - V_{ds}$  characteristic, in the semi-logarithmic scale for a VoG-biosensor incubated in different solutions of rabbit antigen in tumor extract, with concentration 25 fM (green line), 50fM (blue line) and 75fM (red line). Shrinking of the voltage gap as effect of charge compensation from antigen uptake.

points in (a,b) and blue line in (b,c)). The created electric field induces a voltage gap effect appearing as the voltage difference between the current minima for backward and forward regimes. The memristive-biosensors were then incubated in different solutions of VEGF, in a femtomolar range. Data reveal occurring femto-molar detection of VEGF antigen: the voltage gap is reduced with respect to the Ab-functionalized case in all the presented examples, and then decreases as a linear function of increasing uptaken VEGF molecules, thus confirming previous results of rabbit antigen detection [95], and further reducing the detection limit.

#### 5.3.4 Detection of anti-rabbit in breast tumor extract

Here we collect experimental data showing that the novel sensing method based on the voltage gap has the potential to overcome the main limitations in SiNW-FET based sensors of low sensitivity in real human samples, thanks to both the reduced variability of the VoG parameter and the enhanced sensitivity due to the protocol of measurement in air aiming at increasing the Debye screening length. In particular, we demonstrate that we are able to sense pM concentrations of rabbit antigen exogenously added in tumor extract prepared from breast tumor biopsies from patients with fabricated and biomodified memristive structures.

#### Experimental procedure

The experimentation with tumor extract was performed in the wet laboratory of LSI, EPFL. Here, we carefully prepared the dilutions of antigen in extract from breast tumor tissue, obtained from mechanical disruption of a pool of human biopsies diluted in biological solution until reaching a final concentration of 1 mg/ml. The specific rabbit antigen is spiked in the tumor extract using 100.000 fold molar excess of nonspecific tumor proteins. Electrical characterization is performed in air to check the proper functionalization, before and after the different incubations to acquire the voltage gap modification as a function of antigen amount. As for SiNW-FETs, an accurate protocol of washing was employed to maximize the specificity of the sensor surface by removing all the non specific material. All the details relative to the experimental set-up for sensing in tumor samples have been already reported in Section 4.4.1.

#### Results

Figure 5.10 reports the semi-logarithmic  $I_{ds} - V_{ds}$  characteristic of one of the tested biosensors. The three curves, green, blue, and red, are related to three different concentrations of rabbit antigen in tumor extract, 25 fM, 50fM and 75fM, respectively. As clearly demonstrated by the plot, antigen binding determines a shrinking of the voltage gap. The same is demonstrated by the calibration curve in Figure 5.11, obtained by averaging the electrical behavior of different biosensors at increasing concentration of rabbit antigen in tumor extract. Each point in the curve is the voltage gap mean value, and the error bars stand for the standard deviation of the voltage-gap acquisitions from three similar devices under same exposure conditions. The error inter-device is pretty large, thus indicating the need for a larger statistics. It derives mostly from variability of fabrication and biofunctionalization processes, leading to structures with diameter and surface properties slightly different with respect to each other, and thus, different Ab-Ag interactions. Nonetheless, if the single wire is considered, a well defined decreasing behavior of the voltage difference between forward and backward current minima can be observed, as in the case of Figure 5.11. More importantly, with this experiment, we demonstrated that memristive devices, functionalized with specific antibodies, enables the detection of occurring Ab-Ag binding phenomena also in the very hostile tumor landscape. Although the sensitivity of the sensors is reduced, as result of the large amount of nonspecific tumor proteins in the extract, the resolution achieved with the voltage gap (order of pM) is very promising, thus opening the way to the development of this paradigm for more accurate studies of the breast tumor micro-environment.

The repeatable trend of the voltage gap observed in biomodified memristive nanowires when exposed to biomarkers is mainly associated to the surface properties of our devices where surface states behave as charging sites and determine the memory expressed in the voltage gap. Because of the presence of these sites, upcoming charged molecules (or ions) from the surrounding environment induces charge compensation, as it is well illustrated by the increasing trend of the voltage-gap in biofunctionalized wires then contrasted by a decrease upon uptake of molecules with opposite charge.

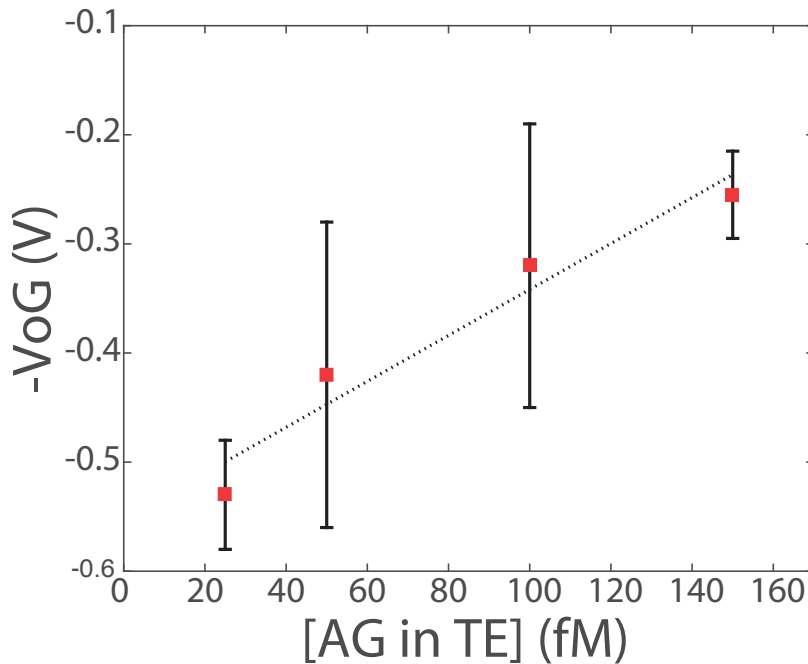


Figure 5.11 – Calibration curve for sensing of rabbit antigen. Average behavior of multiple VoG-biosensors. The target molecules were specifically uptaken on the antibody sites from the starting tumor extract solution, then measured in-air. Error bars stand for the standard deviation of the measurement on different devices.

## 5.4 Chapter summary and contributions

In this chapter, we introduced the novel concept of the voltage-gap approach by presenting the background of the discovery. Then, we examined the suitability of the fabricated in-air memristive-biosensor in different types of experiments.

We started showing the possibility of sensing inorganic ions with measurements in air. We observed that the detection of pH is linked to the varying equilibrium of the ionic species from NaCl solutions, and is expressed as increase of the voltage gap at high pH, and decrease at low pH. More important, these data were acquired in dry conditions. The existence of varying hysteresis properties upon deposition and drying of an electrolyte on top of the device, reveals the formation of a liquid-like thin film at the device surface that enables the interface phenomena leading to ionic mobility, interface phenomena and thus, sensing. We also tested the effect of positive ammonium ions on memristive silicon nanowires, showing the increased memory of the device (voltage gap) as result of surface interactions between the ions in the formed thin film of water and the native oxide surface traps.

Next, we presented the application of the voltage gap based paradigm to biosensing. First, we showed the easier case of detection of cancer markers (vascular growth factors) in the ideal PBS environment, demonstrating that the novel approach enabled us to achieve ultra-high sensitivity of VEGF, thanks to the specificity of the functionalization process, the resolution

of the voltage gap parameter, and the idea of measuring in air to reduce the Debye screening from ions typically big in bulk solution. The data showed a decreasing behavior of the voltage gap as a function of uptaken proteins. Finally, we showed, first time with this approach, same successful results in the more complex breast tumor extract, where rabbit antigen species were diluted using 100.000 fold molar excess of nonspecific tumor proteins. Again the biosensors featured a decrease of the voltage gap parameter when incubated in increasing antigen concentrations.

The sensing results collected in this chapter define the voltage-gap based sensing in memristive silicon nanowires as valid alternative to SiNW-FETs for biosensing applications and show promising potential for the specific detection of angiogenic and inflammatory ligands in the human tumor tissue.



## 6 Modeling the VoG-biosensing

As discussed in Chapter 5, despite available data show the achievement of high-specific and sensitive biosensing with the voltage-gap (VoG) approach, a deeper theoretical study is still missing. In this chapter we propose a physics-based compact model that describes very well the occurrence of the voltage-gap in bio-modified Schottky barrier SiNWs, and links this effect to the interaction of charged species with the surface of the wires. Thanks to this model, we can also propose an accurate physical interpretation of the voltage gap based sensing presented in Chapter 5 through explanation of complex interactions of surface traps with ionic or biomolecular species.

### 6.1 Introduction

As described in detail in Chapter 2, the memristive nanowires are obtained via top-down approach techniques based on chemically-assisted etching processes, such as DRIEs (Section 2.3.4), which are very aggressive and typically result in surface roughness and silicon surface defects [162]. Surface defects are usually associated with dangling bonds defined by missing Si crystal atoms at the surface that leave unsaturated bonds behind them, as schematically presented in Figure 6.1 [155]. These unsaturated bonds at the surface give rise to allowed energy states within the forbidden energy gap that are referred to as *surface states* [154].

Hysteresis in the electrical characteristic of nano-electronic devices, such as CNTs [159, 163, 164] or SiNWs [158, 165], is one of the first indications of the presence of surface traps. Schottky barrier SiNWs with controlled hysteretic features have been used for high-sensitive detection of biomolecules after their functionalization with antibodies (Chapter 5). These biosensors display a complex electrical behavior that is the result of the particular nano-scale structure of the device. The experimental data demonstrate that the hysteretic behavior of the sensor is strongly dependent on the variation of the surrounding environment, such as the temperature [78], the humidity (Section 5.3.1), the charges from dissolved ions in solution (Section 5.3.2), and the functionalization with biomolecules (Section 5.3.3 and 5.3.4). These observations suggest that the VoG-sensing is strictly linked to the presence of dangling bonds on the device surface. In particular, they show that the voltage-gap is related to phenomena of

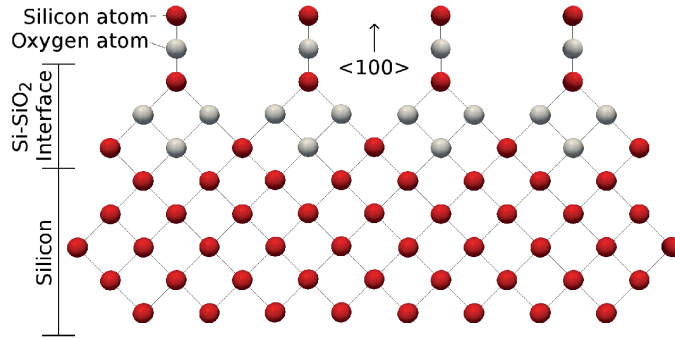


Figura 6.1 – At the silicon surface silicon atoms are missing and unpaired valence electrons exist forming electrically active interface traps.

charge imbalance at the surface where charge traps continuously change their state if solicited by an external bias and modified through exposure of the surface dangling bonds to different concentrations of biomarkers.

## 6.2 Model

### 6.2.1 Equivalent circuit

We can model the biosensor as a combination of multiple interacting transport mechanisms: *i*) the transport through the surface states ( $I_{drift}^{ox}$ ,  $I_{diff}^{ox}$ ), *ii*) the transport in the bulk of the SiNW ( $I_{drift}^{NW}$ ,  $I_{diff}^{NW}$ ), and *iii*) the transport at the Schottky junctions ( $I_{SB1}$ ,  $I_{SB2}$ ). Each of them is represented by a different circuit element in the equivalent circuit sketched in Figure 6.2.

As presented in Section 2.3, the fabricated structures are characterized by a p-doped nano-scale channel of approximately 35nm with surface roughness and defects resulting from the DRIEs process. Surface defects can give rise to energetically-active surface states continuously distributed in energy within the silicon band-gap [154, 166, 167]. Their charge state is Fermi-level dependent [168], thus defining the amphoteric nature of the surface traps. Depending on the position of the semiconductor Fermi level with respect to the charge neutrality level (namely the level at which surface charges are compensated by the bulk doping atoms), the surface states can act either as electron acceptors or electron donors, being associated with either *acceptor-like* or *donor-like* energy levels, respectively [169].

Figure 6.3 illustrates a possible schematic model of the surface of a SiNW with native oxide and surface trap centers where surface state recombination occurs.

All transport mechanisms related to the conductivity of the nanowire at the surface can be subdivided into drift and diffusion components [42, 170, 171]. We describe in detail each of them, separately.



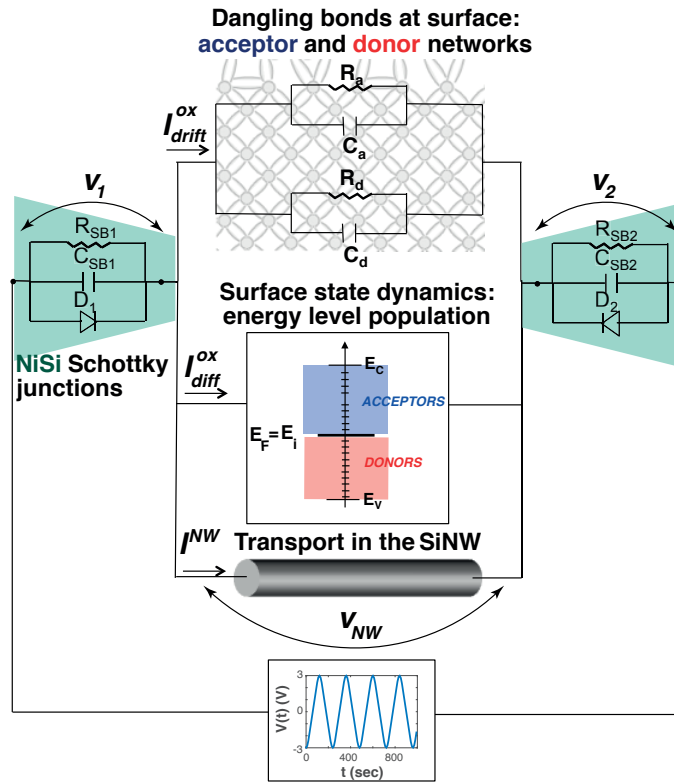


Figure 6.2 – Equivalent circuit representing the multiple transport mechanisms in SiNW. Reprinted from [104].

## 6.2.2 Inter- and intra-band hopping through surface states

### Drift component from surface states

The drift component of donor-like and acceptor-like surface trap centers can be described by resistor-capacitor (RC) networks [171] acting independently when a voltage is applied across them (Figure 6.2). The overall effect arising from the activity at the acceptor (donor) sites is reduced to an equivalent resistance  $R_a$  ( $R_d$ ) in parallel to an equivalent capacitance  $C_a$  ( $C_d$ ). In first approximation and for short wires, the electrical capacitances of acceptor and donor RC networks can be assumed proportional to the amount of negatively charged acceptors  $n_a$ , and positively charged donors  $n_d$ , respectively, because they act as parallel capacitances associated with their respective charges. If  $n_a(t)$ ,  $n_d(t)$  and  $n_n(t)$  denote the time dependent amount of acceptor-like (negatively charged), donor-like (positively charged) and neutral traps, respectively, the total amount of charge states  $N_0$  can be expressed as:

$$N_0 = n_a(t) + n_d(t) + n_n(t) \quad (6.1)$$

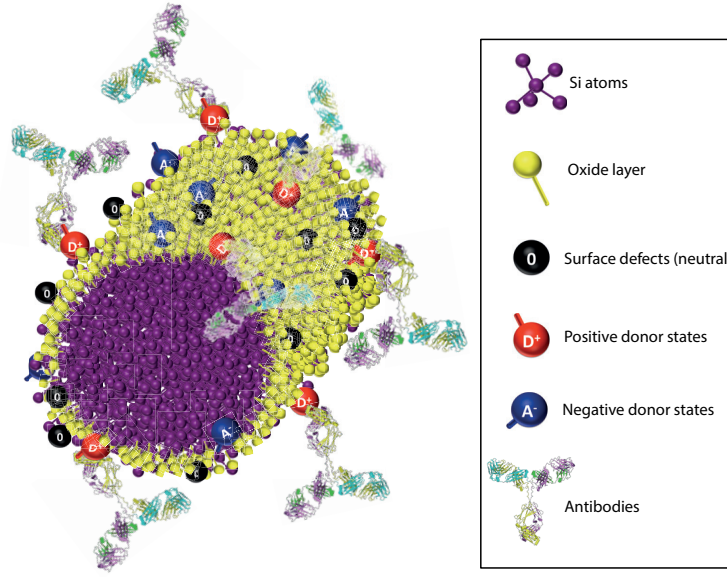


Figura 6.3 – Sketch of the formation/recombination of energetic surface levels. Neutral (black spheres), acceptor-like (blues spheres) and donor-like (red spheres) states are from surface defects. Charging phenomena at the surface take place via binding of charged species such as antibodies. Reprinted from [104].

Therefore, the various capacitances can be defined as:

$$C_{\alpha} = \tilde{C}_{\alpha} \frac{n_{\alpha}(t)}{N_0} \quad (6.2)$$

where  $\alpha = a, d$  (acceptor, donor) and  $\tilde{C}_{\alpha}$  is the overall capacitance of the trap systems, and the initial condition for the  $n_{\alpha}$  are discussed in Section 6.4. The equivalent resistances of surface charged centers,  $R_{\alpha}$ , with  $\alpha = a, d$  can be estimated by means of the Einstein relation [172], and expressed as:

$$R_{\alpha} = \left[ \frac{q n_{\alpha} \mu_{\alpha}}{L} A e^{\frac{\Delta E}{k_B T}} \right]^{-1} \quad (6.3)$$

where  $q$  is the electric charge of a particle,  $\mu_{\alpha}$  stands for the electrical mobilities of the charged traps,  $A$  is the transport area,  $k_B$  is the Boltzmann constant,  $T$  the absolute temperature, and  $\Delta E$  the free energy change for surface traps to vary their states [172].

Using relations (6.2) and (6.3), the drift surface current  $I_{drift}^{ox}$ , driven by the external voltage bias  $V(t)$  and due to the impedance of the resistor-capacitor network, is created by the hopping of charges from one surface trap to another and reads:

$$I_{drift}^{ox}(t) = \frac{R_a + R_d}{R_a R_d} V_{NW}(t) + \frac{d}{dt} [(C_a + C_d) V_{NW}], \quad (6.4)$$

where  $V_{NW}$  is the voltage drop across the nanowire channel (see figure 6.2).

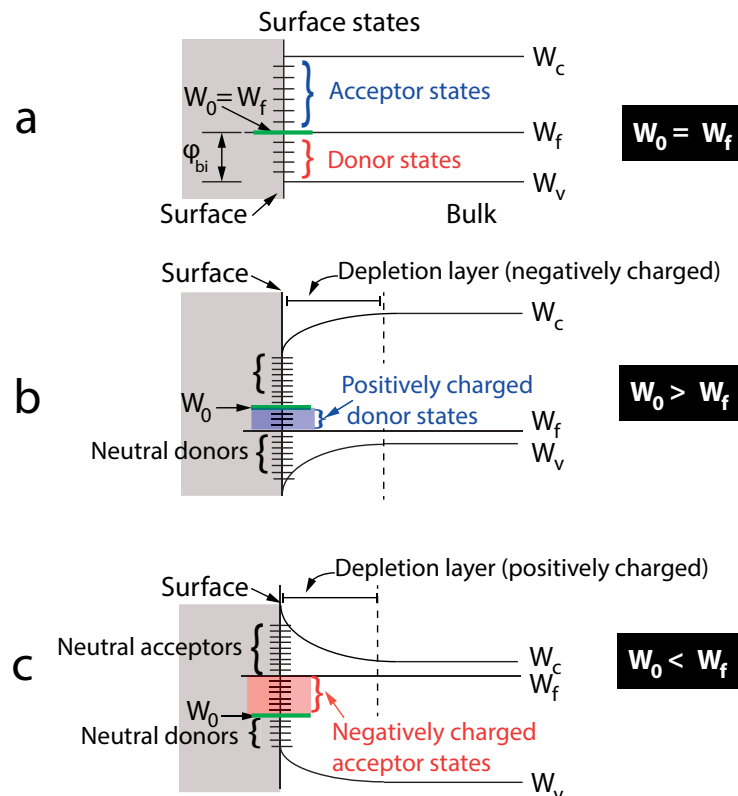


Figura 6.4 – Energy band diagram showing acceptor and donor type surface states and their distribution in the band gap at the surface of the semiconductor. a) The situation when the doping concentration is such that the Fermi level  $W_F$  coincides with the neutral level  $W_0$ . b) The situation where the semiconductor is p-type and a positive net surface charge is created because of unoccupied donor surface states. c) The situation where the semiconductor is n-type and a negative net surface charge is created because of occupied acceptor surface states. Reprinted from [167].

### 6.2.3 Diffusion on surface states: traps energy level population

#### Theory of surface states

In the band energy diagram of a silicon semiconductor, donor surface states lie below the charge neutrality level  $W_0$  and acceptor surface states lie above  $W_0$  [154, 166]. The charge neutrality level  $W_0$  is the energy level associated to a surface state net charge  $Q_{SS}$  fully compensated by the opposite space charge  $Q_{SC}$  inside the semiconductor.

The band energy diagrams in Figure 6.4 schematically describe the change of states of the surface charge traps. The donor surface states are those states that lie below the *charge neutrality level*  $W_0$ , and acceptor surface states the ones that lie above  $W_0$ . When the semiconductor is intrinsic, hence the Fermi level  $E_F$  equals the intrinsic energy state of the material  $E_i$ , the charge neutrality level coincides with the Fermi level  $W_0 = E_F$  (Figure 6.4(a)). In this condition all the donors levels, below  $W_0$ , are occupied and therefore are neutral. Similarly, all the

acceptor levels, above  $W_0$ , are not occupied and hence are neutral. In this condition, the net charge at the surface  $Q_{SS}$  is zero. When  $W_F$  lies below  $W_0$  (Figure 6.4(b)), as in the case of a p-type semiconductor, all the acceptor states are unoccupied and neutral. On the contrary, part of the donor states hold a positive net charge because they lie between  $W_0$  and  $W_F$  and hence are unoccupied by electrons. As a result, the surface states possess a net positive charge density. When  $W_F$  is higher than  $W_0$  (Figure 6.4(c)), as in an n-type semiconductor, all the donor states are unoccupied and neutral, while there is a certain fraction of the acceptor states that have negative net charge because they lie between  $W_F$  and  $W_0$  and hence are occupied by electrons. As a result, the surface states possess a net negative charge density.

In both cases (a) and (b) indicated in Figure 6.4, band bending at the surface occurs as a direct result of the formation of a depletion or accumulation region filled by the bulk majority carriers in the semiconductor that compensate the surface net charge [173].

### **Diffusion components from surface states**

The second contribution to the surface current is given by the diffusion current  $I_{diff}^{ox}$ . The diffusion process is due to the concentration gradient of charged surface states, and it is governed by the equation [104]:

$$I_{diff}^{ox} = e \left( -f_a \frac{dn_a(t)}{dt} + f_d \frac{dn_d(t)}{dt} \right), \quad (6.5)$$

where  $f_a$  and  $f_d$  are self-similarity parameters to be fitted to the experimental data and  $e$  is the electron charge. Eq. 6.5 results from the current continuity equation, and follows the approximation described in [171] and also discussed here below. To determine the form of the diffusion current  $I_{diff}^{ox}$  in Eq. 6.5, we assume that the gradient of the charge density causes a current of diffusion. The concentration of charged surface states at position  $x$  at a particular time  $t$  is denoted as  $n_a(x, t)$  and  $n_d(x, t)$ . Owing to the charge accumulation, the current flowing through the surface of the left electrode [ $I_{diff}^{ox}(x=0, t)$ ] into the SiNW is different from that flowing through the surface of the right electrode [ $I_{diff}^{ox}(x=L, t)$ ] out of the wire. Considering the continuity equation, the diffusion currents at the left and right surface of the electrodes satisfy the following equation:

$$I_{diff}^{ox}(x=L, t) - I_{diff}^{ox}(x=0, t) = e \frac{\partial}{\partial t} N(t) \quad (6.6)$$

where  $N(t)$  is the total number of charged surface traps at the SiNW surface, defined as:

$$N(t) = \int_0^L n(x, t) dx \quad (6.7)$$

and  $I_{diff}^{ox}$  is the diffusion current at position  $x$  and time  $t$ :

$$I_{diff}^{ox}(x, t) = eD \frac{\partial}{\partial t} n(x, t) \quad (6.8)$$

It is assumed that  $I_{diff}^{ox}(t)$  and  $I_{diff}^{ox}$  are different but self-similar as a function of time such that:

$$I_{diff}^{ox}(t) = I_{diff}^{ox}(x=0, t) = c I_{diff}^{ox}(x=L, t) \quad (6.9)$$

where  $c$  is a constant of the order of 1. Considering the distinct contributions of acceptors and donors, and as a direct result of Eq. 6.8, the current  $I_{diff}^{ox}$  in Eq. 6.5 is

$$I_{diff}^{ox}(t) = -f_a e \frac{\partial}{\partial t} n_a(t) + f_d e \frac{\partial}{\partial t} n_d(t) \quad (6.10)$$

where  $f_a = 1/(1 - c_a)$  and  $f_d = 1/(1 - c_d)$  are two parameters to be fitted to the experimental data, and are much larger than 1.

Assuming that acceptor-like and donor-like states have independent dynamics, at low frequency we can approximate the recombination/generation rate of the surface traps  $n_a(t)$  and  $n_d(t)$  as linear function of the surface state densities:

$$\frac{dn_\alpha}{dt} = -k_\alpha^\alpha(V_{NW})n_\alpha + k_n^\alpha(V_{NW})n_n \quad (6.11)$$

where  $\alpha = a, d$  and  $k_d^d$ ,  $k_a^a$  and  $k_n^\alpha$  denote the charge acceptor, donor and neutral rate constants, respectively. The first term on the right hand side (r.h.s.) of Eq. (6.11) represents the inter-band hopping of charge species  $\alpha$  from its band to the neutral band (state recombination), while the second term represents the reverse process (state formation). The rate constants are estimated using the modified Arrhenius rate equations [171]:

$$k_\alpha^\alpha(V_{NW}) = k_{\alpha 0}^\alpha e^{\frac{-\beta_\alpha(E_\beta^\alpha - eV_{NW})}{\sigma T}}, \quad k_n^\alpha(V_{NW}) = k_{n 0}^\alpha e^{\frac{(1-\beta_\alpha)(E_\beta^\alpha - eV_{NW})}{\sigma T}} \quad (6.12)$$

with  $k_{a 0}^a$ ,  $k_{n 0}^a$  and  $k_{d 0}^d$ ,  $k_{n 0}^d$  the rate constants of acceptor and donor traps in their charged or neutral state, respectively, applicable when  $V(t) = 0$ . Moreover, the  $k_{\beta, 0}^\alpha$  are not independent among them and their dependence is discussed in Section 6.4.  $V_{NW}$  is the potential applied at the NW, and  $E_\beta^\alpha$  are the average energies for the inter-band formation/recombination processes determined from the continuum to discrete energy band approximation that is schematically reported in Figure 6.5 and explained in the following. The diffusion current in the oxide  $I_{diff}^{surf}$  (Eq. 6.5), modeling the dynamic variation of the surface state energies, also depends on the energy levels (Eq. 6.12) that are estimated by considering the energy band theory of surface states in Silicon. The surface states are distributed in a continuum of energies in the Silicon band-gap (Figure 6.5a). Considering the discretization of the surface

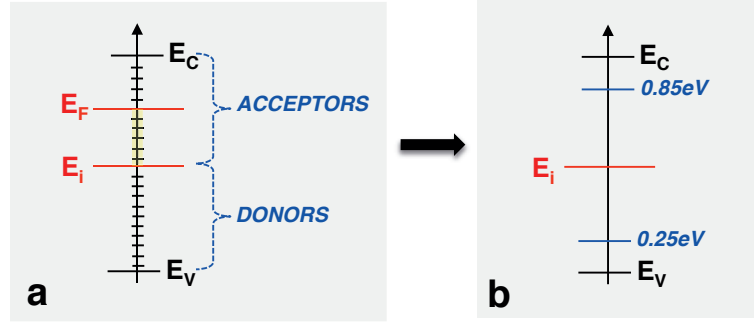


Figura 6.5 – The approximated energy band diagram of silicon surface states. a) Surface state energy levels as continuum in the silicon band gap. b) Approximated view of surface trap energies as discrete energy levels.

trap energies (Figure 6.5b), an approximation is used to define the average energy necessary for acceptors to hop from the negative to the neutral states ( $E_a^a$ ) and vice versa ( $E_n^a$ ), and for donors to hop from the positive to the neutral states ( $E_d^d$ ) and vice versa ( $E_n^d$ ).  $\beta_a$  and  $\beta_d$  represent the symmetrization factors;  $\sigma$  describes the response of the rate constants to the external voltage due to multiple scatterings.

#### 6.2.4 Electronic transport in the bulk of a SiNW

##### Drift

The drift component  $I_{drift}^{NW}$  of the total current flowing inside the NW can be expressed as a function of the wire resistance  $R_{Si}$  and voltage drop  $V_{NW}$  across it:

$$I_{drift}^{NW} = \frac{V_{NW}}{R_{Si}} \quad (6.13)$$

where  $R_{Si}$  is estimated as  $\rho_{p-si} \frac{L}{A}$ , with  $\rho_{p-si}$  the resistivity of low ( $10^{15} cm^{-3}$ ) Boron doped silicon ( $5M\Omega cm$ ),  $L$  and  $A$  the length and the cross section of the wire, respectively.

##### Diffusion

The diffusion component  $I_{diff}^{NW}$  depends on the concentration gradient of the net charge into the nanowire. In this case, we can estimate the total net charge in the bulk as the sum of the net charges  $Q_1$  and  $Q_2$  at the depletion regions induced by the Schottky contacts. Using again the approximation from the continuity law of Eq. 6.8, the diffusion current in the wire can be estimated as:

$$I_{diff}^{NW} = -f_s \frac{d(Q_1 + Q_2)}{dt} \quad (6.14)$$

with  $f_s$  a self-similarity coefficient resulting from the continuity equation approximation. The net charges  $Q_1$  and  $Q_2$  can be evaluated using the standard expression for depletion region net charge [42]:

$$Q_j = -SN_d w_{dj} \quad (6.15)$$

where  $j = 1, 2$ ,  $S$  is the section area of the junctions and  $N_d$  the number of ionized donors of the p-type SiNW.  $w_{d1}$  and  $w_{d2}$  are the thicknesses of the left and right depletion regions formed by the Schottky junctions at the source and drain terminals and can be estimated as [42]:

$$w_{dj} = \sqrt{2\epsilon_0\epsilon_s(\phi_{bi} - v_j)/qN_d} \quad (6.16)$$

with  $\phi_{bi}$  the built-in potential of the NiSi/Si junction, and  $V_1$  and  $V_2$  the voltage across the left and right Schottky barriers, respectively.

### 6.2.5 Electrical phenomena at the junctions

#### Modeling the NiSi Schottky barrier

The last factor affecting the electrical behavior of the VoG-biosensor is the metal-semiconductor interface. The NiSi Schottky barriers can be modeled as different elements in parallel (Figure 6.2): the resistance  $R_{SB1}$  ( $R_{SB2}$ ), capacitance  $C_{SB1}$  ( $C_{SB2}$ ), and the diode  $D1$  ( $D2$ ) define the left (right) NiSi Schottky barrier of the nanowire. From the equivalent circuit, it derives that the current flowing through the left and right Schottky barriers is expressed as:

$$I_{SBj} = C_{SBj} \frac{dv_j}{dt} + \frac{v_j}{R_{SBj}} + I_{Sj} (e^{\frac{qv_j}{k_B T}} - 1) \quad (6.17)$$

with  $j = 1, 2$ , and  $v_j = V_1, V_2$  the potentials applied at the Schottky junctions.  $I_{S1}$  and  $I_{S2}$  are the saturation currents of the left and right diodes and are defined by [170]:

$$I_{Sj} = A^{**} T^2 S \exp[-q\phi_{bi}/k_B T] \quad (6.18)$$

with  $A^{**}$  the Richardson's constant and  $\phi_{bi}$  the built-in potential of the NiSi/Si junction. The resistances of the Schottky diodes  $R_{SB1}$  and  $R_{SB2}$  can be estimated by the contact-resistance relationship [42]:

$$R_c = \frac{k_B}{A^{**} T q} e^{[q\phi_{bi}/k_B T]} \quad (6.19)$$

## Capitolo 6. Modeling the VoG-biosensing

---

The Schottky diode capacitances  $C_{SB1}$  and  $C_{SB2}$  are expressed by the diode capacitance-voltage relationship [174]:

$$C_j = C_{j0}(1 - v_j/\phi_{bi})^{-\gamma} \quad (6.20)$$

where  $C_{j0}$  is the zero-bias junction capacitance and  $\gamma$  is a parameter representing the doping profile of the active junction layer ( $\gamma = 0.5$  for a uniformly doped junction layer). The zero-bias junction capacitance is:

$$C_{j0} = S\epsilon_0\epsilon_r/w_d \quad (6.21)$$

where  $\epsilon_0$  and  $\epsilon_s$  are the vacuum dielectric constant and the relative permittivity of the silicon, respectively,  $S$  is the section area of the junctions, and  $w_d$  the thickness of the depletion region.

### Barrier lowering: the effect of surface defects at the junctions

Dopant atoms introduced in semiconductors are known to have the effect of varying the effective barrier height in a given metal-semiconductor contact [42, 170]. Surface charges have a similar effect on the junctions of our device and induce a Schottky barrier lowering  $\phi_{bi} - \Delta\phi_{bi}$ . The image-force lowering, also known as the Schottky effect or Schottky-barrier lowering, is the image-force-induced lowering of the barrier energy for charge carrier emission, in the presence of an electric field. The charge carriers in our case are represented by the charges related to the surface distribution of acceptor and donor trap states. The barrier lowering is estimated by considering the image-force lowering theory [42]:

$$\Delta\phi_{bi} = \frac{q^3 n_s \psi_s}{8\pi^2 (\epsilon_r \epsilon_0)^3} \quad (6.22)$$

where  $n_s$  is the charge volume density given by the sum of the net surface charge volume density  $\frac{n_d - n_a}{Volume}$  and the bulk doping atoms  $N_d$ , and  $\psi_s$  the surface potential. The barrier lowering affects the Schottky barriers by changing the saturation currents with two terms related to the different effects of positive (donors) and negative (acceptors) mobile charge carriers at the Schottky barriers: positive carriers see a barrier height  $\phi_{bi} - \Delta\phi_{bi}$ , while negative carriers see a barrier  $E_{Si,gap} - \phi_{bi} - \Delta\phi_{bi}$  where  $E_{Si,gap}$  is the Silicon energy band-gap. The diode saturation currents  $I_{S,j}$  thus result in the following expression:

$$I_{S,j} = A^{**} T^2 S \left( e^{-\frac{q(\phi_{bi} - \Delta\phi_{bi})}{k_B T}} + e^{-\frac{q(E_{Si,gap} - \phi_{bi} + \Delta\phi_{bi})}{k_B T}} \right) \quad (6.23)$$

where  $A^{**}$  is the Richardson's constant,  $T$  is the absolute temperature,  $k_B T$  the Boltzman constant,  $S$  the junction section area,  $e$  the electron charge,  $\phi_{bi}$  the built-in potential of the NiSi/Si junction,  $\Delta\phi_{bi}$  the barrier lowering, and  $E_{Si,gap}$  the Silicon energy band-gap.



### 6.3 Model implementation

By combining all the analytical formulation reported in the previous section, the circuit of Figure 6.2 can be solved for a varying external voltage. The phenomena at the silicon nanowire surface, in the bulk, and at the Schottky barriers can be expressed by a system of differential equations in the four variables  $V_1(t)$  (potential at left Schottky junction),  $V_2(t)$  (potential at right Schottky junction),  $n_a(t)$  (amount of negatively charged acceptors), and  $n_d(t)$  (amount of positively charged donors). This system of equations describes the dynamic interaction of the nano-device with the incoming molecules, and its solution defines the current-voltage relation enabling the comparison with the electrical characteristics acquired during the experiments. The analytical model was implemented in Matlab, and the solution to the equation system was calculated throughout an implicit numerical solver endowed of time-step control programmed ad-hoc for this particular problem.

### 6.4 Steady state conditions

In the steady state, and for zero external bias, we can calculate the initial amount of positively charged donor states  $n_{d,0}$  from the ratio  $n_{d,0}/N_0$ , by approximating the number of filled donor energy levels with the ones belonging to the energy band  $E_i - E_f$  and, on the other hand, the total number of surface states in the semiconductor at regime with the states having energies  $E_c - E_i$ :

$$n_{d,0} = \frac{E_i - E_f}{E_c - E_i} \quad (6.24)$$

where the intrinsic energy level for the Si is taken as  $E_i = E_{gap}^{Si}/2 = 1.12/2$  eV,  $E_c$  is the bottom of the conduction band, and the Fermi level has the expression [42]:

$$E_f = E_i - k_B T \ln(N_d/n_i) \quad (6.25)$$

with  $N_d$  the doping atoms density in the bulk, and  $n_i$  the intrinsic carrier concentration. Moreover, by observing that the initial amount of negatively charged acceptor states in a p-type channel, for zero bias, is  $n_a \ll n_d$ , being  $n_a$  representative of the minority carriers, we can also estimate the ratio of the rate constants:

$$\frac{k_{d,0}^d}{k_{n,0}^d} = \frac{E_i - E_f}{E_c - E_f} = \frac{N_0 - n_{d,0}}{n_{d,0}} \quad (6.26)$$

These conditions guarantee that  $n_{d,0}$  is a good approximation for the mean value of  $n_d$  in the period. If we suppose similar dynamics  $k_{a,0}^a \approx k_{d,0}^d$  for acceptors and donors, it follows that  $k_{a,0}^a \gg k_{n,0}^a$ . The  $k_{\beta}^{\alpha}$  are estimated by considering these constraints and fitted to the experimental data via Monte-Carlo simulations.

## 6.5 Results and discussion

The external bias voltage is swept from -2.5 to +2.5 Volts and, in accordance with the experimental measurements, varies as a piecewise increasing and decreasing linear function with a slope of  $\pm 50\text{mV/sec}$ . The current in the  $I_{ds} - V_{ds}$  characteristic is given by the sum of drift and diffusion components both in the surface native oxide ( $I_{drift}^{ox}, I_{diff}^{ox}$ ) and in the bulk of the nanowire ( $I_{drift}^{NW}, I_{diff}^{NW}$ ), and of the effects at the junctions ( $I_{SB1}, I_{SB2}$ ). The implementation of the system of equations required the estimations of different physical parameters for modeling the different components of the current, as well as the fitting of some of them to the experimental data.

First, we considered the case of bare nano-devices, and we compared a real  $I_{ds} - V_{ds}$  measurement acquired from a SiNW after the fabrication and before any modification with biological material (Figure 6.6a) with a simulated characteristic (Figure 6.6b). As clearly evident from the plots, the simulated curve fits well the experimental one and models the pinched hysteretic behavior (Figure 6.6b). Figure 6.6c illustrates the corresponding components of the total current calculated in the simulation, components that are strictly dependent on each other and that affect the total current with their continuous competition/compensation. In the diagram, both forward and backward branches of the current are shown in order to better demonstrate the similarities between the experimental and modeled curves under external voltage sweep.

The current  $I_{drift}^{ox} + I_{diff}^{ox}$  arises from the dynamic exchange of charges at the surface trap states. The drift current in the surface oxide depends on the capacitances and resistances of the surface states in the oxide.  $C_\alpha$  and  $R_\alpha$  affect the total current because their product is comparable to the time of the system. Their effect varies as a function of the charge density  $n_\alpha$  as a result of their definition (Eq. 6.2 and 6.3). Considering that the mobility of negative carriers, related to the acceptor states, is much higher than the one of positive carriers from donor centers ( $\mu_a \approx 20 - 30 \text{ cm}^2/\text{V}\cdot\text{s}$ ,  $\mu_d \approx 10^{-5} \text{ cm}^2/\text{V}\cdot\text{s}$  in p-doped silicon [175–177]), we observe that only the acceptor component contributes to the drift transport, being  $R_a = 10^3 \text{ M}\Omega$  much smaller than  $R_d = 10^6 \text{ M}\Omega$ , as estimated by Eq. 6.3. However, because of the high resistances of the surface trap networks in bare condition, the diffusion  $I_{diff}^{ox}$  related to the occupation of the acceptor and donor energy levels dominates (over  $I_{drift}^{ox}$ ) the electrical transport at the surface (Figure 6.6c).

The energy level related to the negatively charged acceptor states  $n_a$  is estimated [168] to be  $|E_n^a| = 0.85 \text{ eV}$ , while the ones corresponding to the positively charged donor states  $n_d$  is estimated [168] to be  $|E_n^d| = 0.25 \text{ eV}$ . Consequently, the threshold energy associated with the neutral state is  $|E_a^a| = 0.85 - E_i \text{ eV}$  for acceptors and  $|E_d^d| = E_i - 0.25 \text{ eV}$  for donors, respectively, being  $E_i$  the intrinsic energy level of the semiconductor. The terms  $f_a$  and  $f_d$  in Eq. 6.5 are fitted to the experiments via Monte-Carlo simulations. Both in the bare and bio-modified case they appear to be large ( $f_a = 2.8 \cdot 10^{14}$ ,  $f_d = 3 \cdot 10^{10}$  in the simulation curve of Figure 6.6b). This indicates very small variation between the incoming and outgoing diffusion currents through the left and right surfaces of the SiNW, respectively (see Section III of SI). The diffusion

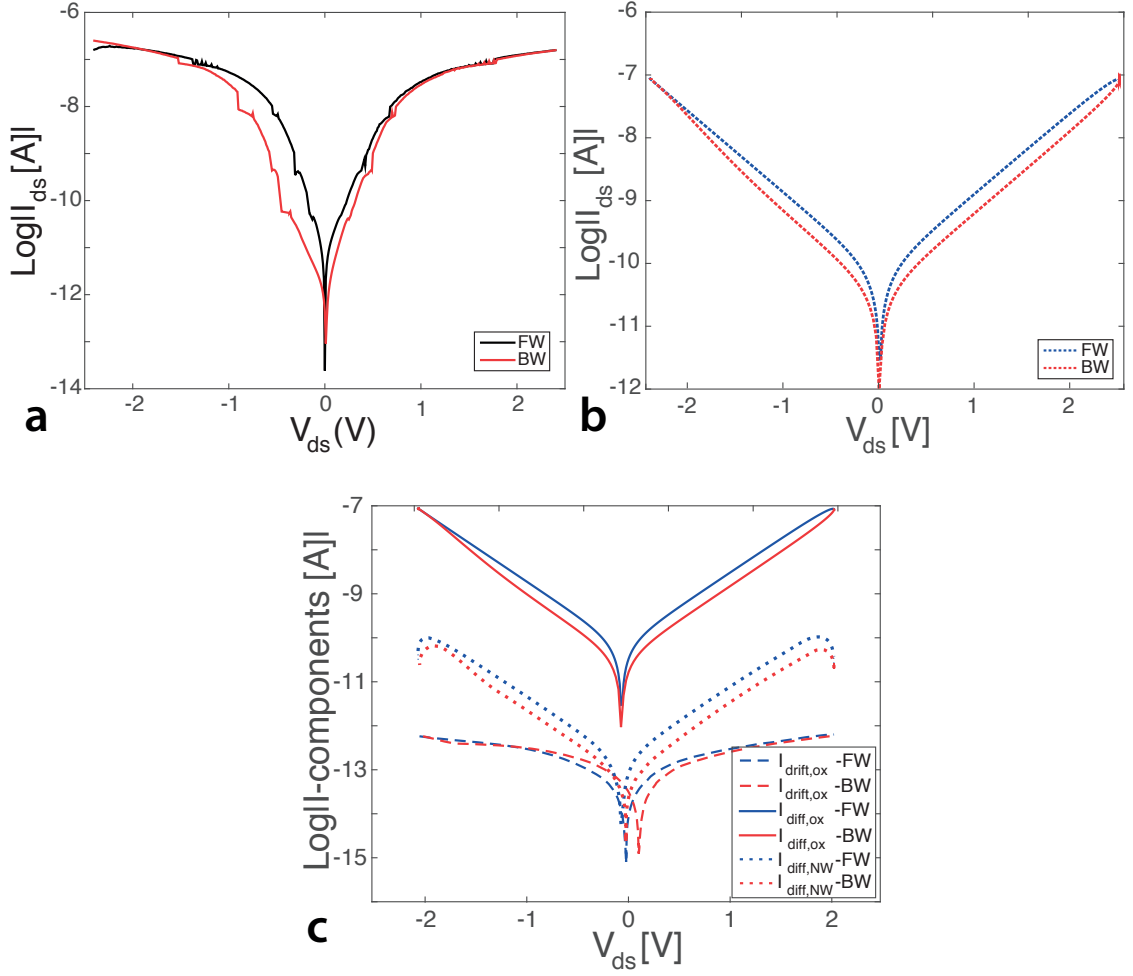


Figure 6.6 – Experimental (a) and simulated (b)  $I_{ds} - V_{ds}$  characteristics of a SiNW before any surface bio-modification. Both curves have pinched hysteresis loop, similar to the hysteresis of memristive-like behavior, and same current peak. Blue and red lines stand for the forward and backward current branches. [The parameters chosen for this simulation are:  $k_{a0}^a = 3.5 \cdot 10^{-4}$  Hz,  $k_{n0}^a = k_{a0}^a / [8.4 \cdot (N_0 - n_{d,0}) / n_{d,0}]$ ,  $k_{n0}^d = 2 \cdot 10^{-4}$  Hz,  $k_{d0}^d = (N_0 - n_{d,0}) / n_{d,0} \cdot k_{n0}^d$ ,  $\tilde{C}_a \sim \tilde{C}_d = 10^{-12}$  F,  $R_a = 10^3$  M $\Omega$ ,  $R_d = 10^6$  M $\Omega$ ,  $\sigma = 6.5$ ,  $\beta_a = \beta_d = 1/2$ ,  $f_a = 2.8 \cdot 10^{14}$ ,  $f_d = 3 \cdot 10^{10}$ ,  $f_s = 2 \cdot 10^{16}$ ,  $\Delta E = 253$  eV,  $n_d / N_0 = 0.01$ ,  $N_0 = 8.5$ ]. Reprinted from [104].

current is plotted with solid line in Figure 6.6c, and as clearly visible in the figure by looking at the amplitude of this component compared to the total curve of Figure 6.6b, it has the most important role in defining the pinched hysteresis loop in bare nanowires.

A further contribution may also come from the electronic transport in the bulk. However, both drift and diffusion currents in the nanowire core seem to be negligible when external charged molecules are absent.  $I_{drift}^{NW}$  is not reported in Figure 6.6c because of its very low amplitude. This is due to the nanowire channel that can be approximated with a fully depleted one as a consequence of the NiSi Schottky barriers at both ends, defining depletion regions with

thickness  $w_{d1} \approx w_{d2} > L/2$ . The depletion in the channel increases the resistance  $R_{Si}$  and makes the drift current of the bulk  $I_{drift}^{NW}$  negligible. Therefore, most of the current contributing to the transport in the SiNW core is given by the diffusion of carriers in the depleted regions (dotted line in Figure 6.6c).

The conductivity both in the SiNW and in the oxide is finally affected by the Schottky barriers (Eq. 6.17), whose height has been estimated to be  $\phi_{bi} \sim 0.45$  V [178]. None or little barrier lowering occurs in the absence of biomolecules. The junctions determine a small voltage drop at the NW contacts that limits the amplitude of the  $I_{ds} - V_{ds}$  characteristics of the device if compared to the bio-modified condition that will be discussed in the following (Figure 6.7). Most importantly, the condition of zero, or very small, voltage-gap is directly related to the null quantity of acceptor states  $n_a$  and the low amount of positively charged donor states  $n_d$  with respect to the total number of surface defects  $N_0$  onto the native oxide of the wire. This value ( $n_d/N_0 = 0.6$ ) demonstrates the balance of charges at the surface of the nanowire (neutral surface states) and the existence of few charged donor states mostly deriving from the doping atoms in the p-type semiconductor.

Figure 6.7 reports the results relative to the case in which the nanowire has been exposed to charged molecules. Again, both forward and backward sweeps are highlighted. In Figure 6.7a, the  $I_{ds} - V_{ds}$  curve acquired from a SiNW functionalized with antibodies, that are positively charged species at physiological pH [179], are plotted. The bio-modification determines the increase of the current peak (two orders of magnitude bigger than the bare case (Figure 6.6)) and, most relevantly, the appearance of a voltage-gap ()efined by the different values acquired by forward and backward curves for zero-current condition. Figure 6.7b shows the plot of the simulated  $I_{ds} - V_{ds}$  curve.

Similarly to the experimental curve, simulations show an increased current peak ( $\sim 10^{-5}$  A) and a voltage-gap of  $\approx 1$  V. The total simulated current in the SiNW is given by the sum of the different contributions (Figure 6.7c) arising from the drift (dashed line) and diffusion (dotted line) current in the surface state network, the diffusion in the nanowire channel (dotted line), and dependent on the effects at the junctions, too. Also in this case,  $I_{drift}^{NW}$  can be neglected because of the fully depleted wire. As shown in Figure 6.7c, the predominant effect is given by the dynamic surface exchange of the energy levels, i.e., the diffusion in the oxide. This component is the result of the competing action of donor and acceptor states described by  $I_{diff,a}^{ox}$  and  $I_{diff,d}^{ox}$ , respectively, in Figure 6.7d. The two currents depend on the constant rates  $k_{\beta}^d$  and  $k_{\beta}^a$  whose values were of the same order of magnitude in the case of pinched-loop hysteresis, i.e., bare devices ( $k_{\alpha,0}^a \sim k_{\alpha,0}^d \approx 10^{-4}$  Hz), but now differ by three to four orders of magnitude one with respect to the other. In particular, the dynamics of the energetic donor levels has increased ( $k_{\alpha,0}^d \approx 2$  Hz), thus demonstrating that biomolecules attached to the NW surface favor the occupation of the donor energy levels. This occurs in combination with the increased amount of negatively charged donor levels  $n_d$ . This can be physically explained by considering the approaching and the binding of positively charged biomolecules, the antibodies, to the surface of the nanowires. In other words, the incoming proteins charge the surface by providing positive charges and determine the occupation of the energetic levels associated with the donor defects. Negatively charged  $n_a$  do not interact with the external

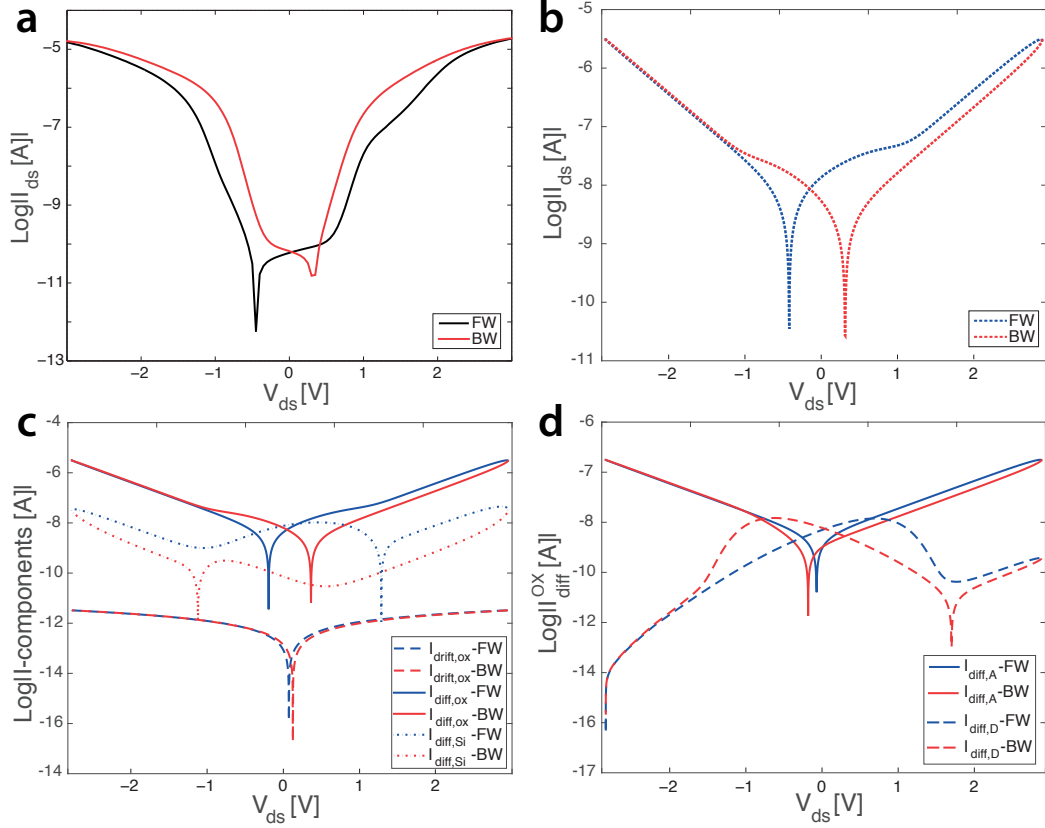


Figure 6.7 – Modeling the voltage-gap. a) Semi-logarithmic  $I_{ds} - V_{ds}$  characteristic from experimental measurements acquired from a fabricated SiNW functionalized with antibodies. The voltage-gap appears as a result of the adsorption of positively charged species onto the nanowire and the interaction with the oxide surface states. b) Simulated total  $I_{ds} - V_{ds}$  curve. c) Components of the characteristic reported in panel b): diffusion current due to the surface states in the oxide (solid line); drift current in the oxide (dashed line); diffusion current in the SiNW (dotted line). d) Individual contributions of acceptor (solid line), and donor (dashed line) states to the diffusive current at the NW surface. [The parameters chosen for this simulation are:  $k_{a0}^a = 3.5 \cdot 10^{-5}$  Hz,  $k_{n0}^a = k_{a0}^a / [14 \cdot (N_0 - n_{d,0}) / n_{d,0}]$ ,  $k_{n0}^d = k_{n0}^{d,BARE} \cdot 10^4$ ,  $k_{d0}^d = (N_0 - n_{d,0}) / n_{d,0} \cdot k_{n0}^d$ ,  $\tilde{C}_a \sim \tilde{C}_d = 10^{-12}$  F,  $\sigma = 6.5$ ,  $\beta_a = \beta_d = 1/2$ ,  $f_a = 2.8 \cdot 10^{14}$ ,  $f_d = 3 \cdot 10^{14}$ ,  $f_s = 2 \cdot 10^{16}$ ,  $\Delta E = 253$  eV,  $n_{d,0} = 0.69$ ,  $N_0 \approx 40$ .] Reprinted from [104].

positive charges and cannot compensate for them, because of their null density at zero bias and in the initial condition of bare surfaces. However, with the adsorption of antibodies, the formed biolayer may lead to the creation of new surface defects. These surface defects can be associated with acceptor energy levels, thus explaining the slowly increasing dynamics exchange for the acceptor-like surface states ( $k_{\beta,0}^{a,BIO} \sim 10^4 \cdot k_{\beta,0}^{a,BARE}$ ). This is also confirmed by the increase of total surface traps  $N_0$  in the curve simulating the VoG change after bio-functionalization ( $N_0^{BIO} \approx 10 \cdot N_0^{BARE}$ ).

The surface trap capacitances  $\tilde{C}_a$  and  $\tilde{C}_d$  increase by two/three orders of magnitude with respect to the simulation of Figure 6.6b, due to the accumulation of a biolayer onto the device

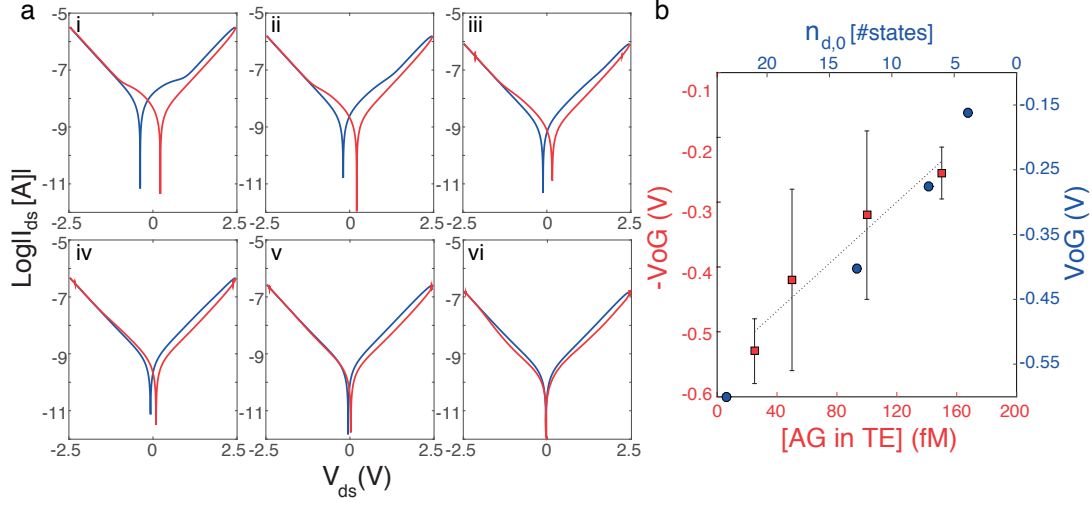


Figure 6.8 – a) Simulated  $I_{ds} - V_{ds}$  characteristics modeling the increasing uptake of antigen molecules onto a bio-modified nanowire. The parameters chosen in these simulations are:  $\sigma = 6.5$ ,  $\beta_a = \beta_d = 1/2$ ,  $\bar{C}_a \sim \bar{C}_d = 10^{-12}$  F,  $\Delta E = 253$  eV,  $f_a = 2.8 \cdot 10^{14}$ ,  $f_d = 3 \cdot 10^{10}$ ,  $f_s = 2.5 \cdot 10^{15}$ . Only some of the parameters in the model vary affecting the hysteresis and the voltage-gap, demonstrating the importance of the charge imbalance induced by the dynamic modification of the surface states. Moving from plot (i) to plot (vi),  $n_{d,0}$  decreases from 0.5 to 0.07,  $N_0$  decreases from 47 to 8.4, and the donor rate constant  $k_{n0}^d$  decreases exponentially from  $k_{n0}^d = 3.5 \cdot 10^4 k_{n0}^{d,BARE}$  (i) to four orders of magnitude smaller in case (vi). b) Reports the variation of VoG as a function of  $n_{d,0}$  (blue axes) and compares it to the calibration data from experiments (Section 5) in breast tumor extract (TE) (red axes). As the antigen concentration increases the positively charged surface states decrease due to charge compensation, thus determining a reduction of the voltage-gap. Reprinted from [104].

surface. However, these capacitances still do not affect in a relevant way the drift current in the oxide because of the low frequency of the biasing signal (order of mHz).

Thanks to the high dependence of the voltage-gap on external charges coming from the surrounding environment, VoG can be used as sensing parameter. As presented in detail in Chapter 5), the sensing is determined by electrical measurement of the voltage-gap decrease from nanowires that have been previously functionalized with antibodies, and successively exposed to increasing concentrations of target species. According to the theory proposed in this chapter, the reduction of VoG in the  $I_{ds} - V_{ds}$  characteristics is related to the charge compensation at the surface of the wire, where surface defects can easily become sites of charge accumulation under external sweeping bias and exposure to proteins. In Figure 6.8 we demonstrate that our theory can quantitatively model this dependence of VoG on the increasing concentration of antigen by correlating it with the formation and recombination of the charged surface states in the oxide of the SiNW.

The subplots in the diagram of Figure 6.8a report, from left to right and from top to bottom, simulated semi-logarithmic curves modeling the fabricated biosensor from the case of zero antigen to the one of uptake of increasing concentrations. According to the surface trap

mediated theory, the reduction of the voltage-gap, combined to the lowering of the current peak, occurs as a result of different varying factors that have been observed from the simulation of the system. In general, they are all related to variation of the surface states amount and their dynamics. Considering a linear variation of the antigen concentration from the case of Figure 6.7, where the NW only carries positively charged antibodies on its surface (0 fM) to the extreme case of antigen concentrations saturating the sensor and determining a reduction of the voltage-gap (Figure 6.8a, case (vi)) back to the starting pinched hysteresis loop (Figure 6.6), the parameter  $n_{d,0}$  decreases from 0.5 to 0.07, the parameter  $N_0$  decreases from 47 to 8.4, and the donor rate constant  $k_{n0}^d$  decreases exponentially from  $k_{n0}^d = 3.5 \cdot 10^4 k_{n0}^{d,BARE}$  (i) to four orders of magnitude smaller in case (vi). The variation of VoG as a function of  $n_{d,0}$  is reported in Figure 6.8b (blue axes) and superimposed to the experimental data (red axes) (Section 5) for comparison. This diagram demonstrates that the simulated results describe well the registered behavior of the voltage-gap in real experiments of antigen sensing in breast tumor extract (TE). It explains the relationship between the sensing parameter and the decreasing amount of positive surface states ( $n_{d,0}$ ) on the wire as effects of increased concentration of antigen and antibody/antigen binding that results in charge compensation.

## 6.6 Physical interpretation of experimental data

At this point, we have all the instruments needed for proposing a complete physical interpretation of the voltage gap based detection in memristive-biosensors. We first consider the case of bare memristive nanowires exposed to varying ionic concentrations, in order to describe the effects of ions on the voltage gap; then, we move to the more interesting electrical behavior observed when the devices are modified with a biomolecular layer and used for antigen detection. The implemented model well fits the experimental data, and also provides fundamental clues for the understanding of the surface interaction phenomena leading to the voltage memory.

### 6.6.1 The effect of ions

In Figure 6.9 we report data related to the effect of ions on the voltage gap. These results have been already presented, from an experimental point of view, in Section 5.3.2. Here, we consider the developed theory to provide their physical interpretation.

In Section 5.3.2 we observed that experiments in highly concentrated NaCl solutions of varying pH associated to modified concentrations of  $\text{Na}^+$  and  $\text{Cl}^-$  led to an increased voltage gap for high pH (pH = 12). As already mentioned, we would expect that protons ( $\text{H}^+$  ions) determine the variation of the voltage gap. Indeed, according to the Gouy–Chapman–Stern theory, this species should be more free to move towards the nanowire surface compare to bigger ions such as  $\text{Na}^+$  and  $\text{Cl}^-$  [157]. If it was so, the implemented model would have predicted a shrinking trend of the voltage gap as a function of the increasing pH, due to the higher

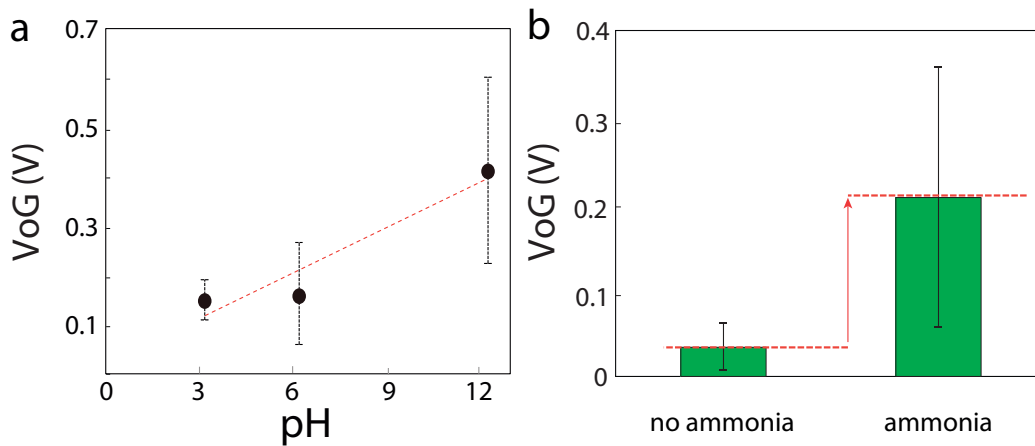


Figure 6.9 – (a) Effects of pH on the voltage gap in NaCl saline solution. (b) Effect of ammonium ions.

concentrations of negative charges deriving from  $\text{OH}^-$  ions (lower amount of  $\text{H}^+$  ions). Thus, we would have found the opposite behavior with respect to the case reported in Figure 6.9(a). Nevertheless, we have to consider that when the molarity of the saline solution is high, things can be more complicated, and the effect of some ions can become dominant in the system, under specific pH conditions. For example, it is known that at very high pH ( $\text{pH} > 10$ ), the concentration of protons in a saline solution can become negligible compared to the highly concentrated Sodium species, thus determining an error in the pH measurement due to the fact that the pH electrode start responding to the increasing amount of  $\text{Na}^+$  and not to the decreasing concentration of  $\text{H}^+$ . This is the so called Sodium error (or alkaline error) in pH sensors [180]. Moreover, we have to note that in the proposed technology, the hysteretic electrical behavior as well as the appearance and modification of the voltage gap are mostly associated to the presence of surface states on a nano-scale surface that is not flat neither passivated by a thick layer of oxide, and interfaces a thin liquid-like film formed by effect of the surrounding environment. This makes our system very different from the one used in the standard ISFET technology. Indeed, the electrical conductivity of the memristive nanowire device is not purely linked to charge accumulation phenomena at the oxide/semiconductor interface, but to the dynamic interactions of charged species in solution with surface traps of the nanowires, where the affinity becomes also an important factor in determining the binding phenomena and, thus, surface state charging.

Consistently with these observations, we can interpret the results reported in Figure 6.9(a) according to the developed theory of compensation/decompensation of charges at the nano-wire surface through surface states recombination/generation processes in the native oxide of the device. Sodium ions have most of the effect on the voltage gap modification, showing a presumable better affinity of surface states in the native oxide for this ionic species compared to the other ions. At high pH, positive  $\text{Na}^+$  ions are in excess with respect both to  $\text{Cl}^-$  and  $\text{H}^+$ ; in these conditions, the voltage gap clearly increases as shown by the mean value registered at  $\text{pH}=12$  (Figure 6.9(a)). As physically demonstrated by our theory, increasing positively



charged donor states at the nanowire surface, generated by binding of external positive species (Sodium in our case) to the donor surface traps, result in an increased value of the voltage gap, compare to the bare (no saline solution) or neutral case (pH=7). Because of these surface interactions, a memory effect in the nanowire, deriving from surface charge unbalance, is now measured when applying a potential at the extremities of the wire. The affinity of Sodium ions is explained both by the lower amount of protons at high pH, and the excess of donor states, initially neutral charged, at the surface of a p-type SiNW. When the pH drops down, the concentration of  $\text{Na}^+$  diminishes, the one of  $\text{Cl}^-$  augments, as well as the amount of protons. The effect is less pronounced in this case as underlined by the smaller difference in the average voltage gap value acquired at pH=6 and pH=3. This further confirms the higher Sodium ions/surface traps binding affinity, and is interpretable as resulting from low compensation phenomena at the surface determined by combined phenomena: disappearance of the excess of Sodium species, increasing concentrations of negatively charged Chlorine ions that compensate the imbalanced surface charge by generating negatively charged acceptor state, and, finally, the increased amount of  $\text{H}^+$  ions that contrast the  $\text{Cl}^-$  effect.

The physical interpretation of the effect of ionic species from dissolved salts in solution would be further strengthened by performing experiments of voltage gap acquisition from nanowires exposed selectively to specific ionic species, one at the time, thanks to the use of ion-selective-membranes. This would, indeed, dissociate the phenomena of surface interactions and facilitate the physical understanding.

As reported in Section 5.3.2(b), we also tested in air the effect of ammonium ions ( $\text{NH}_4^+$ ) released from the solution, and freely moving in the film of water that passively adsorbed on the SiNW surface. The results are consistent with our model. Indeed, when bare devices are exposed to a solution of ammonia 25% in  $\text{H}_2\text{O}$ , positive ions interact and bind to surface donor states thus determining an accumulation of surface charges resulting in enhanced memory effect expressed by the increased voltage gap (Figure 6.9(b)).

### 6.6.2 Antibody VS Antigen: charging/decharging surface phenomena

Data in Figure 6.10 well describe the distinct effects of antibody and antigen species on the voltage gap parameter registered on a large set of memristive-biosensors.

We have already seen in Chapter 5 that antibodies and antigens have a net charge determined by the residues of their specific amino acid side chain: under correct physiological conditions (pH 7.4), arginine and lysine residues are positively charged while aspartic and glutamic acids are negatively charged (Figure 6.11). We observed that the antibodies we used as surface receptors in our experiments, have an excess of positively charged residues compare to the almost similar but still lower distribution of negatively charged ones. When the memristive device is modified with a surface layer of antibody carrying a positive net charge, the electrical response of the nanowire consists of the loss of the pinched loop and the appearance of the voltage gap (blue column in Figure 6.10). According to the voltage gap theory discussed in previous sections, the appearance of the voltage gap is defined by charging phenomena at the surface of the nanowire where the donor states, in excess in a p-type semiconductor

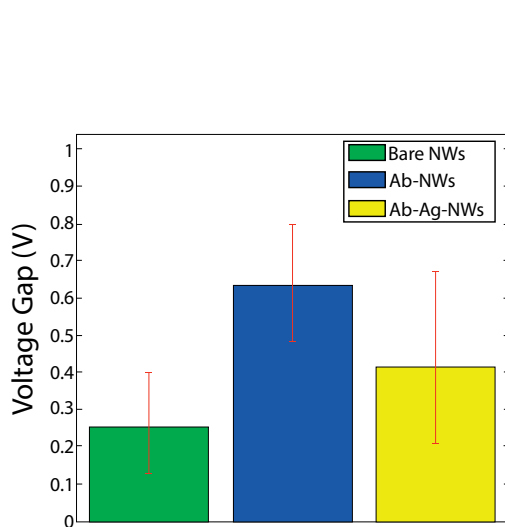


Figure 6.10 – Antibody and antigen effect on the voltage gap.

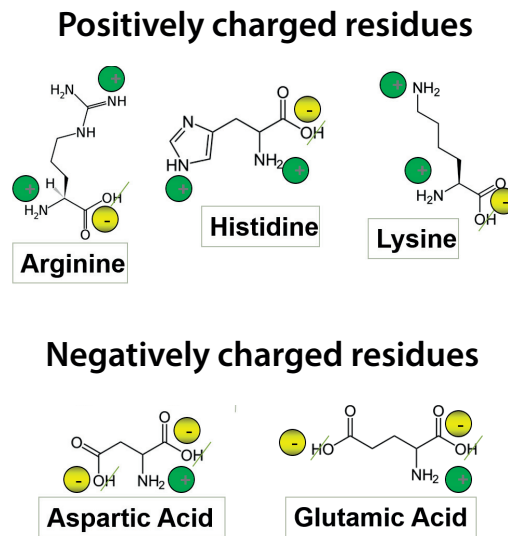


Figure 6.11 – Residues charge at physiological pH.

typically characterized by an amount of acceptor states that is practically negligible in steady conditions, trap the positive charge of the antibodies. This leads to accumulation of positive charge and thus surface charge imbalance that is reflected by the different zero crossing points of the  $I_{ds}$  current in its forward and backward path, i.e. the voltage gap. The experimental data showed that this sort of memory of the biosensors in term of voltage varies with the concentration of biomolecules; specifically, if specific antigen binds to the antibody receptor, the voltage gap decreases. This happens because antigens have a net charge that is negative in order to properly bind to positively charged antibodies via electrostatic interactions. As explained in the model, the voltage gap shrinks as effect of different phenomena related to the reduced dynamics ( $k_{n0}^d$ ) of the donor states (positively charged) with respect to the one ( $k_{n0}^a$ ) of the acceptor states (negatively charged) that now become dominant in the system and compensate for the previously accumulated positive surface charge. In the real case, this is consistent with the recombination/generation surface phenomena resulting from the incoming antigens whose excess of negative charges compensate the positively charged donor states, and form negatively charged acceptor states. The more is the concentration of antigen molecules, the more we have Ab-Ag binding, and the smaller become the voltage gap because of the charge compensation.

## 6.7 Chapter summary and contributions

In this chapter, we showed that the VoG-sensing in Schottky barrier SiNWs is describable by several combined effects of charge transport occurring at the nanowire surface, inside the wire and at the NiSi junctions. Despite the single phenomena occurring in the sensor are relevant

to the determination of the memristive behavior of the device, and its modification in terms of voltage-gap appearance, the major contribution comes from the dynamic occupations of the nanowire surface state energy bands, enabled by the incoming external charges from bio-species. This shows the importance of the surface electrical transport in the oxide of the functionalized device.

Specifically, we presented the implementation of an analytical model able to reproduce and explain the VoG-based behavior in NiSi Schottky barrier SiNW sensors, which successfully accounts for the detection of different concentrations of biomarkers for breast tumor screening. Moreover, the developed theory allows us to capture the dynamics of the voltage-gap by using only a small set of parameters that are linked to the concentrations of antigens, thus enabling a determination of the antigen amount. In view of its compactness, and direct correlation with the physics of the nano-device, our theory can be also used to model and predict the behavior of the VoG parameter in other similar nano-structured devices and sensors. This may be useful for several different applications ranging from biological and chemical sensing to electronics.

Finally, the implemented model also enabled us to give a clear physical interpretation of experimental observations on the effect of ionic concentration and biomolecules. This theory well describes varying voltage gap behavior and, more importantly, antigen sensing with biomodified memristive devices.



## 7 Biosensors integration

In this chapter we present the most recent developments in the field of VoG-biosensors aiming at the integration in multi-panel platforms for advanced multi-biomarkers diagnostic tools in cancer disease. Specifically, we demonstrate the integration of the biosensors with microfluidics and the realization of a CMOS readout circuit for parallel VoG acquisition. In the following, we present the design and the fabrication of a first microfluidic platform prototype, consisting of a PDMS based microfluidic device integrated with the memristive biosensors chip, and an additional metallic layer for interfacing the external circuit for electrical testing. This chapter collects the preliminary results obtained by using the developed microfluidic device for functionalization and incubation of the biosensor, demonstrating the achieved better selectivity and quality of device surface modification. The detailed description of the process flow for integration onto the chip of Aluminum lines and electrodes for electrical contact is also presented. The platform design also envisages the connection of the biosensing chip to an external characterization circuit for fast and parallel voltage gap measurements. Regarding this, we designed a readout CMOS circuit for automated and parallel electrical testing of an array of VoG-biosensors. The circuit has been simulated and already realized. In this thesis we present results from simulations that demonstrate the feasibility of the approach.

### 7.0.1 Introduction

Nanowire-based detection strategies offer several promising opportunities to multiplexed bioanalysis [181]. In particular, VoG-biosensors provide ultra-sensitive electrical detection in a label-free format that can be easily made compatible with portable, microchip-based devices that can process multiplexed data from many individual sensors. Multi-panel platforms for the characterization of array of nanowires, functionalized with antibodies that specifically target different biomarkers in a tumor extract, could lead to the realization of portable biosensing systems enabling characterization of the tumor micro-environment. The possibility to use these technology directly for in-lab measurements would be extraordinarily attractive for the future of diagnostic tools for breast cancer disease.

Two major requirements have to be addressed for achieving label-free, ultra-sensitive, parallel

and fast detection of multiple biomarkers:

- a high-resolution selectivity of the functionalization process enabling different modification of adjacent nanowires with distinct antibodies;
- a design for the biosensing-chip layout compatible with external, or on-chip, readout circuit that concurrently targets several nanowires and enables multiplexed biodetection measurements.

Here, we present our strategies for addressing these conditions with the future aim to realize a portable multi-panel biosensing platforms based on highly sensitive VoG-nanowire biosensors.

As explained in previous chapters, so far our biosensing technology relies on drop-casting methods for the biomodification of nanowires, the exposure to tumor extracts and the washing steps for nonspecific material removal. The approach was demonstrated very successful, as it showed high-sensitive detection of markers (femtomolar resolution) in the highly nonspecific breast tumor tissue environment. However, a number of improvements are fundamental if we want to apply this technology to multiplexed detection of different cancer markers.

In this thesis, we show results of selective biofunctionalization of nanowires with a fabricated microfluidics. The on-chip integration of a microfluidic device is indeed a valid alternative for selective nanowire modification and can also lead to a number of advantages for biosensing in tumor extract. A microfluidic channel enables high selectivity both during the process of surface modification and the incubation with antigen. Thanks to the achievable resolution, the solution can come into contact with a smaller area of the chip, and if enough small, be concentrated in the active area of the sensor. Concerning the resolution, best results would be obtained by nanofluidic devices for selective modification of the single active area. However, because of the complex behavior of fluid at the nano-scale, design and fabrication of nanofluidic systems require a long process of investigation and much more expensive tools for the device manufacturing. As described in the following sections, we opted instead for the development of a micro-scaled fluidic device that provides sufficient selectivity, and, at the same time, requires low-cost fabrication processes based on standard optical lithography and the use of inexpensive material as substrate, such as PDMS (polydimethylsiloxane). Thanks to this selectivity, and the opportunity for addressing only the desired nanowires, different functionalization on adjacent nanowires can be performed, so that it is possible to detect multiple biomarkers at the same time. The selectivity also allows experiments with smaller volumes of solution, that is an important factor for avoiding waste of precious biological material, as in the case of tumor extracts from patient specimens. Furthermore, microfluidics can also lead to increased speed of the measurement, thanks to faster functionalization and incubation processes due to smaller area to modify, and increased interaction rate for binding [182]. Finally, a microfluidic platform could determine improved control over the surface treatments, enabling higher level of homogeneity in the antibody film formation.

The second requirement concerns the measurement set-up for multiplexed electrical measurements. So far, the proposed voltage gap based biosensing have been performed by electrical

testing of the hysteretic  $I_{ds} - V_{ds}$  characteristics in a probe station. However, future biomedical applications, for in-lab, multi-target diagnosis tools in breast cancer disease, require fast, automated and portable biosensing platforms. Automation and portability for faster VoG measurements and improved biosensing performances can be achieved by integration of the biosensing chip with a circuit-reader. This would enable simultaneous-multiplexed testing from arrays of memristive biosensors and large statistics under more controlled conditions. In this chapter, we describe the design for integration of the technology in a biosensing platform in which a microfluidic channel enables the delivery of chemical and biological fluid to the memristive nanowires, and metal lines connect the NiSi source and drain contacts to external electrodes for electrical characterization with external instrumentations. The design of the first biosensing platform prototype is presented in the next section. The detailed description of the process flow for fabrication of a PDMS microfluidic device as well as the lithographic steps for forming the interface electrodes is also reported. It is accompanied by the presentation of the fabrication outcome and of preliminary results demonstrating the improved biofunctionalization achieved by integration of the microfluidic system with the developed sensing device array. As final topic of the thesis, and direct link to future work, we propose the design of a novel CMOS circuit for automated and fast characterization of an array of experimental voltage gap based biosensors. Simulations of the circuit demonstrate the feasibility of the proposed approach opening the way to future development in the field of multi-panel diagnostic systems. Data acquisition from VoG-biosensors, in real experimental conditions, is referred to future work.

### 7.1 The biosensing platform design

In Figure 7.1 we report the conceptual representation of the first designed prototype for integration of microfluidics with the biosensing chip, as well as metallic interface for electrical characterization. The sensory part consists of an array of 8 suspended memristive nanowires arranged in a line for easy access with the microfluidic channel. With the two-fold objective of realizing microfluidics and external circuitry for multi-biomarkers detection, metal lines are necessary for bringing the electrical contacts of the VoG-biosensors outside the active area, *i.e.* the region of the chip where the fluid is delivered to, so that electrical characterization can be performed. Metal lines are designed in such a way that one extremity contacts the source (or drain) NiSi pad of the biosensors, the other one is connected to an external electrode and can be reached for measurement. Aluminum was chosen because of the compatibility with the fabrication procedure. The electrodes have a precise geometry designed to fit to an external 9 pins-connector for easy access with an external measurement circuit specifically designed for the voltage gap based technology (see Section 7.2). The microfluidics is made of a microfluidic channel, where the analyte flows perpendicularly to the nanowire cross section, and two reservoirs, located at the two extremities of the channel, where inlet and outlet can be connected. The detailed description of the microfluidic platform is reported in Section 7.1.1.

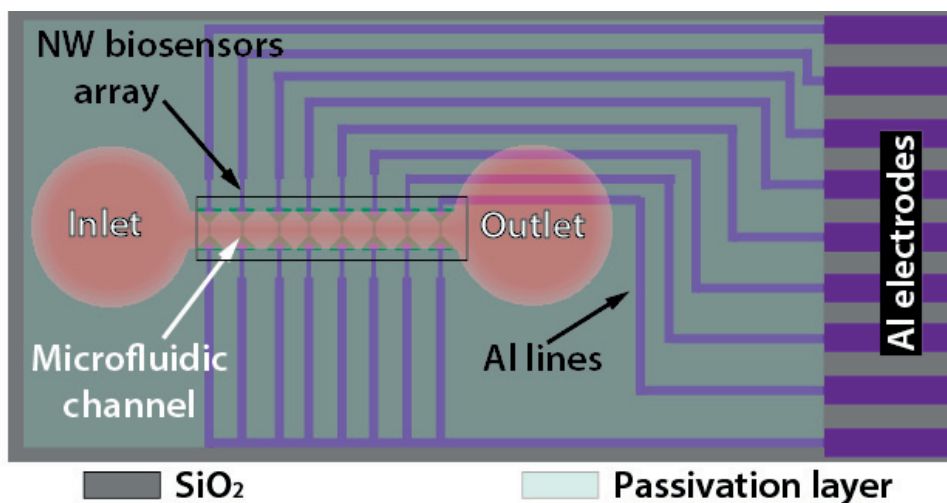


Figura 7.1 – Design of a biosensor chip that integrates the VoG-biosensors array and the microfluidic platform. External electrodes enable the connection to an external CMOS readout circuit for parallel measurements.

### 7.1.1 Microfluidics: mask design

In Figure 7.2 we schematically illustrate the realized microfluidic system, with cross-sectional (a) and top (b) views on the channel for fluid flow. The device is designed so that the micro-channel is formed in between two reservoirs, where the inlet and outlet microtubes are connected. Silicone tubes, connected to a peristaltic pump, are used to pump the solution from an external beaker, to the inlet reservoir and, from there, towards the outlet at the other edge of the channel, passing through the biosensors array. The solution, after interaction of the biological material in the active area of the chip, is then sucked out by the outlet microtube. The two reservoirs are needed for allowing proper connection of the tubing to the channel that has smaller size. Simulations also showed that the fabrication of inlet and outlet reservoirs permits to achieve better flux lines, due to the gradual filling of the reservoirs and slower insertion of the fluid into the channel. Reservoirs and channel have the same thickness of  $20\ \mu\text{m}$ . The sensory part consists of an array of 8 memristive nanowires perpendicularly arranged with respect to the flux (Figure 7.2(b)) for better fluid interaction. Since the main advantage of the microfluidics is to deliver the solution selectively to the nanowires, the channel should be as small as possible. In order to investigate how much smaller, different widths and thicknesses of microfluidic channel were tested, while the length was kept constant and equal to 3 mm in order to define an inter-device gap of  $300\ \mu\text{m}$ . This distance was necessary both for more homogeneous flux and enough left space for metallic contacts. The tests showed that thickness and width below  $20\ \mu\text{m}$  increased the channel resistance to the flux and did not allow the solution to pass through. By considering these constraints, the best solution was found to be a channel  $20\ \mu\text{m}$  thick, and  $500\ \mu\text{m}$  wide, resulting in a cross section of  $10000\ \mu\text{m}^2$ .



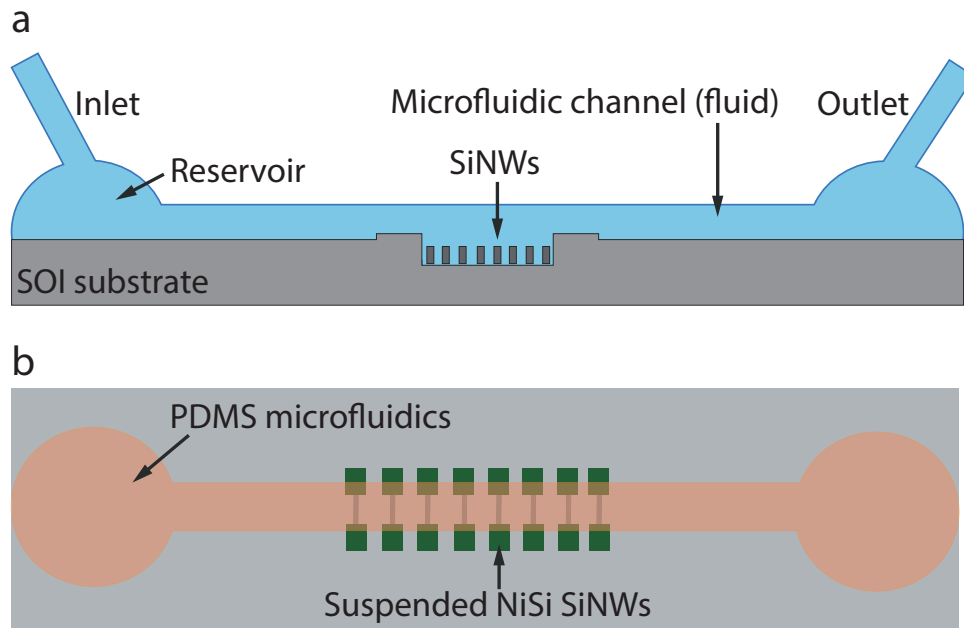


Figure 7.2 – Schematic description of the designed microfluidic device. (a) Cross-sectional view of the channel for delivering the fluid from the inlet reservoir towards the outlet reservoir, flowing through the sensor area. (b) Top view of the system illustrating the disposition of the array of 9 sensors, arranged perpendicular to the fluid flow.

### 7.1.2 Masks fabrication

An array of voltage gap based biosensors is fabricated through EBL techniques according to the procedure already described in Section 2.3. This array is integrated onto a chip together with a microfluidic platform, and an Aluminum layer for interface to external circuits (Figure 7.1). Microfluidics and Aluminum electrodes are patterned via photolithography.

In Figure 7.3(a,b) we report details on the EBL mask used for patterning the NiSi Schottky barriers SiNWs in precise locations on the SOI wafer, and arranged in line for easy access with a microfluidic channel (green layer). In Figure 7.3(c) we illustrate the mask related to the complete chip in order to give an idea of the integration of the microfluidic device (Figure 7.2) with the SiNW devices. The chip consists of (i) an array of 8 memristive biosensors made of vertically-stacked SiNWs bridging two NiSi pillars, (ii) Aluminum metal lines connecting NiSi pads with external Al electrodes for electrical characterization, (iii) a microfluidic platform including inlet, outlet for fluid pumping and a microchannel delivering the solution to the sensor with a flow direction perpendicular to the nanowire cross section.

Both microfluidics and metal lines definition require the fabrication of a mask to transfer the desired layout to the substrate through resist exposure to UV light (optical lithography). Figure 7.4 reports the main steps of the standard lithographic process flow for the fabrication of masks. The starting substrate for mask fabrication is a Chromium mask consisting of glass, Chromium and Chromium oxide layers; the substrate is already coated with positive photoresist (AZ1518) when purchased. The fabrication includes five main steps: (a) the

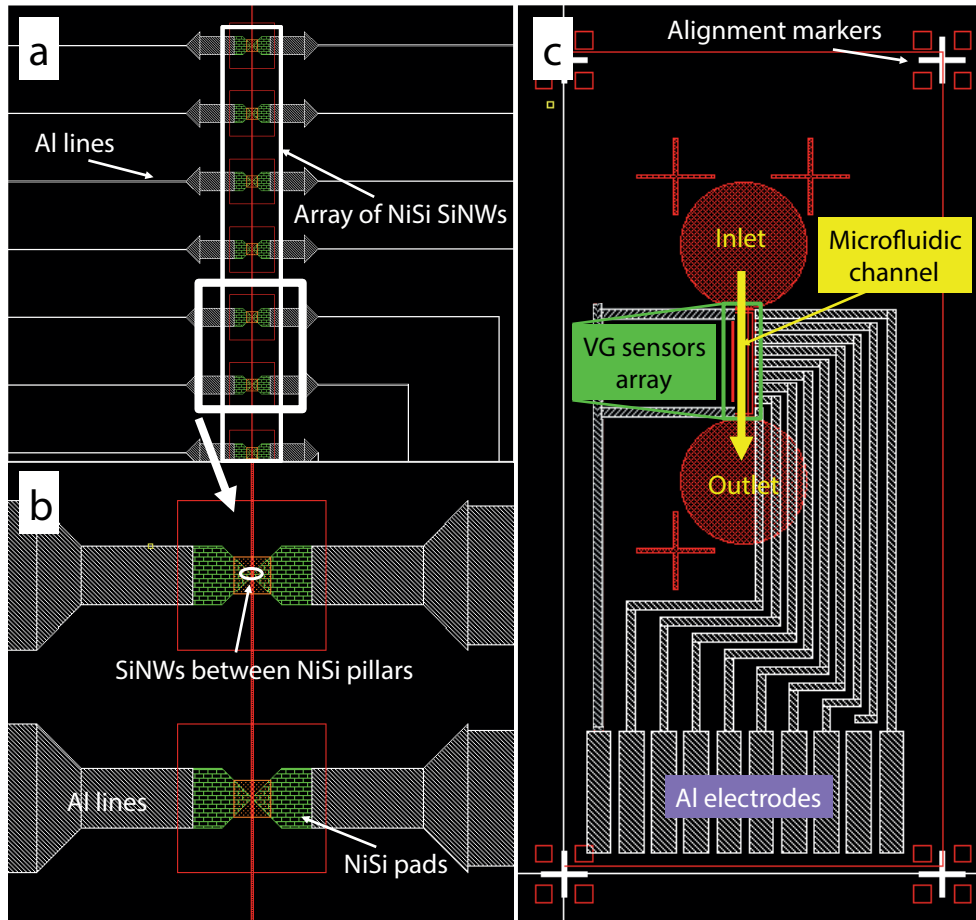


Figure 7.3 – Mask design prepared in Cadence Virtuoso for the lithographic patterning of (a) an array of memristive SiNWs (with zoomed view in (b)), integrated with a microfluidic platform thanks to Al metal lines and external Al electrodes (c).

software Cadence Virtuoso is used to draw the layout; (b) a laser writing system (Heidelberg VPG200) transfers the layout pattern on the resist of the mask; (c) after development in the Süss DV10 tool, the areas of the resist that have been exposed to UV light dissolved, thus leaving the corresponding regions on the mask accessible; (d) Chromium is etched away in acid in the Cr etch bath (Coillard wet bench), followed by a deep cleaning step for acid removal; (e) finally, the resist is stripped away (Technistrip 1316). At the end of the process, the designed layout appears reproduced on to the mask. Pictures of the final masks designed for the fabrication of Aluminum metal lines/electrodes (a), and SU-8 microfluidics are shown in Figure 7.5.

### 7.1.3 Process flow for metal lines integration with the sensor chip

The process flow related to the fabrication of Aluminum metal lines onto the substrate already hosting memristive SiNW devices is schematically summarized in Figure 7.6(a-d). For simpli-

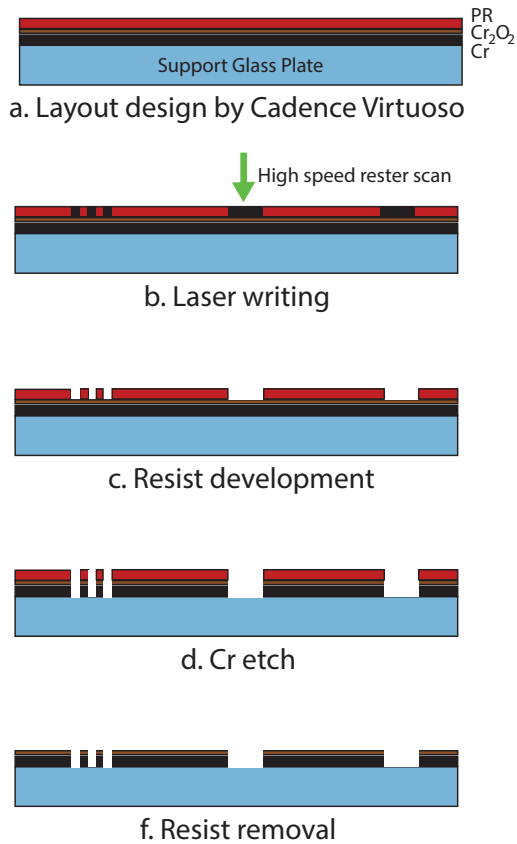


Figure 7.4 – Process flow for the fabrication of a photolithography mask.

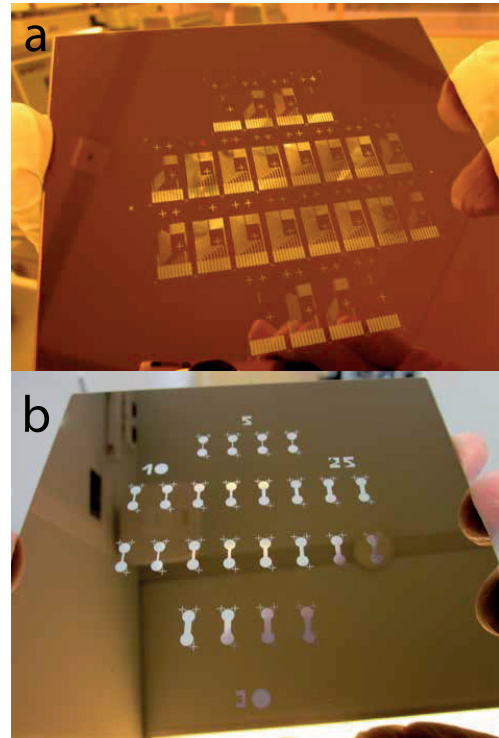


Figure 7.5 – Fabricated masks for Al lines (a) and SU-8 microfluidic mold.

city, we report the appearance of an hypothetical chip including only 4 sensing devices, after the most important steps of manufacturing. Aluminum photolithography is performed on an SOI wafer pre-processed for formation of an array of SB SiNWs (Figure 7.6)(a), arranged in line for easy access with the microfluidic channel, according to the design described in previous sections (Figure 7.1). The substrate is coated with a bilayer resist (Figure 7.6)(b)). A 400 nm thick layer of LOR (lift-off resist) is in direct contact with the wafer and, thanks to the good level of adhesion with metals, facilitates the complete removal of unwanted metal from the wafer during lift off. A second 1.6  $\mu\text{m}$  thick layer of AZ1512 (positive photoresist) is used in the photolithographic step to define the Al lines pattern. After the coating, wafer and mask (Figure 7.5(a)) are aligned, and the resist is exposed to UV light (energy of 24  $\text{mJ}/\text{cm}^2$  for 2.4 sec). UV light weakens the positive photoresist in the exposed areas. After development, the resist dissolves leaving the underlying regions of the SOI substrate exposed to air (Figure 7.6(c)). A layer of Aluminum with 200 nm of thickness is deposited on the wafer by physical vapor deposition (PVD), and after the last step of lift-off in a solution of LOR stripper (SVC-14), for 24 hours, Al lines and electrodes are formed (Figure 7.6(d)).

The wafer after the lithographic process appears as in Figure 7.7(a). It is then cut in rectan-

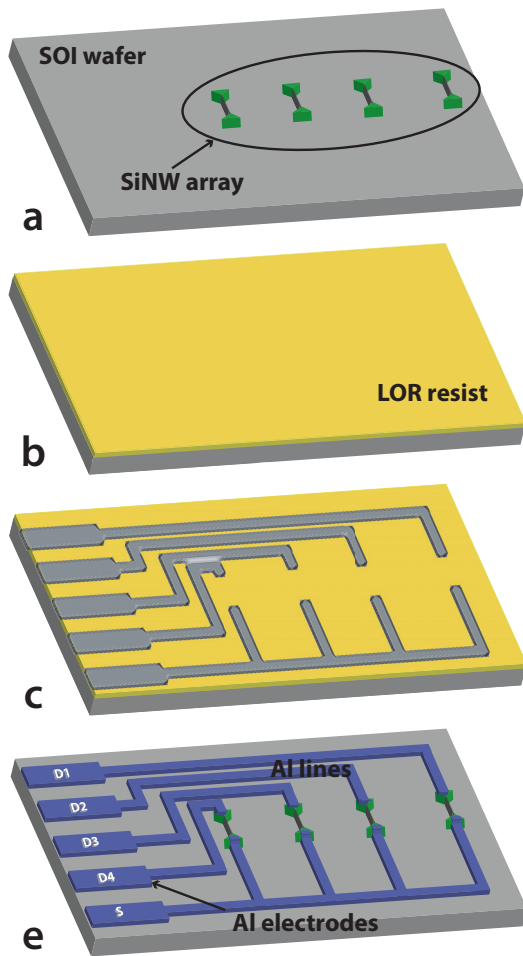


Figura 7.6 – Process flow for the fabrication of Aluminum lines.

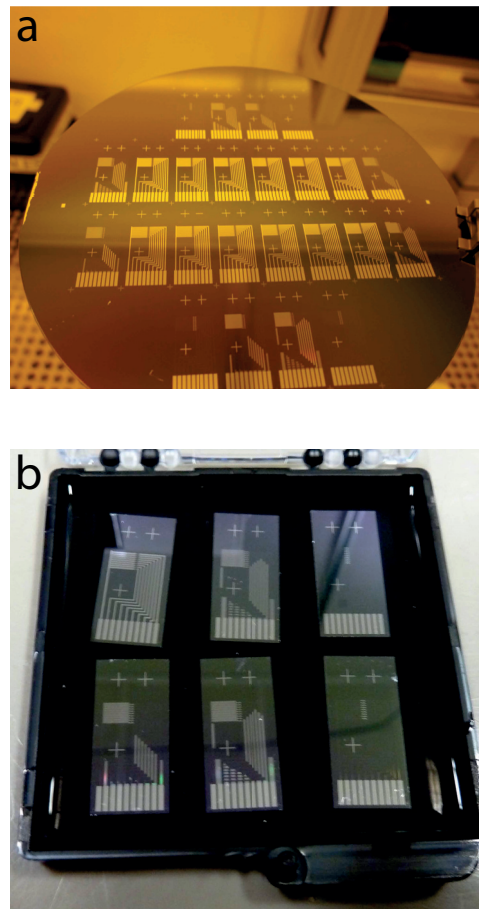


Figura 7.7 – (a) Wafer after photolithography and Al lift-off. (b) Final sensing chips.

gular dies resulting in a number of chips ready to be integrated with the microfluidic system (Figure 7.7(b)). Some details of the Aluminum layer after photolithography are illustrated in Figure 7.8, where (a) and (b) differ in terms of length and width of the Al lines connecting the NiSi source and drain contacts of the SiNWs to the Al electrodes located externally the sensors area. Different geometries were tested in order to see the effect of the resistances on the measurements. Since the voltage gap acquisition is performed at very low current, too large resistance would add too much noise in the electrical characterization of the devices.

#### 7.1.4 Process flow for microfluidic fabrication

As in the most typical applications of microfluidics, also our own work has focused on polymer systems made of PDMS (polydimethylsiloxane). PDMS is a cheap excellent material for

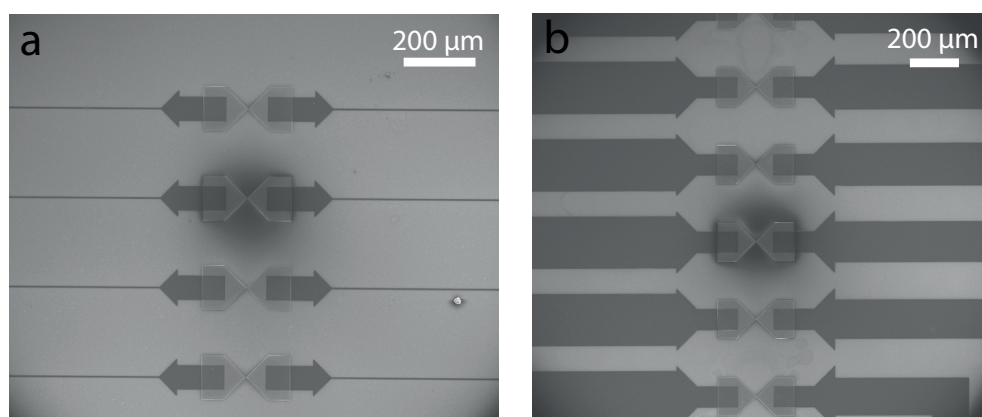


Figure 7.8 – SEM images of metal lines for contacting the NiSi pads of memristive SiNWs. (a) and (b) differ in terms of length and width of the Al lines.

the fabrication of microchannels for use with biological samples in aqueous solutions for a number of reasons [183–185]: (i) features on the micron-scale can be reproduced with high fidelity in PDMS by replica molding; (ii) it is optically transparent down to 280 nm so it can be used for a number of detection schemes (e.g., UV/Vis absorbance and fluorescence); (iii) it cures at low temperatures; (iv) it is nontoxic and compatible with lots of the used organic solvents; (v) it can be deformed reversibly; (vi) it can seal reversibly to itself and a range of other materials by making molecular (van der Waals interactions) contact with the surface, or it can seal irreversibly after exposure to an air plasma by formation of covalent bonds; (vii) its surface chemistry can be controlled by reasonably well-developed techniques; and (viii) because it is elastomeric, it will conform to smooth, non-planar surfaces, and it releases from delicate features of a mold without damaging them or itself.

In Figure 7.9 we illustrate the main fabrication phases for the formation of a PDMS microfluidic channel that enables the delivery of analyte to the  $V_{GAP}$ -biosensors array. We sketch the cross section and top (when needed) view device appearance after the indicated process. Each phase of the process flow consists of different steps that are described in the following. All processes are performed in the clean room of CMI level +1, EPFL, specifically, in zones of class 1000 (less than 1000 particles ( $\geq 0.5 \mu\text{m}$ ) per cubic foot) and 10000 (less than 10000 particles ( $\leq 0.5 \mu\text{m}$ ) per cubic foot), where “dirty” materials, such as PDMS, can be handled.

### Mold fabrication: SU-8 processing

In order to create a microfluidic channel, a mold has to be fabricated first. SU-8 is an epoxy-based negative photoresist commonly used in the fabrication of microfluidics [186] and microelectromechanical systems (MEMS) [187], thanks to its properties of good adhesion, broad range of thickness achievable from one spin (750 nm to 500  $\mu\text{m}$ ), and high aspect ratios ( $\sim 15$  for lines and 10 for trenches). In our process, we used SU-8 for the creation of the negative

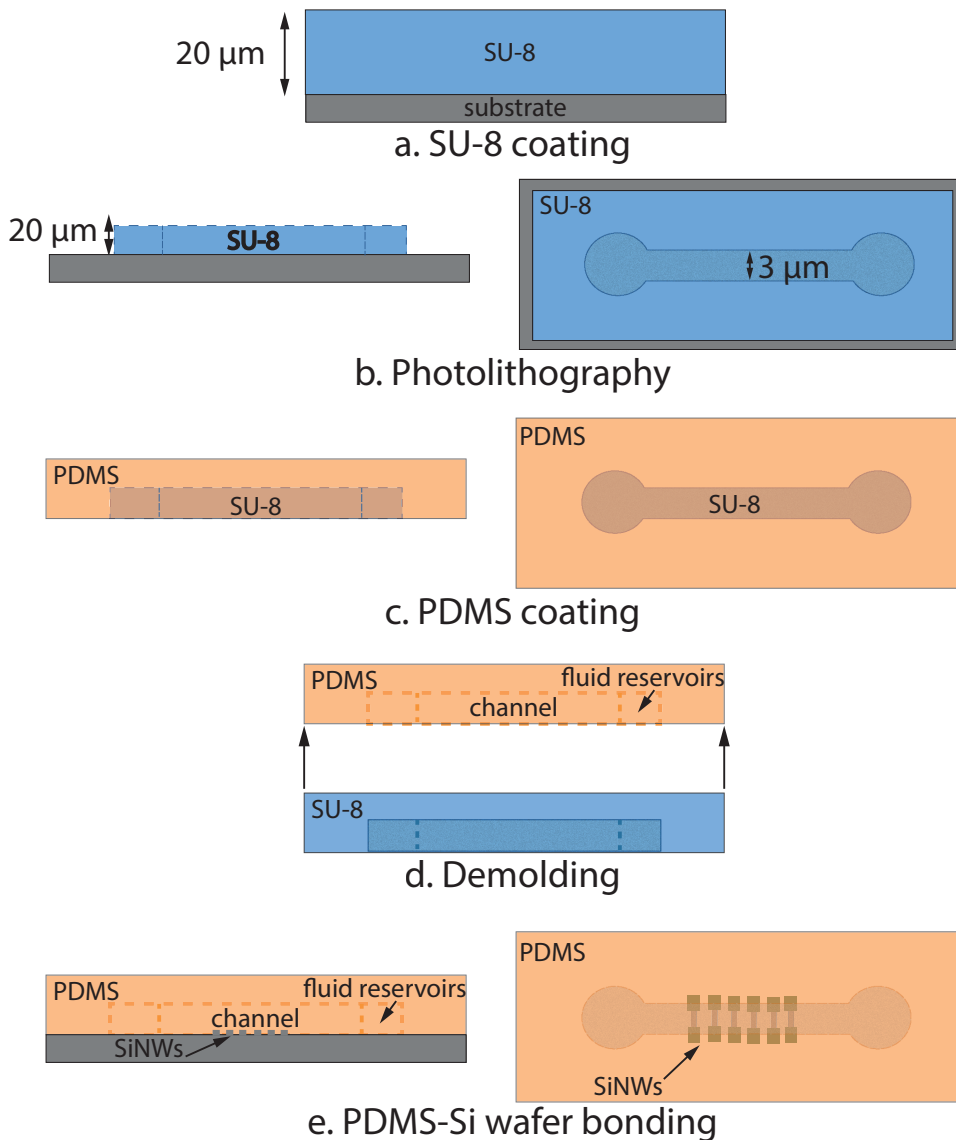


Figura 7.9 – Conceptual representation of the main steps of the process flow for microfluidics fabrication.

mold necessary for the subsequent definition of a 20 μm thick channel in PDMS. Thanks to its low surface roughness, SU-8 can facilitate the adhesion of the resulting PDMS structures to the Si substrate.

For the mold fabrication, we used the standard SU-8 processing. First, the Si substrate is pretreated by cleaning in Oxygen plasma for 2 min, in order to remove organic particles from its surface; then, liquid SU-8 GM 1060 is poured onto it and spin coated (Figure 7.9(a)) by a 8-step spinning procedure (see Table 7.1).

After the coating, the wafer is transfer to a hotplate where hot baking at 30 °C for 10-20 min is performed to achieve better uniformity, and reduce stress formation in the thick layer

## 7.1. The biosensing platform design

Segment#	1	2	3	4	5	6	7	8
Time (sec)	5	5	5	40	1	1	5	5
Speed (rpm)	500	500	1027	1027	2027	1027	1027	0

Tabella 7.1 – SU-8 spin-coating parameters

Segment	Time(s)	T(°C)	Vacuum
1	10	30	ON
2	1800	130	OFF
3	300	130	OFF
4	1800	30	OFF

Segment	Time(s)	T(°C)	Vacuum
1	10	1800	ON
2	1800	90	OFF
3	1800	90	OFF
4	2700	60	OFF
5	2700	30	OFF

(a) SU-8 soft bake parameters

(b) SU-8 post bake parameters

Tabella 7.2 – Hotplate parameters for soft bake of SU-8 before UV exposure (a) and post-exposure bake of the resist (b).

(leading to crack) as the solvents evaporates. Next, a last step of soft baking is needed in order to remove the solvent from the resist and make it solid by strengthening the resist bonds. Soft bake is also composed of different segments, as reported in Table 7.2a. The first segment is a surface cleaning step in low vacuum in order to achieve better purity; the two following segments are needed for the complete polymerization of the resist at high temperature (130 °C), and their duration depends on SU-8 type and desired thickness.

Photolithography is carried out to define the desired pattern on the SU-8 resist (Figure 7.9(b)), by alignment of the fabricated mask to the Si substrate (Section 7.1.2) and exposure to UV light (dose 20 mW/cm<sup>2</sup> for 11.5 sec), in contact mode for better resolution. After exposure, the wafer is put back on the hotplate and a post-exposure bake step is performed with the parameters indicated in Table 7.2b.

The wafer is stored in a storage box for several hours for stress relaxation, before resist development. SU-8 is developed in PGMEA (Propylene Glycol Methyl Ether Acetate), rinsed in isopropanol and dry with nitrogen gun. SU-8 processing leads to the fabrication of molds on the silicon substrate, as shown in Figure 7.10.

### PDMS processing

Once realized, the mold can be used to fabricate the PDMS microfluidics. PDMS requires a proper preparation in order to have the right elasticity. First, the PDMS Silicone base (Sylgard 184) is mixed with the curing agent in a 10:1 ratio, and loaded into a mixer (2000 rpm, for 1 min) until obtaining a liquid PDMS. PDMS is then put under vacuum for 20-30 min for degassing.

The next step is pouring the prepared PDMS onto the SU-8 mold. Surface conditioning of the

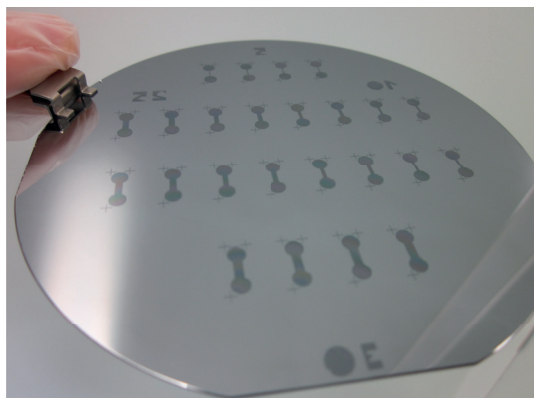


Figura 7.10 – SU-8 mold fabricated on a silicon substrate.

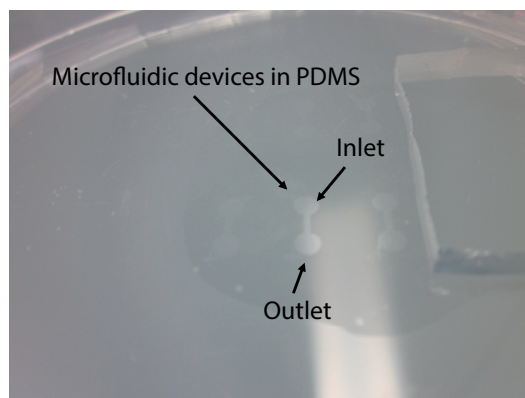


Figura 7.11 – Fabricated PDMS microfluidic devices.

mold is of paramount importance at this stage of the fabrication in order to prevent PDMS sticking. Silanization with TMCS (chlorotrimethylsilane) allows passivation of the surfaces and aides the release of the mold from the PDMS. Silanization is performed in a vacuum chamber for 10 min.

The liquid and degassed PDMS is poured over the mold in a petri dish, and then baked in oven at 80 °C for one hour to strengthen the structure (Figure 7.9(c)).

### Demolding

After baking, the PDMS is ready to be detached from the mold (Figure 7.9(d)) and cut into pieces. Inlet and outlet holes, with diameter of 1.2 mm, are also formed in the PDMS device, prior to the bonding step, by means of a hole puncher. The fabricated PDMS microfluidic devices are reported in Figure 7.11.

### PDMS-chip bonding

The surface of the chip including the fabricated voltage gap biosensors array has to be activated in order to enable both nanowire biofunctionalization and microfluidics-chip bonding. The activation consists of the formation of hydroxyl groups (OH) at the surface that are able to interact and bind to silanes. Silanes are used as linker molecules for antibody immobilization (Chapter 3), and as passivating layer for easier adhesion of PDMS to the sensing chip. As already discussed in Section 3.4, the usual way to activate the surface of the nanowires is by piranha etching. However, piranha is an etchant for Aluminum, and had to be replaced by a localized plasma oxygen, in order not to harm the Al lines. We used the SurfX Atomflo 400L tool, which exploits a localized plasma oxygen carried by Helium flow. The localization of the plasma flux and the high power allow for the formation of long lasting hydroxyl groups on the surface of the nanowires.



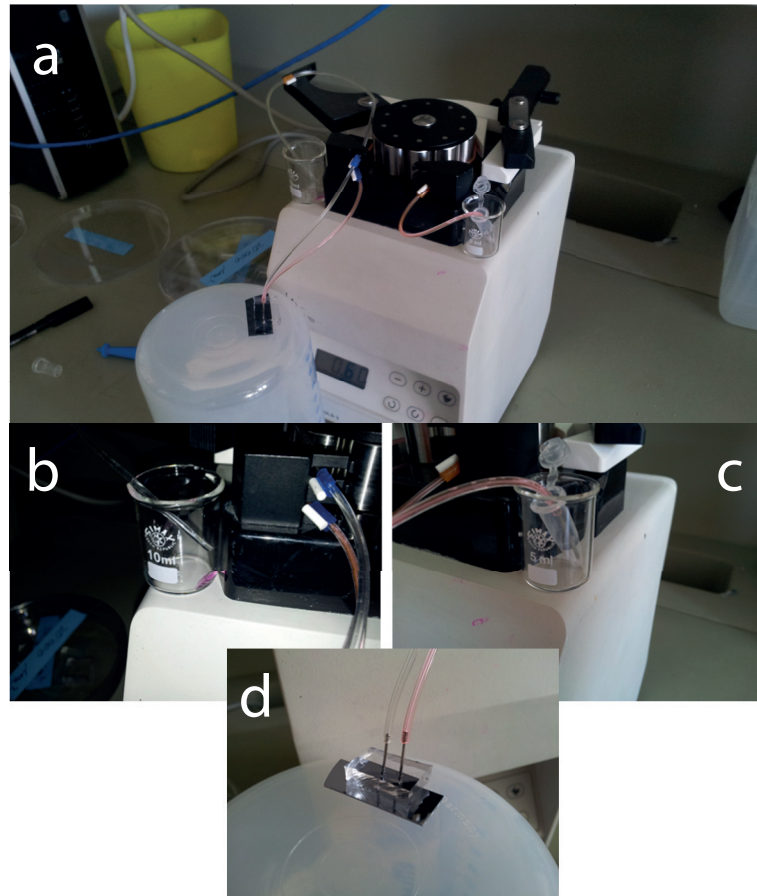


Figure 7.12 – Set-up for experiments with microfluidics. (a) A peristaltic pump is used to pump the liquid inside the microchannel, to the biosensors. (b) One microtube is connected to the outlet and deliver the fluid to a beaker for solution waste. (c) The other microtube is connected to the the inlet and sucks the solution from fresh sample. (d) Zoomed view of the connections to the microfluidic device.

Next, the side of the PDMS microfluidic that was designed for contacting the biosensing chip is exposed to oxygen plasma. Exposure time and power have to be tuned accurately for achieving proper bonding: a too low power or short time can result in scarce generation of hydroxyl groups; too high power or long duration can result in overoxidation, *i.e.* formation of rough brittle layers of silica that prevent the establishment of a complete surface contact. Best results were observed for a power of 29 W and an exposure time to plasma of 30 sec.

Once PDMS microchannel and biosensor surface have been activated, the microfluidic in PDMS is aligned to the biosensors array on SOI chip and the two systems are bonded together (Figure 7.9(e)).



Figura 7.15 – Fluorescence detection of Ab-Cy5 attached on the fabricated chips.

### 7.1.5 Biosensors-microfluidics integration: preliminary results

The proper functioning of the microfluidics was tested by employing it for biomodification of the devices. All steps were carried out at the Ludwig Cancer Center, in Épalinges. The used experimental set-up is reported in Figure 7.12. A Gilson Minipuls 3 peristaltic pump was used to pump the fluid into the microchannel (Figure 7.12(a)), at a rotational speed of 0.5 rpm. For these preliminary experiments, we chose a so low speed in order to prevent the nanowires from breaking under a too fast flow. One tube is connected to the outlet of the microfluidic device and sucks the liquid out the microchannel towards a waste beaker (Figure 7.12(b)). A second tube is connected to the inlet and sucks the solution from a fresh sample into the inlet chamber, from where the fluid is delivered to the devices through the microchannel (Figure 7.12(c)). The connections of the peristaltic pump to the microfluidic platform are represented in Figure 7.12(d).

The functionalization consists of the same surface treatments already described in Chapter 3, with the important difference that they were performed here by means of the microfluidic device and not by simple drop casting. Specifically, the microfluidics allowed us to replace the multiple washing steps for nonspecific material removal with one single washing procedure performed by making the fluid flowing through the microchannel for 5-10 min. In order to have comparable results, we decided to keep the incubation times for silanes-Si and silanes-antibody interactions similar to the ones used in the static case with drop-casted solution or device immersion in liquid for surface interactions. After surface treatment by solution flow, the chip was dried by making a  $N_2$  air flowing into the microfluidic channel so that measurements were still performed in dry conditions. The performance of the system were tested by comparing the results of the two biofunctionalization methods: one chip was modified by simple drop-casting; the other one with the microfluidics. Both were functionalized with anti-rabbit Ab-Cy5 in order to characterize the two modified surfaces with fluorescence imaging. The outcome of the fluorescence detection is reported in Figure 7.15. It is clearly evident that the microfluidic channel well confines the Ab functionalization in the active area including the array of biosensors (Figure 7.15(b)), while drop-casting determines a non homogeneous functionalization that is spread all over the Si oxide layer around the nanowires (Figure 7.15(a)). Moreover, results related to the use of the microfluidic platform show a much more intense fluorescence signal, thus demonstrating the increased binding of antibodies

to the silane groups on the nanowire surface. This is a proof of the enhanced probability of surface interactions due to the increased interaction rate under dynamic flow conditions. The microfluidic channel also allows us not to waste biological material, and to save time.

We also performed electrical characterization of the VoG-biosensors, in bare conditions and after the biomodification process carried out with the microfluidics. The results are consistent with data acquired from devices biomodified with drop-casting method, *i.e.* pinched loop was observed for non-modified SiNWs, and voltage gap appearance for the case of biofunctionalized devices.

## 7.2 CMOS circuit design for fast and parallel VoG acquisition

Here we discuss the design of a novel readout circuit for automated and parallel voltage gap acquisition. This phase required the help from experts in the field of circuit design, and was carried out thanks to a strict collaboration with another Ph.D. student, Mr. Zaher, from Oslo University. The circuit has been designed, simulated and, very recently, also fabricated. Because of time constraints, acquisitions from real biosensors was not possible, and was referred to future work. Nonetheless, the simulations of the VoG CMOS reader demonstrated the feasibility of the approach and the potentials for multiplexed biomarkers detection.

Here, we aim at giving a brief description of the designed circuit mostly focusing on the properties of the circuit and the future integration with our biosensors.

First, we discuss the main requirements for the design of the voltage gap characterization circuit design; then, we describe a first prototype  $2 \times 2$  array of the circuit designed in CMOS technology and thoroughly characterized in simulations.

The circuit aim is to detect the voltage-gap in order to read our biofunctionalized memristive SiNWs. This parameter has been defined as the difference in voltage of the forward and backward crossing points of the  $I_{ds}$  current with the x-axes. The voltage gap process of detection leads to a set of requirements that can be summarized as follows:

1. The voltage across the nanowire should be swept from a negative voltage to a positive voltage and vice versa in a sub-hertz frequency.
2. The voltage gap corresponding to the difference between the voltages where the current zero crossings occur should be extracted, taking into account that current values vary between tens of  $\mu\text{A}$  and  $0\text{A}$ .
3. In case of multiple zero crossings while sweeping in one direction, they should be logged and reported since they contribute to the accuracy of the measurement.
4. Defects introduced with fabrication processes and non-homogeneous functionalization of the nanowire may cause the SiNWs to break down or stop conducting in the right manner. A functionality check for a minimal current at maximum voltage for the nanowire should be thus performed in order to prevent any mistake in the voltage gap calculation.

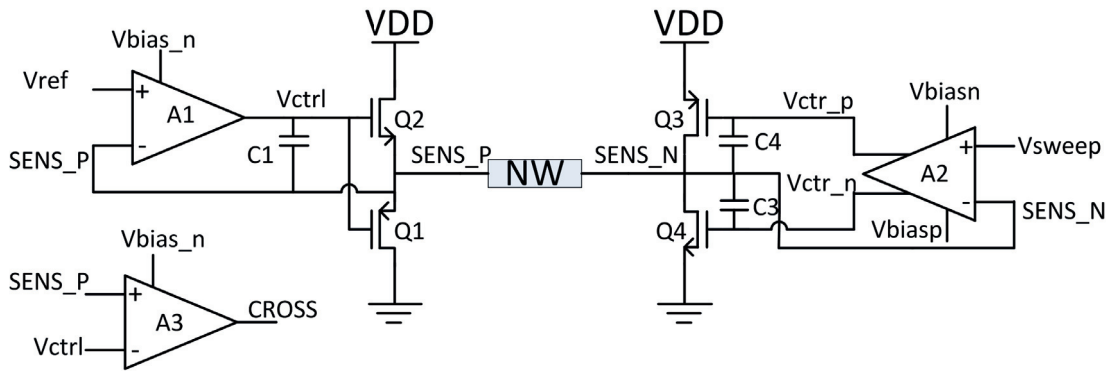


Figura 7.16 – Schematic representation of the circuit solution for voltage gap acquisition on one single biosensor.

The circuit should enable testing of an array of sensors at the same time. Here we present the solution for the implementation of a system composed of a  $2 \times 2$  array. The circuit can be easily scaled to any number of sensors.

### 7.2.1 Circuit description

In Figure 7.16 we report the designed circuit solution for voltage gap detection on one single biosensor. The circuit is designed to extract the voltage gap by identifying the voltages across the nanowire when the current switches direction. One node of the nanowire, *SENS\_P*, is kept at *Vref*, 2.5 V in 5 V technology, by using negative feedback via A1; the other node, *SENS\_N*, is controlled by a voltage ramp sub-circuit linearly sweeping between *VL* and *VH* where 2.5 V is the mid voltage. Typically *VL* is 0 V, and *VH* is 5 V, so that the voltage sweep across the nanowire varies from -2.5 V to +2.5 V.

#### Zero crossing detector

The zero crossing detector is designed to sample the *VswEEP* signal and detect the voltage values at which the zero crossings occur in the forward and backward branches of the biosensor  $I_{ds} - V_{ds}$  characteristic.

The detector of zero crossings consists of four transistors (Q1, Q2, Q3, Q4) that are connected as illustrated in the central part of the circuit in Figure 7.16. Transistors Q2 and Q1 are source connected between *VDD* and *GND* and have the gate in common. The current can flow through two possible paths. The first determines the current to flow from *VDD* via Q2, through *SENS\_P* to *SENS\_N* and down to *GND* via Q4; the second one makes the current flowing from *VDD* via Q3 through *SENS\_N* to *SENS\_P* and down to *GND* via Q1. Between transistor Q1 and Q2, only one is ON and conducting at any moment, and typically they are both OFF at the moment when the current switches direction. That translates to *VGS* of both transistors, defined as *Vctrl*-*Vref*, being positive when Q2 is ON, negative when Q1 is ON, and equal to zero

## 7.2. CMOS circuit design for fast and parallel VoG acquisition

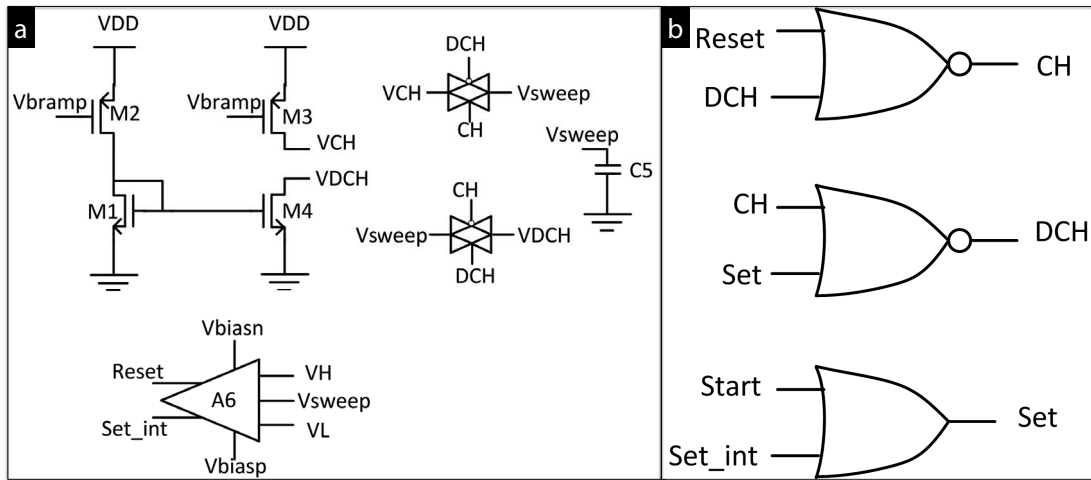


Figure 7.17 – Configurable voltage ramp circuit shared by all sensors. (a) The voltage ramp circuit. (b) Control signals for the voltage ramp circuit.

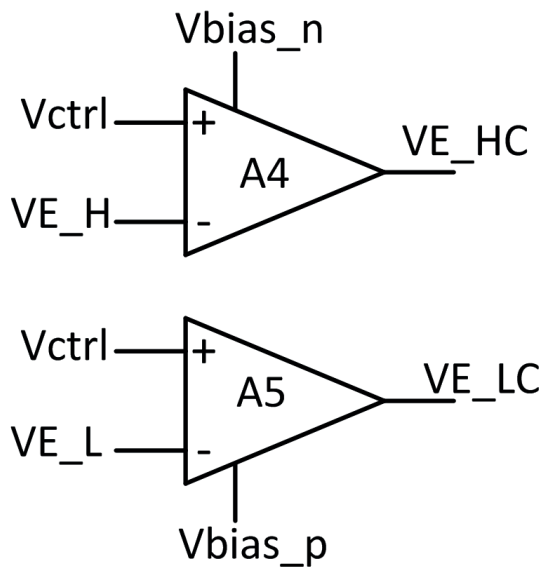


Figure 7.18 – Fault detector circuit.

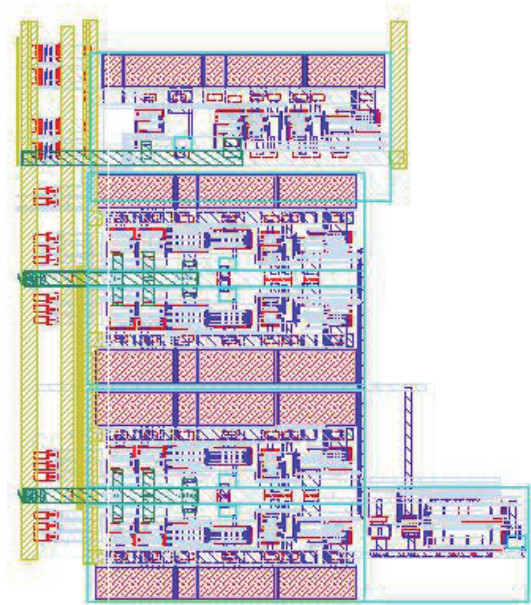


Figure 7.19 – Layout of the analog part.

when the current through the nanowire changes its direction. Notice that this configuration allows Q1 and Q2 to be in the subthreshold region while conducting small currents. So, we define the current zero crossing as the voltage for which  $V_{ctrl}$  is equal to  $V_{ref}$ . A voltage comparator with  $V_{ref}$  and  $V_{ctrl}$  as inputs is used to get a *CROSS* signal that has a rising/falling edge whenever the current switches direction. This is the signal we use in the digital part for zero crossings detection.

### Voltage ramp circuit

The voltage ramp sub-circuit is reported in Figure 7.17. It is made of a current mirror where the PMOS gate voltage  $V_{bramp}$  is controlled from off-chip. Increasing  $V_{bramp}$  decreases the current through transistors M3 and M4 and leads to a longer time constant charging/discharging capacitor C5, *i.e.* a smaller frequency for triangular signal  $V_{sweep}$ , and vice versa. The  $V_{sweep}$  signal varies between  $V_L$  and  $V_H$  through the use of a complementary input comparator A6 by generating the *Reset* and *Set\_int* signals. These two signals are used to generate the control signals for the transmission gate, *CH* and *DCH* (in Figure 7.17(b)), reflecting the charging and the discharging phases of C5. *Reset* and *Set\_int* are also passed to the digital part.

Long channel transistors are used for M1, M2, M3, and M4 to reduce the channel length modulation. By doing that, the charging and the discharging periods only differ within 1%. The charging/discharging time is linear as long as  $V_L$  and  $V_H$  have sufficient headroom from *GND* and *VDD*. By setting  $V_L$  to 100 mV, and  $V_H$  to 4.9V, the highest voltage deviation from linearity is within 1.6% from the linear value.

### Device fault detector

The functionality check for faulty nanowires is depicted in Figure 7.18. The idea is to check for the amount of current through the nanowire when  $V_{sweep}$  is at  $V_H$  and at  $V_L$ , and make sure that it is above a specific value (in nA). This current will go through Q1 or Q2, setting  $V_{ctrl}$  to a specific value ( $VE_H$  in case of Q2 conducting and  $VE_L$  in case of Q1 conducting), corresponding to the current we are after. So, if we compare  $V_{ctrl}$  and  $VE_L$  at the beginning of the charge period, where the current goes through Q2, and find that  $V_{ctrl}$  is smaller than  $VE_L$ , then the nanowire is not conducting the expected amount of current which is a sign of a faulty nanowire. The same applies for  $VE_H$  at the beginning of the discharge period. Signals  $VE_{HC}$  and  $VE_{LC}$ , determined by opamps A4 and A5 are forwarded to the digital domain. In Figure 7.19 we report the layout of the whole analog parts.

### Digital processing

The digital part receives the following input signals: *CH*, *DCH*, *CROSS*,  $VE_{HC}$  and  $VE_{LC}$  (Figure 7.20).  $VE_{HC}$  is not indicated for simplicity. The signals evolve as follows:

1. When *DCH* goes high, a global counter, *GC*, starts from 0.  $VE_{HC}$  is checked and if it is low the circuit detects a faulty nanowire and a flag is set.
2.  $VE_{LC}$  goes high. When *DCH* goes low,  $VE_{LC}$  is checked and in case it switches low, another flag for faulty nanowire is set.
3. *CROSS* goes high, *GC* value is saved into register t1. If *CROSS* switches again, nt1 times, while *DCH* is high, the *GC* value for last crossing is saved into register t1f.
4. *DCH* goes low; the functionality check on  $VE_{LC}$  is done.

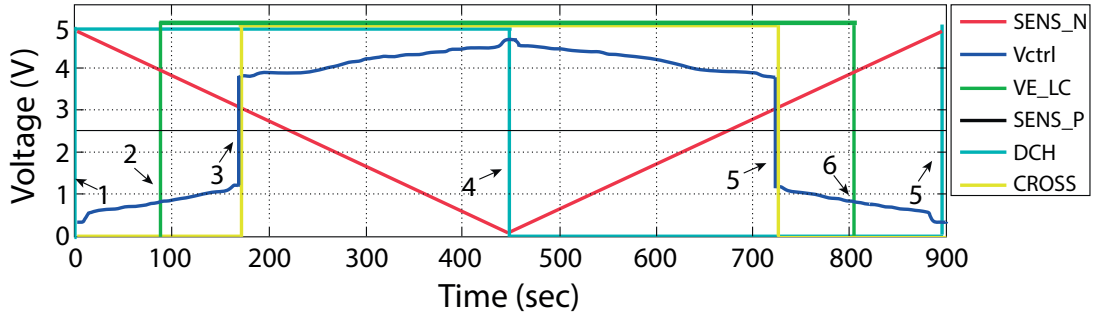


Figure 7.20 – Basic signals arriving from the analog domain to the digital one.

5. *CROSS* goes low, the *GC* value is saved into register *t2*. If *CROSS* switches again, *nt2* times, while *DCH* is low, the *GC* value for the last crossing is saved into register *t2f*.
6. *VE\_LC* goes low, i.e *Vctrl* is lower than the *VE\_L* limit.
7. *DCH* goes high again, the test period is finished; the *GC* value is saved to *t\_total*.

The voltage gap is then calculated as:

$$V\_GAP = |t\_total - t1 - t2| \times \frac{2(VH - VL)}{t\_total} \quad (7.1)$$

The circuit also record the number of crossings happening in one phase (charge or discharge), and calculate how far the first crossing point was from the last one according to the formulae:

$$(t1f - t1) \times \frac{2(VH - VL)}{t\_total} \dots (t2f - t2) \times \frac{2(VH - VL)}{t\_total} \quad (7.2)$$

### 7.2.2 Circuit simulations and results

In this section we report the results of the circuit simulations.

#### Simulation settings

The nanowire device is substituted by a current source implementing a I/V look-up table obtained from prior manual characterizations of the meristive devices. *Vbramp* is set at 3.91 V, *VL* to 100 mV, *VH* to 4.9V, *VE\_H* to 4V, and *VE\_L* to 800 mV. This configuration runs the test for 896 sec and checks for device failure for currents below 2 nA. The digital circuit was implemented in VHDL and simulated with a clock frequency of 1 Hz.

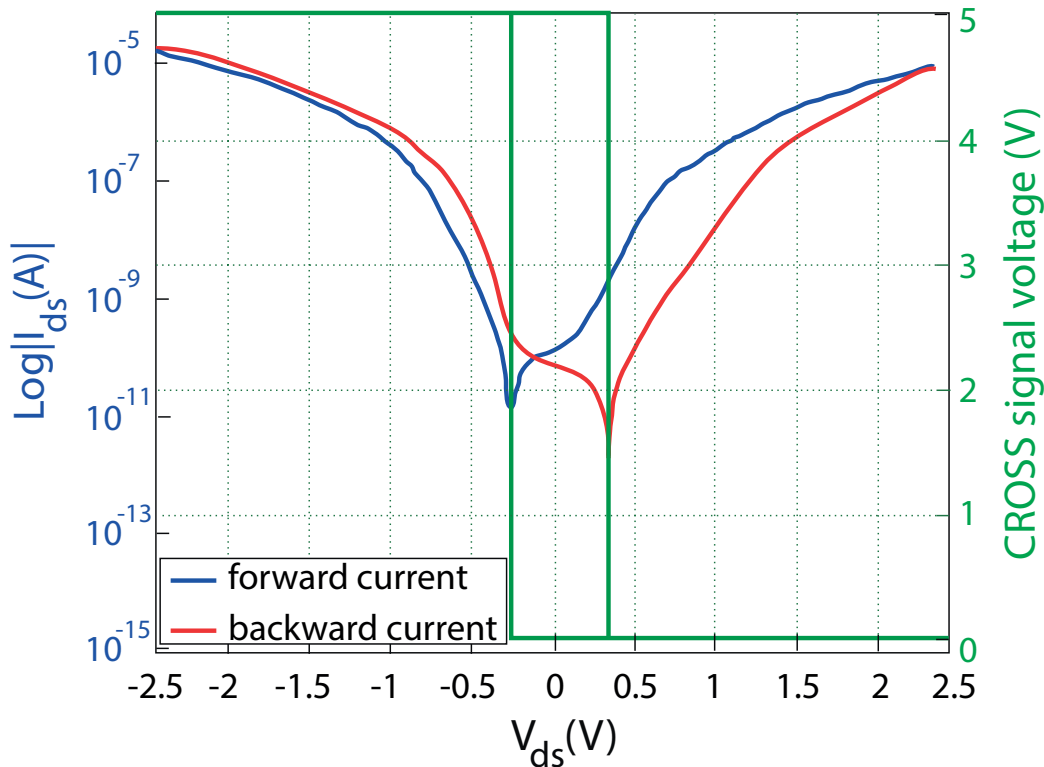


Figura 7.21 – Real measurements from a memristive device after biofunctionalization and antigen uptake are used as input signal of the simulation. The cross signal (green line) demonstrates the proper detection of the current crossings and thus the voltage gap.

### 7.2.3 Results

We ran simulations and post-layout simulations using many lookup tables that were extracted from different nanowires experimentally tested in the lab. Figure 7.21 shows the  $I_{ds} - V_{ds}$  current going through the nanowire ( $W = 100 \text{ nm}$  and  $L = 1 \mu\text{m}$ ) for one particular test run after biomodification of the device surface and antigen uptake. The blue curve is the semi-logarithmic plot of the absolute value of the current when sweeping the voltage from  $+2.5 \text{ V}$  to  $-2.5 \text{ V}$ , while the red one is for sweeping the voltage from  $-2.5 \text{ V}$  to  $+2.5 \text{ V}$ . The *CROSS* signals is indicated in green and it defines the circuit outcome. Notice that the current changes all the way from  $15.4 \mu\text{A}$  to  $0\text{A}$  where  $14.3 \text{ fA}$  is the last detectable value. This is almost  $10^9$  range difference which the circuit is able to react correctly to.

To note that the circuit introduces a small but non negligible error in the voltage gap estimation. For one particular device tested in real experiments, for example, the voltage gap produced by measured currents was  $0.6 \text{ V}$ , while the one produced by the *CROSS* signal when simulating this device with the circuit was  $0.605 \text{ V}$ . This difference is due to the delay between the current crossing zero, and *Vctrl* reacting to that and crossing *SENS\_P*. It is caused by the capacity *C1* in circuit of Figure 7.16 which is used to stabilize the negative feedback loop. This delay depends also on the slope of the zero crossing. If the transition is very slow/flat, this delay will grow



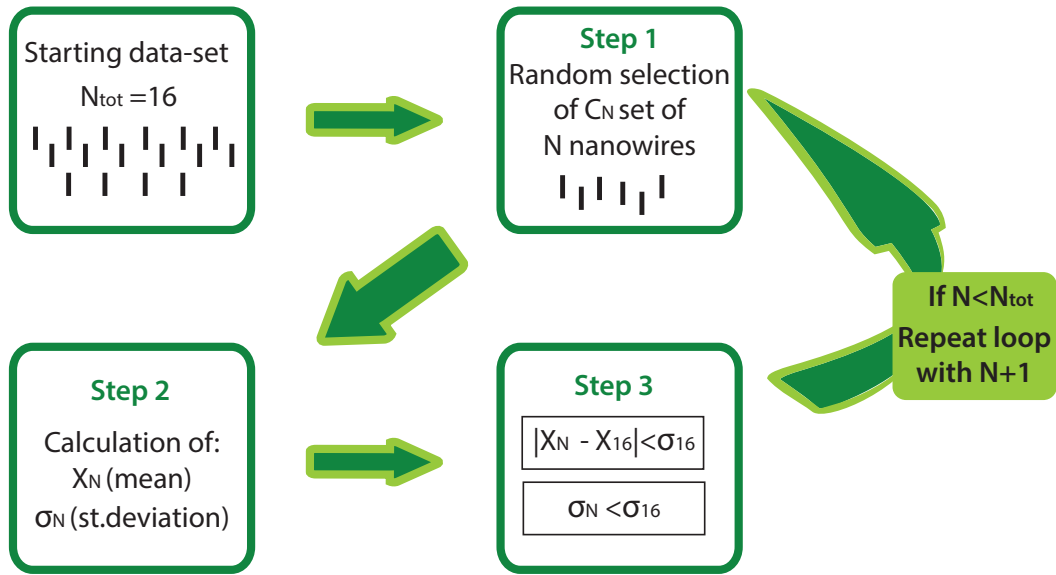


Figura 7.22 – Applied method for statistical analysis. The study consists of three major steps that have to be repeated  $T$  times for any subset containing  $N$  nanowires.

bigger, and vice versa. The delay translates to voltage since  $SENS\_N$  is changing linearly with time.

### 7.3 Redundancy in the voltage gap based biosensing platform

Both the microfluidics and the CMOS circuit we described above can be designed to fit any voltage gap biosensing platform with different number of VoG-biosensors in the array. To note that the chosen number of devices in the array could alter the reliability of the measurement. Indeed, if too few biosensors are used, the statistics resulting from their testing would not be significant. On the other hand, if the set of devices is too big, this could result in larger biosensing area, with the possible drawback of waste of biological material and longer experiments. In this thesis we observed by statistical analysis that it is possible to choose a level of redundancy in the platform to have reliable biosensing with minimum number of devices.

It is worth to mention that the concept of redundancy has been especially developed in electronics to keep such variations under control. In fact, the concept of redundancy has been already successfully proposed for several other domains such as programmable logic devices [188] and dynamic random access memory [189], to minimize the coding digits per message [190], failures selection [191], and other domains.

We adapted the same reasoning to our problem. We performed an experiment in which  $N_{tot} = 17$  devices were electrically tested under different conditions (bare surface, Ab-functionalization, Ab-Ag uptake), and corresponding data were used for t-test statistical analysis. The statistics was performed by considering all the possible  $C_N$  combinations obtainable with a given number  $N$  of devices and by comparing their average behavior  $X_N$  with the expected one, *i.e.* the

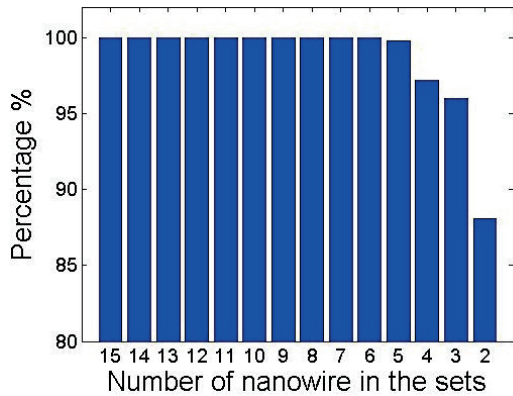


Figura 7.23 – Percentage of sets containing  $N$  bare sensors satisfying condition 1 on their voltage gap mean.

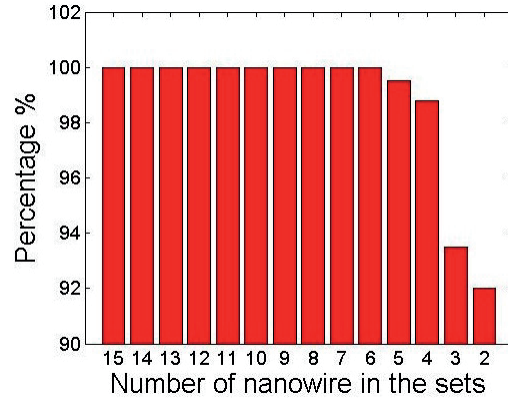


Figura 7.24 – Percentage of sets containing  $N$  Ab-sensors satisfying condition 1 on their voltage gap mean.

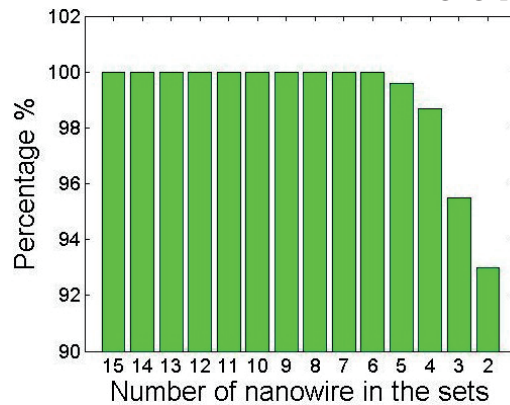


Figura 7.25 – Percentage of sets containing  $N$  Ab-Ag-sensors satisfying condition 1 on their voltage gap mean.

average voltage gap  $X_{tot}$  measured with the total number of available biosensors. Specifically, for each combination formed with a given number of devices, we imposed the two following conditions:

- Condition 1:  $|X_N - X_{tot}| < \sigma_{tot}$   
The deviation of the voltage gap mean value of the considered  $N$  biosensors ( $X_N$ ) must be smaller than the standard deviation of the voltage gap calculated on the total data-set of 16 nanowires  $\sigma_{tot}$ .
- Condition 2:  $\sigma_N < \sigma_{tot}$   
The standard deviation relative to the voltage gap measurement from  $N$  devices ( $\sigma_N$ ) must be smaller is smaller than  $\sigma_{tot}$ . If the two conditions are not satisfied, the loop starts again from step 1, for a different combination  $C_{n,i}$  of data.

### 7.3. Redundancy in the voltage gap based biosensing platform

---

These conditions state that, if the chosen number of devices, *i.e.* the set size  $N$ , gives, in average, a voltage gap that differs too much (more than the deviation  $\sigma_{tot}$  in the total data-set) from the expected result from all the available devices, and if these devices show a too large deviation (bigger than the one expressed by the full data-set), the tested set size is rejected. If it is rejected for all the possible combinations  $C_N$ , it means that the chosen number of device per set is too small and not able to reproduce the same outcome of the full data set. More wires, and thus more redundancy, is needed for reaching a statistically acceptable result. This process is schematically shown in Figure 7.22. The results showed interesting behavior. Importantly, we observed that by decreasing the number  $N$  of biosensors beyond a specific value ( $N = 6$  in the performed experiment) the acquired average voltage gap cannot be considered statistically significant. Any bigger number, instead, lead to the same reproducible result: 100% of the combinations formed by  $N$  determine the same voltage gap measurement we would observe with the total of the available devices. This is well represented by the outcome of the statistics performed on memristive devices before the surface modification (Figure 7.23), after the functionalization with antibody (Figure 7.24), and finally, in the case of antigen uptake (Figure 7.25). As a direct result, we can say that, for this specific case, the choice of using 6 devices would lead to reliable experimental outcome. If this statistical process was repeated for a bigger number of data-sets that would, in average, reproduce the overall properties of the fabricated VoG-biosensors, this principle could be generalized and used to define the average level of redundancy needed in the voltage gap based platform.

#### 7.3.1 Chapter summary and contributions

In this chapter we discussed the most recent developments in the proposed VoG-based biosensing technique, aiming at integrating the fabricated devices in a biosensing platform consisting of microfluidics and interface for external VoG readout circuit. The final goal would be the realization of portable, fast, and high performance multi-panel biosensing platforms.

In the first part, we discussed the design of a microfluidic device for achieving higher sensitivity and reducing the time of the experiments by speeding up the sensing measurement. We described in detail the fabrication process, including both the photolithographic patterning of Al lines and electrodes for future integration with ad-hoc designed circuit for testing, and the process flow for the formation of a PDMS microfluidic device. We showed the results of the fabrication procedures and demonstrated that microfluidics largely improves the bio-functionalization of the nanowires thanks to the achieved selectivity and higher flow-driven interaction rate. These results are very promising and will enable faster and more sensitive measurements of antigen detection.

Finally, as concluding part of the thesis, and link to future works, we also worked on a novel CMOS circuit that interfaces to VoG-biosensor arrays. The circuit has been designed and simulated. The results from the simulations of a  $2 \times 2$  instance of the circuit demonstrated the feasibility of our approach by showing that the reader is able to extract a 600 mV voltage gap with 5mV error in extremely large current range varying from  $\mu\text{A}$  to fA. Very recently, the circuit has been also fabricated; however, because of time constraints, the acquisition of voltage gap

measurements from real memristive biosensors has been referred to future joint work with the Oslo University. Nevertheless, simulation results showed the potentials for automated characterization of arrays of nanowires within few minutes whereas previous manual testing required few hours for SiNW sensors. Moreover, the proposed readout architecture, integrated with the digital part on a single chip, can also be scaled up to interface to a larger number of sensors, thus enabling fast and accurate multiplexed measurements for cancer marker detection or ligand profiling. The number of devices on the platform could be chosen by considering that there is a level of redundancy needed to have reliable behavior. This redundancy could be defined by performing an accurate t-test statistical analysis. The ultimate goal shall be to add the nanowires onto the same AMS 0.35  $\mu\text{m}$  CMOS substrate as the circuits.

The integration of both microfluidics and readout circuit with the novel proposed biosensing technology would allow the development of high-sensitive, fast and portable platforms where different arrays of memristive devices could be functionalized with different antibodies and target distinct specific antigens in the same tumor extract. This would further advance the research in early cancer biomarker detection, adding the opportunity for concurrently profiling angiogenic and inflammatory ligands in the breast tumor microenvironment.

## 8 Conclusions and outlook

This chapter outlines the major achievements of the thesis. It discusses the improvements and advantages of our biosensing nano-devices with respect to the state-of-the-art of SiNW-based technologies. Finally, the chapter provides some recommendations for future development and prospects for potential clinical diagnostics applications.

### 8.1 Main achieved results

The thesis pushed beyond the state-of-the-art nanoelectronics as applied to the detection of biomarkers in tumor tissues. It proposed both improvement and novelty in this research area. We developed major advancements with the objective of realizing a biosensor that, overcoming the main limitations of the traditional ISFET technology, enables the detection and the profiling of angiogenic and inflammatory ligands in the very hostile environment of patient breast tumor specimens. Considering the very low concentrations of these factors at the very early stage of the tumor disease, the thesis proposes technological opportunities for label-free, high-sensitive and specific cancer diagnostic tools.

Specifically, we first investigated the more standard SiNW-FET biosensing technology and improved the performance by combining both the high-quality properties of the fabrication process developed at the Delft University of Technology with the specificity of our biofunctionalization process and the proposed novel paradigm of measurement in dry conditions. We used this technology as benchmark for the development of the VoG-biosensing method with memristive devices, the biosensing properties of which were demonstrated both innovative and promising for future applications in cancer diagnosis and therapeutic treatments.

The main achievements of this work can be divided in two main categories corresponding to the results obtained with: (i) the conductance-based approach in SiNW-FET biosensors; (ii) the VoG-based approach in memristive biosensors.

### 8.1.1 Achievements with SiNW-FET biosensors

#### 1. High-sensitive detection in dry conditions

We enhanced the state-of-the-art of SiNW-FET biosensing technologies by pushing their sensitivity to the limit. The results demonstrates the detection of very small amount of biomarkers (order of few femtomolar) in the ideal phosphate buffered saline (PBS) solution and also in the more challenging tumor extract (TE). We achieved this goal by addressing the issue of the Debye screening length that is the main factor affecting the successful sensing in standard ISFET-based devices. We demonstrated to overcome this limitation by proposing the novel paradigm of in-air detection. Specific antigen uptake occurs in liquid while incubating the sensor in TE. Thanks to the strong interaction between antibody and antigen, the measurement can be subsequently carried out in dry conditions after repetitive washing steps and drying of the devices. Being the bulk of the solution removed, the biosensor features an increased Debye screening length, resulting in the increased responsiveness of the device to the electric field exerted by the charged biomarker, and thus, enhanced sensitivity.

#### 2. High specificity

We achieved high-performance biosensing with the SiNW-FET based devices thanks to the high-quality functionalization process. The biomodification process with antibodies consists of many steps of silicon surface treatments that have to be performed with extremely high accuracy for ensuring repeatability of the experiment. The most important requirement of a good quality receptor layer is its ability to provide sensing while at the same time preventing the nonspecific binding of proteins onto the biosensor surface. This is very critical when working in the tumor landscape because of the presence of large amount of nonspecific, charged species determining false signal in the detection measurement. We performed different tests of surface treatments with distinct surface agents, such as bovine serum albumin (BSA), spacer molecule like polyethyleneglycol (PEG) molecules, and gelatin from fish skin. We ensured the good specificity of the biosensing by choosing the best blocking treatment that was achieved with the use of gelatin from cold fish skin. We demonstrated the achieved specificity by showing that the uptake of nonspecific proteins did not occur as demonstrated by the absence of conductance signal.

#### 3. Detection of biomolecules in tumor extract

In the past few years, several groups have presented the successful detection of antigens with antibody-functionalized NW-FETs with a femto-molar sensitivity in an assay buffer solution [140, 146]. On the contrary, protein detection using nanowires has not been yet adopted to detect cancer in real human tumor samples due to the low signal-to-background. To the best of our knowledge, only few works have been published on SiNW-based sensing in extracts from tumor cells. They all demonstrate DNA detection [46, 75], and not the more challenging antibody/antigen based detection.

In this thesis we achieved femtomolar detection of biomolecules in real tumor extract

with 100.000 fold molar excess of nonspecific molecules. These results show that the approach used here already surpasses current state-of-the-art field effect based sensing with SiNWs. They open the way to future development of SiNW-FET based devices for detection and quantification of angiogenic and inflammatory ligands in real patient specimens.

### 8.1.2 Achievements with VoG-biosensors

#### 1. Top-down fabrication of vertically-stacked memristive SiNWs

The realization of vertically-stacked SiNWs succeeded out of many technological challenges. The outcome of the top-down fabrication process are Schottky barrier freestanding SiNWs bridging NiSi contacts. Two different geometries were designed: nanowires with higher aspect form, 1  $\mu\text{m}$  long and  $90 \pm 9$  nm wide; nanowires with smaller aspect form, 420 nm long and  $35 \pm 10$  nm wide. Both devices showed hysteresis in the  $I_{\text{ds}} - V_{\text{ds}}$  characteristics and peculiar behavior associated with a memristive effect that was revealed fundamental to the VoG-biosensing. The obtained structure were formed on a CMOS compatible substrate, thus enabling future integration of the biosensors with characterization circuit, humidity sensor circuit for calibration, as well as more advanced solutions such as differential configurations leading to digital antigen “absence/presence” reading for enlarged statistics.

#### 2. Biofunctionalization for high-specific biosensing

Although the employed top-down fabrication process, based on DRIE etching, led to nanowires featuring high surface roughness and large amount of surface defects, we achieved the formation of a pretty good layer of antibodies as surface receptors. Because the surface treatments were the same used for the modification of SiNW-FETs, also in this case we prevented nonspecific binding by using gelatin blockers. Despite the promising results, we have to note that some variability of voltage-gap acquisition in TE could also derive from non-perfect surface blocking as result of less homogeneous functionalization, as well as increased sensitivity of the devices having smaller aspect-form with respect to the SiNW-FETs.

#### 3. The voltage-gap (VoG) parameter

We performed a deep investigation of the varying characteristics in memristive nanowires under different surface treatments and external conditions. This led to the first demonstration of the biosensing capabilities of memristive silicon nanowires. This novel mechanism of biosensing is based on the so called *Voltage Gap* (VoG), that is the voltage difference forming between the forward and backward crossing points of the  $I_{\text{ds}} - V_{\text{ds}}$  curve with the x-axes. We showed that the VoG is created, in a very reproducible manner, as effect of biomolecule adsorption and binding to the nanowire surface. The importance of relative humidity was also pointed out, together with the need for future development aiming at automatically calibrate the biosensor for this factor. In addition, we demonstrated experimentally the effect of ionic species (Na, Cl, ammonia) on the

VoG that revealed the formation of a liquid-like thin film at the device surface enabling ionic mobility and interface phenomena.

#### 4. High-sensitive detection of biomarkers in tumor extract

We showed VoG based detection of biomarkers in the ideal PBS environment, demonstrating that the novel approach enabled us to achieve ultra-high sensitivity of VEGF (few femto moles) thanks to the specificity of the functionalization process, the resolution of the voltage-gap parameter, and the idea of measuring in air to reduce the Debye screening from ions typically big in bulk solution.

More importantly, we showed some successful results in the more complex breast tumor extract, where rabbit antigen species were diluted using 100.000 fold molar excess of nonspecific tumor proteins. This result is probably the most important achievement of the thesis because it demonstrates an innovative biosensing paradigm surpassing current limit of detection with the state-of-the-art silicon nanowire technologies.

All the performed experiments demonstrated that the memristive devices have zero or quasi-zero VoG when having bare surface after the modification process, whereas the biosensors feature an increase and a decrease of this parameter in the conditions of antibody functionalization and antigen uptake, respectively. Specifically, biosensing was enabled by observing the decreasing behavior of the VoG as a function of protein uptake.

#### 5. Modeling of the VoG-biosensing

We developed an original theory enabling the physical interpretation and prediction of the mechanisms underlying the VoG-biosensing method in memristive devices. We implemented and simulated an analytical, physics-based model able to reproduce and explain the VoG-based behavior in *Schottky Barriers* (SBs) SiNW sensors. This model considers the combinations of different effects of electrical transport at the surface of the device, inside the nanowire and at the Schottky barriers. Surface trap mediated electronic transport in the oxide of the SiNWs dominates over the other current contributions in determining the appearance and modulation of the voltage-gap. Importantly, the model successfully accounts for the detection of different concentrations of biomarkers for breast tumor screening, too. Together with the detection of femtomolar concentrated biomolecules in tumor extract, this is another relevant achievement of the thesis. Although more complex modeling strategies, such as molecular modeling or tight-binding modeling (electronic band structure modeling), could lead to deeper insights and determination of additional factors relevant to the biosensing mechanism, the theory developed in this thesis is the first theoretical evidence of the phenomena underlying the VoG behavior in memristive biosensors.

#### 6. Integration in microfluidics

We designed and fabricated a first prototype of a microfluidic device and we integrated it with a biosensing platform hosting an array of VoG-biosensors, with the aim of achieving higher sensitivity, reduced biomaterial waste and improved speed of the measurement.



In spite of the need for further tests, we already showed preliminary results of the integration. Importantly, the fabricated microfluidics was found to largely improve the biofunctionalization of the nanowires thanks to the achieved selectivity and increased flow-driven interaction rate. The microfluidic device will enable faster and more sensitive measurements of antigen detection.

### 7. Design and simulation of a CMOS circuit for multiplexed VoG-biosensors testing

Finally, thanks to the collaboration with the Oslo University, we designed and simulated a novel CMOS circuit that interfaces to memristive biosensor arrays. In this thesis, we reported the results from simulations of a  $2 \times 2$  instance of the circuit, demonstrating that it is able to extract a 600 mV VoG with 5mV error in extremely large current range varying from  $\mu\text{A}$  to fA. Very recently, the circuit has been also fabricated, but acquisition of VoG measurements from real memristive biosensors has been referred to future joint work with Oslo University because of time constraints. Simulation results showed the potentials for automated characterization of arrays of nanowires within few minutes whereas previous manual testing required few hours for SiNW sensors. Moreover, the proposed readout architecture can be scaled up to interface a larger number of sensors, thus enabling fast and accurate multiplexed measurements for cancer marker detection.

## 8.2 Prospects on future applications

Some of the possible applications we envisage to use the VoG-biosensor platform for are discussed here below:

- **Profiling of TEMs in breast tumor extract**

The doctoral project has been carried out in collaboration with Dr. Doucey's group, Ludwig Center for Cancer Research of the University of Lausanne, Switzerland. There, the research is focused on the reprogramming of *Tie-2 Associated Monocytes* (TEMs) in breast cancer into cells promoting protective anti-tumor immune responses. The idea relies on the observation that tumor-associated monocytes have an important and adaptive role in the development of the breast cancer. Recently, it has been shown that TEMs can display a high proangiogenic activity when shaped by specific signals in the local tumor microenvironment and controlled by the synergistic action of specific angiogenic and inflammatory protein pathway [192, 193]. This functional heterogeneity of monocytes likely reflects their plasticity and ability to readily adapt to cues from the environment in which they reside. Hence, a very promising strategy in cancer immunotherapy is the design of new approaches to reprogram the monocytes with anti-tumor properties [192–195]. But, in order to mount effective therapeutic monocyte reprogramming strategies, a comprehensive understanding of the functional variations of TEMs in response to interactions with their tumor microenvironment is needed. Thanks to the high sensitivity and specificity, our technologies will enable extensive characterization of TEMs and their microenvironment at the single cell level. The detection

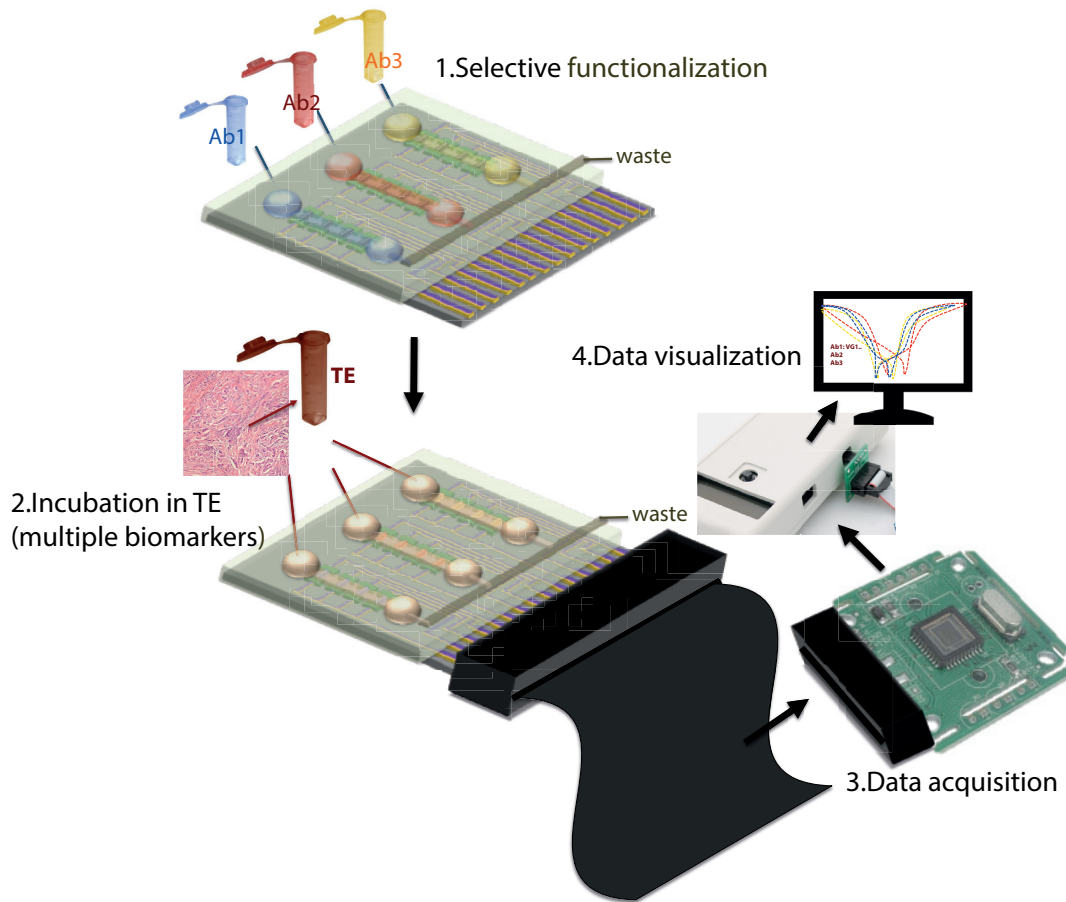


Figura 8.1 – Prototype of a portable biosensing platform based on high-sensitive VoG devices functionalized with different antibodies (Ab1, Ab2, Ab3). The platform will be used for in-lab, fast, automated, and multiplexed detection of biomarkers in tumor extract (TE).

will be performed as already described previously, after incubation in tumor extract and measurements in dry conditions. To prepare the tumor extract, the tumor zones from a section will be dissected by laser capture micro-dissection under a microscope, lysed and electrically characterized with the nanowire array.

• **Multiplexed VoG-detection of biomarkers in the tumor microenvironment**


A further advancement will consist of using the nanowire arrays functionalized with multiple antibodies for multiplexed detection of different ligands to capture the TEM landscape. The biomedical application we envisage for the VoG-biosensors is sketched in Figure 8.1. The figure report a possible prototype for a memristive biosensor platform enabling high-sensitive, fast, automated and portable multiplexed VoG-acquisition for multi-biomarkers detection in tumor extract. An SOI chip hosts an array of VoG-biosensors. Each line in the array is functionalized by means of a microfluidic device with different antibody (Ab1, Ab2, Ab3 in the figure). The same microfluidic is used to deliver a sample of human breast TE to the array of biosensors. Because of the

different molecular probes immobilized on the devices, each line of biosensors in the array targets only one type of biomarkers in the tumor extract, and thus produces a VoG signal in response to the specific protein. Each biosensors can be electrically tested thanks to external metal electrodes. An external circuit, connected to the sensing chip through a connector, concurrently addresses the different biosensors. This enables parallel electrical acquisition on the total number of VoG devices in the platform, and detection of three, or more, breast tumor markers. The data can be sent to an external device for the visualization of the results. Such a system will permit the analysis of the TEM landscape thanks to the concurrent high-sensitive detection of a number of tumor proteins, fast acquisition and readout.

- **Detection of biomarkers by direct chip/tissue slide contact**

A further innovative approach to characterize TEM microenvironment in breast tumor tissue will be to place the VoG-biosensors array directly in contact with a 5  $\mu\text{m}$  slice of tumor tissue section (the chip facing the tissue). Multiples arrays will be used to cover the whole tissue section. The arrays will be left in contact with the tumor section for an optimal time to determine experimentally. The array will be then washed, dried and the VoG will be acquired in dry conditions. This experiment does not use the microfluidic device. The position of each array at the surface of the tumor section will be carefully reported using a special tissue ink. Then, the tissue section will be fixed and stained with antibodies specific for monocyte and other ligands such as cytokeratin. This stained tumor slice will be examined by confocal microscopy to locate the distinct TEM populations in the tumor tissue. Assembling confocal microscopy and VoG results will allow us to capture the inflammatory landscape of TEM and to identify the specific features of their microenvironment. If this approach is successful, different array panels will be designed and used to accurately capture additional variations of the TEM landscape. In conclusion, the experiments that we propose with the nanowires arrays will allow us to compare the performances of detection using FET- and memristive nanowire arrays. Most importantly, these experiments will enable the characterization of both TEM and TEM microenvironment, which represents the first step to design treatments reversing TEM pro-tumoral activity.



- 
- [1] E.M. Raymo and I. Yildiz. Luminescent chemosensors based on semiconductor quantum dots. *Phys. Chem. Chem. Phys.*, 9:2036–2043, 2007.
- [2] N.C. Tansil and Z. Gao. Nanoparticles in biomolecular detection. *Nano Today*, 1(1):28 – 37, 2006.
- [3] S.-J. Park, T.A. Taton, and C.A. Mirkin. Array-Based Electrical Detection of DNA with Nanoparticle Probes. *Science*, 295(5559):1503–1506, 2002.
- [4] A.M. Morales and C.M. Lieber. A laser ablation method for the synthesis of crystalline semiconductor nanowires. *Science*, 279(5348):208–211, 1998.
- [5] Y. Cui, L. J. Lauhon, M.S. Gudiksen, J. Wang, and C. M. Lieber. Diameter-Controlled Synthesis of Single Crystal Silicon Nanowires. *Applied Physics Letters*, 78, 2001.
- [6] X. Duan, Y. Huang, Y. Cui, J. Wang, and C.M. Lieber. Indium phosphide nanowires as building blocks for nanoscale electronic and optoelectronic devices. *Nature*, 409:66 – 69, 2001.
- [7] J. Hu, T.W. Odom, and C.M. Lieber. Chemistry and physics in one dimension: Synthesis and properties of nanowires and nanotubes. *Account of Chemical Society*, 32(5):435–445, 1999.
- [8] X. Liang and S. Y. Chou. Nanogap Detector Inside Nanofluidic Channel for Fast Real-Time Label-Free DNA Analysis. *Nano Letters*, 8(5):1472–1476, 2008.
- [9] N. L. Rosi and C. A. Mirkin. Nanostructures in Biodiagnostics. *Chemical Reviews*, 105(4):1547–1562, 2005.
- [10] K. K. Jain. Applications of biochips: from diagnostics to personalized medicine. *Current Opinion in Drug Discovery & Development*, 7(3):285–289, 2004.
- [11] C. P. Sun, J. C. Liao, Y. H. Zhang, V. Gau, M. Mastali, J. T. Babbitt, W. S. Grundfest, B. M. Churchill, and D. A. Haake E. R. McCabe. Rapid, species-specific detection of uropathogen 16S rDNA and rRNA at ambient temperature by dot-blot hybridization and an electrochemical sensor array. *Molecular Genetics and Metabolism*, 84(1):90 – 99, 2005.

## Bibliografia

---

- [12] M. Curreli, R. Zhang, F. N. Ishikawa, H.K. Chang, R. J. Cote, C. Zhou, and M. E. Thompson. Real-time, label-free detection of biological entities using nanowire-based fetts. *IEEE Transactions on Nanotechnology*, 7:651–667, 2008.
- [13] D. Kim, M.A. Lim, D. Yang, Z. Li, C.O. Park, and I. Park. Ultra-sensitive, low-power and flexible h2s sensors based on palladium nanoparticle-coated metal oxide nanowires. In *Micro Electro Mechanical Systems (MEMS), 2012 IEEE 25th International Conference on*, pages 1372–1375, 2012.
- [14] H. Kim, C. Jin, S. An, and C. Lee. Fabrication and {CO} gas-sensing properties of pt-functionalized ga2o3 nanowires. *Ceramics International*, 38(5):3563 – 3567, 2012.
- [15] F. Miao, B. Tao, and Paul P.K. Chu. Preparation and electrochemistry of pd-ni/si nanowire nanocomposite catalytic anode for direct ethanol fuel cell. *Dalton Trans.*, 41:5055–5059, 2012.
- [16] Z. Ye, H. Liu, I. Schultz, W. Wu, D.G. Naugle, and I. Lyuksyutov. Template-based fabrication of nanowire–nanotube hybrid arrays. *Nanotechnology*, 19(32):325303, 2008.
- [17] H. J. Fan, P. Werner, and M. Zacharias. Semiconductor nanowires: From self-organization to patterned growth. *Small*, 2:700–717, 2006.
- [18] J. Li, Y. Zhang, S. To, L. You, and Y. Sun. Effect of Nanowire Number, Diameter, and Doping Density on Nano-FET Biosensor Sensitivity. *ACS Nano*, 5(8):6661–6668, 2011.
- [19] X.P.A. Gao, G. Zheng, and C.M. Lieber. Subthreshold regime has the optimal sensitivity for nanowire fet biosensors. *Nano Letters*, 10(2):547–552, 2010.
- [20] P. Bergveld. Development of an Ion-Sensitive Solid-State Device for Neurophysiological Measurements. *Biomedical Engineering, IEEE Transactions on*, BME-17(1):70–71, 1970.
- [21] P. Bergveld and A. Sibbald. *Analytical and Biomedical Applications of Ion-Selective Field-Effect Transistors*. Elsevier, Amsterdam, 1988.
- [22] J. Janata, M. Josowicz, P. Vanysek, and D. M. DeVaney. Recent advances in biologically sensitive field-effect transistors (BioFETs). *Analytical Chemistry*, 70:179R–208R, 1998.
- [23] M. Chudy, W. Wróblewski, A. Dybko, and Z. Brzózka. Multi-ion analysis based on versatile sensor head. *Sensors and Actuators B: Chemical*, 78(1–3):320 – 325, 2001.
- [24] G. Taillades, O. Valls, A. Bratov, C. Dominguez, A. Pradel, and M. Ribes. {ISE} and {ISFET} microsensors based on a sensitive chalcogenide glass for copper ion detection in solution. *Sensors and Actuators B: Chemical*, 59(2–3):123 – 127, 1999.
- [25] M.J. Schoning and A. Poghossian. Recent advances in biologically sensitive field-effect transistors (biofets). *Analyst*, 127:1137–1151, 2002.
- [26] P. Bergveld. The future of biosensors. *Sensors and Actuators A: Physical*, 56:65–73, 1996.

- [27] T. Vo-Dinh and B. Cullum. Biosensors and biochips: advances in biological and medical diagnostics. *Fresenius' Journal of Analytical Chemistry*, 366:540–551, 2000.
- [28] G. F. Blackburn. pages 481–530. I. Karube and G. S. Wilson, Oxford University Press, Oxford, 1987.
- [29] F. Patolsky and C. M. Lieber. Nanowire nanosensors. *Materials Today*, 8:20–28, 2005.
- [30] X. Duan and C. M. Lieber. Semiconductor nanowire: Whats next? *Nano Letters*, 10:1529–1536, 2010.
- [31] X. Duan and C. M. Lieber. General synthesis of compound semiconductor nanowires. *Advanced Materials*, 12:298–302, 2000.
- [32] C.M. Lieber. Nanoscale science and technology: Building a big future from small things. *MRS Bulletin*, 28:483–491, 2003.
- [33] P. Mohanty, Y Chen, X. Wang, M.K. Hong, C.L. Rosenberg, D.T. Weaver, and S. Erramilli. *Invited Review in Biosensors and Molecular Technologies for Cancer Diagnostics*. CRC Press, 2012.
- [34] N. Elfstrom, R. Sychugov, T. Karlstrom, and A.E. Linnros. Surface charge sensitivity of silicon nanowires: Size dependence. *Nano Letters*, 7(9):2608–2612, 2007.
- [35] F. Patolsky, G. Zheng, and C. M. Lieber. Nanowire sensors for medicine and the life sciences. *Nanomedicine*, 1:51–56, 2006.
- [36] I. Park, Z. Li, A. P. Pisano, and R. S. Williams. Selective surface functionalization of silicon nanowires via nanoscale joule heating. *Nano Letters*, 7(10):3106–3111, 2007.
- [37] Y. Cui, Q. Wei, H. Park, and C. M. Lieber. Nanowire nanosensors for highly sensitive and selective detection of biological and chemical species. *Science*, 293(5533):1289–1292, 2001.
- [38] Y. Cui, X. Duan, J. Hu, and C. M. Lieber. Doping and electrical transport in silicon nanowires. *Accounts of Chemical Research*, 104(22):5213–5216, 2000.
- [39] Y. Cui, J. Wang, X. Duan, Y. Huang, and C.M. Lieber. Indium phosphide nanowires as building blocks for nanoscale electronic and optoelectronic devices. *Nature*, 409:66–69, 2001.
- [40] R. K. Iler. *The Chemistry of Silica*. Wiley, New York, 1979.
- [41] P. N. Barlett. *Modification of Sensor*. IOP Publishing Ltd, London, 1996.
- [42] S. M. Sze and K. K. Ng. *Physics of Semiconductor Devices, Third Edition*. John Wiley & Sons, New York, 2007.

## Bibliografia

---

- [43] C. M. Lieber and Ji. Hahm. Direct Ultrasensitive Electrical Detection of DNA and DNA Sequence Variations Using Nanowire Nanosensors. *Nano Letters*, 4(1):51–54, 2004.
- [44] F. Patolsky, G. Zheng, O. Hayden, M. Lakadamyali, X. Zhuang, and C. M. Lieber. Electrical detection of single viruses. *Proceedings of the National Academy of Sciences of the United States of America*, 101(39):14017–14022, 2004.
- [45] Y. Cui, Z. Zhong, D. Wang, W. U. Wang, and C. M. Lieber. High Performance Silicon Nanowire Field Effect Transistors. *Nano Letters*, 3(2):149–152, 2003.
- [46] G. Zheng, F. Patolsky, Y. Cui, W. U. Wang, and C. M. Lieber. Multiplexed electrical detection of cancer markers with nanowire sensor arrays. *Nature biotechnology*, 23(10):1294–1301, 2005.
- [47] A. Kim, C. S. Ah, H. Y. Yu, J.-H. Yang, I.-B. Baek, C.-G. Ahn, C.-W. Park, M. S. Jun, and S. Lee. Ultrasensitive, label-free, and real-time immunodetection using silicon field-effect transistors. *Applied Physics Letters*, 91:103901, 2007.
- [48] C. Li, M. Curreli, H. Lin, B. Lei, F. Ishikawa, R. Datar, R. J. Cote, M. E. Thompson, and C. Zhou. Complementary detection of prostate-specific antigen using  $\text{In}_2\text{O}_3$  nanowires and carbon nanotubes. *Journal of the American Chemical Society*, 127(36):12484–12485, 2005.
- [49] CMOS-compatible, label-free silicon-nanowire biosensors to detect cardiac troponin I for acute myocardial infarction diagnosis. *Biosensors and Bioelectronics*, 34(1):267 – 272, 2012.
- [50] J. H. Chua, R.-Er. Chee, A. Agarwal, S. M. Wong, and G.-J. Zhang. Label-Free Electrical Detection of Cardiac Biomarker with Complementary Metal-Oxide Semiconductor-Compatible Silicon Nanowire Sensor Arrays. *Analytical Chemistry*, 81(15):6266–6271, 2009.
- [51] W.U. Wang, C. Chen, K. Lin, Y. Fang, and C.M. Lieber. Label-free detection of small-molecule–protein interactions by using nanowire nanosensors. *Proceedings of the National Academy of Sciences of the United States of America*, 102(9):3208–3212, 2005.
- [52] E. Stern, J. F. Klemic, D. A. Routenberg, P. N. Wyrembak, D. B. Turner-Evans, A. D. Hamilton, D. A. LaVan, T. M. Fahmy, and M. A. Reed. Label-free immunodetection with CMOS-compatible semiconducting nanowires. *Nature*, 445:519–522, 2007.
- [53] Z. Gao, A. Agarwal, A.D. Trigg, N. Singh, C. Fang, C.H. Tung, Y. Fan, K.D. Buddharaju, and J. Kong. Silicon Nanowire Arrays for Label-Free Detection of DNA. *Analytical Chemistry*, 79(9):3291–3297, 2007.
- [54] J. I. Hahm and C. M. Lieber. Direct Ultrasensitive Electrical Detection of DNA and DNA Sequence Variations Using Nanowire Nanosensors. *Nano Letters*, 4:51–54, 2004.



- [55] A. Gao, Y. Chen, X. Li, T. I. Kamins, K. Nauka, and R. S. Williams. Enhanced sensing of nucleic acids with silicon nanowire field effect transistor biosensors. *Nano Letters*, 12:5262–5268, 2012.
- [56] Z. Li, Y. Chen, X. Li, T. I. Kamins, K. Nauka, and R. S. Williams. Sequence-Specific Label-Free DNA Sensors Based on Silicon Nanowires. *Nano Letters*, 4:245–247, 2004.
- [57] E. Stern, A. Vacic, and M.A. Reed. Semiconducting nanowire field-effect transistor biomolecular sensors. *Electron Devices, IEEE Transactions on*, 55(11):3119–3130, 2008.
- [58] Y. L. Bunimovich, Y.S. Shin, W.S. Yeo, M. Amori, G. Kwong, and J.R. Heath. Quantitative Real-Time Measurements of DNA Hybridization with Alkylated Nonoxidized Silicon Nanowires in Electrolyte Solution. *Journal of the American Chemical Society*, 128:16323–16331, 2006.
- [59] P.-L. Chiang, T.-C. Chou, T.-H. Wu, C.-C. Li, C.-D. Liao, J.-Y. Lin, M.-H. Tsai, C.-C. Tsai, C.-J. Sun, C.-H. Wang, J.-M. Fang, and Y.-T. Chen. Nanowire Transistor-Based Ultrasensitive Virus Detection with Reversible Surface Functionalization. *Chemistry Asian Journal*, 7(9):2073–2079, 2012.
- [60] G.-J. Zhang, L. Zhang, M.J. Huang, Z.H.H. Luo, G.K.I. Tay, E.-J.A. Lim, T.G. Kang, and Y. Chen. Silicon nanowire biosensor for highly sensitive and rapid detection of Dengue virus. *Sensors and Actuators, B: Chemical*, 143:138–144, 2010.
- [61] F. Patolsky, B.P. Timko, Yu. G. Y. Fang, A.B. Greytak, G. Zheng, and C.M. Lieber. Detection, stimulation, and inhibition of neuronal signals with high-density nanowire transistor arrays. *Science*, 313:1100–1104, 2006.
- [62] Q. Qing, S.K. Pal, B. Tian, B.P. Timko X. Duan, T. Cohen-Karni, V.N. Murthy, and C.M. Lieber. Nanowire transistor arrays for mapping neural circuits in acute brain slices. *Proceedings of the National Academy of Sciences of the United States of America*, 107:1882–1887, 2010.
- [63] T. Cohen-Karni, B. P. Timko, L. E. Weiss, and C. M. Lieber. Flexible electrical recording from cells using nanowire transistor arrays. *Proceedings of the National Academy of Sciences*, 106(18):7309–7313, 2009.
- [64] J. F. Eschermann, R. Stockmann, M. Hueske, X. T. Vu, S. Ingebrandt, and A. Offenhäusser. Action potentials of HL-1 cells recorded with silicon nanowire transistors. *Applied Physics Letters*, 95(8), 2009.
- [65] T.S. Pui, A. Agarwal, F. Ye, N. Balasubramanian, and P. Chen. Cmos-Compatible Nanowire Sensor Arrays for Detection of Cellular Bioelectricity. *Small*, 5(2):208–212, 2009.
- [66] A. Poghossian, S. Ingebrandt, A. Offenhäusser, and M.J. Schöning. Field-effect devices for detecting cellular signals. *Seminars in Cell Developmental Biology*, 20(1):41 – 48, 2009.

## Bibliografia

---

- [67] B. Tian, T. Cohen-Karni, Q. Qing, X. Duan, P. Xie, and C. M. Lieber. Three-Dimensional, Flexible Nanoscale Field-Effect Transistors as Localized Bioprobes. *Science*, 329(5993):830–834, 2010.
- [68] E. Stern, R. Wagner, F. J. Sigworth, T. M. Fahmy R. Breaker, and M. A. Reed. Importance of the Debye Screening Length on Nanowire Field Effect Transistor Sensors. *Nano Letters*, 7(11):3405–3409, 2007.
- [69] K.-I. Chena, B.-R. Lia, and Y.-T. Chen. Silicon nanowire field-effect transistor-based biosensors for biomedical diagnosis and cellular recording investigation. *Nano Today*, 6(2):131 – 154, 2011.
- [70] S. Carrara, B. Vijayender, C. Stagni, L. Benini, A. Ferretti, F. Valle, A. Gallotta, B. Riccò, and B. Samorí. Label-free cancer markers detection by capacitance biochip. *Sensors and Actuators B: Chemical*, 136(1):163 – 172, 2009.
- [71] G.-J. Zhang, J. H. Chua, R.-E. Chee, A. Agarwal, and S. M. Wong. Label-free direct detection of MiRNAs with silicon nanowire biosensors. *Biosensors and Bioelectronics*, 24(8):2504 – 2508, 2009.
- [72] W. L. Rutten. Selective electrical interfaces with the nervous system. *Annual Review of Biomedical Engineering*, 4:407–452, 2002.
- [73] G.J. Zhang, G. Zhang, J.H. Chua, R.E. Chee, E.H. Wong, A. Agarwal, K.D. Buddharaju, N. Singh, Z. Gao, and N. Balasubramanian. DNA Sensing by Silicon Nanowire: Charge Layer Distance Dependence. *Nano Letters*, 8:1066–1070, 2008.
- [74] J. N. Israelachvili. *Intermolecular & Surface Forces, 2nd Ed.* Academic Press, London, 1991.
- [75] G.-J. Zhang, M.J. Huang, J.J. Ang, E.T. Liu, and K.V. Desai. Self-assembled monolayer-assisted silicon nanowire biosensor for detection of protein–DNA interactions in nuclear extracts from breast cancer cell. *Biosensors and Bioelectronics*, 26(7):3233 – 3239, 2011.
- [76] O. Knopfmacher, A. Tarasov, W. Fu, M. Wipf, B. Niesen, M. Calame, and C. Schönenberger. Nernst limit in dual-gated Si-nanowire FET sensors. *Nano Letters*, 10(6):2264–2274, 2010.
- [77] T. Prodromakis and C. Toumazou. A review on memristive devices and applications. In *Electronics, Circuits, and Systems (ICECS), 2010 17th IEEE International Conference on*, pages 934–937, 2010.
- [78] D. Sacchetto, P.-E. Gaillardon, M. Zervas, S. Carrara, G. De Micheli, and Y. Leblebici. Applications of Multi-Terminal Memristive Devices: A Review. *Circuits and Systems Magazine, IEEE*, 13(2):23–41, Second Quarter 2013.
- [79] G.K. Johnsen. An introduction to the memristor—a valuable circuit element in bioelectricity and bioimpedance. *Journal of Electrical Bioimpedance*, 3(1):20–28, 2012.

- [80] L. O. Chua. Memristor - the missing circuit element. *IEEE Transactions on Circuit Theory*, 18(5):507–519, 1971.
- [81] L.O. Chua and S.M. Kang. Memristive devices and systems. *Proceedings of the IEEE*, 64(2):209–223, 1976.
- [82] D.B. Strukov, G.S. Snider, D.R. Stewart, and R.S. Williams. The missing memristor found. *Nature*, 453(7191):80–83, 2008.
- [83] S. Ecoffey, M. Mazza, V. Pott, D. Bouvet, A. Schmid, Y. Leblebici, M.J. Declercq, and A.M. Ionescu. A new logic family based on hybrid MOSFET-polysilicon nanowires. In *Electron Devices Meeting, 2005. IEDM Technical Digest. IEEE International*, pages 269–272, Dec 2005.
- [84] S.H. Jo, K.-H. Kim, and W. Lu. High-Density Crossbar Arrays Based on a si Memristive System. *Nano Letters*, 9(2):870–874, 2009.
- [85] J. Borghetti, Z. Li, J. Straznicky, D.A.A. Ohlberg X. Li, D.R. Stewart W. Wu, and W.R. Stanley. A hybrid nanomemristor/transistor logic circuit capable of self-programming. *Proceedings of the National Academy of Sciences*, 2009.
- [86] D. Sacchetto, M. Zervas, Y. Temiz, G. De Micheli, and Y. Leblebici. Resistive Programmable Through-Silicon Vias for Reconfigurable 3-D Fabrics, year=2012, volume=11, number=1, pages=8-11, month=Jan., *Nanotechnology, IEEE Transactions on*.
- [87] D. Sacchetto, M. Zervas, Y. Temiz, G. De Micheli, and Y. Leblebici. GMS: Generic Memristive Structure for Non-Volatile FPGAs. *Proc. 2012 IEEE/IFIP 20th Int. Conf. VLSI and Ssystem-on-Chip (VLSI-SoC)*, pages 94–98, 2012.
- [88] V. Y.Pershin and M. Di Ventra. Experimental demonstration of associative memory with memristive neural networks. *Neural Networks*, 23(7):881 – 886, 2010.
- [89] X. Duan, Y. Huang, and C.M. Lieber. Nonvolatile memory and programmable logic from molecule-gated nanowires. *Nano Letters*, 2(5):487–490, 2002.
- [90] D. Sacchetto, M.H. Ben-Jamaa, G. De Micheli, and Y. Leblebici. Fabrication and characterization of vertically stacked gate-all-around si nanowire fet arrays. In *Solid State Device Research Conference, 2009. ESSDERC '09. Proceedings of the European*, pages 245–248, 2009.
- [91] H.M. Ben Jamaa, S. Carrara, J. Georgiou, N. Archontas, and G. De Micheli. Fabrication of memristors with poly-crystalline silicon nanowires. In *Nanotechnology, 2009. IEEE-NANO 2009. 9th IEEE Conference on*, pages 152–154, 2009.
- [92] D. Sacchetto, M.H. Ben-Jamaa, S. Carrara, G. De Micheli, and Y. Leblebici. Memristive devices fabricated with silicon nanowire schottky barrier transistors. In *Circuits and Systems (ISCAS), Proceedings of 2010 IEEE International Symposium on*, pages 9–12, 2010.

## Bibliografia

---

- [93] D. Sacchetto, G. De Micheli, and Y. Leblebici. Ambipolar si nanowire field effect transistors for low current and temperature sensing. In *Solid-State Sensors, Actuators and Microsystems Conference (TRANSDUCERS), 2011 16th International*, pages 2562–2565, 2011.
- [94] D. Sacchetto, M.-A. Doucey, G. De Micheli, Y. Leblebici, and S. Carrara. New Insight on Bio-sensing by Nano-fabricated Memristors. *BioNanoScience*, 1(1):1–3, 2011.
- [95] S. Carrara, D. Sacchetto, M.-A. Doucey, C. Baj-Rossi, G. De Micheli, and Y. Leblebici. Memristive-biosensors: A new detection method by using nanofabricated memristors. *Sensors and Actuators B: Chemical*, 171–172:449 – 457, 2012.
- [96] I. Park, Z. Li, A.P. Pisano, and R.S. Williams. Top-down fabricated silicon nanowire sensors for real-time chemical detection. *Nanotechnology*, 21(1):015501, 2010.
- [97] S. Kim, T. Rim, K. Kim, U. Lee, E. Baek, H. Lee, C.-K. Baek, M. Meyyappan, M.J. Deen, and J.-S. Lee. Silicon nanowire ion sensitive field effect transistor with integrated Ag/AgCl electrode: ph sensing and noise characteristics. *Analyst*, 136:5012–5016, 2011.
- [98] A. Gao, L. Na, P. Dai, T. Li, H. Pei, X. Gao, Y. Gong, Y. Wang, and C. Fan. Silicon-nanowire-based cmos-compatible field-effect transistor nanosensors for ultrasensitive electrical detection of nucleic acids. *Nano Letters*, 11(9):3974–3978, 2011.
- [99] C.-. Lin, C.-H. Hung, C.-Y. Hsiao, H.-C. Lin, F.-H. Ko, and Y.-S. Yang. Poly-silicon nanowire field-effect transistor for ultrasensitive and label-free detection of pathogenic avian influenza {DNA}. *Biosensors and Bioelectronics*, 24(10):3019 – 3024, 2009.
- [100] F. Puppò, M.-A. Doucey, T.S.Y. Moh, G. Pandraud, P.M. Sarro, G. De Micheli, and S. Carrara. Femto-molar sensitive field effect transistor biosensors based on silicon nanowires and antibodies. In *SENSORS, 2013 IEEE*, pages 1–4, 2013.
- [101] F. Puppò, M.-A. Doucey, J.-F. Delaloye, T.S.Y. Moh, G. Pandraud, P.M. Sarro, G. De Micheli, and S. Carrara. SiNW-FET in-Air Biosensors for High Sensitive and Specific Detection in Breast Tumor Extract. *Sensors Journal, IEEE*, PP(99):1–1, 2015.
- [102] F. Puppò, A. Dave, M.-A. Doucey, D. Sacchetto, C. Baj-Rossi, Y. Leblebici, G. De Micheli, and S. Carrara. Memristive Biosensors Under Varying Humidity Conditions. *IEEE Transactions on Nanobioscience*, 13(1):19–30, 2014.
- [103] F. Puppò, M. Di Ventra, G. De Micheli, and S. Carrara. Memristive sensors for pH measure in dry conditions. *Surface Science*, 624:76 – 79, 2014.
- [104] F. Puppò, F.L. Traversa, M. Di Ventra, G. De Micheli, and S. Carrara. Surface trap mediated electronic transport in bio-functionalized silicon nanowires. *Submitted to Nanotechnology*, 2016.

- [105] F. Qian, Y. Li, S. Gradečak, D. Wang, C.J. Barrelet, and C.M. Lieber. Gallium Nitride-Based Nanowire Radial Heterostructures for Nanophotonics. *Nano Letters*, 4(10):1975–1979, 2004.
- [106] V. Schmidt, J.V. Wittemann, S. Senz, and U. Gösele. Silicon Nanowires: A Review on Aspects of their Growth and their Electrical Properties. *Advanced Materials*, 21:2681–2702, 2009.
- [107] C.H. Lee, D.R. Kim, and X. Zheng. Orientation-Controlled Alignment of Axially Modulated pn Silicon Nanowires. *Nano Letters*, 10(12):5116–5122, 2010.
- [108] L. Schubert, P. Werner, N.D. Zakharov, F.M. Kolb, G. Gerth, U. Gösele, L. Long, and T.Y. Tan. Silicon nanowhiskers grown on Si <111>substrates by molecular-beam epitaxy. *Applied Physics Letters*, 84(24):4968–4970, 2004.
- [109] T.I. Kamins, R.S. Williams, X. Li, and X. Liu. Growth and Structure of Chemically Vapor Deposited Ge Nanowires on Si Substrates. *Nano Letters*, 4(3):503–506, 2004.
- [110] A.M. Morales and C.M. Lieber. A Laser Ablation Method for the Synthesis of Crystalline Semiconductor Nanowires. *Science*, 279(5348):208–211, 1998.
- [111] K.M. Ryan, A. Mastroianni, K.A. Stancil, H. Liu, and A.P. Alivisatos. Electric-Field-Assisted Assembly of Perpendicularly Oriented Nanorod [s]uperlattices. *Nano Letters*, 6(7):1479–1482, 2006.
- [112] S. Raychaudhuri, S.A. Dayeh, D. Wang, and E.T. Yu. Precise Semiconductor Nanowire Placement Through Dielectrophoresis. *Nano Letters*, 9(6):2260–2266, 2009.
- [113] E.M. Freer, O. Grachev, X. Duan, S. Martin, and D.P. Stumbo. High-yield self-limiting single-nanowire assembly with dielectrophoresis. *Nature Nanotechnology*, 5:525–530, 2005.
- [114] Y. Huang, X. Duan, Q. Wei, and C.M. Lieber. Directed Assembly of One-Dimensional Nanostructures into Functional Networks. *Science*, 291(5504):630–633, 2001.
- [115] H. Yan, H.S. Choe, S.W. Nam, Y. Hu, S. Das, J.F. Klemic, J.C. Ellenbogen, and C.M. Lieber. Programmable nanowire circuits for nanoprocessors. *Nature*, 470(7333):240–244, 2011.
- [116] R. Sharma and M.S. Strano. Centerline Placement and Alignment of Anisotropic Nanotubes in High Aspect Ratio Cylindrical Droplets of Nanometer Diameter. *Advanced Materials*, 21(1), 2009.
- [117] T.-W. Lin, P.-J. Hsieh, C.-L. Lin, Y.-Y. Fang, J.-X. Yang, C.-C. Tsai, P.-L. Chiang, C.-Y. Pan, and Y.-T. Chen. Label-free detection of protein-protein interactions using a calmodulin-modified nanowire transistor. *Proceedings of the National Academy of Sciences of the United States of America*, 107(3):1047–1052, 2010.

## Bibliografia

---

- [118] L. F. Thompson and J. M. G. Cowie. Introduction to microlithography. *British Polymer Journal*, 18:280, 1986.
- [119] F. Laermer and A. Schilp. Plasma polymerizing temporary etch stop, March 26 1996. US Patent 5,501,893.
- [120] R.M.Y. Ng, T. Wang, F. Liu, X. Zuo, J. He, and M. Chan. Vertically stacked silicon nanowire transistors fabricated by inductive plasma etching and stress-limited oxidation. *Electron Device Letters, IEEE*, 30(5):520–522, 2009.
- [121] M. De Marchi. *Polarity Control at Runtime: from Circuit Concept to Device Fabrication*. PhD thesis, EPFL, Lausanne (CH), 2015.
- [122] E. Herr and H. Baltes. {KOH} etching of high-index crystal planes in silicon. *Sensors and Actuators A: Physical*, 31(1–3):283 – 287, 1992. Proceedings of Eurosensors V.
- [123] D.B.A. Van, J. Bomer, E.T. Carlen, S. Chen, R.A. Kraaijenhagen, and H.M. Pinedo. Method for manufacturing a single crystal nano-wire., June 20 2012. EP Patent App. EP20,100,745,680.
- [124] S. Chen, J.G. Bomer, W.G. van der Wiel, and A. van den Berg E.T. Carlen. Top-Down Fabrication of Sub-30 nm Monocrystalline Silicon Nanowires Using Conventional Microfabrication. *ACS Nano*, 3(11):3485–3492, 2009.
- [125] G. Pennelli. Top down fabrication of long silicon nanowire devices by means of lateral oxidation. *Microelectronic Engineering*, 86(11):2139 – 2143, 2009.
- [126] T.S.Y. Moh, Y. Maruyama, C. Shen, G. Pandraud, L.C.PM.. de Smet, H.D. Tong, C. van Rijn, E.J.R. Sudholter, and P.M. Sarro. Ic compatible top down process for silicon nanowire fet arrays with three 100 surfaces for (bio) chemical sensing. In *Solid-State Sensors, Actuators and Microsystems Conference (TRANSDUCERS), 2011 16th International*, pages 1590–1593, 2011.
- [127] Center of MicroNanoTechnology (CMi) of EPFL. <https://cmi.epfl.ch/>.
- [128] Vistec EBPG5000 at CMi. [http://cmi.epfl.ch/ebeam/VistecEBPG5000\\_introduction.php](http://cmi.epfl.ch/ebeam/VistecEBPG5000_introduction.php).
- [129] Alcatel AMS200 SE at CMi. <http://cmi.epfl.ch/etch/AMS200.php>.
- [130] V.R. Manfrinato, L. Zhang, D. Su, H. Duan, R.G. Hobbs, E.A. Stach, and K.K. Berggren. Resolution limits of electron-beam lithography toward the atomic scale. *Nano Letters*, 13(4):1555–1558, 2013.
- [131] S. Lai, S. Srinivasan, R.J. Westerman, D. Johnson, and J.J. Nolan. Notch reduction in silicon on insulator (SOI) structures using a time division multiplex etch processes, 2005.

- [132] C.K. O'Sullivan and G.G. Guilbault. Commercial quartz crystal microbalances – theory and applications. *Biosensors and Bioelectronics*, 14(8–9):663 – 670, 1999.
- [133] I. Mannelli, M. Minunni, S. Tombelli, and M. Mascini. Quartz crystal microbalance (QCM) affinity biosensor for genetically modified organisms (GMOs) detection. *Biosensors and Bioelectronics*, 18(2–3):129 – 140, 2003.
- [134] J. Homola. Surface Plasmon Resonance Sensors for Detection of Chemical and Biological Species. *Chemical Reviews*, 108(2):462–493, 2008.
- [135] F. Häöök, A. Ray, B. Nordén, and B. Kasemo. Characterization of PNA and DNA Immobilization and Subsequent Hybridization with DNA Using Acoustic-Shear-Wave Attenuation Measurements. *Langmuir*, 17(26):8305–8312, 2001.
- [136] C. Stagni, C. Guiducci, L. Benini, B. Ricco, S. Carrara, B. Samori, C. Paulus, M. Schienle, and R. Thewes M. Augustyniak. CMOS DNA Sensor Array With Integrated A/D Conversion Based on Label-Free Capacitance Measurement. *Solid-State Circuits, IEEE Journal of*, 41(12):2956–2964, 2006.
- [137] N.J. Ronkainen, H.B. Halsall, and W.R. Heineman. Electrochemical biosensors. *Chemical Society Review*, 39:1747–1763, 2010.
- [138] S. Kober, G. Gotesman, and R. Naaman. Surprising Molecular Length Dependence in Conduction through a Hybrid Organic–Inorganic System. *The Journal of Physical Chemistry Letters*, 4(12):2041–2045, 2013.
- [139] L. Rämhildt. *Biochemical functionalization of silicon dioxide surfaces for sensing applications*. Technische Universität Dresden, Dresden, 2014.
- [140] G.-J. Zhang and Y. Ning. Silicon nanowire biosensor and its applications in disease diagnostics: A review. *Analytica Chimica Acta*, 749:1 – 15, 2012.
- [141] L.C.P.M. de Smet, D. Ullien, M. Mescher, and E.J.R. Sudhölter. *Organic Surface Modification of Silicon Nanowire-Based Sensor Devices*. Dr. abbass hashim edition, 2011.
- [142] V. Dugas, A. Elaissari, and Y. Chevalier. Surface Sensitization Techniques and Recognition Receptors Immobilization on Biosensors and Microarrays. In M. Zourob, editor, *Recognition Receptors in Biosensors*, pages 47–134. Springer New York, 2010.
- [143] J. Gibbs. In M. Zourob, editor, *Effective Blocking Procedures*, pages 1–6. Corning Incorporated Life Science, Kennebunk, ME.
- [144] K. Kato, Y. Umeda, F. Suzuki, and A. Kosaka. Improved reaction buffers for solid-phase enzyme immunoassay without interference by serum factors. *Clinica Chimica Acta*, 102:261–265, 1980.

## Bibliografia

---

- [145] R.V. Vogt Jr., D. L. Phillips, L. O. Henderson, W. Whitfield, and F. W. Spierto. Quantitative differences among various proteins as blocking agents for ELISA microtiter plates. *Immunological Methods*, 101:43–50, 1987.
- [146] M.M.A. Hakim, M. Lombardini, K. Sun, F. Giustiniano, P.L. Roach, D.E. Davies, P.H. Howarth, M.R.R. de Planque, H. Morgan, and P. Ashburn. Thin Film Polycrystalline Silicon Nanowire Biosensors. *Nano Letters*, 12(4):1868–1872, 2012.
- [147] A. Hoeben, B. Landuyt, M. Highley, H. Wildiers, A. V. Oosterom, and E. D. Bruijn. Vascular endothelial growth factor and angiogenesis. *Pharmacol Review*, 56(4):549–580, 2004.
- [148] Y. A. Muller, H. W. Christinger, B. A. Keyt, and A. M. de Vos. The crystal structure of vascular endothelial growth factor (vegf) refine to 1.93 Å resolution: multiple copy flexibility and receptor binding. *Pharmacol Review*, 5(10):1325–1338, 1997.
- [149] C.A.Jr. Janeway, P. Travers, M. Walport, and M.J. Shlomchik. *Immunobiology: The Immune System in Health and Disease (5 ed.)*. New York: Garland Science, 2001.
- [150] F. Puppò, M.-A. Doucey, M. Di Ventra, G. De Micheli, and S. Carrara. Memristor-based devices for sensing. In *Circuits and Systems (ISCAS), 2014 IEEE International Symposium on*, pages 2257–2260, 2014.
- [151] H. Li, J. Zhang, B. Tao, L.Wan, and W. Gong. Investigation of capacitive humidity sensing behavior of silicon nanowires. *Langmuir*, 41:600–604, 2009.
- [152] X. Chen, J. Zhang, Z. Wang, and S. Hui. Humidity sensing behavior of silicon nanowires with hexamethyldisilazane modification. *Sensors Actuators B*, 156:631–636, 2011.
- [153] S. Carrara, V. Erokhin, and C. Nicolini. STM image formation of organic thin films: The role of water shell. *Sensors Actuators B*, 16(16):6577–6582, 2000.
- [154] J. Bardeen. Surface States and Rectification at a Metal Semi-Conductor Contact. *Physical Review*, 71:717–727, 1947.
- [155] J.T.Jr. Yates. Surface chemistry of silicon-the behaviour of dangling bonds. *Journal of Physics: Condensed Matter*, 3(S):S143, 1991.
- [156] M. Krems, Y. Pershin, and M. Di Ventra. Ionic Memcapacitive Effects in Nanopores. *Nano Letters*, 10(7):2674–2678, 2010.
- [157] M.W. Shinwari, M.J. Deen, and D. Landheer. Study of the electrolyte-insulator-semiconductor field-effect transistor (EISFET) with applications in biosensor design. *Microelectronics Reliability*, 47(12):2025 – 2057, 2007.
- [158] Y. Paska and H. Haick. Interactive Effect of Hysteresis and Surface Chemistry on Gated Silicon Nanowire Gas Sensors. *ACS Applied Materials & Interfaces*, 4(5):2604–2617, 2012.



- [159] W. Kim, A. Javey, O. Vermesh, O. Wang, Y.M. Li, and H.J. Dai. Hysteresis Caused by Water Molecules in Carbon Nanotube Field-Effect Transistors. *Nano Letters*, 3(2):193–198, 2003.
- [160] G.E. Ewing. *Structure and Bonding*. Springer Verlag, Berlin Heidelberg, 2005.
- [161] G. Chung, C.C. Tin, J.R. Williams, K. McDonald, M. Di Ventra, R.K. Chanana, S.T. Pantelides, L.C. Feldman, and R.A. Weller. Effects of anneals in ammonia on the interface trap density near the band edges in 4h-silicon carbide metal-oxide-semiconductor capacitors. *Applied Physics Letters*, 77(22):3601–3603, 2000.
- [162] T.S.Y. Moh, M. Nie, G. Pandraud, L.C.P.M. de Smet, E.J.R. Sudhölter, Q.-A. Huang, and P.M. Sarro. Effect of silicon nanowire etching on signal-to-noise ratio of sinw fets for (bio)sensor applications. *Electronics Letters*, 49:782–784(2), June 2013.
- [163] R.T. Weitz, U. Zschieschang, F. Effenberger, H. Klauk, M. Burghard, and K. Kern. High-Performance Carbon Nanotube Field Effect Transistors with a Thin Gate Dielectric Based on a Self-Assembled Monolayer. *Nano Letters*, 7(1):22–27, 2007.
- [164] S.H. Jin, A. E. Islam, T. Kim, J. Kim, M.A. Alam, and J.A. Rogers. Sources of Hysteresis in Carbon Nanotube Field-Effect Transistors and Their Elimination Via Methylsiloxane Encapsulants and Optimized Growth Procedures. *Advanced Functional Materials*, 22(11):2276–2284, 2012.
- [165] T. Hanrath and B. A. Korgel. Influence of Surface States on Electron Transport through Intrinsic Ge Nanowires. *The Journal of Physical Chemistry B*, 109(12):5518–5524, 2005.
- [166] K. Schroder and J. A. Babcock. Negative bias temperature instability: Road to cross in deep submicron silicon semiconductor manufacturing. *Journal of Applied Physics*, 94(1):1–18, 2003.
- [167] M.K. Achuthan and K.N. Bhat. *Fundamentals of semiconductor devices*. Tata McGraw-Hill, New Delhi, India, 2007.
- [168] L.-A. Ragnarsson and P. Lundgren. Electrical characterization of  $P_b$  centers in (100)Si-SiO<sub>2</sub> structures: The influence of surface potential on passivation during post metallization anneal. *Journal of Applied Physics*, 88:938–942, 2000.
- [169] P.V. Gray and D.M. Brown. Density of SiO<sub>2</sub>-Si Interface States. *Applied Physics Letters*, 8:31–33, 1966.
- [170] E.H. Rhoderick and R.H. Williams. *Metal-Semiconductor Contacts*. Clarendon Press, Oxford, USA, 1988.
- [171] H.-L. Chu, S.-C. Chiu, C.-F. Sung, W. Tseng, Y.-C. Chang, W.-B. Jian, Y.-C. Chen, C.-J. Yuan, H.-Y. Li, F. X. Gu, M. Di Ventra, and C.-C. Chang. Density of SiO<sub>2</sub>-Si Interface States. *Nano Letters*, 14(2):1026–1031, 2014.

## Bibliografia

---

- [172] M. Zwolak, J. Wilson, and M. Di Ventra. Dehydration and ionic conductance quantization in nanopores. *Journal of Physics: Condensed Matter*, 22(45):454126, 2010.
- [173] H. Luth. *Solid Surfaces, Interfaces and Thin Films*. Springer-Verlag, Berlin, 2015.
- [174] A. Y. Tang, V. Drakinskiy, K. Yhland, J. Stenarson, T. Bryllert, and J. Stake. Analytical Extraction of a Schottky Diode Model from Broadband S-parameters. *IEEE Transactions on Microwave Theory and Techniques*, 61(5):1870–1878, 2013.
- [175] A.M. Goodman. Electron Hall effect in silicon dioxide. *Physical Review*, 164(3):1145–115, 1976.
- [176] R.C. Hughes. Hole mobility and transport in thin SiO<sub>2</sub> films. *Applied Physics Letters*, 26(8):436–438, 1975.
- [177] M. Pecht, R. Radojicic, and G. Rao. *Guidebook for Managing Silicon Chip Reliability*. CRC Press LLC, Boca Raton, Florida, 1998.
- [178] M. De Marchi, D. Sacchetto, S. Frache, J. Zhang, P. Gaillardon, Y. Leblebici, and G. De Micheli. Polarity control in double-gate, gate-all-around vertically stacked silicon nanowire fets. In *Electron Devices Meeting (IEDM), 2012 IEEE International*, pages 8–4, 2012.
- [179] S. Carrara. *Bio/CMOS Interfaces and Co-Design*. Springer, New York Heidelberg Dordrecht London, 2013.
- [180] C. Olá. On the theory of the alkaline error of the glass electrode. *Periodica Polytechnica*, IV(2):141 – 156, 1959.
- [181] B. He, T.J. Morrow, and C.D. Keating. Nanowire sensors for multiplexed detection of biomolecules. *Current Opinion in Chemical Biology*, 12(5):522–528, 2008.
- [182] D. R. Kim and X. Zheng. Numerical Characterization and Optimization of the Microfluidics for Nanowire Biosensors. *Nano Letters*, 8(10):3233–3237, 2008.
- [183] J.C. McDonald, D.C. Duffy, J.R. Anderson, D.T. Chiu, H. Wu, O.J. Schueller, and G.M. Whitesides. Fabrication of microfluidic systems in poly(dimethylsiloxane). *Electrophoresis*, 21(1):27–40, 2000.
- [184] J.C. McDonald and G.M. Whitesides. Poly(dimethylsiloxane) as a Material for Fabricating Microfluidic Devices. *Accounts of Chemical Research*, 35(7):491–499, 2002.
- [185] J.N. Lee, C. Park, and G.M. Whitesides. Solvent Compatibility of Poly(dimethylsiloxane)-Based Microfluidic Devices. *Analytical Chemistry*, 75(23):6544–6554, 2003.
- [186] C.-H. Lin, G.-Bi. Lee, B.-W. Chang, and G.-L. Chang. A new fabrication process for ultrathick microfluidic microstructures utilizing SU-8 photoresist. *Journal of Micromechanics and Microengineering*, 12(5):590, 2002.

- 
- [187] H. Lorenz, M. Despont, N. Fahrni, N. LaBianca, P. Renaud, and P. Vettiger. SU-8: a low-cost negative resist for MEMS. *Journal of Micromechanics and Microengineering*, 7(3):121, 1997.
- [188] S.C. Wong, H.C. So, J.H. Ou, and J. Costello. A 5000-gate CMOS EPLD with multiple logic and interconnect arrays. In *Custom Integrated Circuits Conference, 1989, [P]roceedings of the IEEE 1989*, pages 5.8/1–5.8/4, 1989.
- [189] M. Yoshimoto, K. Anami, H. Shinohara, T. Yoshihara, H. Takagi, S. Nagao, S. Kayano, and T. Nakano. A divided word-line structure in the static RAM and its application to a 64k full CMOS RAM. *Solid-State Circuits, IEEE Journal of*, 18(5):479–485, 1983.
- [190] D.A. Huffman. A method for the construction of minimum-redundancy codes. *Resonance*, 11(2):91–99.
- [191] H. Peng, L. Fulmi, and C. Ding. Feature selection based on mutual information criteria of max-dependency, max-relevance, and min-redundancy. *Pattern Analysis and Machine Intelligence, IEEE Transactions on*, 27(8):1226–1238, 2005.
- [192] P. Allavena and A. Mantovani. Immunology in the clinic review series; focus on cancer: tumour-associated macrophages: undisputed stars of the inflammatory tumour microenvironment. *Clinical and Immunological Oncology*, 167:195–205, 2012.
- [193] K.B. Long and G.L. Beatty. Harnessing the antitumor potential of macrophages for cancer immunotherapy. *OncImmunity*, 2(12):e26860(1–9), 2013.
- [194] C. Guo, A. Buranych, D. Sarkar, P.B. Fisher, and X.Y. Wang. The role of tumor-associated macrophages in tumor vascularization. *Vascular Cell*, 5(20):1–12, 2013.
- [195] J. Cook and T. Hagemann. Tumour-associated macrophages and cancer. *Current Opinion in Pharmacology*, 13(4):595 – 601, 2013.



- 04.2012 **Ph.D. in Microsystems and Microelectronics**
- 04.2016 Integrated Systems Laboratory École Polytechnique Fédérale de Lausanne, (EPFL), Lausanne (CH)
- 09.2008 **Master of Science, Neuroengineering**
- 07.2011 University of Genoa (UNIGE), Genoa (IT)  
Grade: 110/110 Summa Cum Laude
- 09.2005 **Bachelor of Science, Biomedical Engineering**
- 10.2008 University of Genoa (UNIGE), Genoa (IT)  
Grade: 110/110

- 04.2015 **Visiting Scholar, Department of Physics, UCSD**
- 09.2015 University of California, San Diego, California (USA)  
**Exchange Research Project:**  
Physics-based modeling of a novel biosensing approach based on memristive effects in Silicon Nanowires (SiNWs), the VoG-biosensors
- 04.2012 **Research Bioengineer and Doctoral Candidate**
- 04.2016 Integrated Systems laboratory (LSI), EPFL  
École Polytechnique Fédérale de Lausanne (EPFL), Lausanne (CH)  
**Ph.D. Thesis:**  
*"SiNW-based Biosensors for Profiling Biomarkers in Breast Tumor Extract"*
  - Top-down fabrication of CMOS compatible SiNWs
  - Study and electrical characterization of memristive SiNWs an SiNW Field Effect Transistors (SiNW-FETs)
  - Silicon bio-functionalization
  - Femtomolar detection of cancer markers in breast tumor
- 09.2010 **Exchange Master Student, Research Intern**
- 06.2011 **Master Project - awarded of a 9-month scholarship**  
Integrated Systems laboratory (LSI), EPFL  
**Master Thesis:**  
*"Design, fabrication and feasibility study of a Carbon Nanotube Filled Effect Transistors (CNT-FETs) array to provide biosensing based on the P450 cytochrome"*
  - Microfabrication of a biosensor based on a CNT-FETs array
  - Langmuir-Blodgett self-assembly of CNTs
  - Electrochemical based sensing of drugs (voltammetry)

16.2012 **Research Intern at the Department of Biophysics and Electronic Engineering**  
 04.2016 **(DIBE)**, University of Genoa (IT)

**Bachelor Thesis:**

*"The problems of multiple disparities detection: a computational model of cortical neural networks in the perception of the world through transparencies"*

- Analysis of biological visual processing
- Implementation and testing of a new algorithm emulating the ability of cortical neurons to perceive the world through transparent surfaces

**Journal articles:**

- [1] F. Puppo, A. Dave, M.-A. Doucey, D. Sacchetto, C. Baj-Rossi, Y. Leblebici, G. De Micheli, and S. Carrara, *Memristive Biosensors Under Varying Humidity Conditions*, *IEEE Transactions on NanoBioscience*, 13(1), 19-30, 2014 (doi:10.1109/TNB.2013.2295517).
- [2] F. Puppo, M. Di Ventra, G. De Micheli, and S. Carrara, *Memristive sensors for pH measure in dry conditions*, *Surface Science*, 624, 76-79, 2014 (DOI: 10.1016/j.susc.2014.01.016).
- [3] F. Puppo, M.-A. Doucey, J.-F. Delaloye, T.S. Moh, G. Pandraud, P.M. Sarro, G. De Micheli, and S. Carrara, *SiNW-FET in-Air Biosensors for High Sensitive and Specific Detection in Breast Tumor Extract*, *Sensor Journals, IEEE*, vol. PP(99), 2015 (DOI: 10.1109/JSEN.2015.2433836).
- [4] I. Tzouvadaki, F. Puppo, M.-A. Doucey, G. De Micheli, and S. Carrara, *Computational Study on the Electrical Behavior of Silicon Nanowire Memristive Biosensors*, *Sensor Journals, IEEE*, vol.15 (11), 6208-6217, 2015.(DOI: 10.1109/JSEN.2015.2456336)
- [5] F. Puppo, F.L. Traversa, M. Di Ventra, G. De Micheli, S. Carrara, *Surface trap mediated electronic transport in bio-functionalized silicon nanowires*, submitted to *ACS Nano*.

**Conference articles:**

- [6] F. Puppo, M.-A. Doucey, T.S.Y. Moh, G. Pandraud, P.M. Sarro, G. De Micheli, and S. Carrara, *Femto-Molar Sensitive Field Effect Transistor Biosensors Based on Silicon Nanowires and Antibodies*, *Proceedings of the IEEE Sensors 2013*, Baltimore, Maryland, USA, Nov. 4-6, 2013 (DOI: 10.1109/ICSENS.2013.6688205).
- [7] F. Puppo, M.-A. Doucey, M. Di Ventra, G. De Micheli, and S. Carrara, *Memristor-Based Devices for Sensing*, *IEEE International Symposium on Circuits and Systems (ISCAS) 2014*, Melbourne, Australia, June 1-5, 2014 (DOI: 10.1109/ISCAS.2014.6865620).
- [8] A. Zaher, F. Puppo, P. Häfliger, G. De Micheli, S. Carrara, *Novel Readout Circuit for Memristive Nanowire Cancer Detection Sensors*, *IEEE Biomedical Circuits and Systems Conference (BioCAS2014)* Lausanne, Switzerland, 2013 (DOI: 10.1109/BioCAS.2014.6981759).
- [9] F. Puppo, M.-A. Doucey, J.-F. Delaloye, T.S. Moh, G. Pandraud, P.M. Sarro, G. De Micheli, and S. Carrara, *High Sensitive Detection in Tumor Extracts with SiNW-FET in-Air Biosensors*, *Proceedings of the IEEE Sensors 2014*, Valencia, Spain, Nov. 3-5, 2014 (DOI:10.1109/ICSENS.2014.6985137) [Among 5% Best Selected Papers invited to journal special issue].
- [10] L. Ardan, F. Puppo, D. Demarchi, M.-A. Doucey, G. De Micheli, and S. Carrara, *Reliable Redundancy with Memristive-Biosensors to achieve Statistical Significance in Immunosensing*, *Proceedings of the 6th IEEE International Workshop on Advances in Sensors and Interfaces (IWASI)*, 2015 (10.1109/IWASI.2015.7184969).
- [11] I. Tzouvadaki, F. Puppo, M.-A. Doucey, G. De Micheli and S. Carrara, *Modeling Memristive Biosensors*, *IEEE Sensors 2015*, Busan, South Korea, 2015.
- [12] I. Tzouvadaki, A. Vallero, F. Puppo, G. De Micheli and S. Carrara, *Resistance impact on the electrical behavior of Memristive Biosensors due to external electrodes*, accepted for presentation at the *IEEE International Symposium on Circuits and Systems (ISCAS) 2016*, Montreal, Canada (USA), May 22-5, 2016.

